Kinematic Evolution, Metamorphism and Exhumation of the Greater Himalayan Sequence, Mount Everest Massif, Tibet/Nepal

Micah John Jessup

Dissertation submitted to the faculty of the Virginia Polytechnic Institute and State University in partial fulfillment of the requirements for the degree of

Doctor of Philosophy in Geosciences

Committee
Richard D. Law
Michael P. Searle
Robert J. Tracy
James A. Spotila

April 30, 2007
Blacksburg, VA

Keywords: mean kinematic vorticity, pressure-temperature paths, kinematic analysis, structure, tectonics, metamorphism, Himalayas, Tibetan plateau, exhumation

Kinematic Evolution, Metamorphism and Exhumation of the Greater Himalayan Sequence, Mount Everest Massif, Tibet/Nepal

Micah John Jessup

ABSTRACT

The Himalayan orogen provides an incredible natural laboratory to test models for continent-continent collision. The highest peaks of the Himalayas are composed of the Greater Himalayan Sequence (GHS), which is bound by a north-dipping low angle detachment fault above (South Tibetan detachment; STD) and by a thrust fault below (Main Central thrust; MCT). Assuming simultaneous movement on these features, the GHS can be modeled as a southward extruding wedge or channel. Channel flow models describe the coupling between mid-crustal flow, driven by gradients in lithostatic pressure between the Tibetan Plateau and the Indian plate, and focused denudation on the range front. Although the general geometry and shear sense criteria for these bounding shear zones has been documented, prior to this investigation, relatively few attempts had been made to quantify the spatial and temporal variation in flow path history for rocks from an exhumed section of the proposed mid-crustal channel. Results from this investigation demonstrate that mid-crustal flow at high deformation temperatures was distributed throughout the proposed channel. As these rocks began to exhume to shallower crustal conditions and therefore lower temperatures, deformation began to become partitioned away from the core of the channel and into the bounding shear zones. Based on these results a new method (Rigid Grain Net) to measure the relative contributions of pure and simple shear (vorticity) is proposed. Detailed thermobarometric analysis was conducted on rocks from the highest structural level in the Khumbu region, Nepal to construct pressure-temperature-time-deformation paths during the tectonic evolution of the GHS between ~32-16 Ma. Another aspect of the project suggests that the most active feature of the region is the N-S trending Ama Drime Massif (ADM). By combining new structural interpretation with existing remote sensing data this investigation proposes that the ADM is being exhumed during extension that is coupled with denudation in the trans-Himalayan Arun River gorge. Together these data provide important insights into the dynamic links between regional-scale climate and crustal-scale tectonics.

In memory of

John B. Reid

for opening my eyes to science

ACKNOWLEDGEMENTS

"To dabble fatuously in trivialities in the face of Everest's grandeur would be sacrilege"

Captain John Noel, 1928

"If by some fiat I had to restrict all this writing to one sentence, this is the one I would choose: The summit of Mt. Everest is marine limestone."

John McPhee, Basin and Range, 1981

Since I first visited the Karakoram Range in northern Pakistan with a small international climbing expedition, during my second year at Hampshire College (1994) I aspired to develop the skills necessary to conduct Himalayan tectonics research. Many people and resources enabled me to fulfill this long-standing goal that is represented, in part, by this dissertation.

First and foremost, John B. Reid, to which this dissertation is dedicated, who introduced me to the scientific inquiry as a first year undergraduate at Hampshire College. John's enthusiasm and mentoring breathed time-scales and processes into landscapes that I had never appreciated before. Mike Williams taught me structural geology and tectonics at the University of Massachusetts. Mike encouraged me to pursue graduate school and connected me with Karl E. Karlstrom at the University of New Mexico.

Karl Karlstrom taught me how to map and transition from micro-to macro-scale thinking. He also provided a research group of peers with an incredible synergy including Amada Tyson, Mark Quigley, Mike Timmons, Colin Shaw and Annie McCoy. Karl invested an enormous amount of energy to help me develop my thoughts and clarify my presentation of complex concepts. Colin Shaw, now at the University of Montana, had a critical role in masterminding and writing the successful National Science Foundation proposal that funded my research project in the Black Canyon of the Gunnison, Colorado. During my master's program I was also fortunate to work closely with Jane Selverstone and join two of her students, Kurt Stephen and Jaime Barnes, on a trip to the Griner shear zone in the Alps, during which I gained an immense appreciation for the inseparable connection between metamorphism and deformation.

As co-advisors, Rick Law and Mike Searle, have been invaluable. Rick's meticulous attention to detail and Mike's indulgence in tectonic-scale thinking created an incredible balance and powerful combination to cultivate my taste for Himalayan tectonics. Mike's open invitation to spend as much time as possible at Oxford learning from him and his research group proved to be one of my most intellectually satisfying experiences. Dinner at the high table of Worcester College, morning and afternoon tea in the Earth Sciences department, and pints at the Rose and Crown will always resound as good memories. Dave Water's willingness to tutor me in THERMOCALC and shared enthusiasm for pursuing the elusive Everest Series established a challenging but rewarding interaction. Bob Tracy's process orientated approach to metamorphism and willingness to teach me how to use the electron microprobe and scanning electron microscope have ensured that our thermobarometric calculations and interpretations are of the highest caliber. Jim Spotila watched my interests develop and nurtured my curiosity about geomorphology and neotectonics that culminated in my research project on the Ama Drime Massif.

I was fortunate to collaborate with a group of peers while at Virginia Tech to whom I owe thanks. Ryan Thigpen was great for bouncing ideas off of and brainstorming about various aspects of vorticity analysis. Victor Lygois helped with my initial probe analysis in 2004. Clayton Loehn and I spent many hours pouring over probe data for thermobarometry and in situ monazite geochronology. Although they were enrolled at different universities, Dennis Newell (University of New Mexico) and John Cottle (Oxford University) were incredible peers. During our projects together, we began to apply a novel approach to addressing fundamental questions about the Himalayan orogenic system by integrating structure, metamorphism, U-Th-Pb geochronology and isotopic geochemistry of spring water. Through our grassroots collaboration we have etched out our own space in the, often critical and clubby, Himalayan scientific community as well as laid a solid foundation for many future projects.

Interaction with Tibetans and Nepalese is one of the most rewarding aspects of Himalayan research expeditions. Our Tibetan guide and friend, Sonam Wangdu's wit, insight, patience, generosity, and exceptional cooking have brought me through many arduous treks, frustrating yaks and broken jeeps. For one day, I am particularly indebted to Sonam. After summating a minor peak, John, Dennis and I became separated from the rest of the group and we were forced to bivouac at ~5000m in the Ama Drime range. Sonam managed to find us late the following day, as we were committing to our second cold bivouac in a cave without food.

Tashi Sherpa, who lives in Kathmandu, has helped with logistics for organizing our trips and has always welcomed us to his home. Sitting on Tashi's roof in the foothills of the Himalayas on a warm afternoon drinking a San Miguel is a perfect place to let the hardships of the previous expedition slip away and metamorphose into good stories for the pub. In addition, Dawa Sherpa, helped us as a porter and guide in 2004 to the Khumbu region and enabled us to complete an incredible west-east traverse in the Khumbu from Chukuhm to the Chame valley and across the Nangpa La to peer into Tibet.

Finally, my friends and family have been an incredible source of support and encouragement throughout all of my life's endeavors including this dissertation. My fiancée, Laura, is a wonderful part of my life and has provided her tireless support throughout this project.

ATTRIBUTIONS

Chapter two was published as "Jessup, M.J., Law, R.D., Searle, M.P. & Hubbard, M.S. (2006) Structural evolution and vorticity of flow during extrusion and exhumation of the Greater Himalayan Slab, Mount Everest Massif, Tibet/Nepal: implications for orogen-scale flow partitioning. In: Law, R.D., Searle, M.P. & Godin, L. (eds) *Channel Flow, Extrusion, and Exhumation in Continental Collision Zones*. Geological Society, London, Special Publications, 268, 379-414. M.J. Jessup was responsible for collecting the samples in Tibet and Nepal and conducting the majority of the vorticity analyses. R.D. Law helped conceive the original project, conducted some of the vorticity analysis, particularly the Everest summit samples from the pioneering British expeditions that are archived at Oxford and Cambridge Universities. R.D. Law also wrote the microstructural descriptions of these samples since they were inaccessible to M.J. Jessup. M.J. Jessup was responsible for drafting all the figures and writing the manuscript. M.P. Searle helped conceive the original project and collected samples during 2003 and 2004 research expeditions to the three sides of Mt Everest. M.S. Hubbard provided samples from her research on the Main Central Thrust zone.

Chapter three was published as "Jessup, M.J., Law, R.D. & Frassi, C. (2007) The Rigid Grain Net (RGN); An alternative method for estimating mean kinematic vorticity (W_m). *Journal of Structural Geology* 29, 411-421. M.J Jessup conceived the project, was responsible for data acquisition, drafting figures and writing text. R.D. Law contributed his expertise in vorticity analysis and helped clarify the text and figures. C. Frassi helped develop the original idea and was involved in brain storming sessions that culminated in this manuscript.

Chapter four was submitted to *Journal of Metamorphic Geology* "Jessup, M.J., Searle, M.P., Cottle, J.M., Law, R.D., Tracy, R.J., Newell, D.L. & Waters, D.J. P-T-t-D paths of the Everest Series schist, Nepal." M.J. Jessup was responsible for conceiving the project, writing the text, drafting the figures and data acquisition. M.P. Searle helped develop the hypothesis and tie the results into the remainder of the Everest region. J.M. Cottle dated the Nuptse granite and helped collect samples in 2004. R.D. Law helped develop the hypothesis and clarify sections of the text. R.J. Tracy helped teach M.J. Jessup how to use the electron microprobe and scanning electron microprobe. R.J. Tracy also helped interpret the electron microprobe data. D.L. Newell helped collect samples in 2004. D.J. Waters taught M.J. Jessup how to use the program THERMOCALC.

Chapter five was a proposal submitted by M.J. Jessup to the National Science Foundation International Research Fellowship program entitled "Exhumation of the Ama Drime Massif during east-west extension coupled with focused denudation in a trans-Himalayan river gorge; testing the Himalayan paradigm." M.J. Jessup was responsible for conceiving the project, writing the text and drafting the figures.

Chapter 6 was submitted to *Geology* "Jessup, M.J., Newell, D.N. & Cottle, J.M. Coupled crustal extension, exhumation and denudation in the trans-Himalayan Arun River Gorge, Ama Drime Massif, Tibet-Nepal." M.J. Jessup conceived the project, wrote the text and drafted the figures. D.N. Newell and J.M. Cottle helped develop the hypothesis and conducted fieldwork in 2005 and 2006.

TABLE OF CONTENTS

LIST OF FIGURES

CHAPTER 2

CHAPTER 3

CHAPTER 4

CHAPTER 5

LIST OF TABLES

GRANT INFORMATION

2010 Fellowship from the College of Science, Virginia Tech
Geological Society of America Research Grant
Southeastern Section of the Geological Society of America Research Grant
W. D. Lowry Geosciences Graduate Research Award, Virginia Tech
Sigma Xi Research Grant
Graduate Research and Development Program Grant, Virginia Tech
American Alpine Club Research Grant
National Science Foundation Grant EAR 0207524 to R.D. Law and M.P. Searle
National Science Foundation Supplementary Grant EAR 0608599 to R.D. Law

CHAPTER 1

Introduction

Pioneering attempts to merge geological and geophysical data with the distribution of focused denudation from the Himalayan orogenic system culminated in channel flow models that described the relationship between lateral flow of mid-crustal rocks and their exhumation to the surface as related to focused denudation along the orogenic front. Channel flow models propose southward extrusion of a low viscosity mid-crustal channel beneath the Tibetan plateau that is driven by gradients in lithostatic pressure between the high elevation of Tibet and lowlands of the Indian plate. The mid-crustal channel is exhumed to the surface as a slab of migmatitic rocks *via* focused denudation along the orogenic front of the Himalayas. Movement during the early tunneling stage as well as the exhumation of this mid-crustal slab are accommodated by coeval movement, during the Miocene, on two shear zones; the South Tibetan detachment system (STDS) above and the Main Central thrust zone below (MCTZ).

Many orogen-scale kinematic and thermal-mechanical extrusion models have been proposed to describe the general concept of extrusion during crustal convergence. However, relatively few investigations have attempted to quantify the kinematics (vorticity) of flow within the slab and explore its relationship with progressive exhumation of the Greater Himalayan Sequence (GHS). The initial focus of this dissertation stemmed directly from an NSF proposal written by R.D. Law and M.P. Searle, who argued that through an integration of petrofabric, vorticity and microstructural analysis, the spatial and temporal variations in flow path history of these rocks could be quantified and thereby contribute to the development of future models.

A portion of these results are presented in Chapter 2, "*Structural evolution and vorticity of flow during extrusion and exhumation of the Greater Himalayan Slab, Mount Everest Massif, Tibet/Nepal: implications for orogen-scale flow partitioning*", which was published in Geological Society Special Publication 268 in 2006. Our work demonstrates that flow was spatially and temporally partitioned throughout the slab. Polyphase folding, similar to that in many other orogenic belts, dominated the core of the slab until ~24 Ma when a fundamental switch occurred. At this time, deformation shifted to the margins of the slab where intense shearing of the bounding faults created extensive mylonite zones.

We applied established techniques to determine mean kinematic vorticity number (W_m), a measure of the relative contributions of pure and simple shear (W_m; where W_m = 1.0 for simple shear, W_m = 0 for pure shear, and pure shear = simple shear at W_m = 0.71). Our results demonstrate that extrusion beneath the STDS - a passive roof fault - at the top of the slab was dominated by simple shear (0.74-0.91; 45-28% pure shear). Amphibolite facies gneisses (Rongbuk formation) at slightly deeper structural levels recorded higher contributions of pure shear (W_m = 0.57-0.85; 62-35 % pure shear) while the base of the slab (Main Central thrust) records higher contributions of pure shear (W_m = 0.63-0.77; 58-44% pure shear). We attribute the highest contributions of pure shear within the MCTZ to increased lithostatic pressure created by the overlying GHS of the hangingwall. Furthermore, we interpreted our observations within the STDS as the record of a juxtaposition of rocks from a deeper structural position (amphibolite facies gneisses; higher contribution of pure shear) with greenschist facies rocks (Everest Series schist, calc-silicate, marbles) and sheared limestone (highest contribution of simple shear) during exhumation.

We encountered several difficulties while testing the hypothesis of the original NSF proposal, three of which I will mention here: 1) The proposed vorticity techniques rely on samples that contain rigid porphyroclasts that are surrounded by a ductile matrix. However, rocks in the high-grade core of the GHS reached significant enough temperatures that mineral phases (feldspar) that remained rigid at lower temperatures record evidence for plastic deformation. This problem resulted in our data acquisition being limited to the bounding shear zones instead of throughout the entire GHS. 2) The original proposal included the application of three “independent” vorticity techniques (PHD, Wallis and Passchier) to test the consistency of these results. Two of these techniques (PHD and Passchier) rely on the presence of sigma-and delta-type recrystallized tails on rigid porphyroclasts while the other (Wallis) uses tailless grains. Unfortunately, most of the samples from the Everest transect lack the appropriate tails and are therefore limited to a single rigid grain vorticity technique (Wallis). 3) Many of the samples that we processed from the Everest transect were pushing the limits of the rigid grain assumptions, including grain interaction and high contrast between a rigid phase and the ductile matrix, particularly those from the deepest structural positions. When data from these types of samples are plotted, the transition that defines W_m is often gradual instead of abrupt, making interpretations of the results ambiguous.

In response to the last two above mentioned problems, we pioneered a new vorticity technique that unified the three main existing methods (PHD, Wallis and Passchier), which is presented the Chapter 3, *“The Rigid Grain Net (RGN): An alternative method for estimating mean kinematic vorticity (W_m)”* and published in the March, 2007 issue of the Journal of Structural Geology. We created the Rigid Grain Net (RGN) by plotting semi-and full-hyperbolas that define the relationship between aspect ratio, angle of the long axis from the foliation and W_m during the rotation of porphyroclasts in a ductile matrix. Through the RGN, we unified the existing vorticity methods by treating all of the porphyroclasts as tailless. We also demonstrated that the RGN provides a more robust means to define the critical threshold between porphyroclasts that rotate infinitely and those that reach a stable sink positions; the unique point that defines vorticity. The RGN eliminates ambiguity in defining this critical threshold because it provides a net of the predicted orientation of theoretical porphyroclasts against which natural more complex data set can be compared. The RGN can be imported into an Excel© worksheet where data can be easily plotted and manipulated and will potentially help standardized future investigations.

Chapter 4, *"P-T-t-D paths of the Everest Series schist, Nepal"*, was submitted to the Journal of Metamorphic Geology in March, 2007. The Everest Series schist and calc-silicates represent the highest structural position in the Everest region. Previous investigations focused on the more accessible Main Central Thrust zone and high-grade anatectic core of the area. To quantify the *P-T-t-D* history of the Everest Series schist, we have integrated traditional thermobarometry, THERMOCALC and structural analysis, with U-Th-Pb geochronology. These results suggest that the margins of the Greater Himalayan Sequence (GHS) record an early high *P* moderate *T* metamorphism whereas the core is dominated by low *P* high *T* metamorphism associated with decompression. To constrain the maximum age of movement on a major detachment that accommodated the southward extrusion of the GHS, John Cottle dated the Nuptse granite, the largest leucogranite body at the top of the GHS in the Everest region. We combine our detailed investigation at the top of the GHS with a synthesis of ~20 years of *P-T-t* work in the region to generate a new, more holistic model for the *P-T-t-D* evolution of this section of the Himalayas, including an improved definition of the Lhotse detachment; a controversial structural feature that is essentially inaccessible in its type-locality.

Recently, my Ph.D. project has expanded to lay the foundation for future research projects that will focus on a new aspect of the Himalayas that stems from my last two field seasons (2005 and 2006) in Tibet. During these trips, I came to realize that although the Everest transect represents a "classic" transect through the Himalaya, including incredible exposure of the GHS, MCTZ and STDS; these features are inactive today. If channel flow models are used to describe the coupling of the mid-crustal flow, as inferred from interpretation of partial melt zones beneath the Tibetan plateau, with focused denudation on the topographic front of the range, than the faults and shear zones proposed to link these modern signatures should also be active. Therefore, since the STDS and MCTZ are inactive, another set of active faults must couple this system.

Chapter 5, *"Exhumation of the Ama Drime Massif during east-west extension coupled with focused denudation in a trans-Himalayan river gorge; testing the Himalayan paradigm"* is a rejected proposal for a National Science Foundation International Research Fellowship to work with Mike Searle at Oxford University and Andy Carter at the London Thermochronology Research Group. This proposal represents my first attempt at writing and submitting a proposal and will provide the foundation for future proposals to the Tectonics division of NSF. It proposes an integration of field- and lab-based structural analysis and low-temperature thermochronology on samples collected during 2005 and 2006 to test the following novel hypothesis: *Driven by the local extensional stress field, the Ama Drime range - potentially the most active feature in the Everest region - is being exhumed as a core complex with exhumation being enhanced by focused precipitation in the Arun River gorge.*

The Ama Drime Massif (ADM) protrudes 70 km north from the crest of the Himalayas, narrows from 35 to 1 km in width from south to north. 300 m wide, N-S striking shear zones and active normal faults, we term the Ama Drime Detachment (ADD), bound the ADM and offset the South Tibetan detachment. The ADD preserves a progression from a distributed shear zone through mylonites and into discrete detachments – all of which record east-west extension. Active normal faults within the ADD offset lacustrine, fluvial and alluvial deposits. The footwall of the ADD includes the deepest structural position exposed in the central Himalayas, as recorded by eclogite bearing lenses, granulitic mafic layers and migmatitic augen gneiss (Cottle et al., *submitted*). Hot springs along the western limb and nose of the ADD suggest that the modern structure is tapping into warm, upwelling lower crustal material (Newell et al. *submitted*). Major rivers are displaced around the ADM in valleys filled by alluvium, except where they cross into the footwall block where they are marked by bedrock gorges. The Arun River gorge begins at the knick point on the southern end of the ADM where the drainage crosses the western limb of the ADD into the footwall block. Previous investigations suggest that, south of this point, the Arun River follows the crest of the Arun antiform. Furthermore, it has been suggested that the Arun River gorge is spatially related to focused denudation and elevated erosion index, relative to the surrounding area, resulting in a mini tectonic aneurysm. We propose that the ADM is a core complex that juxtaposes a deep crustal block with the GHS during active east-west extension. Exhumation of the southern end of the core complex is enhanced by focused denudation in the Arun River gorge. Thus, the ADM is an active feature within this section of the Himalayas and exists due to focused denudation and exhumation coupled with east-west extension; not shortening. This hypothesis is presented in Chapter 6, *Coupled crustal extension, exhumation and denudation in the trans-Himalayan Arun River Gorge, Ama Drime Massif, Tibet-Nepal*, which was submitted to Geology in March, 2007.

Manuscripts generated by aspects of this dissertation

<u>First author</u>

Jessup, M.J., Law, R.D., Searle, M.P. & Hubbard, M.S. (2006) Structural evolution and vorticity of flow during extrusion and exhumation of the Greater Himalayan Slab, Mount Everest Massif, Tibet/Nepal: implications for orogen-scale flow partitioning. In: Law, R.D., Searle, M.P. & Godin, L. (eds) *Channel Flow, Extrusion, and Exhumation in Continental Collision Zones*. Geological Society, London, Special Publications, 268, 379-414.

Jessup, M.J., Law, R.D. & Frassi, C. (2007) The Rigid Grain Net (RGN): An alternative method for estimating mean kinematic vorticity (W_m): *Journal of Structural Geology*, 29, 411-421.

Jessup, M.J., Searle, M.P., Cottle, J.M., Law, R.D., Tracy, R.J., Newell, D.L. & Waters, D.J. (*submitted 2007*) Metamorphic and microstructural evolution of the Everest Series, Mount Everest Massif, Tibet-Nepal. Submitted to *Journal of Metamorphic Geology*.

Jessup, M.J., Newell, D.N., & Cottle, J.M., (*submitted 2007)* Coupled crustal extension, exhumation and denudation in the trans-Himalayan Arun River Gorge, Ama Drime Massif, Tibet-Nepal: Submitted to *Geology*.

<u>Coauthor</u>

Searle, M.P., Law, R.D. & Jessup, M.J. (2006) Crustal structure, restoration and evolution of the Greater Himalaya: implication for channel flow and ductile extrusion of the middle crust: In Law, R.D., Searle, M.P. & Godin, L. (eds) *Channel Flow, Extrusion, and Exhumation in Continental Collision Zones*. Geological Society, London, Special Publications, 268, 355-378.

Cottle, J.M., Jessup, M.J., Newell, D.L, Searle, M.P., Law, R.D., & Noble, S.R. (*in review)* Structural Evolution of the South Tibetan Detachment System, Dzakaa Chu section, Kharta region, Eastern Himalaya. Submitted to *Journal of Structural Geology*.

Newell, D.L., Jessup, M.J., Cottle, J.M., Hilton, D.R., Fischer, T. & Sharp, Z. (*submitted*) Mineral springs of southern Tibet: a geochemical window into three structural levels of the lithosphere beneath the Tibetan plateau. Submitted to *Earth and Planetary Science Letters*.

Cottle, J.M., Noble, S.R, Jessup, M.J., Newell, D.L, Parrish, R.R., & Waters, D.J. (*submitted*) Structure, petrology and high precision U-Th-Pb geochronology of eclogites from the Ama Drime Massif, Southern Tibet. Submitted to *Earth and Planetary Science Letters*.

Searle, M.P., Law, R.D., Jessup, M.J., Streule, M.J., Cottle, J.M., Godin, L. & Larson, K. (*in prep*) Defining the Himalayan Main Central Thrust in Nepal. In preparation for the *Geological Society of London*.

CHAPTER 2

Structural evolution and vorticity of flow during extrusion and exhumation of the Greater Himalayan Slab, Mount Everest Massif, Tibet/Nepal: implications for orogen-scale flow partitioning

MICAH J. JESSUP [1], RICHARD D. LAW [1], MICHAEL P. SEARLE[2] & MARY S. HUBBARD[3]

[1.] *Department of Geosciences, Virginia Tech, Blacksburg, Virginia 24061, USA*
[2.] *Department of Earth Sciences, Oxford University, Oxford OX1 3PR, UK*
[3.] *Department of Geology, Kansas State University, Manhattan, Kansas 66506, USA*

Published December 2006 in: LAW, R. D., SEARLE, M. P. & GODIN, L. (eds) *Channel Flow, Ductile Extrusion, and Exhumation in Continental Collision Zones*. Geological Society, London, Special Publications, **268**, 379-413.

Abstract

The Greater Himalayan Slab (GHS) is composed of a north-dipping anatectic core, bounded above by the South Tibetan detachment system (STDS) and below by the Main Central thrust zone (MCTZ). Assuming simultaneous movement on the MCTZ and STDS, the GHS can be modeled as a southward extruding wedge or channel. New insights into extrusion-related flow within the GHS emerge from detailed kinematic and vorticity analyses in the Everest region. At the highest structural levels, mean kinematic vorticity number (W_m) estimates of 0.74-0.91 (c.45-28% pure shear) were obtained from sheared Tethyan limestone and marble from the Yellow Band on Mount Everest. Underlying amphibolite facies schists and gneisses, exposed in Rongbuk valley, yield W_m estimates of 0.57 - 0.85 (c.62-35% pure shear) and associated microstructures indicate that flow occurred at close to peak metamorphic conditions. Vorticity analysis becomes progressively more problematic as deformation temperatures increase towards the anatectic core. Within the MCTZ rigid elongate garnet grains yield Wm estimates of 0.63-0.77 (c.58-44% pure shear). We attribute flow partitioning in the GHS to spatial and temporal variations that resulted in the juxtaposition of amphibolite grade rocks, which record early stages of extrusion, with greenschist to unmetamorphosed samples that record later stages of exhumation.

Introduction

The >2500 km length of the Himalayan orogen is cored by a suite of north-dipping metamorphic rocks (the Greater Himalayan Slab; GHS), that are bounded above and below by the normal-sense South Tibetan Detachment system (STDS) and reverse-sense Main Central thrust zone (MCTZ), respectively (Figs 2.1 & 2.2). Assuming simultaneous movement along these crustal-scale bounding shear zones (see review by Godin *et al. 2006a*), the GHS is often modeled as a north-dipping wedge or channel of mid-crustal rocks that was extruded southward from beneath the Tibetan plateau (Fig.

2.2) beginning in early Miocene time (e.g. Burchfiel & Royden 1985; Burchfiel *et al.* 1992; Hodges *et al.* 1992). Although consensus on this general concept of extrusion during crustal convergence exists, and a range of orogen-scale kinematic and thermal-mechanical extrusion models have been proposed, surprisingly little research has focused on quantifying the kinematics (vorticity) of flow within the slab and its potential causal relationship with progressive exhumation of the GHS.

The use of vorticity analysis to quantify flow within sheared rocks has proven to be a useful tool for quantifying the nature and distribution of flow regimes within a range of tectonic settings including contractional (e.g. Simpson & De Paor 1997; Xypolias & Doutsos 2000; Xypolias & Koukouvelas 2001, Xypolias & Kokkalas *2006*), extensional (Wells 2001; Bailey & Eyster 2003), and transpressional (Wallis 1995; Klepeis *et al.* 1999; Holcombe & Little 2001; Bailey *et al.* 2004) regimes. Vorticity analysis enables estimation of the relative contributions of pure and simple shear, yielding important constraints for GHS extrusion models. Identification of a pure shear component is critically important because such flow would result in: 1) thinning and transport-parallel extension of the slab itself and 2) an increase in both strain rates and extrusion rates relative to strict simple shear. Attempts to quantify flow within the GHS that accommodated this southward extrusion are limited to: 1) a single transect through the lowermost 900 m of the GHS exposed in the Sutlej valley of NW India (Fig. 2.1; Grasemann *et al.* 1999; Vannay & Grasemann 2001); 2) preliminary results from the top of the GHS exposed in the Rongbuk valley on the north side of the Everest massif, Tibet (Law *et al.* 2004); and 3) preliminary results from the middle of the GHS in the Bhutan Himalaya (Carosi *et al.* 2006). Quantifying and characterizing flow within the GHS is important for development of more realistic models for evolution of the Himalaya, particularly those that propose a synergistic interplay between extrusion, erosion, and exhumation (e.g. Beaumont *et al.* 2001, 2004, *2006*; Hodges *et al.* 2001; Grujic *et al.* 2002; Jamieson *et al.* 2004, 2006; Hodges 2006).

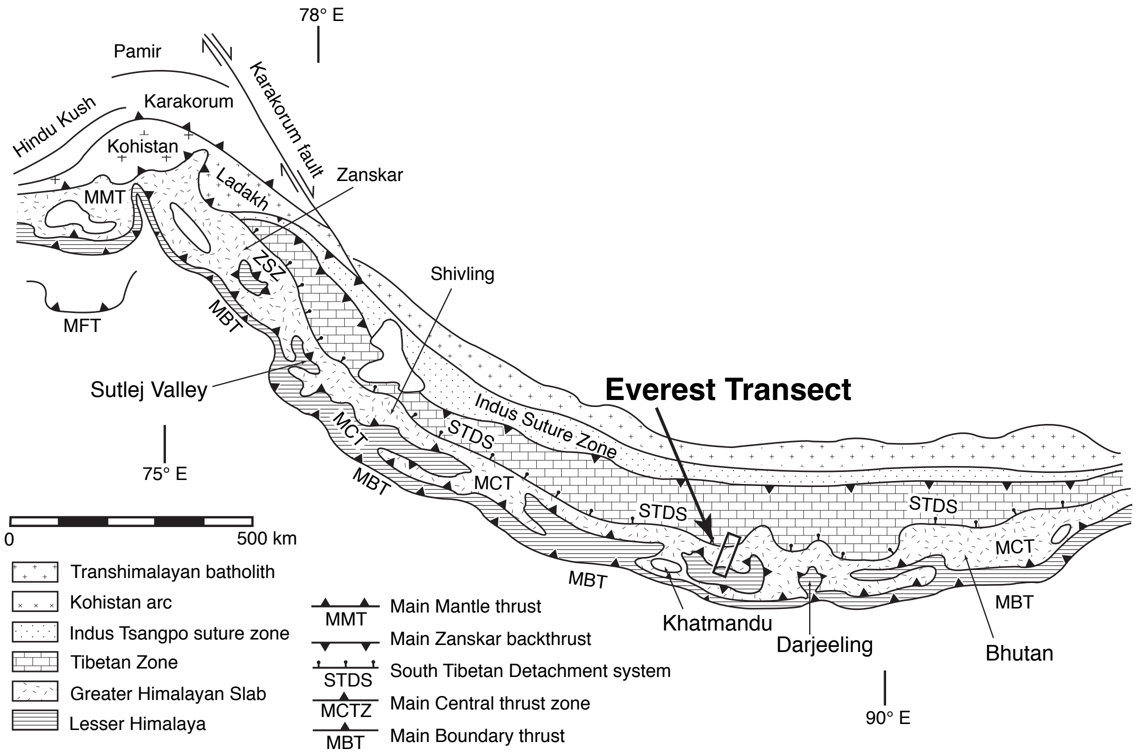

Figure 2.1. Simplified geologic map of the Himalaya including the distribution of the main lithotectonic elements of the orogen. Hollow black rectangle marks the location of the Everest transect. Significant geographical locations and areas referred to in text are also included. The Himalaya marks the transition from high elevations of the Tibetan plateau to the lowlands of the Indian plate. MBT, Main Boundary thrust; MCTZ, Main Central thrust zone; MFT, Main Frontal thrust; MMT, Main Mantle thrust; STDS, South Tibetan detachment system; ZSZ, Zanskar shear zone.

The topographic relief of the Everest massif, Tibet/Nepal (Fig. 2.1), provides a window into mid-crustal processes responsible for extrusion of the GHS, and a particularly appropriate field area to test the various components of extrusion models. In this paper, we combine field-based structural analysis with detailed vorticity analyses of samples from a N-S transect through the GHS in the Everest region using the rigid grain technique of Wallis *et al.* (1993) and Wallis (1995). Samples collected for vorticity analyses are from a variety of structural and lithologic settings, including high-altitude and summit samples collected during two pioneering climbing expeditions (1933 and 1953) on the north-and south-sides of Mount Everest, respectively. Rigid grain analysis using elongate garnet porphyroclasts quantify flow along the MCTZ and, by integration with microstructural analysis, constrain the timing of mylonite formation in relation to peak metamorphism (Hubbard 1988, 1989). Field-based structural analysis characterizes deformation in the core of the GHS where deformation temperatures exceed the upper limit for robust rigid grain vorticity analysis. As the first attempt to quantify flow in a transect across the entire GHS, many new insights into vorticity of flow emerge, including an understanding of how flow was partitioned during extrusion and exhumation of the GHS.

Tectonic Setting

The Himalaya-Tibet orogenic system has accommodated crustal convergence since initiation of collision between India and Asia at *c.*55-50 Ma (Searle *et al.* 1987; Hodges 2000; Yin & Harrison 2000; Figs 2.1 & 2.2). The Tibetan plateau encompasses an area of > $5x10^6$ km^2 of subdued topography (Fig. 1, inset a), with an average elevation of *c.* 5000 m (Fielding *et al.* 1994). To the south stretches the flat, low elevations characteristic of the undeformed internal margin of the Indian plate. Between lies the crest of the Himalaya, which extends for *c.* 2500 km-along-strike, contains the highest elevations in the world (8850 m), and provides exposure of mid-crustal rocks belonging to the GHS (Figs 1 & 2). The GHS forms a 5-30-km-thick section of metasedimentary rocks that are intruded by leucogranite dikes and migmatized to varying degrees (Hodges 2000). The age of leucogranite crystallization (*c.*23-13 Ma) suggests they were part of a protracted event that marks the culmination of peak metamorphism (Searle 1996; Hodges 2000).

The metamorphic evolution of the GHS is often split into two tectonothermal events that may mark distinct thermal pulses or a thermal continuum. Kyanite-grade

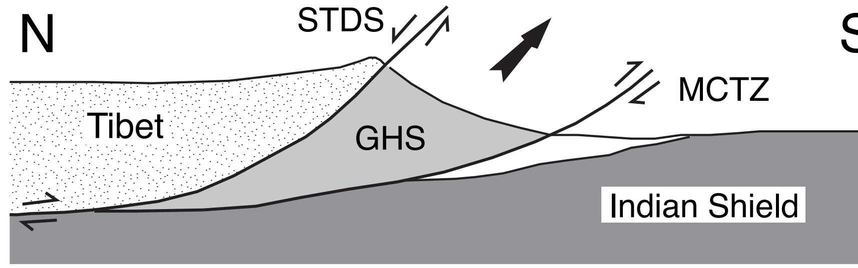

(a) Model 1. Adapted from Burchfiel & Royden (1985)

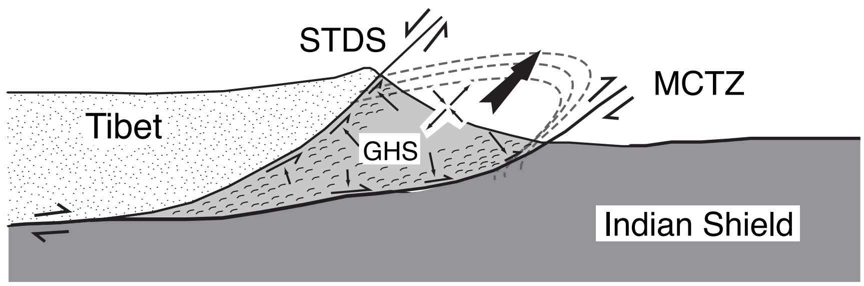

(b) Model 2. Adapted from Grasemann et al. (1999)

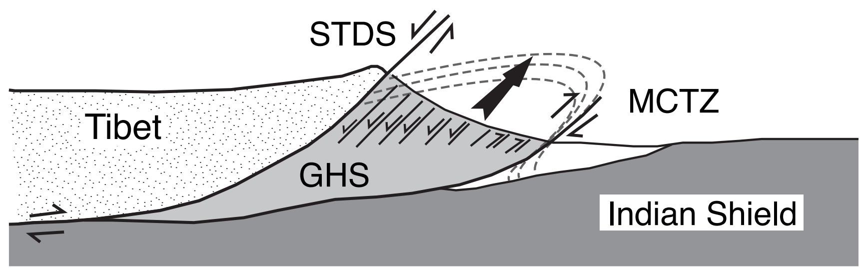

(c) Model 3. Adapted from Grujic et al. (1996)

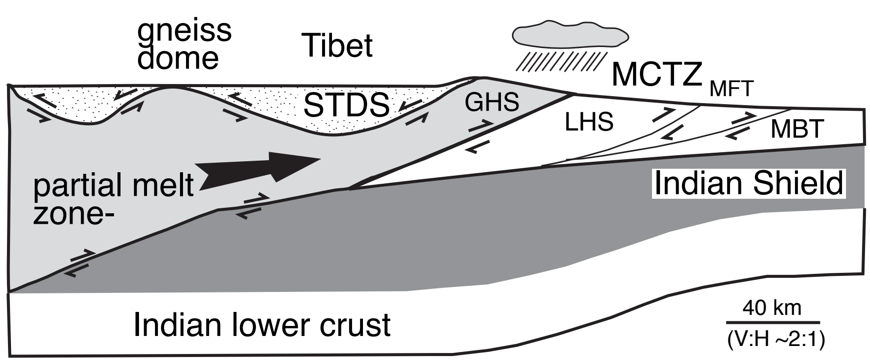

(d) Model 4. Adapted from Beaumont et al. (2004)

Figure 2.2. Extrusion and channel flow models (**a-d**) proposed for the evolution of the Greater Himalayan Slab (GHS). See text for detailed review of each model. GHS, Greater Himalayan Slab; LHS, Lesser Himalayan Sequence; MBT, Main Boundary thrust; MCTZ, Main Central thrust zone; FT, Frontal thrust; STDS, South Tibetan detachment system.

assemblages are interpreted as relicts of an early event (M1) that U-Th-Pb monazite geochronology suggest occurred at *c.* 35-30 Ma (Walker *et al.* 1999; Simpson *et al.* 2000). M1 is often overprinted by the pervasive high temperature-low pressure tectonothermal event (M2; *c.*23-17 Ma) associated with decompression, migmatization, and emplacement of leucogranite sills (Hodges 2000; Simpson *et al.* 2000). $^{40}Ar/^{39}Ar$ thermochronology of muscovite and biotite from leucogranites yield cooling ages that are usually only slightly younger than the U-Pb crystallization age of the leucogranites, suggesting rapid decompression following their emplacement (e.g. Hodges *et al.* 1998 for the Everest transect).

Two shear zones bound the GHS: the STDS above and the MCTZ below (Figs 2.1 & 2.2). The STDS juxtaposes Tethyan sedimentary rocks of the Tibetan Zone against the GHS, while the MCTZ separates the GHS above from rocks of the Lesser Himalaya Zone (LHZ) below (for detailed review see Godin *et al.* 2006b).

Extrusion models

Despite on-going controversy regarding evidence for simultaneous movement on the MCTZ and STDS (see Godin *et al.* 2006b), many researchers continue to view the tectonic evolution of the GHS in the context of models involving southward extrusion of mid-crustal rocks from beneath the Tibetan plateau towards the topographic surface at the plateau margin. All of these models assume simultaneous motion on the upper and lower surfaces of the extruding unit. Two types of models may be distinguished: (1) *kinematic models* for wedge extrusion (Figs 2.2a-c) based on the assumption that the STDS and MCTZ join at depth as, for example, suggested by early interpretations of INDEPTH seismic data (Nelson *et al.* 1996); (2) more complex *coupled thermal-mechanical finite-element models* involving lateral flow of relatively low viscosity material within a tabular mid-crustal channel in response to a horizontal gradient in lithostatic pressure between the Tibetan plateau and Himalayan foreland (Fig. 2.2d;

Beaumont *et al.* 2001, 2004, 2006).

Kinematic models

Model 1 In the original wedge extrusion model (Burchfiel & Royden 1985; Royden & Burchfiel 1987; Kündig 1988, 1989; Burchfiel *et al.* 1992; Hodges *et al.* 1993), the extruding wedge developed by gravity-driven collapse in response to the extreme topographic gradient developed along the southern margin of the Himalayan orogen. In this basic conceptual framework, only one main phase of N-S extension, triggered by a fundamental, non-reversible change in the stress state of the orogenic system as a whole (e.g. England & Molnar 1993), occurred in the Himalaya. Syn-convergence extrusion, rather than gravity-driven collapse, has been emphasized in more recent models. In the original wedge extrusion model the nature of deformation/flow within the interior portions of the wedge was not explicitly addressed (Fig. 2.2a), although a broad zone of reverse-sense shearing along the base of the wedge was suggested (e.g. Brunel & Kienast 1986; Hubbard 1988, 1989, 1996; but also see Harrison *et al.* 1999) as a potential explanation for the long-known inversion of metamorphic isograds adjacent to the MCT (Heim & Gansser 1939). Based on the mapping of antiformally folded isograds in the Zanskar section of the GHS, this was expanded upon in an alternate model by Searle & Rex (1989) who proposed that the entire sequence of rocks contained between the MCT and STDS (Zanskar shear zone) were isoclinally folded during extrusion. More recently proposed kinematic extrusion models are largely based on local evidence for spatial strain path (or vorticity) partitioning within the GHS, and the relative importance of pure shear and simple shear flow components.

Model 2 Quantitative evidence for a significant pure shear deformation component associated with flow along the base of the GHS was reported by Grasemann *et al.* (1999) from the Sutlej Valley (NW India) section of the MCTZ (Fig. 2.1). Based on correlation between: (1) a downward *increase* in estimated pure shear component, (2) a downward *decrease* in deformation temperatures within this zone of inverted isograds, and (3) a high pure shear component indicated by late vein sets, Grasemann *et al.* (1999) proposed that their vorticity data was most readily interpreted as indicating a temporal (rather than spatial) change in flow regime associated with a decelerating strain path (Simpson & De Paor 1997; Fossen & Tikoff, 1997), where simple shear flow at higher temperatures is replaced by pure shear dominated flow at lower temperatures. Grasemann *et al.* (1999) proposed a model for wedge extrusion in which deformation is concentrated towards the boundaries of the wedge and, due to strain compatibility, the center of the wedge extrudes mainly by pure shearing (Fig. 2.2b). An important aspect of this model is that the wedge is detached from the footwall and hanging wall.

Model 3 Microstructural and quartz petrofabric data was employed by Grujic *et al.* (1996) to qualitatively investigate deformation/flow within the lower-central portion of the GHS exposed in Bhutan. These data indicated that at least the lower-central part of the slab had undergone plane strain to weakly constrictional deformation, with flow involving components of both simple shear (reverse or top-to-the south shear sense) and pure shear. Based on these data, Grujic *et al.* (1996) proposed a wedge extrusion model in which pervasive shearing occurred throughout the evolving wedge, with opposite shear senses on the top and bottom halves of the wedge (and highest extrusion velocities in the center) leading, as previously proposed by Searle & Rex (1989) for the Zanskar Himalaya, to antiformal folding of isograds (Fig. 2.2c; see Godin *et al. 2006b*). The pure shear component indicated by petrofabric data was not explicitly addressed in this channel flow model, although Grujic *et al.* (1996) did note that pure shear would lead to thinning and transport-parallel stretching of the wedge/channel during extrusion. Subsequent fieldwork in Bhutan led Grujic *et al.* (2002) to abandon their wedge-shaped model for the GHS and to regard the GHS as a 10-15 km thick mid-crustal layer, or channel, extending for at least 200 km northward beneath Tibet. In this revised channel flow model (incorporating combined Couette and Poiseuille flow; see review by Grujic this volume) the influence of changing thermal conditions (viscosity) on flow patterns was considered, and qualitative predictions made on the likely influence of changes in boundary conditions and viscosities on domainal variation in flow vorticities within the channel. Grujic *et al.* (2002, p.188) emphasized that general flow (i.e. combined simple and pure shear) *"is implicit in the Poiseuille flow, and therefore in channel flow."*

Thermal-Mechanical models

Model 4 Thermal-mechanical models build on the concept originally proposed by Nelson *et al.* (1996) that the GHS represents hot low-viscosity mid-crustal material extruded southwards from beneath Tibet towards the Himalayan front during continental convergence, and the overlapping proposal that this extrusion can be modeled using the concept of channel flow driven by a horizontal gradient in lithostatic pressure between the Tibetan plateau and the Himalayan front (Grujic *et al.* 1996). These concepts, and a broad range of Himalayan structural, pressure–temperature-time (*P-T-t*) and geochronologic data, have been successfully modeled in two dimensions with time-varying, plane strain, coupled thermal-mechanical finite-element models in which channel viscosities are reduced by mantle heat flux and radiogenic heating (Beaumont *et al.* 2001, 2004, 2006; Jamieson *et al.* 2002, 2004, 2006). Models begin with a tectonically thickened crust, which is then thermally weakened, and flows in a mid-crustal channel towards the orogenic front. Varying input parameters and model specifications produces variants of the basic model. In these models, channels are exhumed and exposed by denudation focused on the high-relief transition between the plateau and orogenic front (Fig. 2.2d). Implicit in these models is that the structures now exposed at the topographic front will probably have formed during the last stages, or cessation of extrusion/exhumation of the channel material, rather than being directly related to processes operating when these rocks were flowing at mid-crustal levels beneath the plateau.

Everest Transect: geologic background

In this section we outline the major lithotectonic units and structures of the Everest transect in order to provide a foundation for the detailed discussions of key areas used for our vorticity analyses. This transect begins with the STDS at the top of the GHS, as exposed in Rongbuk valley, Tibet, extends southward to the summit of Everest, and continues southward through the GHS to the more limited exposures in the Nepalese foothills of rocks belonging to the MCTZ. Detailed structural, metamorphic, and geochronologic reviews of the Everest transect (some limited to specific sections) are given by Lombard (1958); Bordet (1961); Brunel & Kienast (1986); Hubbard (1988, 1989); Lombardo *et al.* (1993); Pognante & Benna (1993); Carosi *et al.* (1998, 1999a, b); Searle (1999a, b) and Searle *et al.* (2003, 2006). Geologic maps covering different sections of the transect have been published by Bordet (1961), Lombardo *et al.* (1993), Carosi *et al.* (1998) and Searle (2003).

Two major detachments belonging to the STDS have been mapped in the sidewalls of the Rongbuk valley southward to Changtse and Mount Everest, the upper brittle Qomolangma detachment (QD) and lower ductile Lhotse detachment (LD) (Fig. 2.3; Searle 1999a; Searle *et al.* 2003; see also Lombardo *et al.* 1993; Carosi *et al.* 1998, 1999b; and Sakai *et al.* 2005). As originally defined, the LD is a distinct ductile high-strain zone that marks a metamorphic break between amphibolite facies rocks below and greenschist facies (Everest Series) rocks above (Searle 1999a). More recent detailed thermobarometric results from samples collected at the base of the Lhotse wall (Jessup *et al.* 2004, 2005) and East Rongbuk glacier (Waters *et al.* 2006), demonstrate temperatures of *c.*650°C immediately above and below the proposed detachment, and suggest that the LD may mark the upper limit of leucogranites, but not a break in metamorphic grade. The two detachments merge into one major ductile-brittle shear zone near the northern limit of Rongbuk valley (Fig. 2.3; Carosi *et al.* 1998, 1999b; Searle 1999a). Because

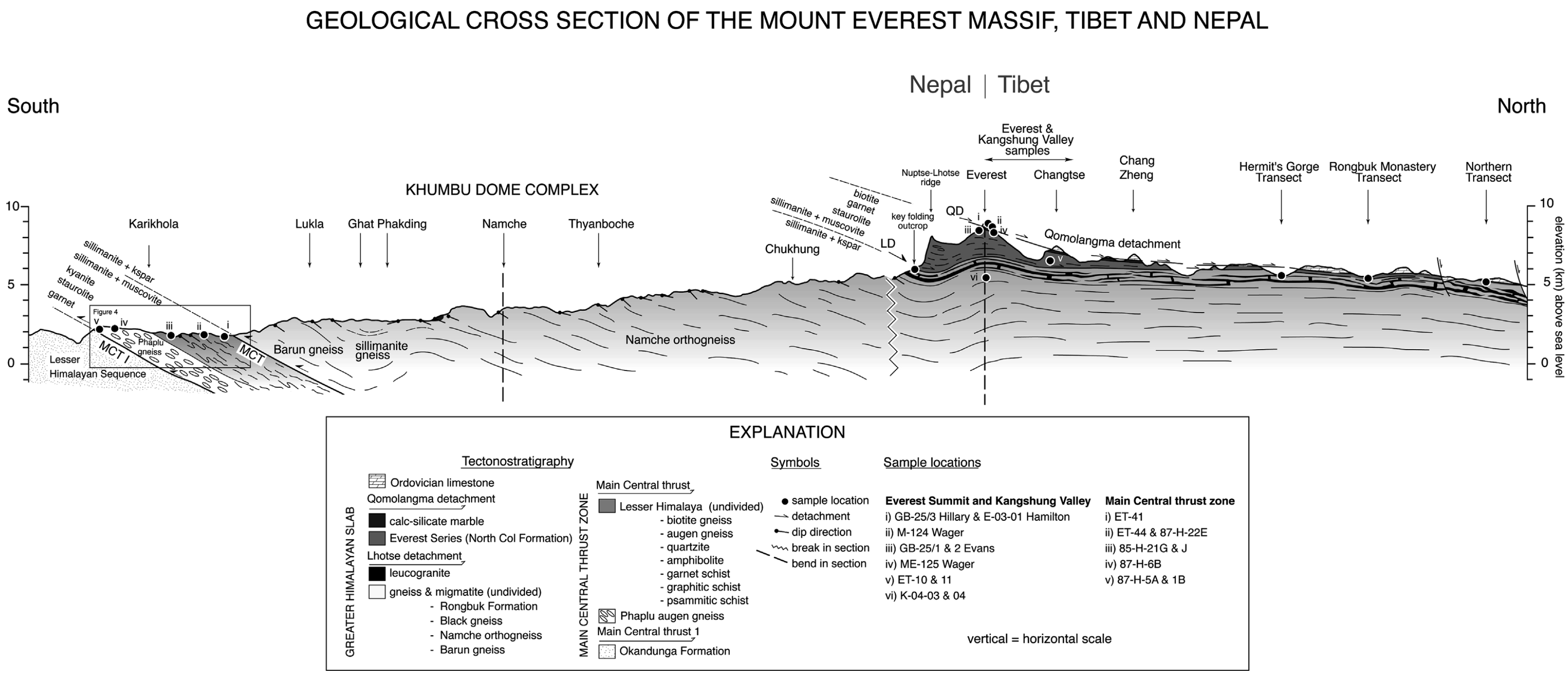

Figure 2.3. Simplified geologic cross section of the Mount Everest massif. Based on a compilation of original data for this investigation, Arita, 1983; Hubbard 1988, 1989; Lombardo *et al.* 1993; Carosi *et al.* 1999a; Catlos *et al.* 2002; Searle *et al.* 2003. Metamorphic isograd distribution proposed on the Nuptse/Lhotse wall is based on Jessup *et al.* (2004, 2005) and Waters *et al.* (2006). Location of key outcrop of folding relationships at base of Lhotse wall is indicated. MCT, Main Central thrust (MCT at top, MCT1 at base); LD, Lhotse detachment; QD, Qomolangma detachment.

the QD dips more steeply than the LD, a northward-tapering wedge of Everest Series is mapped between the two detachments (Searle *et al.* 2002, 2003; Searle 2003).

Previous detailed kinematic investigations are limited to the Rongbuk valley located on the north side of the Everest massif (Fig. 2.3). Cross-girdle quartz c-axis fabrics from GHS rocks exposed in the Rongbuk valley demonstrate that penetrative deformation, along at least this local section of the STDS, occurred under approximately plane strain conditions, and their asymmetry confirms the top-to-the-north shear sense (Law *et al.* 2004). Vorticity analysis (using three techniques) on reconnaissance samples, collected from the top of the GHS in the Rongbuk area, indicate pure shear components representing *c.* 13-53% of the total recorded deformation, depending on rock type and structural position (Law *et al.* 2004). Integration of strain and vorticity data, in the reconnaissance samples, indicated a shortening of 10-30% perpendicular to the upper surface of the GHS and, as previously suggested by Grasemann *et al.* (1999) for the MCTZ at the base of the slab in NW India (see below), confirmed that the STDS is a stretching fault (in the sense of Means 1989) with estimated down-dip stretches of 10-40% (assuming plane strain deformation as demonstrated by petrofabric results) parallel to the flow plane - transport direction.

A *c.*100 m thick mylonite zone, capped by a breccia zone of variable thickness, characterizes the uppermost section of the GHS in Rongbuk valley and projects *c.*35 km southward to the summit of Mount Everest. Structure contours of the detachment (QD) on the summit of Everest, and two peaks to the north (Changtse; 7583 m & Chang Zheng; 7583 m), suggest the detachment dips *c.*10° NNE on the summit and shallows to *c.* 5° NNE in the northern limits of Rongbuk valley (Fig. 2.3). On Mount Everest and Changtse, the QD separates Tethyan limestone of presumed early-middle Ordovician age (Yin & Kuo 1978) above from underlying marble of the Yellow Band (Everest Series) (Burchfiel *et al.* 1992; Searle 1999a, 2003). On the NE ridge of Everest, the QD is marked by a 5-40 cm thick breccia zone in the basal limestone, which rests on intensely foliated Yellow Band marble containing shear bands and drag folds (Sakai *et al.* 2005).

The structurally highest section of the Everest-Lhotse massif is predominantly composed of greenschist to lower-amphibolite facies Everest Series metasedimentary rocks, while the lower ramparts consist of sillimanite-grade schist that grade into migmatitic gneiss (Fig. 2.3; Lombardo *et al.* 1993; Pognante & Benna 1993; Carosi *et al.* 1998, 1999b; Searle 1999a, b; Searle *et al.* 2003). A variably deformed leucogranite sill complex that parallels the pervasive fabric within these rocks is limited to a zone immediately below the Everest Series. Searle (1999a) proposed that the LD is present along this transition and also proposed that a late-stage thrust (Khumbu thrust) is present along the base of the underlying, most extensive, leucogranite sill complex (Fig. 2.3). Variably migmatized, interlayered gneiss, calc-silicate, quartzite, schist, and orthogneiss are predominant beneath the LD (or the composite LD-QD in the northern Rongbuk valley), and extend downwards through the middle section of the GHS to the upper section of the MCTZ (Lombardo *et al.* 1993; Searle *et al.* 2003). Deformation within the core of the GHS is characterized by several phases of folding that culminate in a pervasive foliation that is broadly warped by late stage NW-and NE-trending hinge lines of recumbent folds that create dome structures (Carosi *et al.* 1999a, b). Mylonite zones, typically found at the margins of the slab, are absent in the core.

As exposed in the Duhd Kosi drainage south of Everest, the MCTZ consists of sheared quartzite, calc-silicate, amphibolite, garnet-kyanite-staurolite schist, graphitic schist, and augen gneiss (Hubbard 1988, 1989; Catlos *et al.* 2002). Although debate continues about the exact location of the thrust zone (see Godin *et al.* 2006b; Searle *et al.* 2006), we choose to relate our vorticity results to the original context proposed by Hubbard (1988, 1989). In the Duhd Kosi drainage, a combined *downward* increase in apparent penetrative strain, and *upward* increase in metamorphic temperatures that exceed the kyanite stability field, marks the top (MCT) of the 5 km thick high-strain zone, while the Okhandunga orthogneiss marks the base (MCT I; Fig. 2.4). Because the

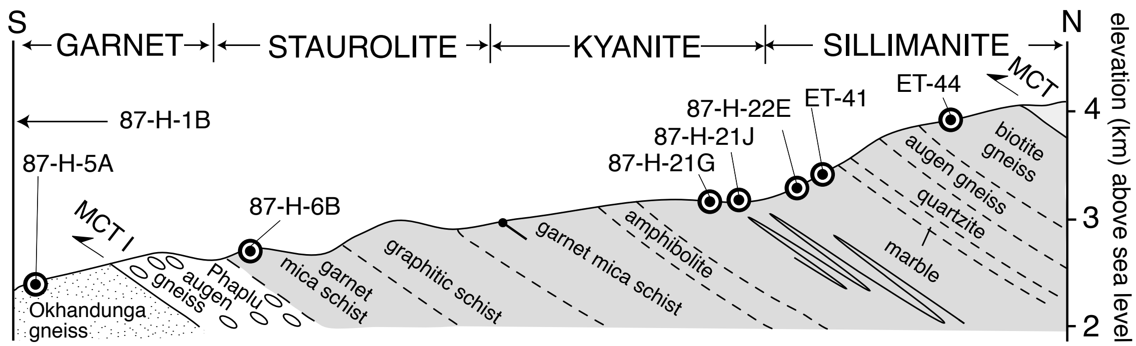

Figure 2.4. Generalized cross section of the Main Central thrust zone (MCTZ); after Hubbard (1988). Locations of isograds are approximate. Dip of the units is based on work from this investigation.

apparent increase in strain coincides with a change in rock type (migmatitic gneiss above and pelitic schist below), the downward increase in penetrative foliation intensity may be controlled by lithology rather than structural position. The pervasive north-dipping foliation overprints several phases of folding and foliation development that are only preserved in lower-to moderate-strain domains within the high-strain zone. Variation in foliation orientation is the result of late-stage folding also present at structurally higher positions in the core of the GHS.

Vorticity analysis

Introduction to techniques

Mean kinematic vorticity number (W_m) is a measure of the relative contributions of pure ($W_m = 0$) and simple ($W_m = 1$) shear. Several analytical methods exist for estimating W_m in high-strain rocks; however only in rare cases are individual samples suited for vorticity analysis using multiple techniques (see Law *et al.* 2004 for detailed discussion). We focus on a suite of samples collected from the Everest transect that are suitable for the rigid grain-based vorticity analysis developed by Wallis *et al.* (1993) and Wallis (1995). This suite of 51 samples (Table 2.1) includes the 7 reconnaissance samples

Table 2.1 Mean kinematic vorticity (W_m) data

Sample	Rock type ‡	Elevation (m)	Distance(m) from QD/LD	Method 1 (Wm)
NORTHERN TRANSECT				
R03-10	lim	5010	10 above	0.87-0.91
R03-12	mar	5000	0	0.88-0.91
R03-15	calc	4995	5	0.75-0.78
R03-16	calc	4993	7	0.68-0.79
R03-17	qtz	4991	9	0.81-0.84
R03-18	calc	4988	12	0.73-0.80
R03-18 (A)	calc	4988	12	0.75-0.80
R03-19	calc	4987	13	0.62-0.71
R03-20	leu	4982	18	0.69-0.80
R03-21	leu	4979	21	0.76-0.80
R03-24	leu	4974	26	0.76-0.79
R03-25	leu	4965	35	0.75-0.81
R03-26	leu	4964	36	0.76-0.82
R03-26 (A)	bt	4934	46	0.74-0.79
RONGBUK MONASTERY TRANSECT				
R03-55	lim	5767	67 above	0.82-0.84
R03-56	lim	5716	16 above	0.77-0.80
R03-58	lim/mar	5663	37	0.76-0.79
R03-59	mar	5655	45	0.79-0.82
R03-63	calc	5650	50	0.81-0.84
TI-05	bt	*c.*5600	100	0.77-0.79
ET-15	bt	5450	250	0.82-0.85
R03-67	calc	5380	320	0.75-0.80
ET-14	bt	5350	350	0.67-0.73
R03-70	bt	5255	445	0.73-0.77
ET-13	bt	5250	450	0.75-0.80
ET-12	bt	5100	600	0.72-0.77
HERMIT'S GORGE TRANSECT				
R03-46	lim	5748	5 above	0.74-0.77
R03-44	mar	5739	0	0.74-0.77
R03-43	mar	5737	2	0.72-0.75
R03-39	calc	5698	41	0.64-0.70
R03-38	bt	5688	51	0.75-0.78
ET-08[+]	bt	5650	89	0.79-0.84
R03-31	leu	5950	211	0.57-0.64
R03-33	bt	5398	341	0.69-0.80
EVEREST & KANGSHUNG VALLEY TRANSECTS				
25/3 Hillary	lim	8836		0.87-0.89
E-03-01 Hamilton	lim	8840		0.87-0.89
ME-124 Wager	lim	8568		0.84-0.86
25/1&2 Evans	lim	8689		0.85-0.87
ME-125 Wager	lim	8260		0.83-0.85
ET-10	bt	>7000		0.81-0.84
ET-11	bt	>7000		0.77-0.79
K04-03	gn	5340		0.68-0.77
K04-04	gn	5320		0.72-0.76
MAIN CENTRAL THRUST ZONE TRANSECT				
ET-41	grt-sill			0.63-0.73
ET-44	grt-sill			0.63-0.70
85-H-22E	grt-sill			0.72-0.77
85-H-21J	grt-ky			0.70-0.72
85-H-21G	grt-ky			0.60-0.64
87-H-6B	grt			0.69-0.71
87-H-5A	gn			0.69-0.77
87-H-1B	grt			0.66-0.70

‡ Abbreviations for rocks types: leu, leucogranite; bt, biotite schist; lim, limestone; ma, marble; calc, calc-silicate; gn, gneiss; grt-sill, garnet + sillimanite schist; grt-ky, garnet + kyanite schist; grt, garnet schist; qtz-rich layer in calc-silicate.

described by Law *et al.* (2004) from the Rongbuk valley - Changtse ridge part of the transect, some of which had previously proven suitable for multiple methods of vorticity analysis.

Using the founding principles of Ghosh & Ramberg (1976) and Passchier (1987), Wallis *et al.* (1993) and Wallis (1995) proposed that, for rigid clasts rotating in a flowing ductile matrix, a unique relationship exists between W_m, clast aspect ratio (R) and the angle (θ) between clast long axes and matrix foliation. For a given Wm, clasts with a specific aspect ratio will reach a unique stable sink position (i.e. angle from the foliation). The method involves measuring the clast aspect ratio and angle between the clast long axis and foliation for both back-and forward-rotated clasts (in sections cut perpendicular to the foliation and parallel to the macroscopic stretching lineation). The distribution of clasts is displayed on a plot of R vs. θ (Fig. 2.5a-d). A transition between clasts that rotate infinitely and those that reach a stable sink orientation define the critical threshold (R_c). R_c is then used to calculate W_m using the relationship proposed by Passchier (1987):

$$W_m = (R_c^2-1)/ (R_c^2+1) \qquad \text{Eqn. 1}$$

In practice, a range of likely Rc values is usually indicated for a given sample using the Wallis plot, leading to a range of estimated W_m values (Law *et al.* 2004; see also Carosi *et al.* 2006; Xypolias & Kokkalas 2006). Whether the Wallis method may consistently under- or over-estimate W_m values probably depends on individual sample characteristics. The method may tend to underestimate W_m if clasts of large aspect ratio are not present, and in such samples the upper bound of the estimated Wm range is probably closest to the true value (Law *et al.* 2004). In contrast, if finite strains are low, then clasts of high aspect ratio may not have had time to reach stable sink orientations and the observed range of R_c values would tend to overestimate Wm (Bailey, Polvi, & Forte *in press*).

The rigid grain vorticity method assumes: (1) that the clasts undergo no internal deformation (e.g. by crystal plasticity or pressure solution), (2) no mechanical interaction occurs either between adjacent rotating clasts, or between the clasts and their matrix, and (3) high enough strain has developed to ensure that all clasts have rotated into their current position. Samples were avoided where deformation temperatures exceeded the onset of internal plastic deformation within otherwise rigid phases, or where excessive interaction had occurred between rotated grains. We tentatively assume plane strain deformation for these samples, based on the original petrofabric data of Law *et al.* (2004,

p. 313), which strongly indicate that flow was monoclinic to orthorhombic Law *et al.* (2004, p. 314). Due to the lack of robust strain markers, it was impossible to quantify strain in any of the samples from the Everest transect aside from those published by Law *et al.* (2004). Rigid grain data plots for all 51 samples used for vorticity analysis are reproduced in the Appendix to this paper. Full details of the mineral(s) used as rigid grain markers are given on each plot. Details of sample locations, and estimated range of W_m values for each sample, are summarized in Table 2.1.

Representative rigid grain data plots for different structural levels

Four representative samples are used to describe and discuss the characteristics of the major rock types within the Everest transect used for vorticity analysis: (1) sheared Tethyan limestone above the QD system, (2) biotite gneiss/schist within the uppermost 100 m of the footwall to the composite QD-LD system, (3) high-grade gneiss at a deeper structural level (< 2 km) in the footwall to the LD, and (4) pelitic rocks within the MCTZ (Fig. 2.5a-d).

Tethyan limestone Sample GB-25/3, collected from just below the summit (8836 m) by Edmund Hillary (Harker Collection records, Cambridge University) during the first accent of Mt. Everest via the South Col in 1953, is an example of sheared limestone in the immediate hanging wall to the QD (Fig. 2.3). Other samples that share the same microstructural characteristics and spatial proximity to the QD, were collected in the sidewalls of the Rongbuk valley. Abundant equant - elongate detrital quartz grains are interpreted as rigid clasts that rotated within a ductile calcite matrix (Fig. 2.6a). The distribution of quartz grains on the Wallis plot defines (Fig. 2.5a) an abrupt transition from grains that rotate infinitely ($R \leq 3.80$) to those that reach a stable sink orientation

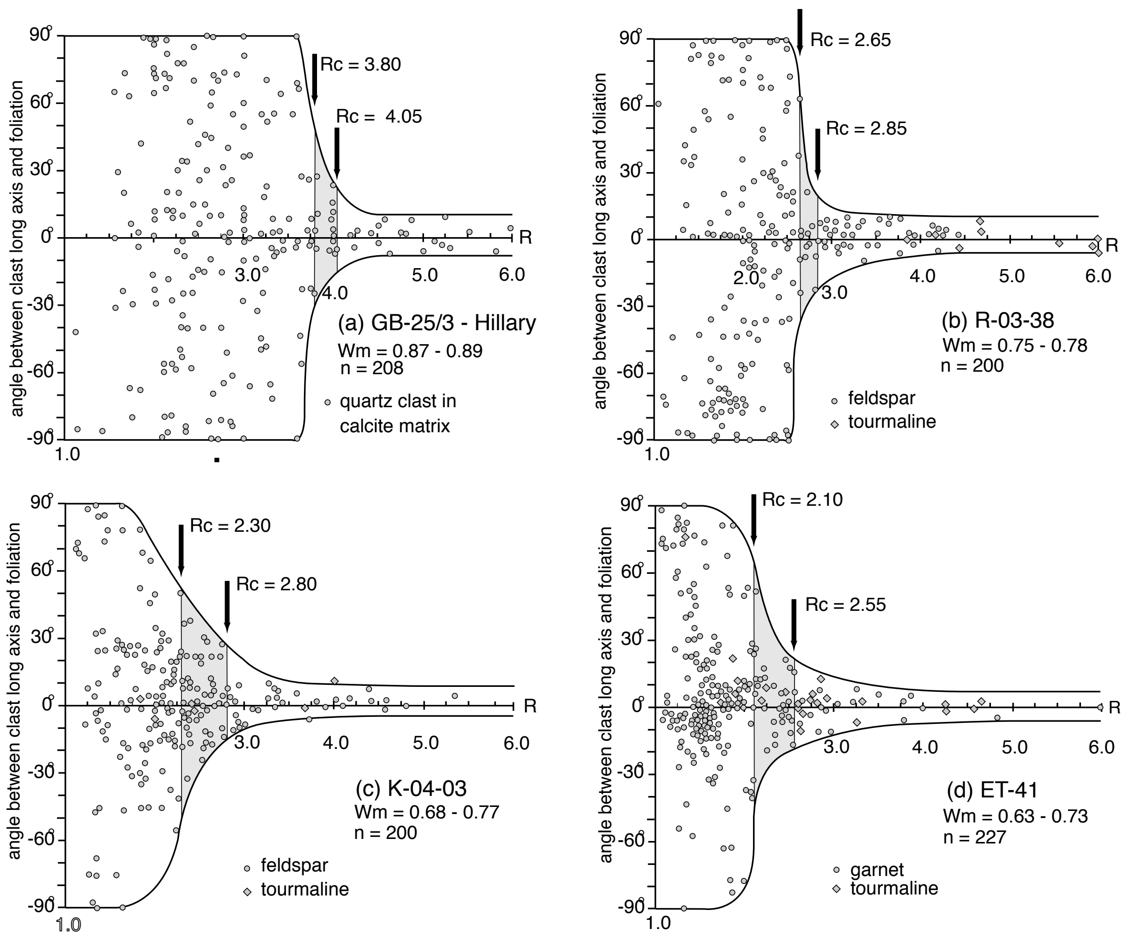

Figure 2.5. Rigid grain plots using the Wallis *et al.* (1993) and Wallis (1995) technique (see text for details). Four representative plots are used to discuss the main rock types used in this investigation: **(a)** sheared limestone in the hanging wall of the Qomolangma detachment; **(b)** mylonitic metapelites, calc-silicates and leucogranites from the upper 600 m of the GHS; **(c)** GHS gneiss sample from Kangshung valley with broad range of potential R_c values which are typical of samples where the originally rigid phase (feldspar) begins to deform internally; **(d)** garnet schist from the Main Central thrust zone where rigid elongate garnets were used to estimate mean kinematic vorticity number (W_m).

($R \geq 4.05$). Using this range in R_c values (3.80-4.05) yields a W_m estimate of 0.87-0.89 (*c.*32-28% pure shear).

Immediate footwall to LD and composite QD-LD system Sample R03-38 represents the amphibolite grade rocks (marble, calc-silicate, leucogranite, and biotite schist/gneiss) within the upper 100 m of the GHS. These samples often contain several rigid phases such as feldspar, epidote, zircon, amphibole, and tourmaline in a matrix of dynamically recrystallised quartz. At the upper limit to these deformation temperatures (amphibolite grade), large feldspar porphyroclasts remain rigid while smaller grains begin to deform internally. R03-38 is a biotite schist with abundant feldspar and tourmaline suitable for rigid grain analysis (Fig. 2.6b). The narrow range in R_c (Fig. 2.5b) yields a fairly robust W_m estimate of 0.75-0.78 (45-42% pure shear).

Structurally deeper levels of LD footwall Sample K-04-03 was collected from outcrops of high-grade gneiss in the western end of the Kangshung valley. These gneisses are situated at a structural depth of *c.*2 km beneath the LD (Fig. 2.3) and continue downward into the underlying anatectic core of the GHS. Feldspar grains in these gneisses are generally separated from each other by a matrix of biotite laths and dynamically recrystallised (Regime 3 of Hirth & Tullis 1992) quartz (Fig. 2.7a). However, many of the feldspar grains exhibit at least moderate undulatory extinction and minor grain flattening, indicating that they did not behave as perfectly rigid markers. *"Rigid grain"* plots using these feldspar grains are characterized by a broad transition in potential R_c values (Fig. 2.5c), and therefore greater uncertainty in defining W_m. We propose that these plots are typical of samples that contain a semi-rigid phase, and caution against over interpretation of Wm estimates from such samples.

MCTZ The fourth example, sample ET-41, is a garnet-mica schist typical of pelite samples collected from the MCTZ. These pelite samples contain elongate garnet porphyroclasts that are wrapped by biotite and muscovite, and surrounded by a matrix of quartz and feldspar (Fig. 2.7b). The evolution of these elongate garnets is discussed in detail below. The orientation distribution and range in aspect ratio of these garnets confirms their appropriateness for rigid grain vorticity analysis (Fig. 2.5d). A limited range in R_c defines W_m estimates of 0.63-0.73 (58-48% pure shear). The major drawback to using metamorphic phases for rigid grain analysis in these pelitic MCTZ samples is the number of appropriate porphyroblasts available within a thin section; where possible we have used combined data from parallel sections in individual samples. For example, sample 85-H-21G contained a minimal number of garnet porphyroblasts (n = 59) that just begins to define a minimum R_c, whereas 87-H-22E contained many garnets (n = 275) that define R_c much better (Fig. 2.A5). For several MCTZ samples, such as ET-41, the rigid grain analysis proved highly successful and provides a unique opportunity to explore the relationship between peak metamorphism and mylonite formation.

Petrography and results of vorticity analyses

Rongbuk valley transects

We collected oriented samples for vorticity analysis along three transects in the eastern sidewalls of the Rongbuk valley (Fig. 2.8). A similar lithotectonic sequence is observed in each transect consisting (traced structurally downwards) of limestone, marble, calc-silicate, leucogranite and biotite-sillimanite schist/gneiss (Figs 2.8 & 2.9).

Tethyan limestone forms the structurally highest lithotectonic unit and is truncated along the base by the underlying QD. A 5-10 m thick section of marble marks the upper limit to pervasive ductile deformation beneath the detachment. Lenses of mylonitic leucogranite are commonly found within the sheared marble, demonstrating that ductile deformation outlasted their emplacement (*c.*17 Ma; Murphy & Harrison, 1999). Interlayered and pervasively foliated calc-silicate and quartzofeldspathic layers, defined in outcrop by alternating black/green and white layers, are present below the sheared marble. Dark layers contain diopside and are either amphibole or tourmaline-rich, while white layers contain abundant quartz and feldspar. Feldspar is commonly fractured and within one thin section a complete gradation from angular clasts to rounded porphyroclasts rotating in a quartz matrix is common.

Microstructures in quartz-rich layers include the development of subgrains and bulging grain boundaries, which indicate dynamic recrystallization under Regime 2-3 conditions as defined by Hirth & Tullis (1992), and suggest deformation temperatures of *c.*490-530 °C (Stipp *et al.* 2002). Micro-boudinage of diopside, garnet, and tourmaline grains suggest that some components of fabric development post-dated their growth. Tension gashes, nearly perpendicular to the NNE-or SSW-trending stretching lineation, suggests a progression in deformation mechanisms from ductile to brittle occurred during exhumation of the GHS.

Structurally beneath the calc-silicate layers (at least at the northern end of the Rongbuk valley) is a 10-20 m-thick mylonitic leucogranite sill complex. Quartz and feldspar record evidence for grain-scale processes operating at similar deformation condition to those indicated in the overlying calc-silicate rich unit. S-C fabrics with extensional shear bands dominate the detachment-parallel sills.

The structurally lowest unit exposed in the Rongbuk valley is composed of biotite schist (Rongbuk Formation of Carosi *et al.* 1998, 1999a) that is migmatized and injected by foliation-parallel, variably deformed, leucogranite lenses and sills; cross cutting leucogranites are less commonly observed (Searle *et al.* 2006, their figures 6 & 7). Based on quartz *c*-axis fabric opening angles, Law *et al.* (2004) documented progressive increasing deformation temperatures of 525–625 ± 50 °C in the biotite schists at depths of 300-650 m beneath the mapped position of the LD in the Rongbuk Monastery and Hermit's Gorge transects (see below). Rotation of the rigid grains used as vorticity markers in this paper, either pre-dated or (more likely) were synchronous with plastic flow of the quartz-rich matrix associated with these deformation temperatures. Fibrolite in the biotite schist is drawn into extensional shear bands, but remains pristine, suggesting shear band development occurred in the sillimanite stability field (Law *et al.* 2004). At depths greater than 100 m beneath the composite QD-LD system, feldspar begins to deform plastically (as indicated by undulose extinction) and grains tend to become more elongate and oriented sub-parallel to foliation. At a given depth, this

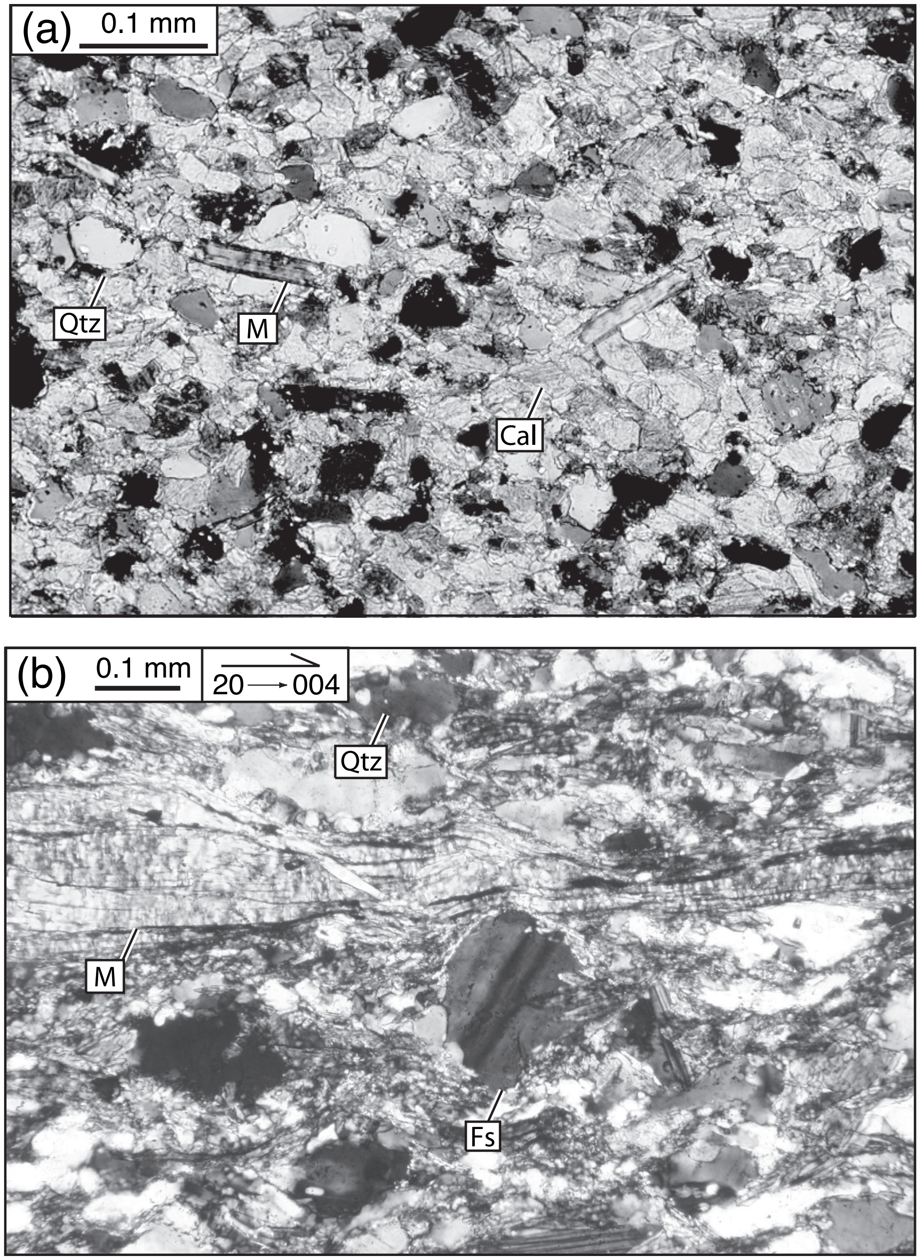

Figure 2.6. **(a)** Photomicrograph (crossed polars) of sample GB-25/3 (collected by E. Hillary in 1953 at *c.*8836 m) showing microstructures typical of sheared limestone collected near the Qomolangma detachment. Abundant detrital quartz grains act as the rigid phase rotating in a calcite (Cal) matrix. Some randomly oriented white mica (M) is present. Rigid grain plot of the sample is shown in Figure 2.5a. **(b)** Photomicrograph (crossed polars) of sample R03-38; section cut perpendicular to the foliation and parallel to the lineation. Microstructures include rigid feldspar (Fs) rotating in a ductile quartz (Qtz) matrix. Large feldspar porphyroclasts in the center of the image has an aspect ratio of *c.*1.6 with a long axis *c.* 80° from the foliation as defined by aligned white mica (M). Rigid grain plot of sample shown in Figure 2.5b. Images taken by M.J. Jessup.

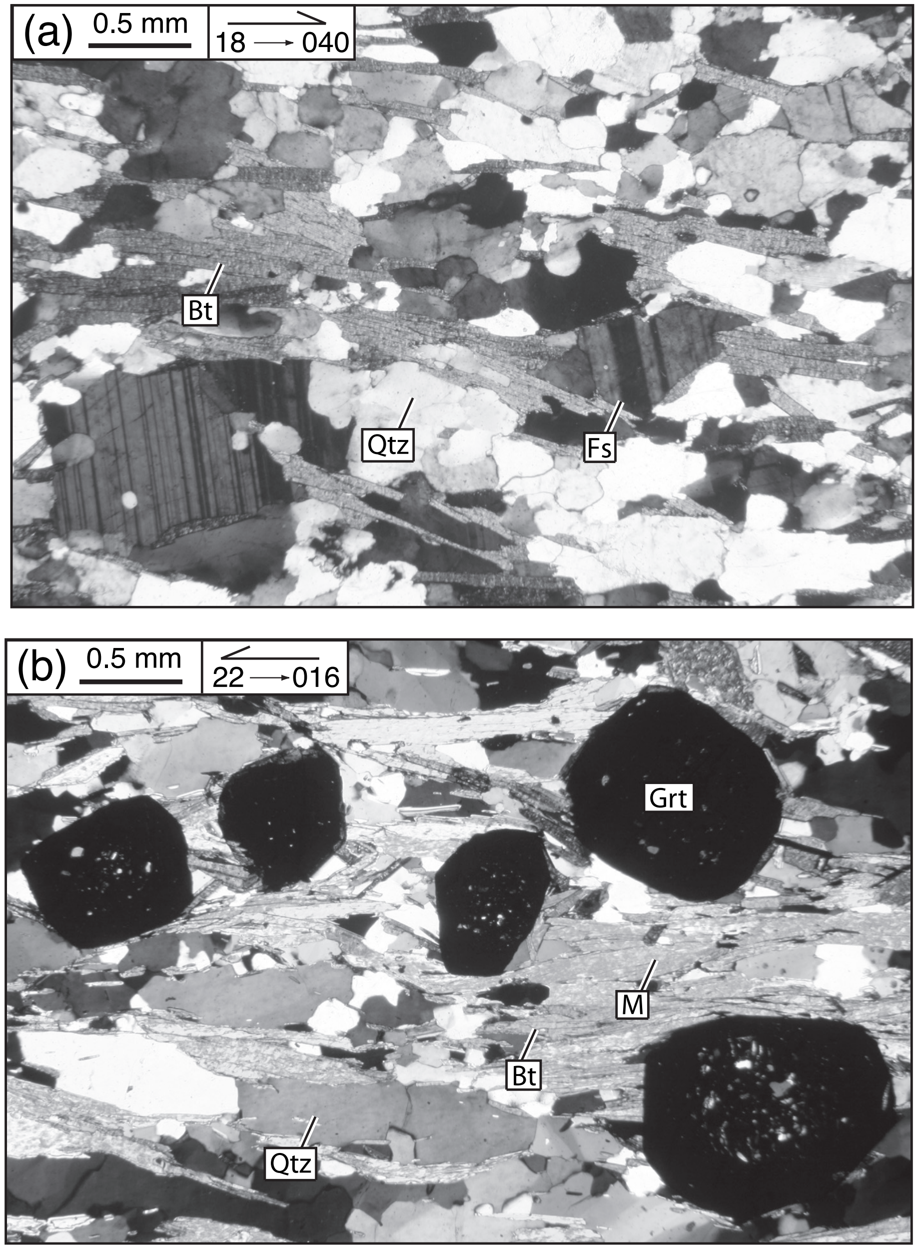

Figure 2. 7. **(a)** Photomicrograph (crossed polars) of sample K04-03 collected in Kangshung valley, Tibet. Biotite (Bt) defines the foliation that is aligned NW-SE in the image. Irregularly shaped feldspar (Fs) that begins to align with the foliation suggests high deformation temperatures where feldspar begins to deform internally. Rigid grain plot of this sample is shown in Figure 2.5c. These microstructures typify samples from the core of the Greater Himalayan Slab that are unsuited for rigid grain analysis. **(b)** Photomicrograph (crossed polars) of sample ET-41 from the Main Central thrust zone (Fig. 2.4). Garnets (Grt) of variable aspect ratios and angles from the foliation are present. Quartz (Qtz) inclusions are present in several of the garnet cores. Aligned biotite (Bt) and white mica (M) defines the foliation (E-W in image). Rigid grain plot using garnet porphyroblasts is shown in Figure 2.5d. Details of garnet evolution discussed in the Main Central thrust zone section of text. Images taken by M.J. Jessup.

brittle-plastic transition in feldspar deformation seems to be grain size controlled (Law *et al.* 2004, p. 311). Incipient conjugate sets of shear bands, defined by biotite, creates a lattice network that dominates the microstructure in the structurally deeper samples. Polygonal quartz grains are common suggesting a component of annealing. Many of these structurally deeper samples are unsuited for vorticity analysis (as discussed above for sample K-04-03). However, even at depths of 600 m beneath the detachment, samples with limited evidence for internal deformation of feldspar yield a well-defined R_c threshold, and therefore a meaningful Wm estimate.

Below we summarize the results of vorticity analyses in our three transects through the eastern sidewalls of the Rongbuk valley (Fig. 2.8); each transect begins in the sheared limestone or within the composite QD-LD system and progresses downward into the migmatitic biotite schist. Results are presented on plots of W_m versus relative distance below the QD to show the spatial distribution of Wm domains in each transect (Figs 2.10 & 2.11). Because the location of the QD is more readily determined in the field than the LD, and in the northern section of Rongbuk valley the LD either merges with or is cut out by the QD, we use the QD as a reference structural level in these plots.

Northern transect: Vorticity analysis results from the northern transect (Fig. 2.8 inset a & Fig. 2.9) are shown in Figure 2.10a. Sample R03-10 (limestone) and sample R03-12 (marble), collected *c.*10 m above and within the QD, respectively, yield W_m estimates of 0.87-0.91 and 0.88-0.91, indicating the lowest component of pure shear (30-25 %) for the entire transect. Four out of six calc-silicate samples from below the sheared footwall marble yield a range in W_m of 0.68-0.80 (*c.*52-40% pure shear). The other two calc-silicate samples are outliers to this trend and yield slightly higher (R03-17; Wm = 0.81-0.84; 40-35% pure shear) and lower (R03-19; W_m = 0.62-0.71; *c.* 58-49% pure shear) Wm estimates. The large range in potential R_c values recorded by calc-silicate samples R03-16 and 19 (together with leucogranite sample R03-20) suggest they are less suitable for rigid grain analysis than the other samples. Five leucogranite samples yield a range in W_m estimates that are consistent with the majority of the calc-silicate samples (0.70-0.82). Although large, the range in W_m for sample R03-20 overlaps with W_m values in the calc-silicate and leucogranite samples. The single biotite schist sample (R03-26A) at the base of the transect has a narrow range in estimated Wm values (0.74-0.79) that is indistinguishable from the calc-silicate and leucogranite samples. The sheared limestone and marble in the immediate hanging wall and footwall to the QD yield the highest W_m values (0.87-0.91), and therefore highest percentage simple shear values, recorded in the Rongbuk valley transects. At distances of *c.* 10-46 m beneath the detachment, the majority of samples yield W_m estimates of 0.70-0.80 (*c.* 50-40% pure shear).

*Rongbuk Monastery transect**:*** The Rongbuk Monastery transect is located *c.*7 km to the south of the northern transect (Fig. 2.8, inset b). Three limestone samples at the top of the transect (R03-55, 56 & 58) yield Wm estimates of 0.76-0.84, with the greatest simple shear component (*c.* 63%) recorded in the structurally highest sample (Fig. 10b). The one marble sample (R03-59), located beneath the detachment, yields a W_m estimate (0.79-0.82) that is indistinguishable from W_m values for the limestone sample above and the calc-silicate sample below (R03-63; Wm = 0.81-0.84). Five of the seven samples below calc-silicate R03-63, including one calc-silicate (R03-67), one hornblende-epidote schist (TI-5), and three biotite schist samples, record a fairly consistent range in estimated W_m values (0.72-0.80). The two outliers yield slightly higher (leucogranite ET-15; W_m = 0.82-0.85) and lower (biotite schist ET-14; W_m = 0.67-0.73) W_m estimates. Samples TI-5, ET-14, ET-13, and ET-12 also proved appropriate for several other vorticity analysis techniques (Law *et al.* 2004), referred to in Figure 2.10B as method II (the PHD method of Simpson & De Paor 1997) and method III (the combined strain and quartz c-axis fabric method of Wallis 1995). For TI-5, the rigid grain technique of Wallis *et al.* (1993) and method II yield indistinguishable results. For the other three samples,

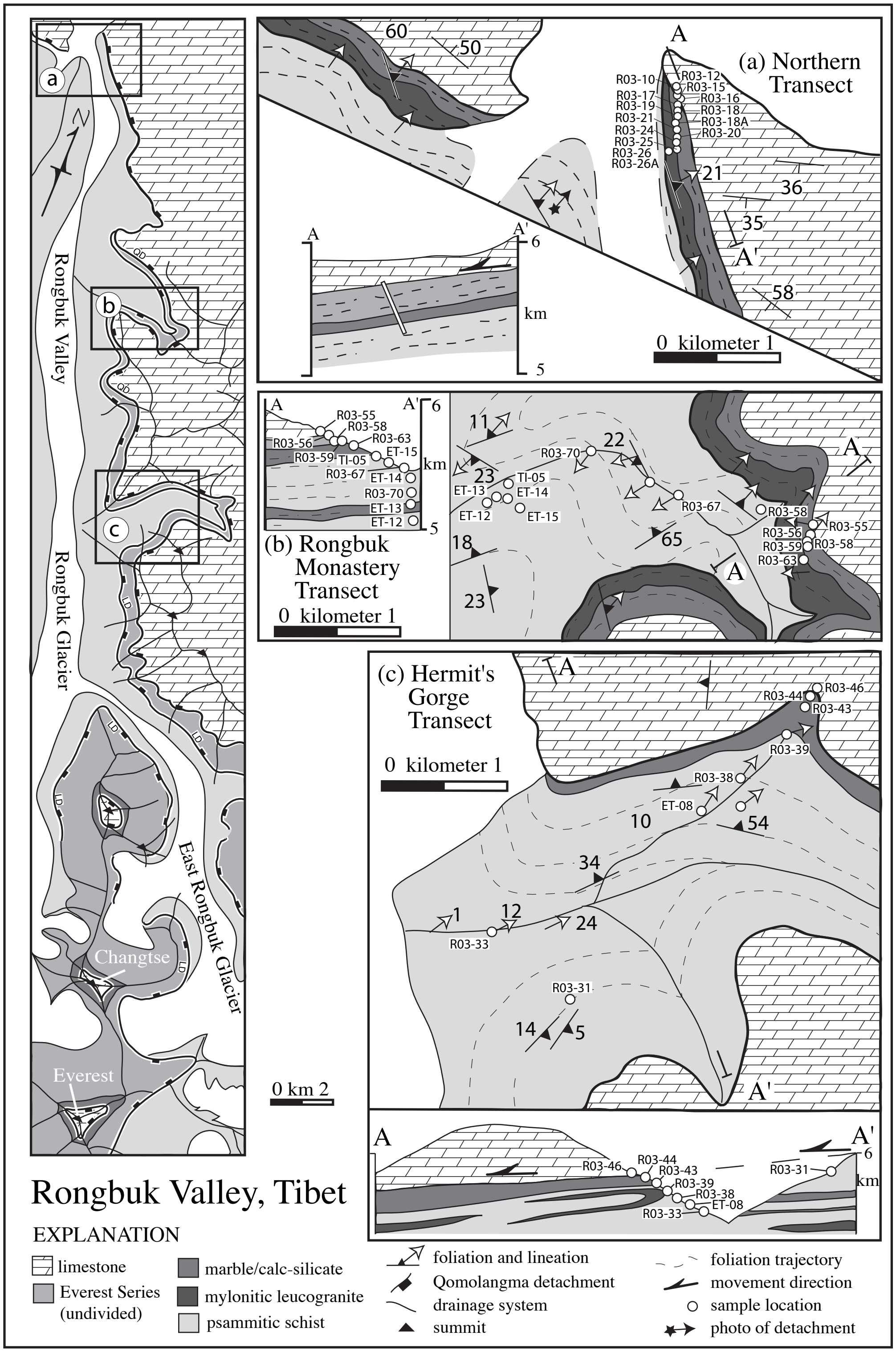

Figure 2.8. Simplified geologic map of Rongbuk valley, Tibet. Insets **(a-c)** are enlargements of detailed sample transects. Spatial distribution of samples is also shown on the cross section through each transect. North is oblique to the long axis of the figure. Image compilation created using original mapping from this investigation and other sources (Burchfield *et al.* 1992; Murphy & Harrison 1999; Searle *et al.* 2003; Law *et al.* 2004).

method III consistently yields higher W_m estimates than the rigid grain technique (see Law *et al.* 2004 for detailed discussion). In summary, rigid grain analyses from the Rongbuk Monastery transect yield W_m estimates of 0.72-0.84 (*c.* 48-36% pure shear) and represent deformation conditions to a maximum depth of *c.* 600 m beneath the composite QD-LD fault system. We regard the structurally deepest samples as yielding the least reliable W_m estimates, as all size fractions of feldspar grains display at least limited evidence for crystal plasticity, and thereby undermine the fundamental assumptions of the rigid grain technique.

Hermit's Gorge transect: Our third transect is located in Hermit's Gorge (and one of its side valleys) which intersects the Rongbuk valley at Everest Base Camp (Fig. 2.8 inset c). One sheared limestone sample (R03-46) was collected *c.*5 m above the top of the marble section and presumed location of the QD. It yields a narrow range in W_m estimates of 0.74-0.77 (*c.*45% pure shear) that is indistinguishable from the two marble samples (R03-43 and 44) below. The single calc-silicate sample (R03-39) yields a W_m estimate (0.64-0.70) that is significantly lower than both the marble above and biotite schist below (R03-38; 0.75-0.78). Sample ET-8, a biotite-rich psammite, yields the highest W_m estimate of the entire transect (0.79-0.84); in contrast method III analysis on this sample yields higher estimated W_m values (Law *et al.* 2004), as noted for samples from the Rongbuk Monastery traverse. R03-31, a piece of mylonitic leucogranite float collected at an altitude of *c.*5950 m, yields the lowest W_m estimate of 0.57-0.64. Although collected at the highest altitude of the transect, due to its position on the south side of the gorge and the northerly dip of the structural units, this sample probably comes from a relatively deep structural position. The structurally lowest sample (R03-33), collected near the mouth of Hermit's Gorge at *c.* 340 m beneath the QD, yields the largest range in estimated W_m values (0.69-0.80) for the transect. We attribute the large range in uncertainty of R_c (and hence W_m) for this sample to the onset of plastic deformation in the feldspar marker grains. This sample is probably close to the maximum structural depth for robust rigid grain vorticity analysis.

Summit of Mount Everest - Kangshung valley

Our final transect across the top of the GHS is composed of Tethyan limestone and Yellow Band (Everest Series) marble samples from near the summit of Mount Everest, samples of Everest Series inter-layered pelite and calc-mylonite collected from talus piles at Advance Base Camp beneath the North Col - Changtse Ridge, and samples of high-grade gneiss from outcrops in the western end of the Kangshung valley (Figs. 2.3, 2.12 & 2.13). Only the Kangshung valley samples, already discussed above (Fig. 2.5), are oriented.

The highest altitude sample (GB-25/3), from the Harker Collection at Cambridge University, is of Tethyan limestone collected by Edmund Hillary on 29 May 1953 at '40 feet beneath the summit of Mount Everest' (Harker Collection records). This sample is augmented by a second, lithologically identical, summit sample (E-03-01) collected by Scottish alpinist, David Hamilton in 2003. Our third, and structurally deepest Tethyan limestone sample (ME-124), from the Lawrence Wager Collection in the Oxford University Museum of Natural History, was collected by Wager 'from a band forming the First Step' (Wager Collection records; see also Wager 1934, 1939) on the NE Ridge of Everest during the 1933 Everest expedition. The highest altitude Yellow Band marble sample (GB-25/1+2), two pieces of intensely foliated and lineated white calc-mylonite from the Harker Collection, was collected by Charles Evans on 26 May 1953 at 'approximately 28500 feet' (Harker Collection records) on the SE ridge of Everest. Our structurally deeper Yellow Band sample (ME-125) was collected by Wager from a 'typical yellow schistose marble forming Yellow Band' on the NE ridge at approximately 300 feet beneath the 1933 Camp VI (Wager Collection records).

Figure 2.9. Photograph of the composite Qomolangma and Lhotse detachments (black line) where they are proposed to merge in the northern limits of Rongbuk valley. Location where image was taken is shown as solid black star on Figure 8. The northern transect is located where the road and detachment are closest. The general rock types from structurally highest to lowest are: (1) limestone, (2) marble, (3) calc-silicate, (4) leucogranite, and (5) migmatized biotite schist (a.k.a. Rongbuk Formation). View is towards the north-east. Arrow points to jeep on two-lane dirt road for scale. Image taken by M.J. Jessup.

Tethyan limestone: Sheared Tethyan limestone samples (GB-25/3, E03-01, ME-124) contain abundant white mica laths and subangular-subrounded detrital quartz grains set in a calcite matrix (Fig. 2.6a). The calcite matrix grains are completely recrystallized, and no remnants of a sedimentary fabric have been preserved (J.F. Read, pers. comm. 2006). The calcite grains are equant - slightly elongate in cross section, and an incipient foliation is defined by weak preferred orientation of the more elongate matrix grains, together with aligned films of an extremely fine-grained opaque phase. Calcite-and quartz-filled microfaults truncate the incipient foliation at moderate to high angles, particularly in sample ME-124 collected from immediately above the QD (Fig. 2.13). Anastomosing quartz-filled fractures subparallel to foliation are also present.

The matrix calcite grains range in size from 20-50 μm. Larger single and polygonal calcite grains (200-250 μm), together with randomly oriented white mica laths (up to 100 μm in length) and equant-elongate detrital quartz grains (generally 40-80 μm long) are scattered throughout the matrix (Fig. 2.6a). Weak undulose extinction within the quartz grains suggests a minor component of plastic deformation, and a high concentration of fluid inclusions gives a dusty appearance to some of these grains. E-twins in the larger calcite grains are straight and thin (<5 mm), suggesting deformation temperatures < 170-200°C (Burkard, 1993; Ferrill *et al.* 2004). The presence of slightly wider twins (>5 mm) in some of the smaller matrix grains suggest that deformation temperatures may have reached >200°C (Burkhard 1993; Ferrill *et al.* 2004). Observed microstructures, and well-defined R_c values in all three of these sub-greenschist facies Tethyan *"limestone"* samples indicate that the detrital quartz grains acted as at least semi-rigid clasts rotating in a plastically flowing and dynamically recrystallizing calcite matrix. W_m estimates (Fig. 2.11b) in these samples range from 0.84-0.89 (35-30% pure shear).

The pristine grain boundaries of the white mica laths in the limestone suggest that they may have recrystallized during deformation, rather than being of detrital origin (G. Oliver pers comm. 2006). We attribute the lack of a well-developed grain-shape foliation

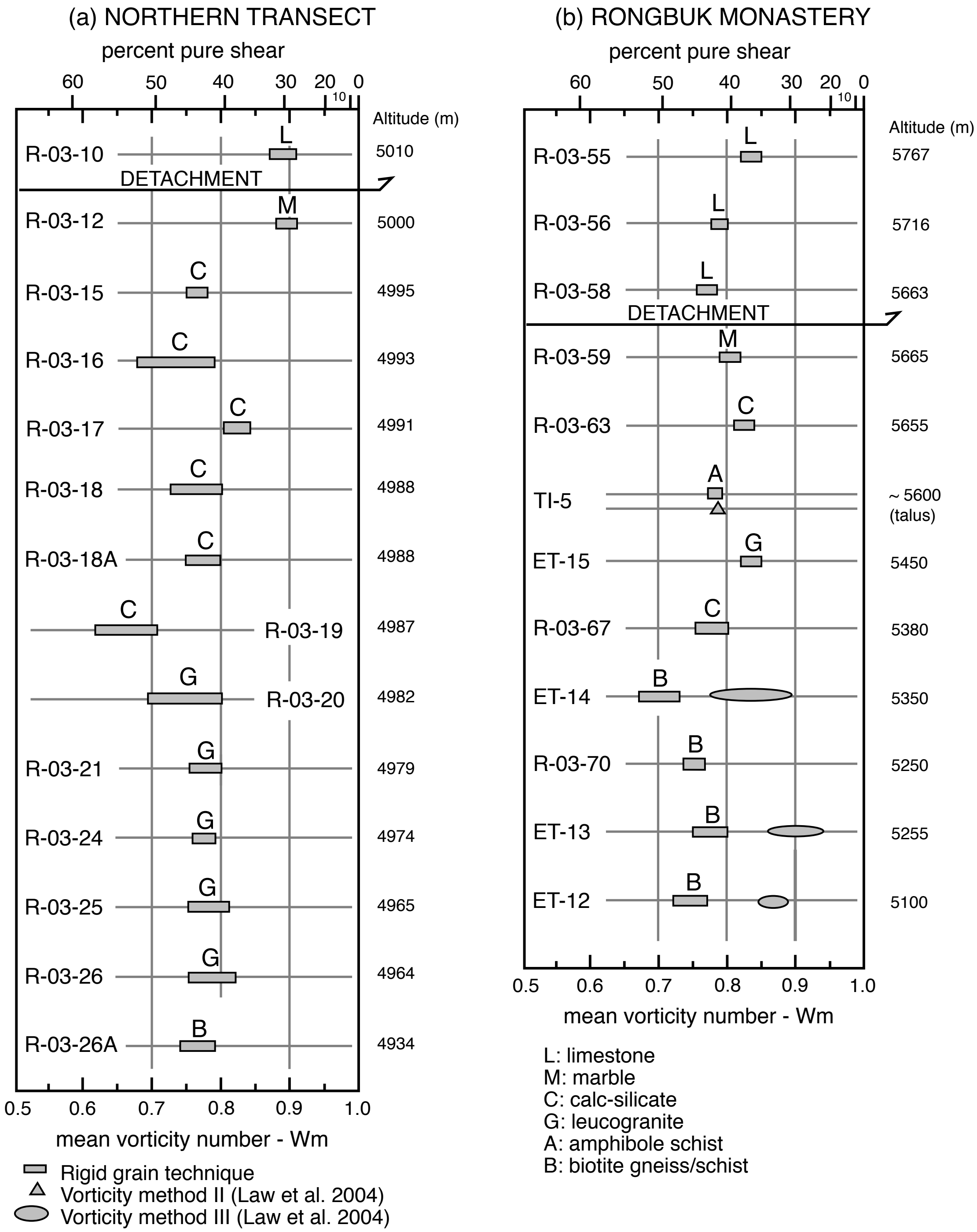

Figure 2.10. Bar charts for range of mean kinematic vorticity numbers (W_m) estimated by the rigid grain method for samples collected in the Northern **(a)** and Rongbuk Monastery **(b)** transects, Rongbuk valley, Tibet. Sample locations shown in Figure 2.8. Range of W_m values estimated by alternate methods (Law *et al.* 2004) are also indicated.

within the calcite matrix, together with the lack of any sedimentary structures, to the operation of grain boundary migration recrystallization, as indicated by the observed microstructures in this sample.

Samples of Everest summit *"limestone"* have previously been described by Gansser (1964, p. 164-171) and Sakai *et al.* (2005). The microstructures described by Gansser (including samples originally described by Gysin & Lombard 1959, 1960) are very similar to those recorded in our samples, except for the presence of crinoid fragments (see also Odell 1965). In contrast, the sample described by Sakai *et al.* (2005), and collected at *c.* 6 m beneath the summit (8850 m), contains crinoid, brachiopod and trilobite fragments, and seems to be much less extensively sheared and recrystallized.

Everest Series, Yellow Band marble: Microstructurally, the most obvious difference between the summit limestone and the underlying Yellow Band marble is the change in size of recrystallized matrix calcite grains, which abruptly increases from 20-50 μm in the Tethyan limestone above the QD to 150-200 μm in the Yellow Band marble beneath the detachment. The calcite grains are equant to slightly elongate and define a weak foliation in thin section that is parallel to the strong macroscopic foliation. Larger single calcite grains (400-800 μm), together with randomly oriented white mica laths (up to 100 μm in length) and equant-elongate detrital quartz grains (generally 25-80 μm long) are scattered throughout the matrix. Calcite twins are thicker and more closely spaced than in the Tethyan limestone, and both multiple twin sets and tight chevron-style buckling of twin lamellae are commonly developed in the larger calcite grains (particularly in sample GB-25/1+2). The presence of thick twins and microstructural evidence for widespread calcite recrystallization involving grain boundary migration indicates deformation temperatures > 250 °C (Ferrill *et al.* 2004). However, the detrital quartz grains exhibit very little undulose extinction, and appear to have acted as semi-rigid porphyroclasts in the flowing calcite matrix, indicating deformation temperatures <300-350 °C (i.e. below

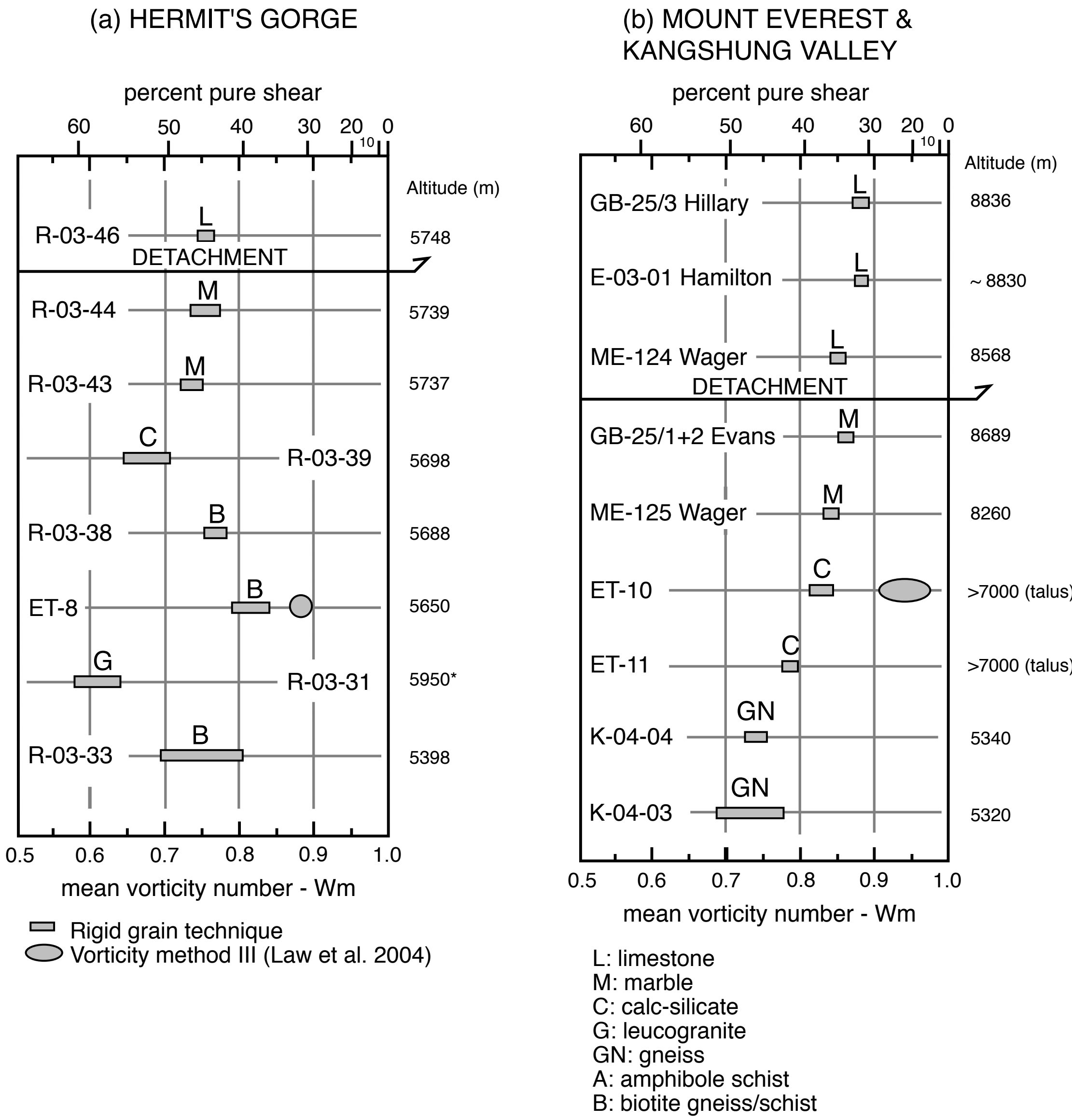

Figure 2.11. Bar charts for range of mean kinematic vorticity numbers (W_m) estimated by the rigid grain method for samples collected in the Hermit's Gorge **(a)** and Mount Everest & Kangshung valley **(b)** transects, Tibet. Sample locations shown on Figures 2.8, 2.12 & 2.13. Range of W_m values estimated by alternate methods (Law *et al.* 2004) are also indicated.

generally accepted minimum temperatures for on-set of plastic deformation in quartz at natural strain rates; see Stipp *et al.* 2002 and references therein). W_m values of 0.83-0.87 (36-32% pure shear) are indicated for samples 25/1+2 and ME-125 using the detrital quartz grains as rigid markers (Fig. 2.11b).

Structurally deeper levels of Everest Series: Talus samples of biotite grade inter-layered phyllite-psammite and calc-mylonite (ET-10 and ET-11), shed from the structurally deeper sections of the Everest Series exposed on the North Col - Changtse Ridge (Figs 2.3 & 2.12), clearly indicate a strong matrix control on deformation mechanisms operating in detrital quartz grains. Even at the thin section scale, a strong partitioning of deformation mechanisms is observed. Detrital quartz grains deform plastically (with minor pressure solution) in the pelite layers when surrounded by phyllosilicates (biotite and white mica), but remain as rigid clasts in the calc-mylonite layers where the calcite grains have accommodated the penetrative strain. W_m values of 0.77-0.84 (42-37% pure shear) are indicated for samples ET-10 and ET-11 using the detrital quartz grains in the calcite-rich layers as rigid grains (Fig. 2.11b). The combined strain and quartz c-axis fabric method of Wallis (1995) in the quartz-mica layers yielded W_m estimates of 0.91-0.98 (Law *et al.* 2004) and correspondingly lower pure shear components (Fig. 2.11b; ET-10, method III).

Main Central Thrust Zone

The base of the GHS is marked by the MCTZ (Fig. 2.3). In the Everest transect the MCTZ is approximately 5 km thick, and characterized by a general decrease in metamorphic grade towards deeper crustal levels (Fig. 2.4), as constrained by the appearance of index minerals and geothermobarometry (Hubbard 1988, 1989; Searle *et al.* 2003). Seven samples of garnet-bearing schist and one sample of orthogneiss were selected from different structural levels of the MCTZ for rigid grain analysis (Figs 2.3 & 2.4). Three basic types of garnet grains are distinguished in the schist: round garnets, small irregularly shaped garnets, and elongate garnets (Fig. 2.14). Round garnets preserve concentric zoning defined by inclusion-rich (commonly sigmoidal) cores and inclusion-free rims (Fig. 2.14a). Elongate garnets commonly contain sigmoidal inclusion trails or more planar inclusion trails at a high angle to the grain long axis (Fig. 2.14b, c).

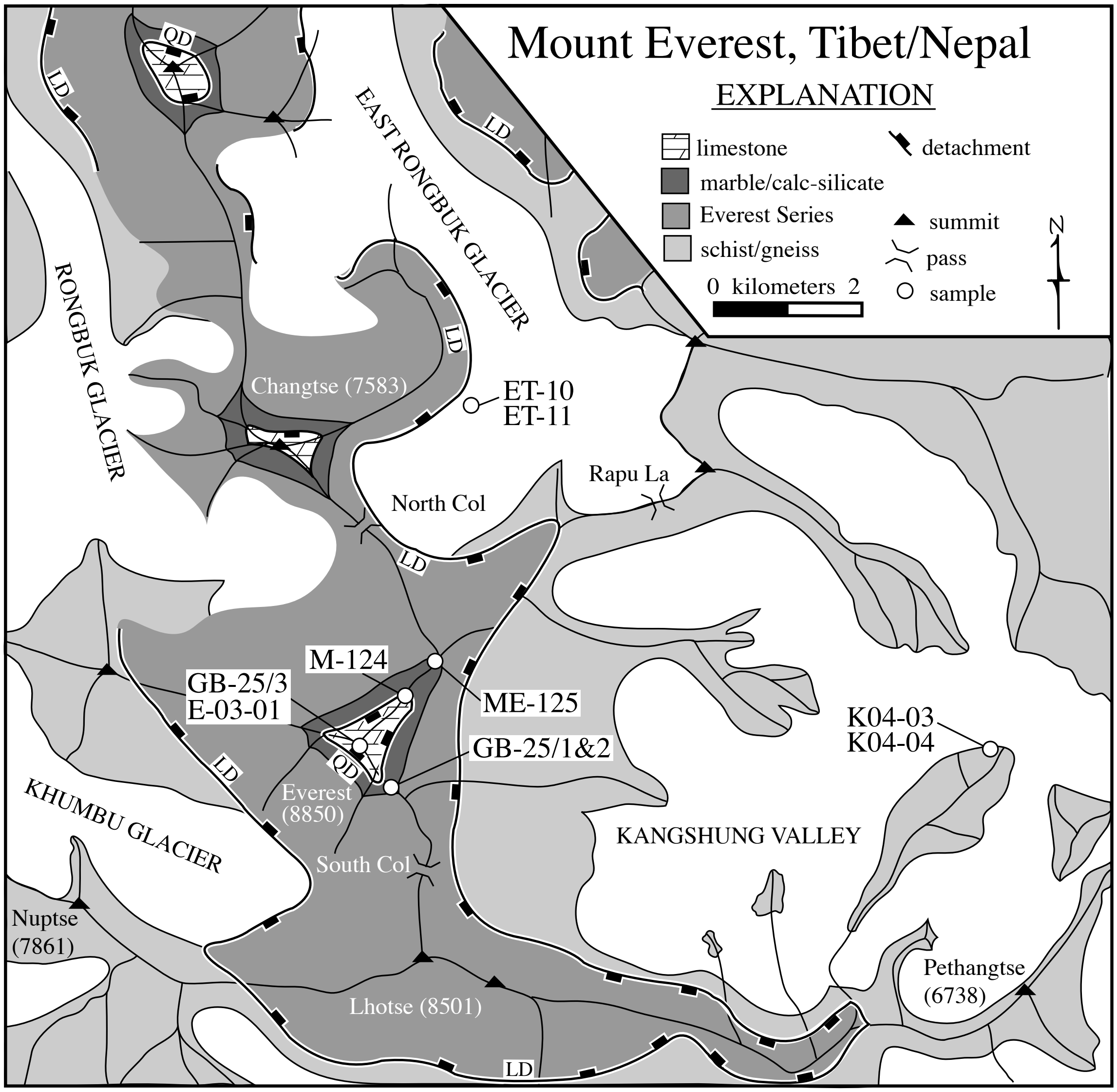

Figure 2.12. Simplified geologic map of the Mount Everest massif and Kangshung valley, Tibet. Compilation based on mapping during this project (Kangshung valley) and Searle *et al.* (2003). QD, Qomolangma detachment; LD, Lhotse detachment.

Small irregular garnets are dominantly inclusion-free (Hubbard 1988, 1989).

We propose a three-step evolution for these garnets (Fig. 2.14d, steps 1-3): (1) formation of inclusion-rich cores during initial garnet nucleation and growth (as preserved by round garnets), (2) growth of inclusion-free rims during a second phase of garnet growth, (3) local removal of garnet rim/core material by a combination of brittle fracturing and pressure solution during late stage penetrative shearing and foliation development within the MCTZ. At least some of the observed irregular garnets may be fracture fragments. These microstructures (Fig. 2.14) indicate that deformation associated with both rotation of these elongate truncated garnets, and formation of the observed enveloping penetrative foliation, must either postdate or have outlasted peak metamorphic conditions, as previously suggested by Hubbard (1988, 1989, 1996) (see also Brunel & Kienast 1986 for a similar interpretation along strike in the Makalu section of the MCTZ). Results of our vorticity analyses, based on the dispersion of these garnet porphyroblasts, must also relate to penetrative flow that outlasted or postdated peak metamorphism. Many of the garnets in these samples are the same ones used by Hubbard (1988, 1989) to define the inverted metamorphic isograds along the Dudh Kosi section of the MCTZ. Therefore, these isograds may have formed prior to this phase of deformation and shearing along the MCTZ (Hubbard 1996), which is potentially associated with relative late stage extrusion of the GHS.

Locations of samples used for rigid grain analysis are shown in a schematic cross section through the MCTZ (Fig. 2.4). The structurally highest samples (ET-44, ET-41, and 87-H-22E) are within the sillimanite stability field of the MCTZ and yield W_m estimates of 0.63-0.77 (*c.*45-55% pure shear; Fig. 2.15). Elongate garnet porphyroclasts in kyanite-bearing samples (87-H-21J and 87-H-21G) yield W_m estimates of 0.60-0.72 (*c.*60-48% pure shear). One sample (87-H-6B), thought to roughly coincide with the staurolite zone, yields a similar W_m estimate of 0.69-0.71 (*c.*50% pure shear). Sample 87-H-5A collected from within a sheared section of the Okhandunga gneiss yields a W_m estimate of 0.69-0.77 using feldspar grains. Sample 87-H-1B was collected further south, in an essentially unmapped section of the MCTZ, yet yields a W_m estimate of 0.66-0.70 using garnet porphyroblasts. The range in W_m estimates from these MCTZ samples (0.60-0.77; average minimum and maximum W_m values of 0.67 and 0.72) suggests a *c.*55-45% pure shear component at the base of the GHS following peak metamorphic conditions.

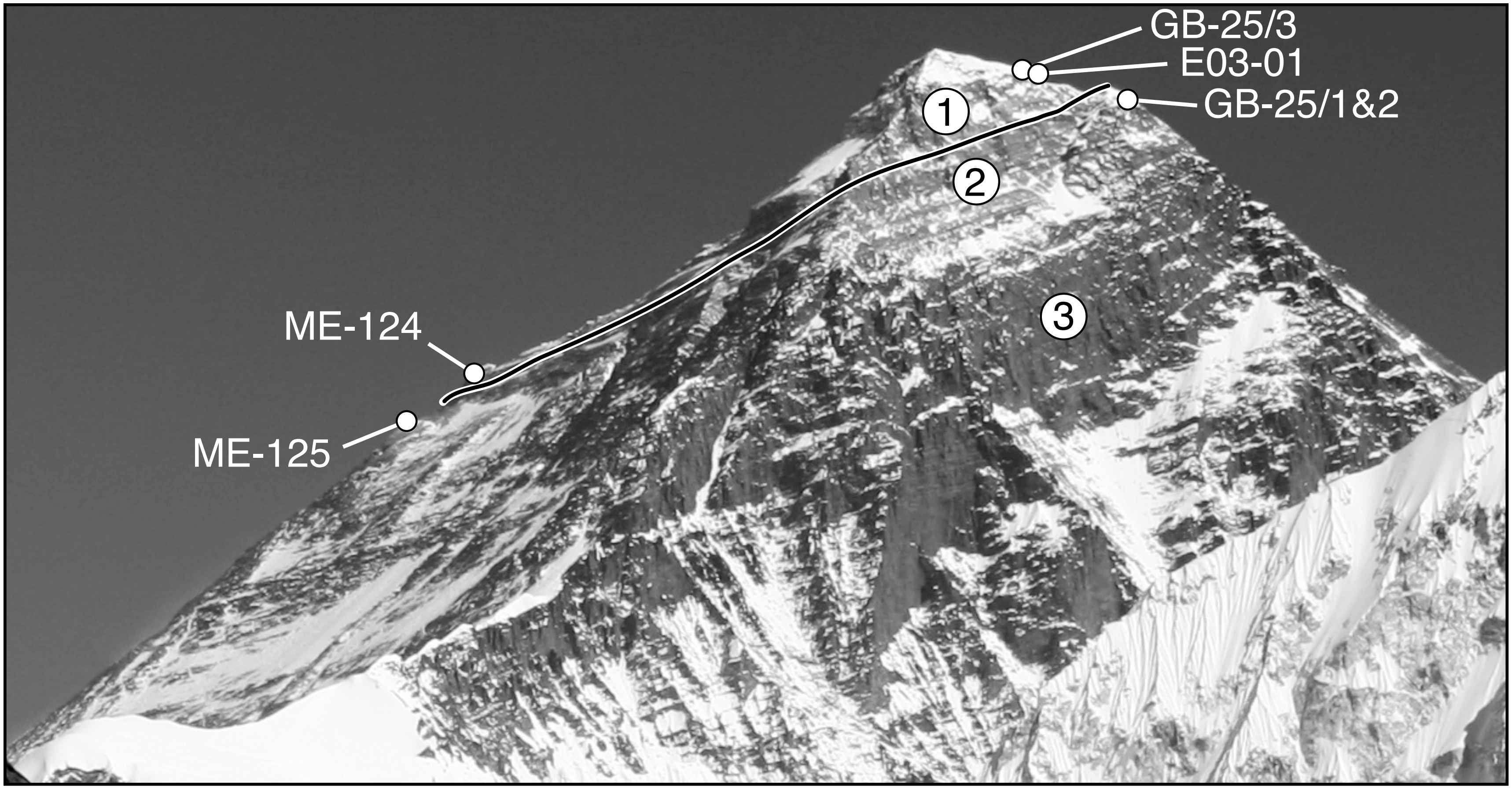

Figure 2.13. Photograph of the summit of Mount Everest (viewed towards the east) taken from Renjo La (5340 m), Nepal, using a 300 mm lens. Qomolangma detachment is highlighted by line and separates Tethyan limestone (1) above from Yellow Band marble (2) and Everest Series (3) below. Approximate locations of samples collected by Wager in 1933 (ME-124 & 125), Evans in 1953 (GB-25/1 & 2), Hillary in 1953 (GB-25/3), and Hamilton in 2003 (E-03-01) are indicated. Photomicrograph of summit sample collected by Hillary shown in Figure 6a, and the corresponding rigid grain plot is shown in Figure 2.5a. Image taken by M.J. Jessup.

Core of the Greater Himalayan Slab

Vorticity analyses in the anatectic core of the GHS were not possible because these high-grade rocks lack mineral phases that remain rigid at high deformation temperatures. Deformation in the core of the GHS is markedly different from along its bounding margins (STDS and MCTZ). Polyphase deformation of the metasedimentary rocks produced at least two phases of folds that are migmatized to variable degrees and injected by numerous leucogranite sill complexes. Key overprinting relationships exposed throughout the core provide critical insight into the structural evolution of the GHS.

One such exposure is located on the lower ramparts of the Nuptse-Lhotse wall where at least two phases of folding are preserved in a single outcrop composed of interlayered quartzite and pelites (Figs 2.3 & 2.17). The first phase of deformation (D1) is recorded by isoclinal F1 folds (14° -- 29°W) that fold graded bedding in quartzite and create a composite S0-S1 foliation (N15°E, 35°NW). Within the F1 hinges zones, white mica is aligned at a high angle to S0 and defines an axial planar foliation. Quartz microstructures within the quartzite layers record a limited degree of annealing. Isoclinal folds were refolded during a second phase of deformation (D2), producing both open F2 folds (13° -- N38°W) that broadly warp the composite S0 and S1 foliation in the quartzite layers and tighter crenulation folds (14° -- N39°W) in the mechanically weaker pelite layers (Fig. 2.16). The axial planes and fold axes of both the open F2 folds in the quartzite, and the crenulations in the pelitic layers, are parallel to each other (N50°W, 64°NE) indicating that they are part of the same deformation phase. Broad NE-and NW-trending subhorizontal folds in the Khumbu region have been documented by many previous studies (Hubbard 1988; Carosi *et al.* 1999 a & b; Catlos *et al.* 2002; Searle *et al.* 2003) and are here termed the Khumbu Dome Complex (Fig. 2.3). An undeformed layer-parallel leucogranite sill, which is partially exposed above this outcrop on the

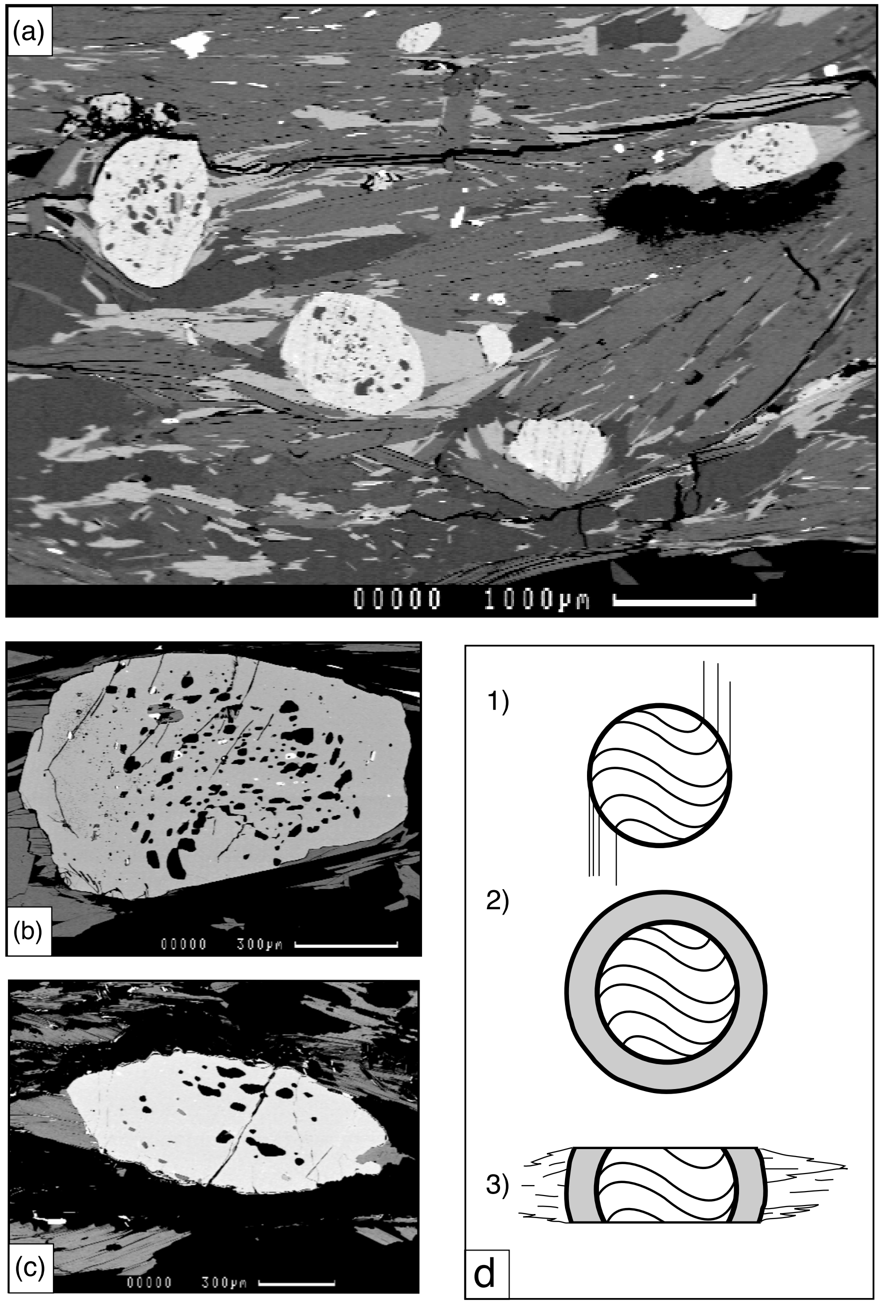

Figure 2.14. **(a)** SEM image of garnets typical of sample ET-41 from the Main Central thrust zone. Foliation is defined by aligned muscovite (intermediate gray). Biotite (light gray) forms tails on some garnet porphyroblasts and also defines the foliation. **(b)** Scanning electron microscope image of an elongate garnet in sample ET-41. Foliation is oriented E-W in the image. Sigmoidal inclusion trails defined by quartz (dark gray), biotite (intermediate gray), and oxides (white). Inclusion-free rims are preserved on both ends of the garnet. **(c)** SEM image of another example of an elongate garnet porphyroblast in sample ET-41. **(d)** Three-step evolution of elongate garnets used for rigid grain analysis (see text for details). Rigid grain plot for this sample is shown in Figure 2.5d and a photomicrograph in Figure 2.7b. Images taken by M.J. Jessup.

Nuptse-Lhotse wall, suggests that at least D1 and D2 pre-dated its emplacement. Other leucogranite sills in the upper section of the GHS core also contain little evidence for solid-state fabric development, suggesting that much of the anatectic melting and leucogranite injection post-dated the polyphase folding that characterizes the core of the slab.

Summary of vorticity data for Everest transect

Our vorticity data are taken from three lithotectonic units: (1) sheared Tethyan limestone and underlying greenschist facies Everest Series calc-mylonites, including the Yellow Band marble; (2) sheared leucogranite sills and amphibolite facies schists and gneisses in the footwall to the LD and composite QD-LD system; (3) schists from the zone of inverted metamorphic isograds within the MCTZ in which shearing either outlasted or postdated peak metamorphism. Arithmetic averages for minimum and maximum Wm values obtained in each of these lithotectonic units is summarized in Figure 2.17.

The highest average minimum and maximum W_m values (0.81 and 0.84) are recorded in the Tethyan limestone and Everest Series calc-mylonites at the top of the GHS, with a total range in estimated W_m values of 0.74-0.91 (16 samples). Lower average minimum and maximum W_m values (0.73 and 0.78) are recorded in the underlying leucogranites and amphibolite facies calc-silicates and schists with a total range in estimated W_m values of 0.57-0.85 (25 samples not including Kangshung valley samples). The lowest average minimum and maximum W_m values (0.67 and 0.72) are recorded in the MCTZ schists with a total range in estimated W_m values of 0.63-0.77 (8 samples). These average minimum and maximum estimated W_m values correspond to *c.*38-36, 48-41, and 53-48 percent pure shear components in the three lithotectonic units (Fig. 2.17). To what extent this distribution of estimated vorticity values might reflect a structural, lithologic or temporal partitioning of flow within the GHS is discussed below. Interpretation of our data is limited by the absence of vorticity data from the anatectic core of the 20-30 km thick slab, and it should be kept in mind that our data is limited to samples collected either from the top 2 km of the slab (with most samples coming from the top 600 m or less) and to samples collected from the bottom 5 km of the slab.

Discussion

Potential lithologic, structural, and temporal controls on flow partitioning

Accurate assessment of the relative importance of lithologic, structural, and temporal controls on flow path evolution is critical for interpreting the tectonic evolution of the GHS. Data from the Everest transect indicates that the most pronounced spatial transition in W_m values occurs at the top of the slab. Here, the increase in W_m values towards the structurally highest parts of the slab coincides with an upward transition from amphibolite facies schist (mica-rich) and leucogranite (quartz-feldspar-rich) to low-grade and unmetamorphosed marble and limestone. This could be interpreted in several different end-member, as well as potentially overlapping, ways including: (1) a lithologic control on vorticity of flow; (2) a progressive spatial variation in flow type controlled by structural position within the margin of the extruding slab or channel, in which individual sampling positions have not moved significant distances laterally from each other during flow/extrusion; (3) large-scale foreland-directed extrusive lateral flow resulting in tectonic emplacement of high-grade rocks (originally flowing under general shear conditions at mid-crustal depths) beneath cooler upper-crustal rocks deforming by sub-simple shear.

From a mechanics approach, rheologic competency can partition flow if sub-simple shear deformation is concentrated in relatively incompetent units while general shear is concentrated in more competent units (Lister & Williams 1983). Assuming that limestones and marbles at the top of the GHS are the rheologically weakest units, and that sub-simple shear flow has been concentrated in these units, a case could be made

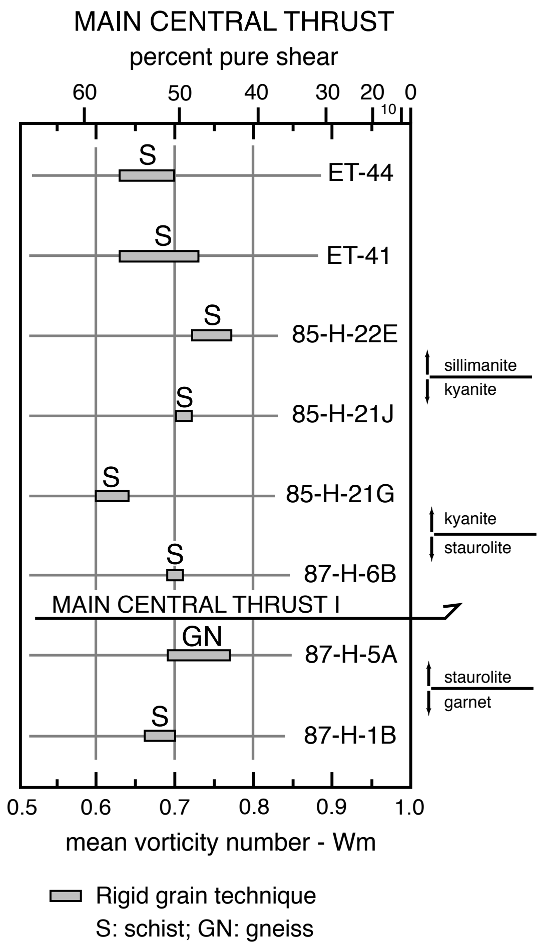

Figure 2.15. Bar chart for range of mean kinematic vorticity numbers (W_m) estimated by the rigid grain method for samples collected in the Main Central thrust zone, Khumbu region, Nepal. Metamorphic isograd locations are approximate. Sample locations shown in Figures 2.3 & 2.4.

for this interpretation. This interpretation ignores the microstructural, petrofabric, and petrologic data that indicate flow in the amphibolite facies schists and leucogranites occurred at close to peak metamorphic conditions (Law *et al.* 2004), while shearing in the overlying marble and limestone occurred at greenschist to sub-greenschist facies conditions.

At the top of GHS, the apparent upward *increase* in W_m values approaching the composite QD-LD system coincides with a progressive apparent *decrease* in deformation temperatures. If this correlation between W_m values and upward decrease in deformation temperatures is real, than our data could indicate an original rapid upward increase in W_m values within one flow regime or the structural juxtaposition of different flow regimes during extrusion. In the second interpretation, the structurally deeper and higher

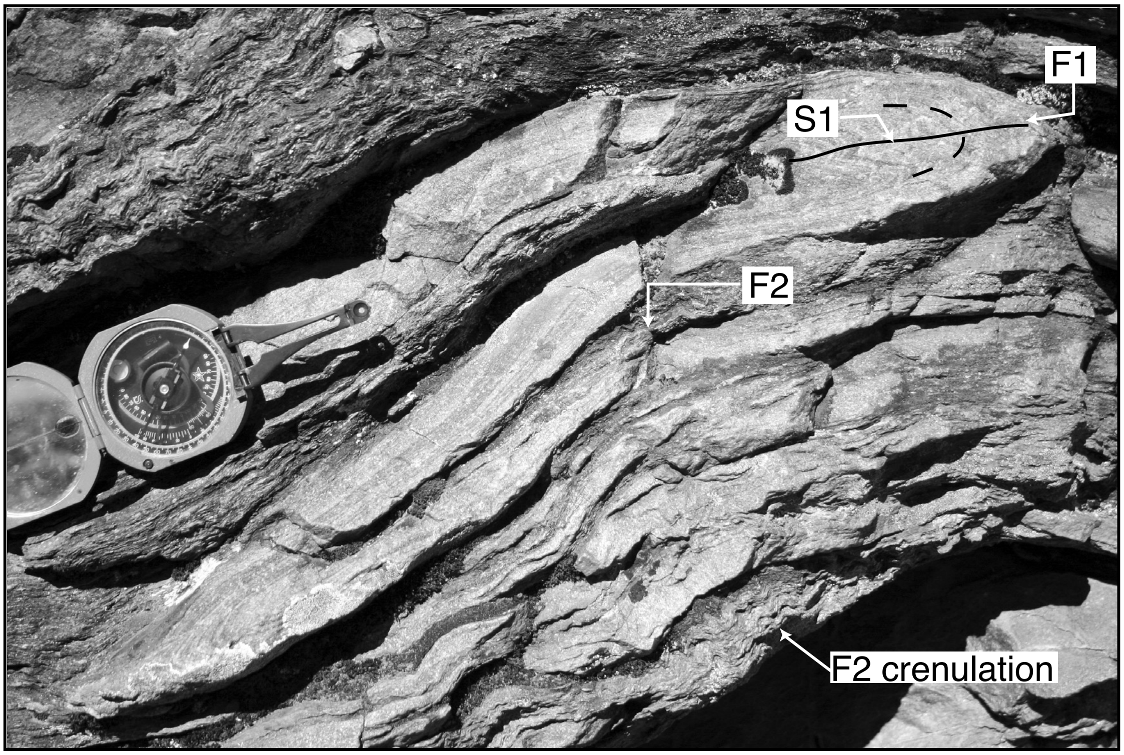

Figure 2.16. Photograph of key outcrop exposure of overprinting folds/fabrics used to define at least two phases of deformation in the core of the Greater Himalayan Slab. Uniform light gray layer is quartzite with bedding defined by biotite. Surrounding material is pelitic schist. See text for details. Brunton compass for scale. Image is of a vertical wall viewed towards the west. Approximate location of outcrop shown on Figure 2.3. Image taken by M.J. Jessup.

temperature samples provide information on flow that occurred at deeper crustal levels during earlier stages of channel flow/extrusion (low W_m values), while the structurally higher, lower temperature, samples only record information on flow (at higher W_m values) that occurred at much higher crustal levels.

An upward decrease in deformation temperatures within the upper 600 m of the GHS and overlying Everest Series and Tethyan rocks is indicated by: (1) decreasing opening angles of quartz *c*-axis fabrics from the schists beneath the composite QD-LD system (Law *et al.* 2004, their figure 8b); (2) a progression from quartz recrystallization dominated by grain boundary migration (Regime 3 of Hirth & Tullis 1992) in

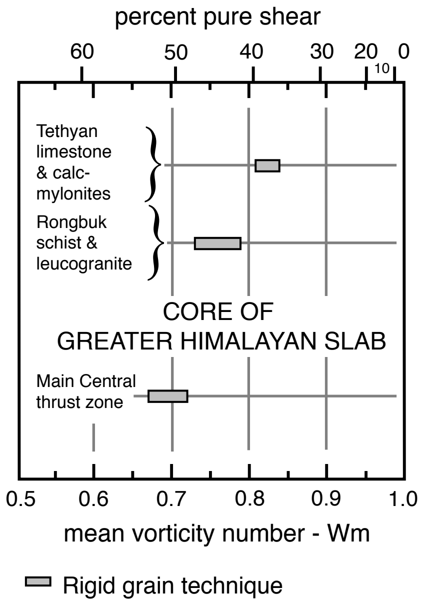

Figure 2.17. Bar chart of average minimum and average maximum W_m values for: 1) Tethyan limestone, calc-mylonites and marble of the Everest Series, and calc-silicates in immediate footwall to Qomolangma-Lhotse Detachment system; 2) schists and mylonitic leucogranites of the Rongbuk Formation; 3) garnet schist from the Main Central thrust zone.

the deeper schists to combined subgrain rotation (Regime 2) and grain boundary migration recrystallization in the immediate footwall to the detachment system; (3) an upward increase in brittle deformation of feldspar grains; (4) a transition from plastic deformation of quartz below the detachment system to brittle deformation of quartz (albeit within a mechanically weaker calcite matrix) in the overlying Everest Series calc-mylonites and sheared Tethyan limestones; (5) an abrupt transition in twinning regime (and dynamically recrystallized grain size) between the Everest Series Yellow Band marble and overlying Tethyan limestone.

Law *et al.* (2004) previously argued that the strains in our samples are too low for the extreme apparent thermal gradient (*c.* 330 °C/km) indicated by microstructures and fabric opening angles to be solely explained by strain-induced telescoping of isotherms during extrusion. We suggest that, traced structurally upwards towards the top of the GHS, the inverse relationship between W_m values (*increasing*) and deformation temperatures (*decreasing*) reflects both a spatial and temporal flow partitioning, with structurally deeper and higher temperature samples preserving information on flow that occurred at deeper crustal levels during earlier stages of channel flow/extrusion (low W_m

values). The structurally higher, lower temperature, samples only record information on flow (higher W_m values) that occurred at much higher crustal levels, probably during the later stages of exhumation. In this interpretation, strain rate may also play a role in controlling the nature of local flow. However, using the available data, we cannot unequivocally choose between our preferred model, in which the low temperature samples record deformation during late stages of extrusion-exhumation, and a model in which both low and high temperature samples were deformed simultaneously at different structural levels in the crust. As previously discussed by Grasemann *et al.* (1999) and Williams *et al.* (2006), extrusion models involving a component of pure shear require an increase in strain rate at the margins of the extruding slab/wedge traced from the hinterland to the foreland. Thus the progressive evolution from more ductile to more brittle behavior, which we infer to indicate flow at progressively structurally shallower levels and in more foreland parts of the orogenic system, may be a composite effect of decreasing temperature and increasing strain rate.

Distribution of flow regimes within the GHS and tectonic implications

In both basic channel flow models (e.g. Grujic *et al.* 1996, 2002) and extrusive flow models (e.g. Williams *et al.* 2006), a symmetric distribution of flow paths is predicted at any one instant in time, with lowest flow vorticities in the center of the channel and a progressive increase in flow vorticities towards the boundaries of the channel (Grujic *et al.* 2002, their figure 7; see also Grujic 2006, his Figure 1c). In coupled thermal-mechanical finite-element models (which assume a reduction in channel viscosities by partial melting) material in the central parts of the channel originates at mid-lower crustal depths and *"tunnels"* for great distances laterally before extruding into upper-crustal rocks as it approaches the topographic surface (Beaumont *et al.* 2001, 2004, 2006; Jamieson *et al.* 2002, 2004, 2006; Godin *et al.* 2006b). Our microstructural and vorticity data from the top of the GHS are compatible with components of all these models. Due to the high deformation temperatures, presumably associated with flow, no vorticity markers have been preserved in the core of the slab. Our field data indicate that this penetrative flow in the core occurred during the relatively earlier stages of decompression (see above) and therefore is probably slightly earlier than flow recorded in the amphibolite - subgreenschist facies rocks at the margins of the slab. These interpretations are also compatible with the above channel flow / extrusion models. Assuming flow associated with our data is essentially synchronous in the upper and lower parts of the slab, our vorticity data from the MCTZ are incompatible with these models. Our analyses, although limited, indicate that the MCTZ is characterized by the lowest average W_m values (i.e. highest pure shear components) in our transect across the slab. The MCTZ lacks any convincing progressive increase in W_m values at deeper structural levels that might, as predicted for example by channel flow models, mirror the increase in W_m values at the top of the slab. From a mechanics perspective, an increase in lithostatic pressure towards the base of the slab, as implied in gravity-driven collapse / spreading models for thrust belt evolution, provides a potential explanation for the highest pure shear component being recorded at the deepest structural levels (see Simpson & De Paor 1997; review by Merle 1998).

Results of our vorticity analyses from the Everest transect share some similarities with those from the Sutlej River section of the MCTZ where Grasemann *et al.* (1999) demonstrated a progressive downward decrease in W_m values towards the base of the GHS. Grasemann *et al.* (1999) proposed that their vorticity data indicated a temporal (rather than spatial) change in flow regime associated with a decelerating strain path (Simpson & De Paor 1997) in which progressively more general shear replaced high temperature simple shear flow during cooling. In the Everest transect, our microstructural data from the MCTZ demonstrate that low W_m values (indicating a general shear) are related to flow and foliation development that postdates peak metamorphic conditions (see also Hubbard 1988, 1989). Evidence such as flow at higher temperatures in the structurally higher sections of the MCTZ, and at lower temperatures in the structurally deeper levels (e.g. chlorite wings on garnet porphyroclasts), suggest that penetrative flow may have progressed to deeper structural levels over time, as suggested for the Sutlej River section by Grasemann *et al.* (1999).

Timing constraints on the kinematic evolution of the GHS are provided by a wealth of geochronologic data from the Everest region. Mylonitic leucogranite sills parallel to the combined QD/LD system along the top of the slab suggest that ductile shearing lasted until *c.* 17 Ma after which brittle motion on the upper strand of the detachment system occurred until *c.* 16 Ma (Murphy and Harrison 1999; Searle *et al.* 2003). Timing of amphibolite-grade metamorphism and early deformation (*c.* 500-550°C) on the MCTZ is constrained to *c.*21 Ma (Hubbard & Harrison 1989). Monazite inclusions in garnets from the Everest section of the MCTZ, dated at *c.* 14 Ma by Catlos *et al.* (2002), provide a maximum age constraint for garnet growth (assuming they predate garnet growth) and hence flow associated with these W_m data. Based on available isotopic age data, this phase of flow along the base of the GHS, which is associated with the lowest average W_m values in the Everest transect, may be younger than the documented flow regimes at the top of the slab.

This interpretation does not exclude the possibility that earlier reverse-sense shearing on the MCTZ (possibly involving sub-simple shear as required for example by channel flow models) was synchronous with normal-sense shearing at the top of the slab. Instead this interpretation suggests that the microstructural evidence for this earlier shearing may have been overprinted as the core of the channel locked up at *c.*16 Ma and flow was partitioned into the foreland to accommodate continued crustal shortening (see Godin *et al.* 2006b).

Conclusions

Structural analyses of rocks collected along the Everest transect provide the first quantitative information on how flow was partitioned within the Greater Himalayan Slab during extrusion and exhumation. Results of vorticity analyses along the top of the slab indicate that the higher-grade, structurally deeper rocks, record general shear at close to peak metamorphic conditions, while the lower-grade, structurally higher rocks, record sub-simple shear. Vorticity measurements in the core of the slab are problematic due to the high metamorphic grade they reached; however, the penetrative fabrics in the core most likely developed at mid-crustal depths during the early stages of decompression. The highest average pure shear components are recorded at the base of the slab, and are associated with deformation that postdates peak metamorphism. We attribute the distribution of flow regimes to spatial and temporal partitioning of flow in which higher temperature samples record the early stages of channel flow/extrusion (general shear) at mid-crustal depths in the interior of the channel. The structurally higher, lower temperature, samples at the top of the slab only record information on flow (sub-simple shear) that occurred along the upper margin of the channel at much higher crustal levels, probably during the later stages of exhumation. Although flow paths in the upper and lower parts of the slab may have been similar during channel flow and extrusion, as required by the different models, microstructural evidence for earlier shearing at peak metamorphic conditions along the base of the slab was overprinted as the channel flow / extrusion system locked up at *c.*16 Ma and the locus of deformation migrated towards the foreland in order to accommodate continued crustal shortening.

Acknowledgements

We are grateful to Bob Tracy, Dave Waters, Fred Read, Karl Karlstrom, and Grahame Oliver for discussion and advice on various aspects of this project. We thank T. Sherpa, D. Sherpa, R. Rai, J. Cottle, D. Newell, J. Ashby, and L. Duncan for assistance in the field and many stimulating discussions over tea and dhal bhat. Also, many thanks to R. Schrama and S. Dhakta for help with organizing field seasons in Tibet. We also thank Steve Laurie (Cambridge University) and Dave Waters (Oxford University Museum of Natural History) for generously providing access to high altitude Mount Everest samples from the Harker and Wager collections. Christopher Bailey, Laurent Godin, and Paris Xypolias are thanked for their detailed and helpful reviews of an earlier version of the manuscript. This work was funded by National Science Foundation grant EAR 0207524 to RDL and MPS. MJJ was also funded by Geological Society of America and Sigma Xi graduate student research grants, a W.D. Lowry Geosciences Graduate Research Award from Virginia Tech Dept. of Geosciences, and a 2010 Graduate Fellowship from Virginia Tech College of Science-Graduate School. Fieldwork by MSH was funded by NSF grant EAR-8414417 to K.V. Hodges.

References

ARITA, K. 1983. Origin of the inverted metamorphism of the Lower Himalayas, central Nepal. *Tectonophysics*, **95**, 43-60.

BAILEY, C.M., POLVI, L.E. & FORTE, A.M. in press. Pure shear-dominated high-strain zones in basement terranes. In: Hatcher, R. D. Jr., Carlson, M. P., McBride J. H., and Catalán, J. R. M (eds) Four Dimensional Framework of Continental Crust, *Geological Society of America Memoir.*

BAILEY, C.M. & EYSTER, E.L. 2003. General shear deformation in the Pinaleno Mountains metamorphic core complex, Arizona. *Journal of Structural Geology*, **25**, 1883-1892.

BAILEY, C.M., FRANCIS, B.E. & FARNHEY, E.E. 2004. Strain and vorticity analysis of transpressional high-strain zones from the Virginia a Piedmont, USA. In: ALSOP, G.I., HOLDSWORTH, R.E., MCCAFFREY, K.J.W. AND HAND, M. (eds) *Flow Processes in Faults and Shear Zones.* Geological Society, London, Special Publications, **224**, 249-264.

BEAUMONT, C., JAMIESON, R.A., NGUYEN, M.H. & LEE, B., 2001. Himalayan tectonics explained by extrusion of a low-viscosity crustal channel coupled to focused surface denudation. *Nature*, **414**, 738-742.

BEAUMONT, C., JAMIESON, R.A., NGUYEN, M.H. & MEDVEDEV, S. 2004. Crustal channel flows: 1. Numerical models with applications to the tectonics of the Himalayan – Tibetan orogen. *Journal of Geophysical Research*, **109**, B06406 29p.

BEAUMONT C., NGUYEN, M., JAMIESON, R. & ELLIS, S. this volume. Crustal flow modes in large hot orogens. In: Law, R.D., Searle, M.P. & Godin, L. (eds) Channel Flow, Ductile Extrusion and Exhumation in Continental Collision Zones. *Geological Society, London, Special Publications*, **268**, 91-145.

BORDET, P. 1961. Recherches Géologiques dans l'Himalaya du Népal, Région du Makalu. Centre Nationale de recherche Scientifique, Paris, 275p.

BRUNEL, M. & KIENAST, J.-R. 1986. Étude pétro-structurale des chevauchments ductiles himalayens sur la transversale de l'Everest-Makalu (Népal oriental). *Canadian Journal Earth Science,* **23**, 1117-1137.

BURCHFIEL, B.C. & ROYDEN, L.H. 1985. North-south extension within the convergent Himalayan region. *Geology*, **13**, 10; 679-682.

Burchfiel, B.C., Zhiliang, C., Hodges, K.V., Yuping, L., Royden, L., Changrong, D. & Jiene, X. 1992. The South Tibetan Detachment System, Himalayan Orogen: extension contemporaneous with and parallel to shortening in a collisional mountain belt. *Geological Society of America Special Paper*, **269**, 41 p.

Burkard, M. 1993. Calcite-twins, their geometry, appearance and significance as stress-strain markers and indicators of tectonic regime: a review. *Journal of Structural Geology*, **15**, 351-368.

Carosi, R., Lombardo, B., Molli, G., Musumeci, G. & Pertusati, P. 1998. The South Tibetan detachment system in the Rongbuk valley, Everest region. Deformation features and geological implications. *Journal of Asian Earth Sciences*, **16**, 299-311.

Carosi, R., Lombardo, B., Musumeci, G. & Pertusati, P. 1999a. Geology of the Higher Himalayan crystallines in Khumbu Himal (Eastern Nepal). *Journal of Asian Earth Sciences*, **17**, 785-803.

Carosi, R., Musumeci, G. & Pertusati, P.C. 1999b. Extensional tectonics in the higher Himalayan crystallines of Khumbu Himal, eastern Nepal. In: Macfarlane, A., Sorkhabi, R.B. & Quade, J. (eds) *Himalaya and Tibet: Mountain Roots to Mountain Tops*. Geological Society of America Special Paper **328**, 211- 223.

Carosi, R., Montomoli, C., Rubatto, D. & Visona, D. this volume. Normal-sense shear zones in the core of the Higher Himalayan Crystallines (Bhutan Himalayas): evidence for extrusion? *In*: Law, R. D., Searle, M. P. & Godin, L. (eds) *Channel Flow, Ductile Extrusion, and Exhumation in Continental Collision Zones.* Geological Society, London, Special Publications, **268**, 425-444.

Catlos, E.J., Harrison, T.M., Manning, C.E., Grove, M., Rai, S.M., Hubbard, M. & Upreti, B.N. 2002. Records of the evolution of the Himalayan orogen from in situ Th-Pb ion microprobe dating of monazite: Eastern Nepal and western Garhwal. *Journal of Asian Earth Sciences*, **20**, 459-80.

England, P. & Molnar, P. 1993. Cause and effect among thrust and normal faulting, anatectic melting and exhumation in the Himalaya. . *In*: Treloar, P.J. & Searle, M.P. (eds) *Himalayan Tectonics*. Geological Society, London, Special Publications, **74**, 401-411.

Ferrill, D.A., Morris, A.P., Evans, M.A., Burkhard, M., Groshong, R.H. & Onasch, C.M. 2004. Calcite twin morphology: a low temperature geothermometer. *Journal of Structural Geology*, **26**, 1521-1530.

Fielding, E., Isacks,B., Barazangi, M. & Duncan, C. 1994. How flat is Tibet? *Geology*, **22**, 163-7.

Fossen, H., & Tikoff, B. 1997. Forward modeling of non-steady-state deformations and the "minimum strain path". *Journal of Structural Geology,* 19, 987-996.

Gansser, A. 1964. *The Geology of the Himalayas*. Wiley Interscience, 289 pp.

Ghosh, S. K. & Ramberg, H. 1976. Reorientation of inclusions by combination of pure and simple shear. *Tectonophysics*, **34**, 1-70.

Godin, L., Grujic, D, Law, R.D. & Searle, M.P. 2006 a. Channel flow, extrusion, and exhumation in continental collision zones: an introduction. *In*: Law, R. D., Searle, M. P. & Godin, L. (eds) *Channel Flow, Ductile Extrusion, and Exhumation in Continental Collision Zones.* Geological Society, London, Special Publications, **268**, 269-292.

Godin, L., Gleeson, T., Searle, M.P., Ullrich, T.D. & Parrish, R.R. this 2006b. Locking of southward extrusion in favor of rapid crustal-scale buckling of the Greater Himalayan sequence, Nar valley, central Nepal. *In*: Law, R. D., Searle, M. P. & Godin, L. (eds) *Channel Flow, Ductile Extrusion, and Exhumation in Continental Collision Zones.* Geological Society, London, Special Publications, **268**, 1-23.

Grasemann, B., Fritz, H. & Vannay, J-C. 1999. Quantitative kinematic flow analysis from the Main Central Thrust zone, (NW Himalaya): implications for a decelerating strain path and the extrusion of orogenic wedges. *Journal of Structural Geology*, **21**, 837-853.

Grujic, D. this volume. Channel flow and continental collision tectonics: an overview. *In*: Law, R. D., Searle, M. P. & Godin, L. (eds) *Channel Flow, Extrusion, and Exhumation in Continental Collision Zones.* Geological Society, London, Special Publications.

Grujic, D., Casey, M., Davidson, C., Hollister, L., Kundig, K., Pavlis, T. & Schmid, S. 1996. Ductile extrusion of the Higher Himalayan crystalline in Bhutan: evidence from quartz microfabrics. *Tectonophysics*, **260**, 21-43.

Grujic, D., Hollister, L. & Parrish, R.R. 2002. Himalayan metamorphic sequence as an orogenic channel: insight from Bhutan. *Earth and Planetary Science Letters*, **198**, 177-191.

Gysin, M. & Lombard, A. 1959. Note sur la composition des roches métamorphiques et sédimentaires des sommets du Mont Everest-Lhotse (Himalaya). *Archives des Sciences, Genève*, **12**, 98-101.

GYSIN, M. & LOMBARD, A. 1960. Observations complémentaires de pétrographie et de géologie dans le Massif du Mont Everest-Lhotse. *Eclogae Geologicae Helvetiae*, **53**, 189-204.

HARRISON, T. M., GROVE, M., LOVERA, O. M., CATLOS, E. J. & ANDREA, J.D. 1999. The origin of Himalayan anatexis and inverted metamorphism: Models and constraints. *Journal of Asian Earth Sciences*, **17**, 755-772.

HEIM, A. & GANSSER, A. 1939. Central Himalaya. Geological observations of the Swiss expedition, 1939. *Denkschriften der Schweizerrischen Naturforschenden Gesellschaft*, **73**, 1-245.

HIRTH, G. & TULLIS, J. 1992. Dislocation creep regimes in quartz aggregates. *Journal of Structural Geology*, **14**, 145-160.

HODGES, K. V. 2000. Tectonics of the Himalaya and southern Tibet from two perspectives. *Geological Society of America Bulletin*, **112**, 324-350.

HODGES, K.V. this volume. The channel tunneling-extrusion hypothesis as developed for the Himalayan-Tibetan orogenic system. In: LAW, R.D., SEARLE, M.P. & GODIN, L. (eds) *Channel Flow, Ductile Extrusion, and Exhumation in Continental Collision Zones. Geological Society, London, Special Publications,* ***268****, 71-90.*

HODGES, K. V., PARRISH, R. R., HOUSCH, T. B., LUX, D. R., BURCHFIEL, B. C., ROYDEN, L. H. & CHEN, Z. 1992. Simultaneous Miocene extension and shortening in the Himalayan orogen. *Science*, **258**, 1466-1470.

HODGES, K.V., BURCHFIEL, B.C., ROYDEN, L.H., CHEN, Z. & LIU, Y. 1993. The metamorphic signature of contemporaneous extension and shortening in the central Himalayan orogen: data from the Nyalam transect, southern Tibet. *Journal of Metamorphic Geology*, **11**, 721-737.

HODGES, K. V., BOWRING, S., DAVIDEK, K., HAWKINS, D. & KROL, M. 1998. Evidence for rapid displacement on Himalayan normal faults and the importance of tectonic denudation in the evolution of mountain ranges. *Geology*, **26**, 483-6.

HODGES, K.V., HURTADO, J.M. & WHIPPLE, K.X. 2001. Southward extrusion of Tibetan crust and its effect on Himalayan tectonics. *Tectonics*, **20**, 799-809.

HOLCOMBE, R.J. & LITTLE, T.A. 2001. A sensitive vorticity gauge using rotated porphyroblasts and its application to rocks adjacent to the Alpine Fault, New Zealand. *Journal of Structural Geology,* **23**, 979-990.

Hubbard, M.S. 1988. Thermobarometry, 40Ar/39Ar geochronology, and structure of the Main Central Thrust zone and Tibetan Slab, eastern Nepal Himalaya. PhD thesis, Massachusetts Institute of Technology, Cambridge, 169p.

Hubbard, M.S. 1989. Thermobarometric constraints on the thermal history of the Main Central Thrust Zone and Tibetan Slab, eastern Nepal Himalaya. *Journal of Metamorphic Geology*, **7**, 19-30.

Hubbard, M. S. 1996. Ductile shear as a cause of inverted metamorphism: Example from the Nepal Himalaya. *Journal of Geology*, **104**, 493-499.

Hubbard, M. S. & Harrison, T. M. 1989. $^{40}Ar/^{39}Ar$ age constraints on deformation and metamorphism in the Main Central Thrust zone and Tibetan Slab, eastern Nepal Himalaya. *Tectonics*, **8**, 865 - 880.

Jamieson, R.A., Beaumont, C., Nguyen, M.H. & Lee, B. 2002. Interaction of metamorphism, deformation and exhumation in large convergent orogens. *Journal of Metamorphic Geology*, **20**, 9-24.

Jamieson, R. A., Beaumont, C., Medvedev & Nguyen, M.H. 2004. Crustal channel flows: 2. Numerical models with implications for metamorphism in the Himalayan-Tibetan orogen. *Journal Geophysical Research*, **109**, B06407, doi:10.1029/2003JB002811.

Jamieson R.A., Beaumont, C., Nguyen, M.H. & Grujic, D. this volume Provenance of the Greater Himalayan Sequence and associated rocks: Predictions of channel flow models. In: Law, R.D., Searle, M.P. & Godin, L. (eds) *Channel Flow, Extrusion, and Exhumation in Continental Collision Zones. Geological Society, London, Special Publications*.

Jessup, M.J., Searle, M.P., Tracy, R. & Law, R.D. 2004. Staurolite schist marks right-way up metamorphic isograds at the top of the High Himalayan Slab, Mount Everest, Tibet/Nepal. (abstract) In: Searle, M.P. Law, R.D. & Godin, L. (convenors) Programme and abstracts for conference on: Channel Flow, Ductile Extrusion and Exhumation of Lower-mid Crust in Continental Collision zones, 6th-7th December 2004, *Geological Society, London*.

Jessup, M.J., Searle, M.P., Tracy, R., Law, R.D., Cottle, J.M. & Waters, D. 2005. Thermal-mechanical evolution of the upper-section of the Greater Himalayan Slab, Everest-Lhotse massif, Nepal. Geological Society of America Abstracts with Programs, 37, No. 7, 388.

KLEPEIS, K.A., DACZKO, N.R. & CLARKE, G.L. 1999. Kinematic vorticity and tectonic significance of superposed mylonites in a major lower crustal shear zone, northern Fiordland, New Zealand. *Journal of Structural Geology*, **21**, 1385-1406.

KÜNDIG, R. 1988. Kristallisation und deformation in Higher Himalaya, Zanskar, NW-Indien). PhD thesis, ETH-Zürich, 188 pp.

KÜNDIG, R. 1989. Domal structures and high grade metamorphism in the Higher Himalayan Crystalline, Zanskar Region, northwest Himalaya. *Journal of Metamorphic Geology*, **7**, 43-55.

LAW, R.D., SEARLE, M.P. & SIMPSON, R.L. 2004. Strain, deformation temperatures and vorticity of flow at the top of the Greater Himalayan Slab, Everest massif, Tibet. *Journal of the Geological Society, London*, **161**, 305-320.

LISTER, G.S. & WILLIAMS, P.F. 1983. The partitioning of deformation in flowing rock masses. *Tectonophysics*, **92**, 1-33.

LOMBARD, A. 1958. Un itinéraire géologique dans l'Est du Népal, Massif du Mont Everest. *Mémoires de la Societé Helvétiques des Sciences Naturelles,* **82/1,** 107p.

LOMBARDO, B., PERTUSATI, P. & BORGI, S. 1993. Geology and tectonomagmatic evolution of the eastern Himalaya along the Chomolungma - Makalu transect. In: TRELOAR, P.J. & SEARLE, M.P. (eds) *Himalayan Tectonics,* Geological Society, London, Special Publications, **74**, 341-355.

MEANS, W.D. 1989. Stretching faults. *Geology*, **17**, 893-896.

MERLE, O. 1998. *Emplacement Mechanisms of Nappes and Thrust Sheets.* Kluwer Academic Publishers, Dordrecht, 159 pp.

MURPHY, M.A. & HARRISON, T.M. 1999. Relationship between leucogranites and the Qomolangma Detachment in the Rongbuk valley, south Tibet. *Geology*, **27**, 831-834.

NELSON, K.D., ZHAO, W., BROWN, L.D., KUO, J., CHE, J., LIU, X., KLEMPERER, S.L., MAKOVSKY, Y., MEISSNER, R., MECHIE, J., KIND, R., WENZEL, F., NI, J., NABELEK, J., LESHUO, C., TAN, H., WEI, W., JONES, A.G., BOOKER, J., UNSWORTH, M., KIDD, W.S.F., HAUCK, M., ALSDORF, D., ROSS, A., COGAN, M., WU, C., SANDVOL, E. & EDWARDS, M. 1996. Partially molten middle crust beneath southern Tibet; synthesis of Project INDEPTH results. *Science,* **274,** 1684-1688.

ODELL, N.E. 1965. The highest fossils in the world. Geological Magazine, 104, 73-76.

PASSCHIER, C.W. 1987. Stable positions of rigid objects in non-coaxial flow—a study in vorticity analysis. *Journal of Structural Geology*, **9**, 679-690.

POGNANTE, U. & BENNA, P. 1993. Metamorphic zonation, migmatization and leucogranites along the Everest transect of eastern Nepal and Tibet: record of an exhumation history, In: TRELOAR, P.J. & SEARLE, M.P. (eds) *Himalayan Tectonics,* Geological Society, London, Special Publications, **74**, 323 - 340.

ROYDEN, L.H. & BURCHFIEL, B.C. 1987. Thin-skinned N-S extension within the convergent Himalayan region: gravitational collapse of a Miocene topographic front. In: Coward, M.P., Dewey, J.F. & Hancock, P.L. (eds) *Continental Extensional Tectonics*. Geological Society, London, Special Publications, **28**, 611-619.

SAKAI, S., SAWADA, M., TAKIGAMI, Y., ORIHASI, Y., DANHARA, T., IWANO, H., KUWAHARA, Y., DONG, Q. & LI, J. 2005. Geology of the summit limestone of Mount Qomolangma (Everest) and cooling history of the Yellow Band under the Qomolangma detachment. *The Island Arc*, **14,** 297-310.

SEARLE, M.P. 1996. Cooling history, erosion, exhumation, and kinematics of the Himalaya-Karakorum-Tibet orogenic belt. In: Yin, A. & Harrison, T.M. (eds) *The Tectonic Evolution of Asia*. Cambridge University Press, Cambridge, 110-137.

SEARLE, M.P. 1999a. Extensional and compressional faults in the Everest – Lhotse massif, Khumbu Himalaya, Nepal. *Journal of the Geological Society, London*, **156**. 227-40.

SEARLE, M.P. 1999b. Emplacement of Himalayan leucogranites by magma injection along giant sill complexes: examples from the Cho Oyu, Gyachung Kang and Everest leucogranites (Nepal Himalaya). *Journal of Asian Earth Sciences*, **17**, 773-783.

SEARLE, M.P. 2003. *Geological map of the Everest massif, Nepal and South Tibet.* Scale 1:100,000, Dept. Earth Sciences, Oxford University.

SEARLE, M.P. & REX, A.J. 1989. Thermal model for the Zanskar Himalaya. *Journal of Metamorphic Geology*, **7**, 127-134.

SEARLE, M.P., WINDLEY, B.F. & COWARD, M.P. 1987. The closing of Tethys and tectonics of the Himalaya. *Geological Society of America Bulletin*, **98**, 678-701.

SEARLE, M.P., SIMPSON, R.L., LAW, R.D., WATERS, D.J. & PARRISH, R.R. 2002. Quantifying displacement on the South Tibetan detachment normal fault, Everest massif, and the timing of crustal thickening and uplift in the Himalaya and South Tibet. *Journal of Nepal Geological Society*, **26**, 1-6.

SEARLE, M.P., SIMPSON, R.L., LAW, R.D., PARRISH, R.R. & WATERS, D.J. 2003. The structural geometry, metamorphic and magmatic evolution of the Everest massif, High Himalaya of Nepal-south Tibet. *Journal of Geological Society, London*, **160**, 345-66.

SEARLE, M.P., LAW, R.D. & JESSUP, M.J. *this volume*. Crustal structure, restoration and evolution of the Greater Himalaya in Nepal – South Tibet: implications for channel flow and ductile extrusion of the middle crust. *In*: LAW, R.D., SEARLE, M.P. & GODIN, L. (eds) *Channel flow, Extrusion, and Exhumation in Continental Collision Zones.* Geological Society, London, Special Publications.

SIMPSON, C. & DE PAOR, D.G. 1997. Practical analysis of general shear zones using porphyroclast hyperbolic distribution method: an example from the Scandinavian Caledonides. In: SENGUPTA, S. (ed) *Evolution of Geological Structures in Micro- to Macro-scales.* Chapman and Hall, London, 169-184.

SIMPSON, R. L., PARRISH, R. R., SEARLE, M. P. & WATERS, D. J. 2000. Two episodes of monazite crystallization during metamorphism and crustal melting in the Everest region of the Nepalese Himalaya. *Geology*, **28**, 403-406.

STIPP, M., STUNITZ, H., HEILBRONNER, R. & SCHMID, S. 2002. Dynamic recrystallization of quartz: correlation between natural and experimental conditions. In: DE MEER, S., DRURY, M.R., DE BRESSER, J.H.P. & PENNOCK, G.M. (eds) *Deformation Mechanisms, Rheology and Tectonics: Current Status and Future Perspectives.* Geological Society, London, Special Publications, **200**, 171-190.

VANNAY, J.-C. & GRASEMANN, B. 2001. Himalayan inverted metamorphism and syn-convergence extension as a consequence of a general shear extrusion. *Geological Magazine*, **138**, 253-276.

WAGER, L.R. 1934. A review of the geology and some new observations. In: RUTTLEDGE, H. *Everest 1933*. Hodder and Stoughton, London, 312-337.

WAGER, L.R. 1939. The Lachi series of N. Sikkim and the age of the rocks forming Mount Everest. Rec. Geological Survey of India, **74**, 171-188.

Walker, J.D., Martin, M. W., Bowring, S. A., Searle, M. P., Waters, D. J. & Hodges, K. V. 1999. Metamorphism, melting and extension: Age constraints from the High Himalayan slab of Southeastern Zanskar and Northwestern Lahoul. *Journal of Geology*, **107**, 473-95.

Wallis, S. R. 1995. Vorticity analysis and recognition of ductile extension in the Sanbagawa belt, SW Japan. *Journal of Structural Geology*, **17**, 1077-1093.

Wallis, S. R., Platt, J.P. & Knott, S.D. 1993. Recognition of syn-convergence extension in accretionary wedges with examples from the Calabrian Arc and the Eastern Alps. *American Journal of Science*, **293**, 463-495.

Waters, D.J., Law, R.D. & Searle, M.P. 2006. Metamorphic evolution of the upper parts of the Greater Himalayan Slab, Everest area, from the 1933 sample collection of L. R. Wager. (abstract) 21st annual Himalayan-Karakoram-Tibet workshop. *Journal of Asian Earth Sciences*, 26, 168.

Wells, M.L. 2001. Rheological control on the initial geometry of the Raft River detachment fault and shear zone, western United States. *Tectonics*, **20**, 435-457.

Williams, P.F., Jiang, D. & Lin, S. this volume. Interpretation of deformation fabrics of infrastructure zone rocks in the context of channel flow and other models. *In*: Law, R. D., Searle, M. P. & Godin, L. (eds) *Channel Flow, Extrusion, and Exhumation in Continental Collision Zones.* Geological Society, London, Special Publications,

Xypolias, P. & Doutsos, T. 2000. Kinematics of rock flow in a crustal-scale shear zone: implications for the orogenic evolution of the southwestern Hellenides. *Geological Magazine*, **137**, 81-96.

Xypolias, P. &, Koukouvelas, I. K. 2001. Kinematic vorticity and strain patterns associated with ductile extrusion in the Chelmos shear zone (External Hellenides, Greece). *Tectonophysics*, **338**, 59-77.

Xypolias, P. & Kokkalas, S. this volume. Heterogeneous ductile deformation along a mid-crustal extruding shear zone: an example from the External Hellenides (Greece). *In*: Law, R. D., Searle, M. P. & Godin, L. (eds) *Channel Flow, Extrusion, and Exhumation in Continental Collision Zones.* Geological Society, London, Special Publications.

Yin, C.H. & Kuo, S.T. 1978. Stratigraphy of the Mount Jolmo Lungma and its north slope. *Scientia Sinica,* **21**, 629-644.

Yin, A. & Harrison, T.M. 2000. Geologic evolution of the Himalayan-Tibetan orogen. *Annual Review of Earth and Planetary Sciences*, **28**, 211-280.

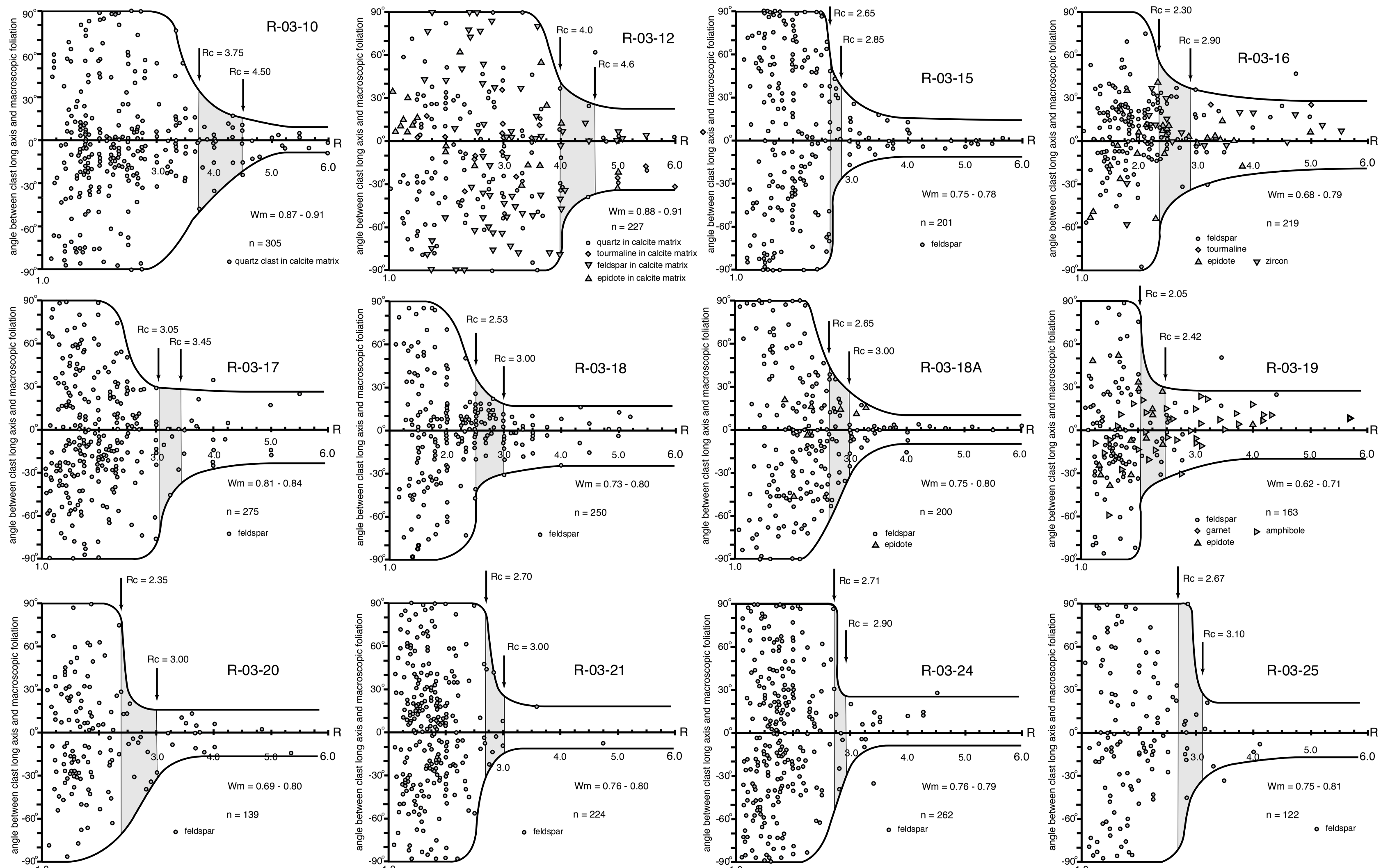

Figure 2.A1. Northern transect. Positive and negative angles between clasts long axis and foliation indicate that clasts either inclined towards the local shear sense (top-to-north) or against shear sense, respectively.

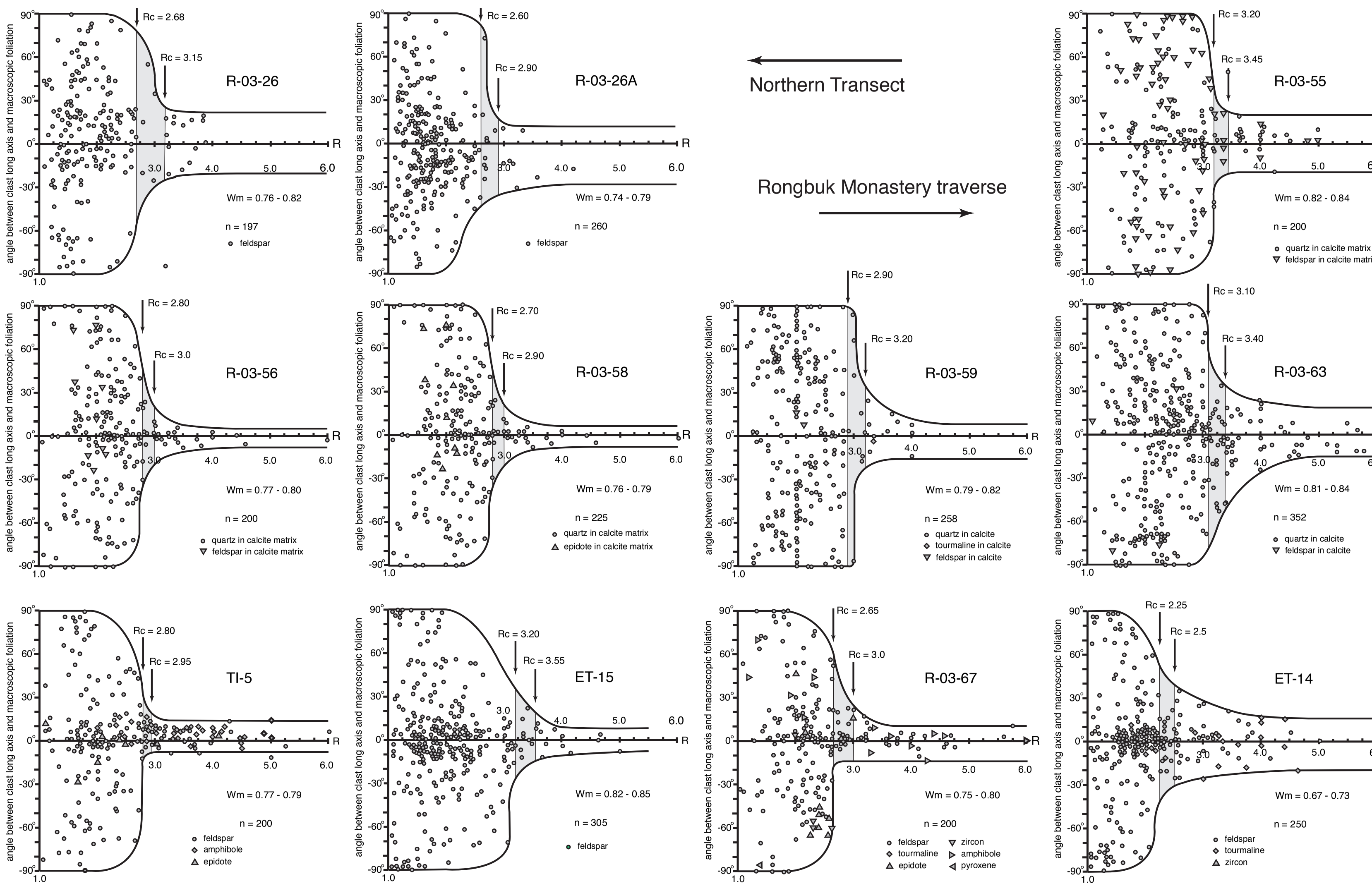

Figure 2.A2. Northern and Rongbuk Monastery transects. Positive and negative angles between clasts long axis and foliation indicate that clasts either inclined towards the local shear sense (top-to-north) or against shear sense, respectively.

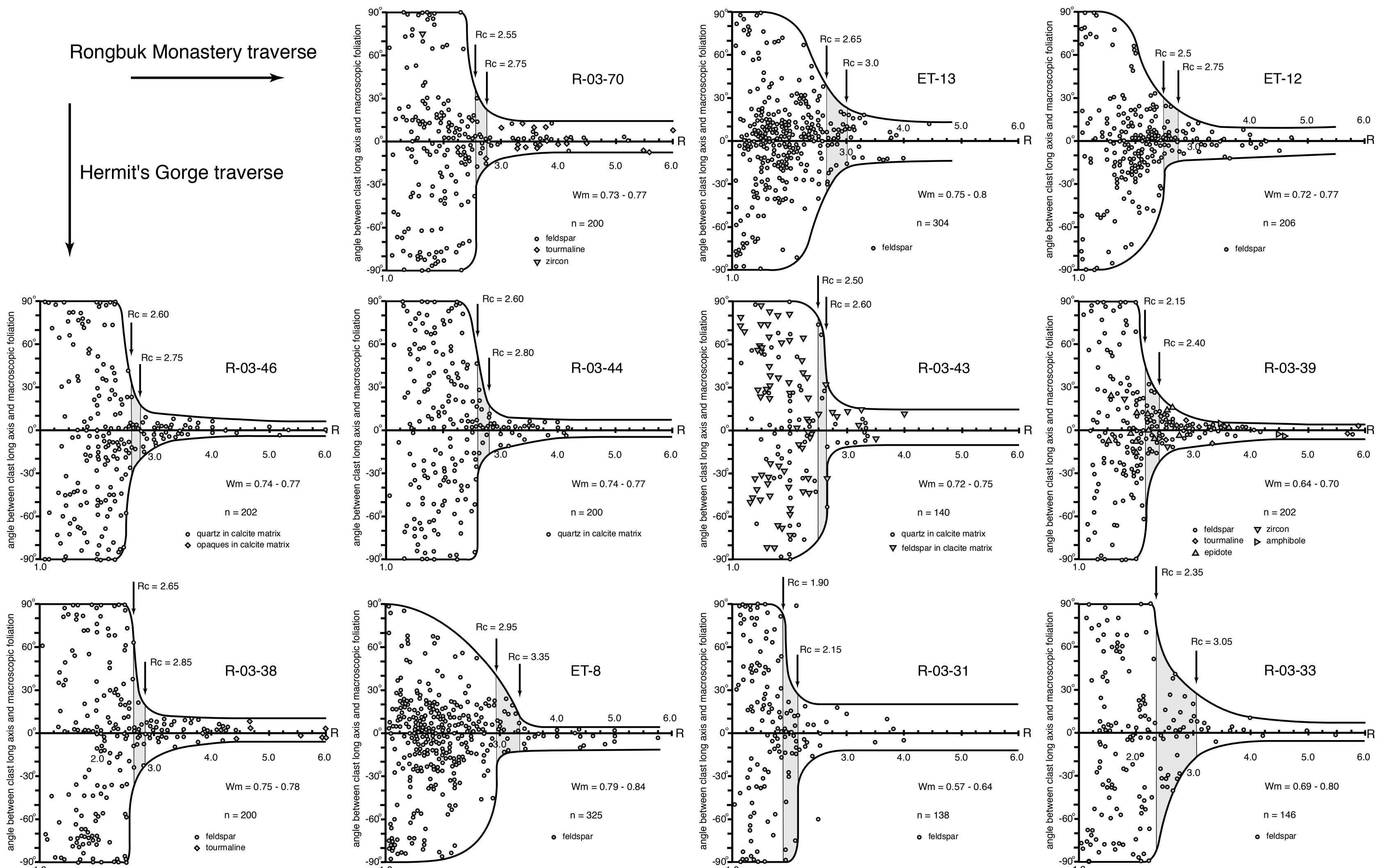

Figure 2.A3. Rongbuk Monastery and Hermit's Gorge transects. Positive and negative angles between clasts long axis and foliation indicate that clasts either inclined towards the local shear sense (top-to-north) or against shear sense, respectively.

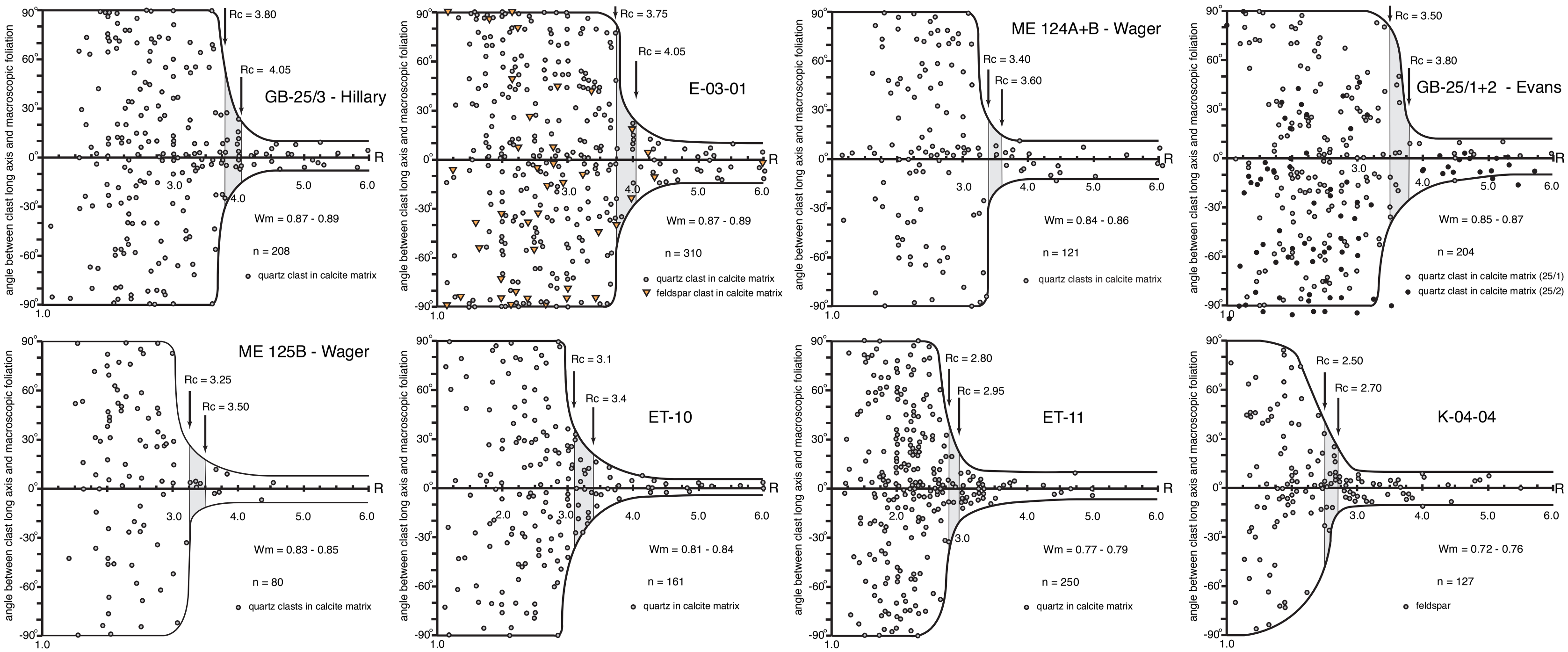

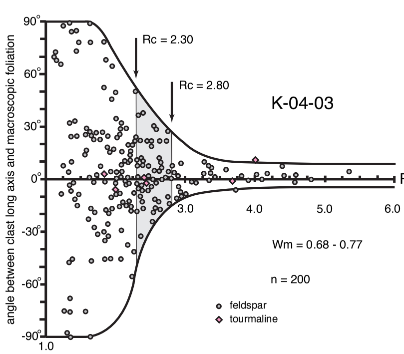

Figure 2.A4. Mount Everest - Kangshung valley. Only samples K-04-03 and K-04-04 from Kangshung valley are oriented. Positive and negative angles between clasts long axis and foliation indicate that clasts either inclined towards the local shear sense (top-to-north) or against shear sense, respectively.

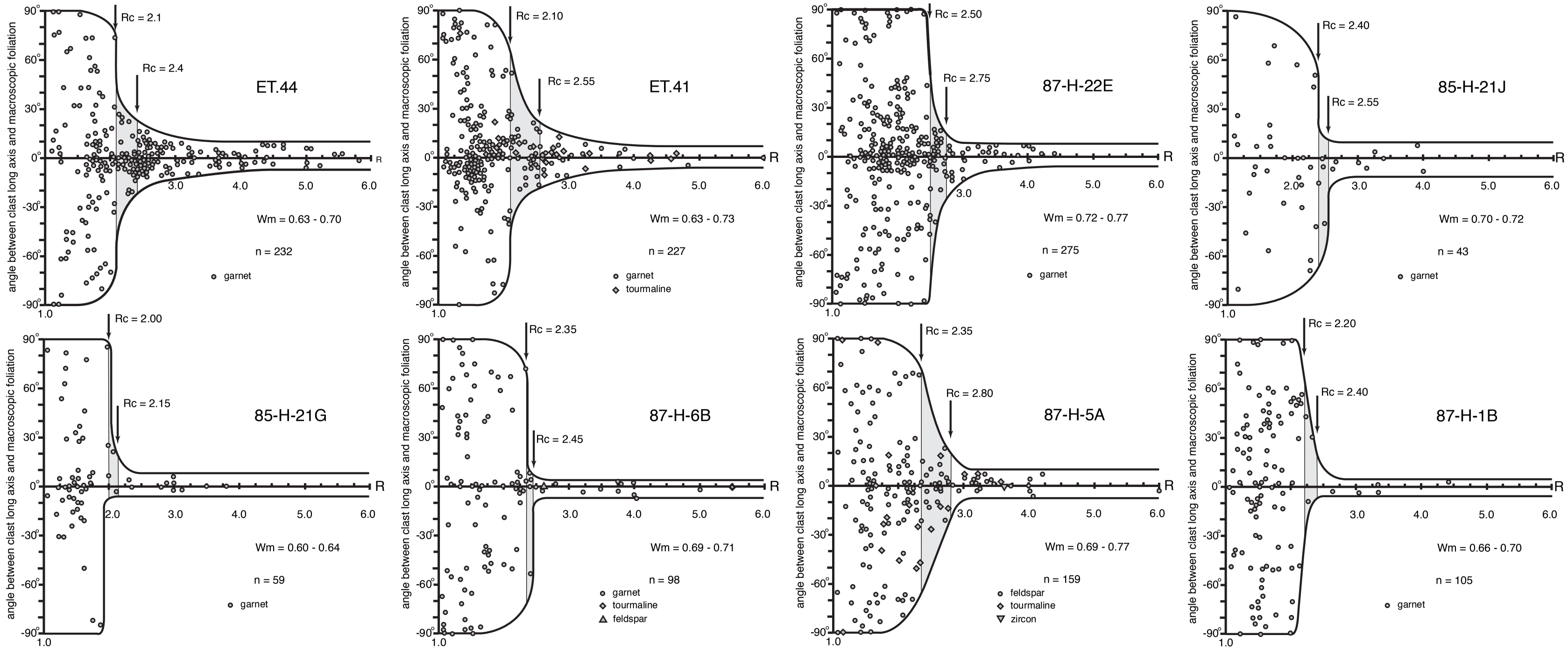

Figure 2.A5. Main Central thrust zone. Positive and negative angles between clasts long axis and foliation indicate that clasts either inclined towards the local shear sense (top-to-south) or against shear sense, respectively.

CHAPTER 3

The Rigid Grain Net (RGN); An alternative method for estimating mean kinematic vorticity number (*Wm)*

MICAH J. JESSUP[1], RICHARD D. LAW[1], & CHIARA FRASSI[2]
1) Department of Geosciences, Virginia Tech., Blacksburg, Virginia 24061, USA
2) Dipartimento di Scienze della Terra, Università di Pisa, 56126 Pisa, Italy

Published February 2007 in the *Journal of Structural Geology*, 29, 411-421.

Abstract

The use of porphyroclasts rotating in a flowing matrix to estimate mean kinematic vorticity number (W_m) is important for quantifying the relative contributions of pure and simple shear in penetratively deformed rocks. The most common methods, broadly grouped into those that use tailed and tailless porphyroclasts, have been applied to many different tectonics settings; however attempts have not been made to unify the various methods. Here, we propose the Rigid Grain Net (RGN) as an alternative graphical method for estimating W_m. The RGN contains hyperbolas that are the mathematical equivalents to the hyperbolic net used for the porphyroclast hyperbolic distribution (PHD) method. We use the RGN to unify the most commonly used W_m plots by comparing the distribution of theoretical and natural tailless porphyroclasts within a flowing matrix. Test samples from the South Tibetan detachment, Tibet yield indistinguishable results when the RGN is compared with existing methods. Because of its ease of use, ability for comparing natural data sets to theoretical curves, potential to standardize future investigations and ability to limit ambiguity in estimating W_m, the RGN makes an important new contribution that advances the current methods for quantifying flow in shear zones.

Key words: vorticity, PHD, South Tibetan detachment, porphyroclast, mylonite, shear zone, Gondasampa, Rongbuk Valley

Introduction

Attempts to use the aspect ratio and orientation of rigid objects rotating in a flowing matrix to characterize the relative contributions of pure and simple shear (vorticity) began with the pioneering work of Jeffery (1922) and Ghosh and Ramberg (1976). Subsequent investigations contributed to these founding principles by applying the early theory to geologic samples (Passchier, 1987; Simpson and De Paor, 1993, 1997; Wallis, 1992,

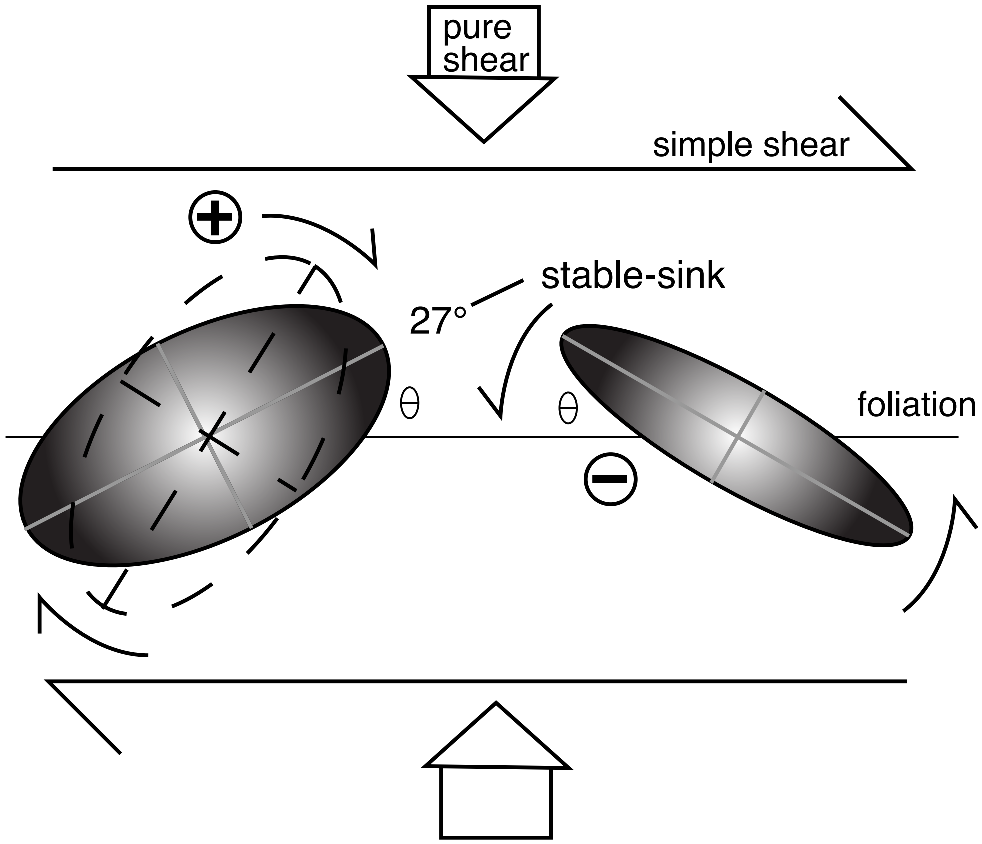

Figure 3.1. Rotation of two simplified elliptical porphyroclasts within a regime of general shear. Porphyroclast on the left has an aspect ratio of 2 (B^* = 0.6) and is in the stable-sink orientation of θ = 27° and represents one of many possible original orientations that rotated forward to the stable-sink position. The porphyroclast on the right is back rotated, due to the pure shear component, and has a long axis at a negative angle (θ) to the foliation.

1995; Wallis et al., 1993). Rigid porphyroclast analyses are now commonly employed to characterize flow within shear zones in a variety of tectonic settings (e.g., Klepeis et al., 1999; Xypolias and Doustos, 2000; Holcombe and Little, 2001; Xypolias and Koukouvelas, 2001; Bailey and Eyster, 2003; Law et al., 2004; Jessup et al., 2006; Xypolias and Kokkalas, 2006).

Models for the rotation of elliptical objects in a fluid demonstrate that during simple shear (mean kinematic vorticity number W_m = 1) rigid objects will rotate infinitely, regardless of their aspect ratio (R). With increasing contributions of pure shear ($0 < W_m <$

Nomenclature

W_m	mean kinematic vorticity number
R	porphyroclast aspect ratio (long axis/short axis)
$B*$	shape factor of Bretherton (1962) [Eq. 2]
M_n	short axis of the porphyroclast
M_x	long axis of the porphyroclast
θ	angle between long axis and the foliation [Eq. 1]
X'_2- X'_3	plane normal to the rotational axis
X'_1	rotation axis
β	angle between the stable-sink and source sink in the X'_2- X'_3 plane [Eq. 3 and 7]
R_c	critical threshold between grains that rotate infinitely and those that reach a stable-sink position.
R_{cmin}	minimum R_c as defined by Law et al. (2004)
R_{cmax}	maximum R_c as defined by Law et al. (2004)

Table 3.1. Critical threshold values

R	Wm	θ at *Rc*	B*	β	cos (β)
1.1	0.1	42	0.1	84	0.1
1.21	0.2	39	0.2	78	0.2
1.3	0.3	36	0.3	73	0.3
1.5	0.4	33	0.4	66	0.4
1.7	0.5	30	0.5	60	0.5
2	0.6	27	0.6	53	0.6
2.5	0.7	23	0.7	46	0.7
3	0.8	18	0.8	37	0.8
4.2	0.9	13	0.9	26	0.9

R = aspect ratio (long axis/short axis)
Wm = mean kinematic vorticity number
θ = angle from foliation
Rc = critical threshold

1), porphyroclasts will either rotate with the simple shear component (forward) or against it (backward) until they reach a stable-sink orientation that is unique to R and W_m (Fig. 3.1; Ghosh and Ramberg, 1976; Passchier, 1987; Simpson and De Paor, 1993, 1997).

Three main analytical techniques (Passchier, 1987; Simpson and De Paor, 1993, 1997; Wallis, 1995) use rigid porphyroclasts to estimate W_m in high strain zones, all of which rely on the same fundamental mathematical relationships between W_m, R or shape factor ($B*$), and angle of porphyroclast long axis with respect to the macroscopic foliation (θ), to define a critical threshold (R_c) below which they continuously rotate, and above

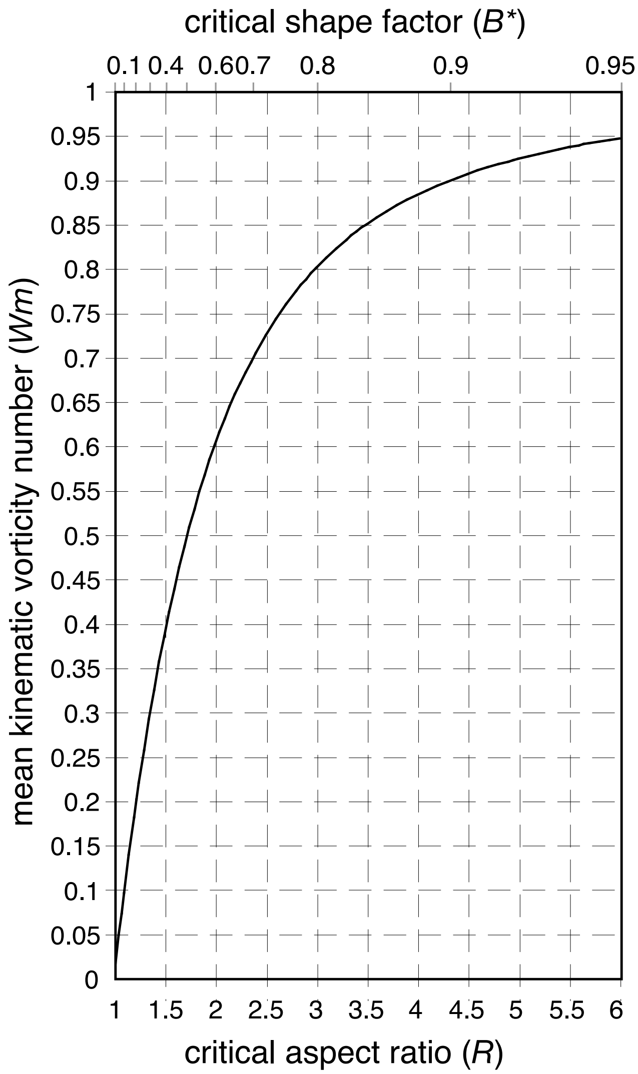

Figure 3.2. Plot showing the relationship between mean kinematic vorticity number (W_m), shape factor ($B*$), and aspect ratio (R) at critical values.

which they record a stable-sink orientation (Table 3.1; Fig. 3.2; Jeffery, 1922; Ghosh and Ramberg, 1976). We refer to the Passchier (1987) and Wallis (1995) methods as the Passchier and Wallis plots respectively (Fig. 3A-B). For the third approach, we use the name porphyroclast hyperbolic distribution (PHD) plot of Simpson and De Paor (Fig. 3D; 1993; 1997).

Because these methods rely on the same founding principles of Jeffery (1922) and Bretherton (1962), they should yield similar W_m estimates. However, prior to this investigation, no attempts were made to compare or unify the three techniques. Without a standard method for estimating W_m by comparing natural datasets to the orientations of porphyroclasts as predicted by Ghosh and Ramberg (1976), ambiguity was introduced into various adaptations of the three methods. To help standardize vorticity analysis using rigid porphyroclast in a flowing matrix, ease plotting of data, and limit ambiguity in estimating W_m, we build on the Passchier (1987) plot to create the Rigid Grain Net (RGN); a series of modified semi-hyperbolas that represent the stable configuration of porphyroclasts predicted for specific W_m values. Since the relative importance of sigma- and delta-type tails on these porphyroblasts has already received considerable attention (Passchier, 1987; Simpson and De Paor, 1993, 1997), and to make this comparison of techniques applicable to the most common types of porphyroclasts found in mylonitic rocks, we simplify our investigation to treating all data as tailless porphyroclasts. Plots of theoretical and natural tailless porphyroclasts on the RGN, Passchier, Wallis and PHD plots unify the four methods for using rigid tailless porphyroclasts to estimate W_m. By providing a net representing the theoretical orientations of rigid porphyroclasts in a flowing matrix that can be imported into an Excel© chart, against which natural dataset can be compared, the RGN offers a less ambiguous, easier to use, alternative method for estimating W_m in high strain zones.

Review of techniques

During general shear, rigid grain analysis assumes that the orientation of porphyroclasts within a flowing matrix record a critical threshold (R_c) between porphyroclasts that rotate indefinitely (low aspect ratio), and therefore do not develop a preferred orientation, and those that reach a stable-sink orientation (higher aspect ratio; Fig. 3.1). This unique combination of W_m, R or $B*$ and θ define the value of R_c between these two groups of rigid grains (Table 3.1; Figs. 3.2 and 3.3). If a porphyroclast is axially-symmetric, then there is only one stable-sink position. Alternatively, if the porphyroclast is axially non-symmetric, then two stable-sink positions exist (Passchier, 1987). Passchier (1987)

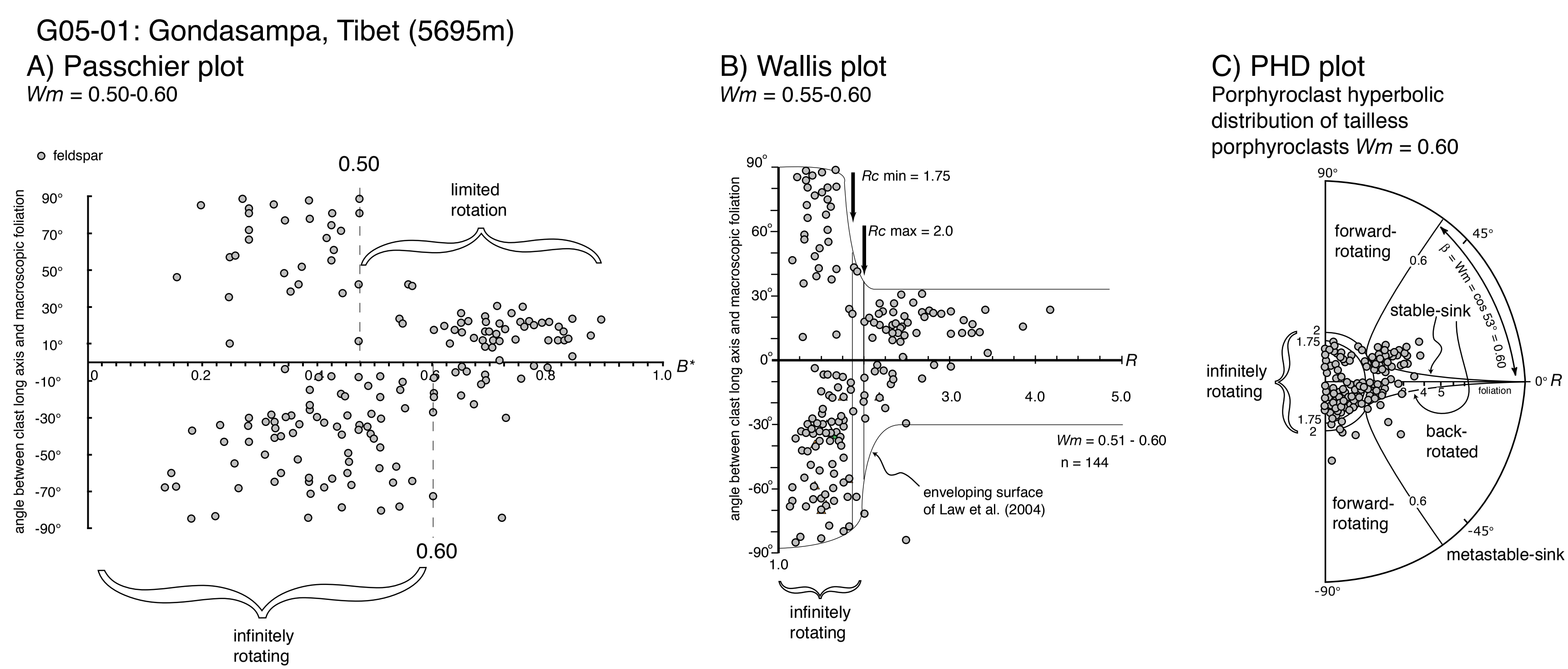

Figure 3.3. Examples of tailless porphyroclast data from sample G05-01 plotted using the Passchier plot (A), Wallis plot (B), and the porphyroclast hyperbolic distribution (PHD) plot (C) to estimate mean kinematic vorticity (W_m). The Passchier plot uses the shape factor $B^* = (M_x^2 - M_n^2)/(M_x^2 + M_n^2)$ (where M_n = short axis and M_x = long axis of the porphyroclast) vs. angle θbetween porphyroclast long axis and foliation (θ) to define the critical threshold used to estimate W_m (0.50-0.60). The Wallis plot uses the aspect ratio (R = long axis/short axis) and angle from macroscopic foliation (θ) to locate the critical threshold (R_c). W_m is calculated using R_c where $W_m = (R_c^2 - 1)/(R_c^2 + 1)$. Upper and lower R_c values are used to estimate a range in likely W_m estimates of 0.51-0.60. The PHD plot uses the hyperbolic net to plot aspect ratio (R) and θ. Following the methods of Simpson and De Paor (1993) the cosine of the opening angle (β) of the best-fit enveloping hyperbola yields a W_m estimate of 0.60.

related W_m to $B*$ and θ through the following equations:

$$\theta = \tfrac{1}{2} \sin^{-1} W_m/B*\{(1-W_m^{\ 2})^{1/2}-(B*^2-W_m^{\ 2})^{1/2}\} \qquad (1)$$

$$B* = (M_x^{\ 2} - M_n^{\ 2})/(M_x^{\ 2} + M_n^{\ 2}) \qquad (2)$$

where:

M_n = short axis of clast

M_x = long axis of clast

Eq. (1) links $B*$, W_m and θ and will generate a hyperbolic curve in θ vs. $B*$ space that represents the ideal distribution of grains for a particular W_m. The vertices of this hyperbola marks the unique R_c value where $W_m = B*$. Assuming relatively high strain, a natural distribution of porphyroclasts should define a limb of this hyperbola for a range of $B*$ values that is greater than $B*$ at R_c. With relatively low strains, a misleading distribution of porphyroclasts has the potential to overestimate the simple shear component because high aspect ratio porphyroclasts have yet to rotate into their stable-sink orientation (Passchier, 1987; Vissers, 1989; Bailey et al., *in press*). Porphyroclasts with a $B* < B*$ at R_c will rotate infinitely and should define a broad distribution with θ ± 90°. In contrast, porphyroclasts with a $B* > B*$ at R_c are predicted to reach stable-sink orientations with a limited range in θ values (Fig. 3.3A). Whether a porphyroclast will rotate forward or backward to a stable-sink position depends on the initial θ (i.e., prior to the onset of deformation) at a specific $B*$ and W_m. When treating all porphyroclasts as tailless, R_c should be defined by the distribution of both the orientation and either $B*$or R, as well as an abrupt change in range of θ values (Figs. 3.3A and B).

Passchier (1987) proposed the following equation for the two possible stable-sink orientations for axially non symmetric objects in the X'_2- X'_3 plane:

$$\cos \beta = W_m/B* \qquad (3)$$

where:

β = angle between the source and sink in the X'_2- X'_3 plane

X'_2- X'_3 = plane normal to the rotational axis (X'_1)

The long axis of the porphyroclast is predicted to rotate towards the two stable-sink positions when:

$$W_m < B^* \quad (4)$$

For example, assuming a W_m of 0.6 where $B^* = W_m$, then using Eq. (3), β = 53.13°, the stable-sink position for a porphyroclast with $R = 2$ has a θ = 26.56° (Table 3.1; Fig. 3.2). Passchier (1987) predicts that when $W_m < B^*$ (i.e., the aspect ratio of the porphyroclasts is greater than when $W_m = B^*$ at R_c), two-stable sink positions for axially non-symmetric objects exist. The positive/negative angles from the foliation for tailless porphyroclasts long axes cannot uniquely define their rotational history (i.e., forward vs. back-rotated sigma and delta porphyroclasts of Passchier 1987; Simpson and De Paor, 1993).

Although the distribution of porphyroclasts on the original Passchier plots can be informative, particularly for the highest quality datasets (Fig. 3.3A), without a reference frame for comparing complex natural data with the theoretical values established by Eq. (1), defining R_c will remain ambiguous. Passchier (1987) attributes the deviation of natural samples from orientations predicted by theory to: 1) variation of non-axially symmetric porphyroclasts between the two possible stable-sink positions, 2) changes in B^* of porphyroclasts (i.e., shape change) during progressive deformation attributed to recrystallization without instant reorientation of the object, 3) variation in the frame of reference (e.g., recrystallized tails or foliation).

Wallis (1995) used equations from Passchier (1987) to create the Wallis plot that uses tailless porphyroclasts to define R_c and therefore W_m. The Wallis plot still uses θ on the Y-axis, but replaces B^* with the more intuitive porphyroclast aspect ratio (R = long axis/short axis) on the X-axis (Fig. 3.3B; Wallis, 1992, 1995). W_m is calculated from the R_c values separating porphyroclasts that reach a stable-sink orientation ($\theta < \theta$ at R_c) from those that rotate continuously ($\theta > \theta$ at R_c). Although using R is more intuitive, W_m estimates cannot be determined directly from the plots, as with the Passchier plot, and must be calculated using the following equation:

$$W_m = (R_c^2 - 1)/(R_c^2 + 1) \quad (5)$$

Wallis et al. (1993)

Where R_c = critical aspect ratio

The distribution of porphyroclasts in natural systems often defines a gradual transition between these two populations using the Wallis plot, instead of an abrupt change between continuously rotating (random orientation) porphyroclasts and stable-to semi-stable porphyroclasts that define R_c. In response, researchers modified the original Wallis plot by creating an enveloping surface to better-define the grain distribution (Fig. 3.3B), and use a range in possible W_m values (R_{cmin} and R_{cmax}; Fig. 3.3B; Law et al., 2004; Jessup et al., 2006). Xypolias and Kokkalas (2006) also plot the best-fit curve using Eq. (1) for a specific W_m as a comparison with their natural data. As with the Passchier plot, ambiguity exists without an external reference frame created by theoretical curves that help justify which porphyroclasts are used to define R_c.

The porphyroclast hyperbolic distribution (PHD) method estimates W_m by using R and the angle between the pole to foliation and long axis of tailed porphyroclasts (Fig. 3.3C), plotted using the hyperbolic net (HN; De Paor, 1983; Simpson and De Paor, 1993; 1997). Each hyperbola of the HN represents the theoretically predicted orientation of porphyroclasts for a particular R and W_m as plotted in polar coordinates. The opening angle of each hyperbola = θ. The vertex of each hyperbola defines R_c, and θ at R_c, for each W_m value. This relationship between stable-sink orientation, as defined by Passchier (1987; Cartesian coordinates) in Eq. (1), and the hyperbolic net (HN; De Paor, 1983; polar coordinates) is established in Eq. (11) of Simpson and De Paor (1993):

$$B^* = W_m/\cos(2\theta) \quad (6)$$

As with Passchier (1987), when $B^* = W_m$ porphyroclasts reach their stable-sink orientation at the minimum angle from the foliation, R_c is defined as the vertices of the hyperbola. One limb of the hyperbola represents the stable-sink orientation for

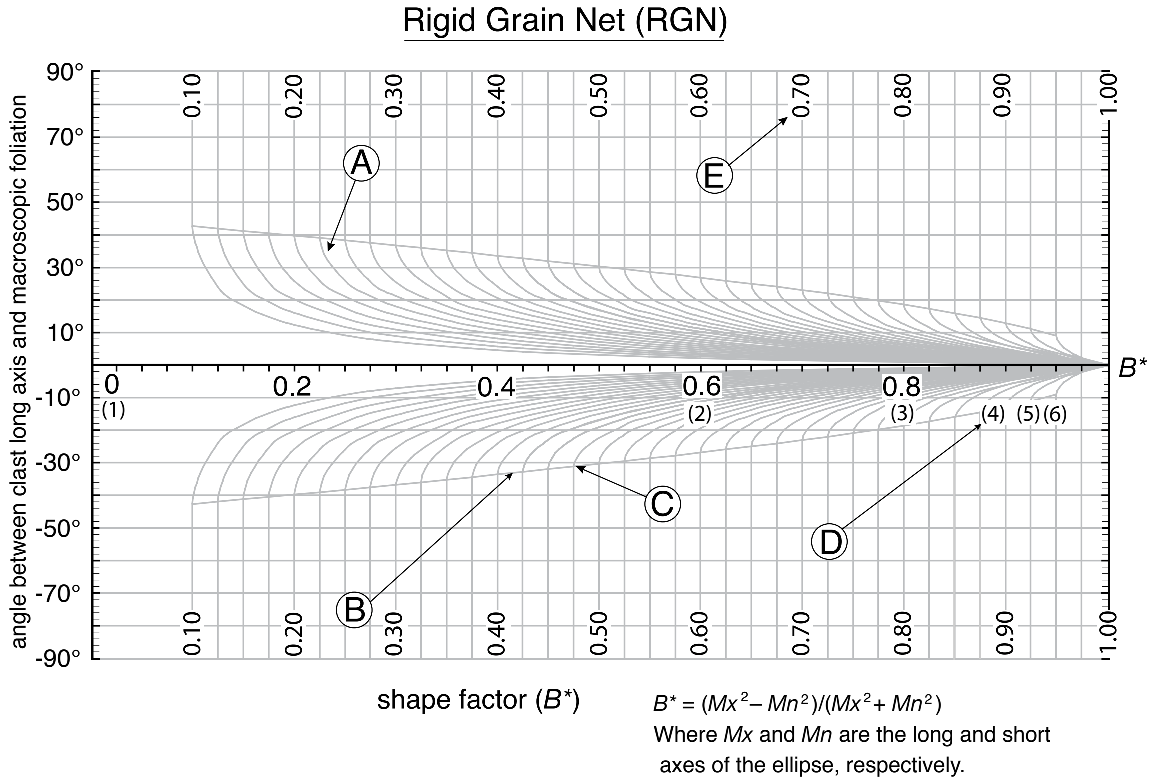

Figure 3. 4. The rigid grain net (RGN) using semi-hyperbolas. Location A is an example of a semi-hyperbola; location B highlights the vertices curve; location C is an example of a R_c value when $W_m = B*$; location D points to one of a series of aspect ratio (R) values included on the RGN to demonstrate its relationship with the less intuitive shape factor ($B*$); location E is a W_m value for a semi-hyperbola. See text for details.

porphyroclasts clasts while the other is the metastable position (i.e., the source-sink position of Passchier, 1987; Fig. 3.3C). At θ > the metastable orientation, porphyroclasts will rotate forward until they define another semi-hyperbolic cluster on the concave side of the same hyperbola. Assuming significant shear, back-rotated clasts with variable aspect ratios, plotted on the HN, should define a semi-hyperbolic cluster representing the stable-sink orientation. The linear cluster is then rotated to find the best-fit hyperbola whose limbs represent the two eigenvectors of flow, one of which is asymptotic to the foliation (i.e., the source-sink and stable-sink positions of Passchier, 1987). The vertex of this hyperbola separates the low aspect ratio porphyroclasts with random orientation (i.e., infinitely rotating), from higher aspect ratio porphyroclasts with a narrow range of orientations (Fig. 3.3C).

The Rigid Grain Net (RGN)

Prior to this investigation, the relationship between the PHD, Wallis and Passchier plots was largely unaddressed, particularly using only tailless porphyroclasts. To explore this further, we propose the RGN as an alternative method for estimating W_m. To create the RGN, we modified the Passchier plot and then tested the compatibility of results obtained from the RGN, Wallis and PHD plot using theoretical and natural datasets of tailless porphyroclasts. Eq. (1) was used to calculate semi-hyperbolas for a range of W_m values that express the relationship between θ and $B*$ (Fig. 3.4, location A). The second set of curves represent the possible R_c (vertices curves) values for when $W_m = B*$ (Fig. 3.4, location B; Table 3.1). Each semi-hyperbola was calculated for a particular W_m and a series of $B*$ values. We use the shape factor ($B*$, Eq. 2) as defined by Bretherton (1962) and subsequently employed by Passchier (1987) because it enables W_m values to be obtained directly from the RGN.

For the RGN, positive and negative semi-hyperbolas are plotted at 0.025 increments for a range in W_m (0.1 – 1.0) by solving for θ using Eq. (1) (θ = θ at R_c, when $B* = W_m$). For a particular shape factor, when $B* = W_m$ and θ > θ at R_c, the semi-hyperbolas transition into vertical lines to define the maximum $B*$ value below which grains begin to rotate freely (Fig.3. 4, location C; Passchier, 1987). To highlight the continuity in R_c values for the range in W_m values represented by the RGN, a second curve (vertices curve) links the R_c values on each hyperbola (Fig. 3.4, location B). To relate the more intuitive aspect ratio (*R)* of the Wallis plot to $B*$ values, they are placed below the $B*$ values on the x-axis of the RGN (Fig. 3.4, location D). Together the semi-hyperbolas and R_c curves for positive and negative θ values define the RGN against which natural data sets can be compared (Fig. 3.4).

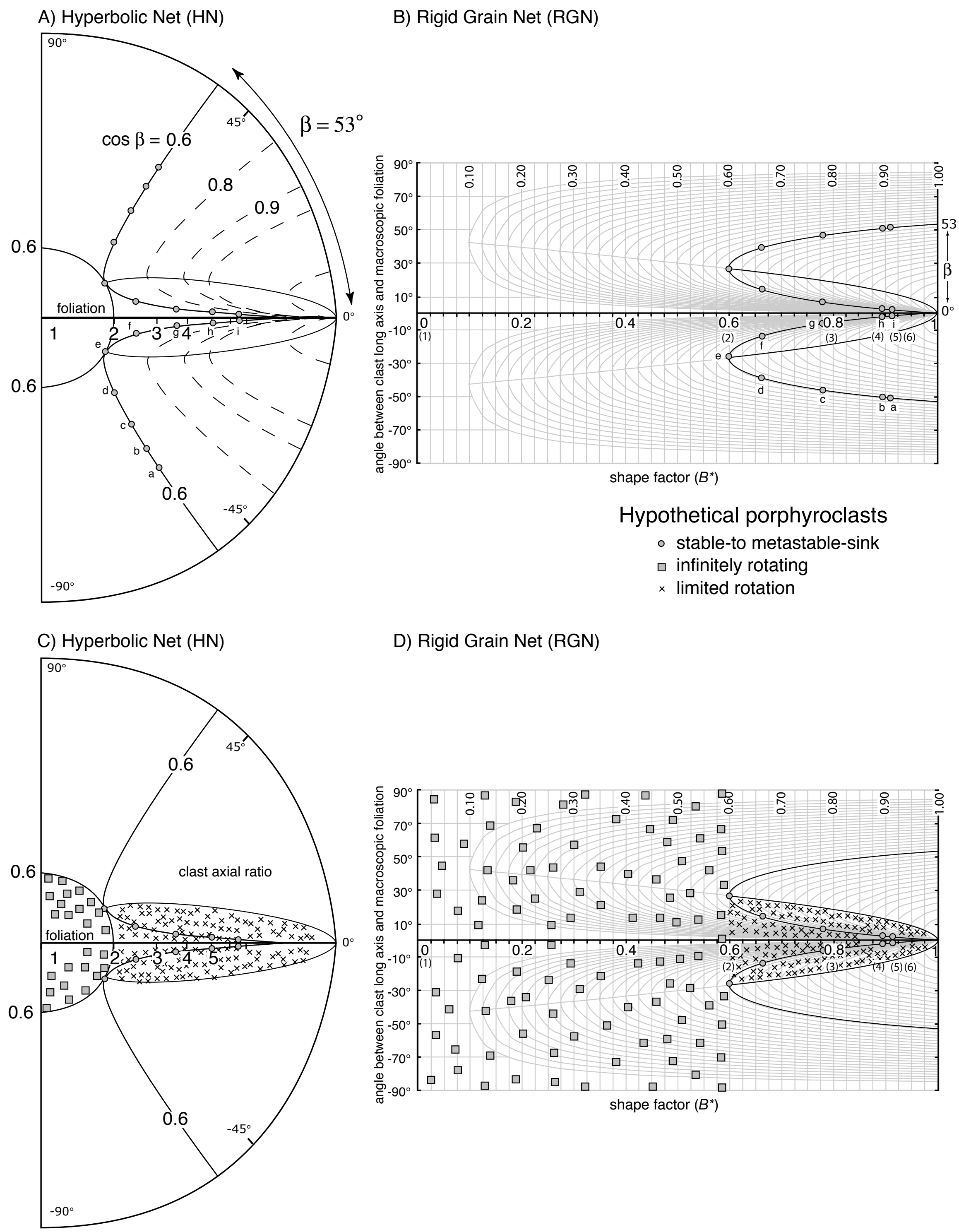

Figure 3.5. A) Half of the hyperbolic net (HN) simplified to graphically demonstrate the relationship between one hyperbola ($W_m = 0.60$) and the vertices curve for that hyperbola. The vertices curve is drawn using the vertices of several hyperbolas (dashed) for a range in W_m values greater than the W_m for the sample (0.60). Gray circles with letters (a-i) on the hyperbola for $W_m = 0.60$ are shown to compare how tthe HN and RGN (Fig. 3.5B). (continued next page)

Figure 3.5. cont. The circle that defines the highest aspect ratio (R = 2) below which porphyroclasts are predicted to rotate infinitely is also included. B) The RGN with complete hyperbolas. Highlighted in black are the positive and negative hyperbolas that correspond to a W_m = 0.60, as well as the section of the vertices curve for $B^* > B^*$ at R_c. A series of gray circles represent equivalent points on the RGN and HN. C) The same plot as (A) with an overlay of different types of hypothetical porphyroclasts in their predicted distribution; gray squares are infinitely rotating, black crosses are limited rotation, gray circles are stable-to metastable-sink positions. D) The same plot as (B) with hypothetical porphyroclasts distributed in various sections of the RGN.

To relate hyperbolas on the HN and the RGN, we plot the full hyperbolas on the RGN, highlight the critical curves used to define a W_m = 0.6, and plot a hypothetical distribution of porphyroclasts (Fig. 3.5). The two hyperbolas that are included on the simplified HN are highlighted in black on the RGN (W_m= 0.6) for positive and negative θ (Figs. 3.5A and B). Clasts whose initial orientation plots within any of the stability fields represented by the hyperbolas will, given the slightest perturbation, rotate towards a stable-sink position (Ghosh and Ramberg, 1976). If axial symmetric, these grains will reach a single stable-sink position whereas axial non-symmetric porphyroclasts (whose $B^* > W_m$) will potentially reach two stable-sink positions (Eqs. 3 and 4). For porphyroclasts that plot on the metastable limb (locations a-d of Figs. 3.5A and B) of the negative hyperbola, they will respond to any component of pure shear by back rotating until they reach a stable-sink position, as dictated by their R and W_m, to define a semi-hyperbolic linear cluster (locations e-i, Figs. 3.5A and B). Porphyroclasts with original orientations outside of the metastable limb of the hyperbola will forward rotate, until they reach the convex side of the stable limb of the hyperbola. Forward rotating grains that accumulate between the two stable limbs of the negative and positive hyperbolas have an $R > R$ at R_c (Eq. 3 and 4).

Fields of the HN and RGN plots that represent the maximum aspect ratio for porphyroclasts that are predicted to rotate forward infinitely, and thereby have a complete range in θ between ± 90°, are represented by a circle of constant R for all orientations that is tangential to the vertex of each hyperbola and plotted on the center of the HN

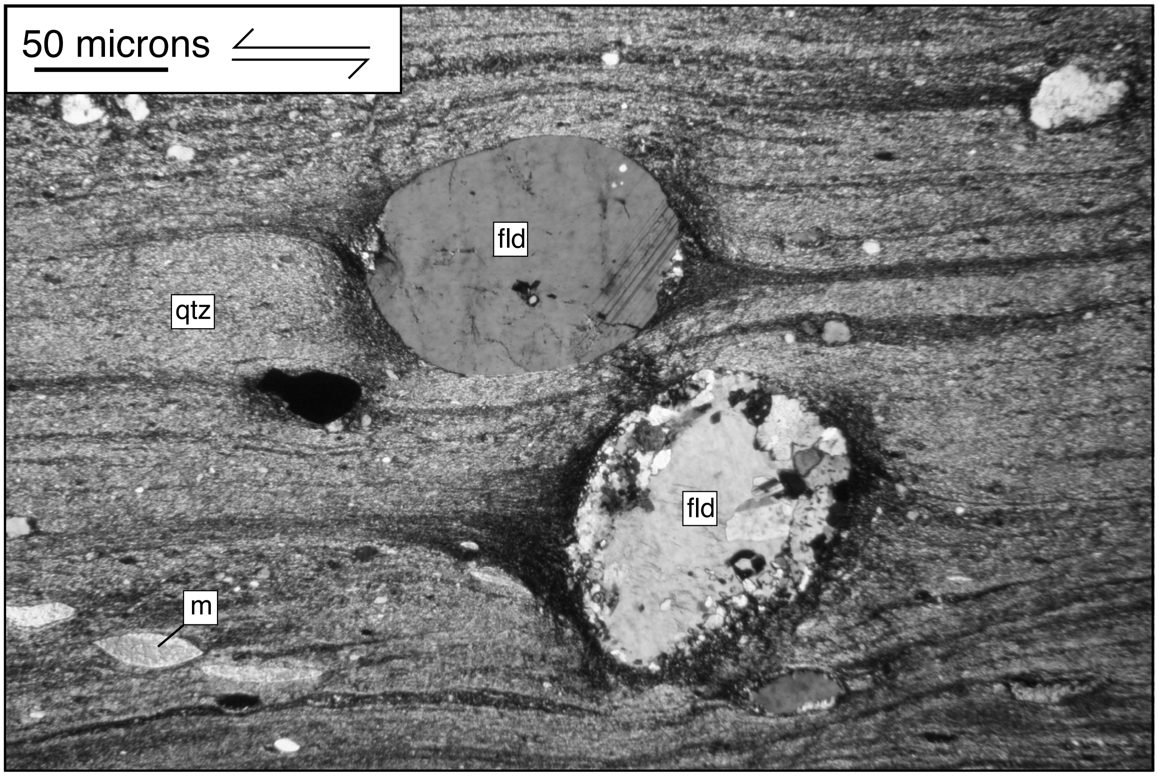

Figure 3.6. Photomicrograph with crossed polars of a typical section of sample G05-01 (collected at an altitude of 5695 m). Section cut perpendicular to foliation and parallel to lineation. Abbreviations used for various phases are: m, white mica; fld, feldspar; qtz, quartz. Although representative of the types of porphyroclasts in the thin section, because they are in such close proximity to each other, these two porphyroclasts are unsuited for the RGN. Image taken by M.J. Jessup.

(i.e., when $B^* < W_m$; Figs. 3.3C, 3.5A and C). On the RGN, this area includes all of the potential range in B^* between 0 and B^* at R_c (i.e., to the left of the apex of the hyperbolas; Figs. 3.5B and D). An additional section of the RGN is highlighted on the HN that defines porphyroclasts that will rotate to the vertices curve for R_c values ≥ the "true" R_c for the sample. On the HN, this curve is defined by linking the R_c value from each potential hyperbola greater than the "true" R_c for this sample to generate a small section of the vertices curve as shown on the RGN (Figs. 3.5A and C). This important clarification shows that these porphyroclasts must be considered as stable-sink orientations when choosing the best-fit hyperbola. Because the hyperbolas on the HN and RGN with full-hyperbolas are mathematical equivalents, an ideal dataset of tailless or tailed porphyroclasts (i.e., $R = 2.0$ and $W_m = 0.60$) are predicted to define this hyperbola on both plots. According to Passchier (1987), all grains with the slightest B^* above B^* at R_c will reach a stable-sink position (crosses of Figs. 3.5C and D) whereas those below will rotate infinitely and therefore could potentially reach $\theta = \pm 90°$ (gray squares of Figs. 3.5C and D).

A major benefit to using the RGN is that data can be entered into an Excel© worksheet, as they are obtained on the microscope, and plotted directly on a RGN that is imported as a background to an Excel© chart. This enables the user to immediately monitor how the distribution of porphyroclasts is developing during data acquisition. Each measured porphyroclasts can be compared to the theoretically predicted curves on the RGN. As the plot evolves, the porphyroclasts that define R_c should become obvious. With increased use, the RGN may provide a means to calibrate the results of future investigations (see appendix for a reproducible version of the RGN and the data repository for a JPEG© image of the RGN for use on Excel© charts and an Excel© worksheet).

A Natural Test: The South Tibetan detachment, Tibet

Ultra-mylonitic leucogranite samples from the South Tibetan detachment (STD), exposed near Gondasampa and Rongbuk Valley, Tibet, are particularly well-suited for testing the hypotheses presented above as well as for demonstrating the utility of the RGN. Samples are from within the upper 30 m of the north-dipping ductile shear zone that marks the transition from the metamorphic core of the Greater Himalayan Slab to overlying

Figure 3.7. Next page. Samples G05-01 (A; collected at an altitude of 5695 m) and G05-03 (B; collected at an altitude of 5765 m) from the South Tibetan detachment exposed near Gondasampa, Tibet. The Wallis plot (left), PHD plot (center), and RGN (right) are shown for each sample to demonstrate relationships between the three methods. Notice that all porphyroclasts are treated as tailless. See text for details.

A) G05-01, Gondasampa, Tibet

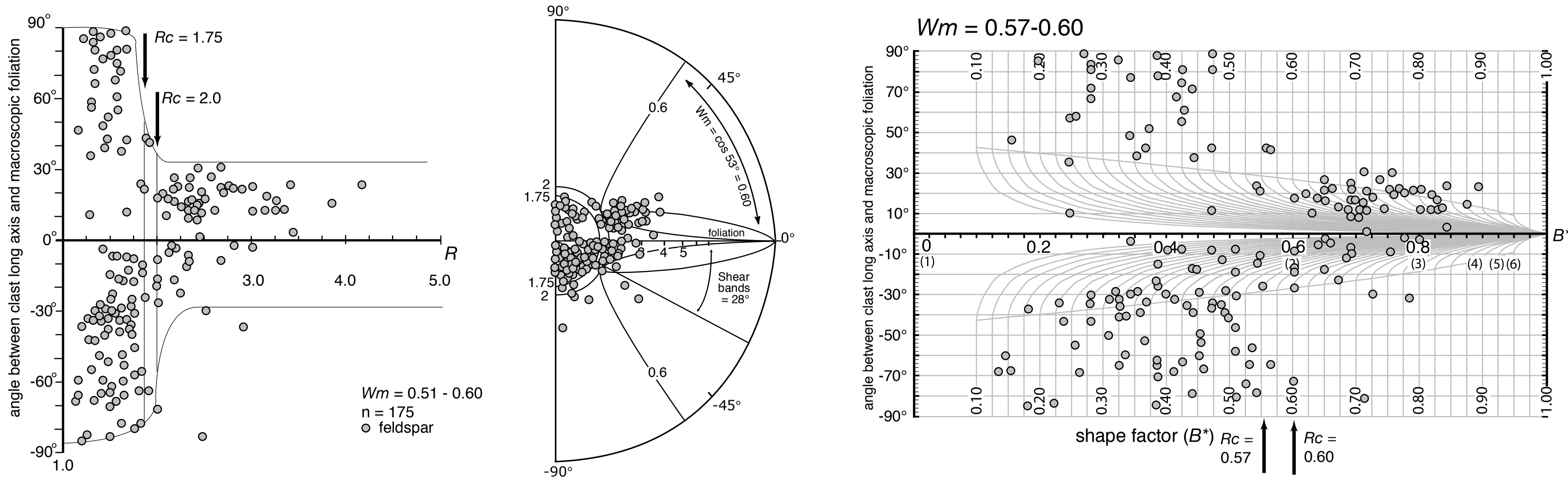

B) G05-03, Gondasampa, Tibet

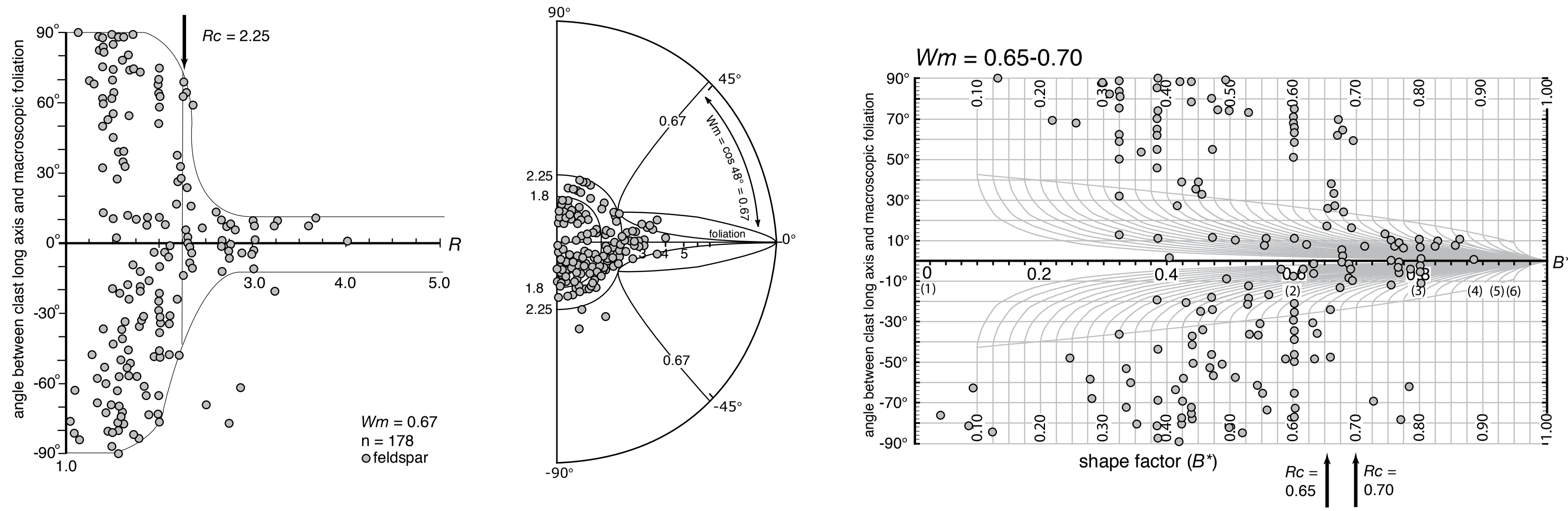

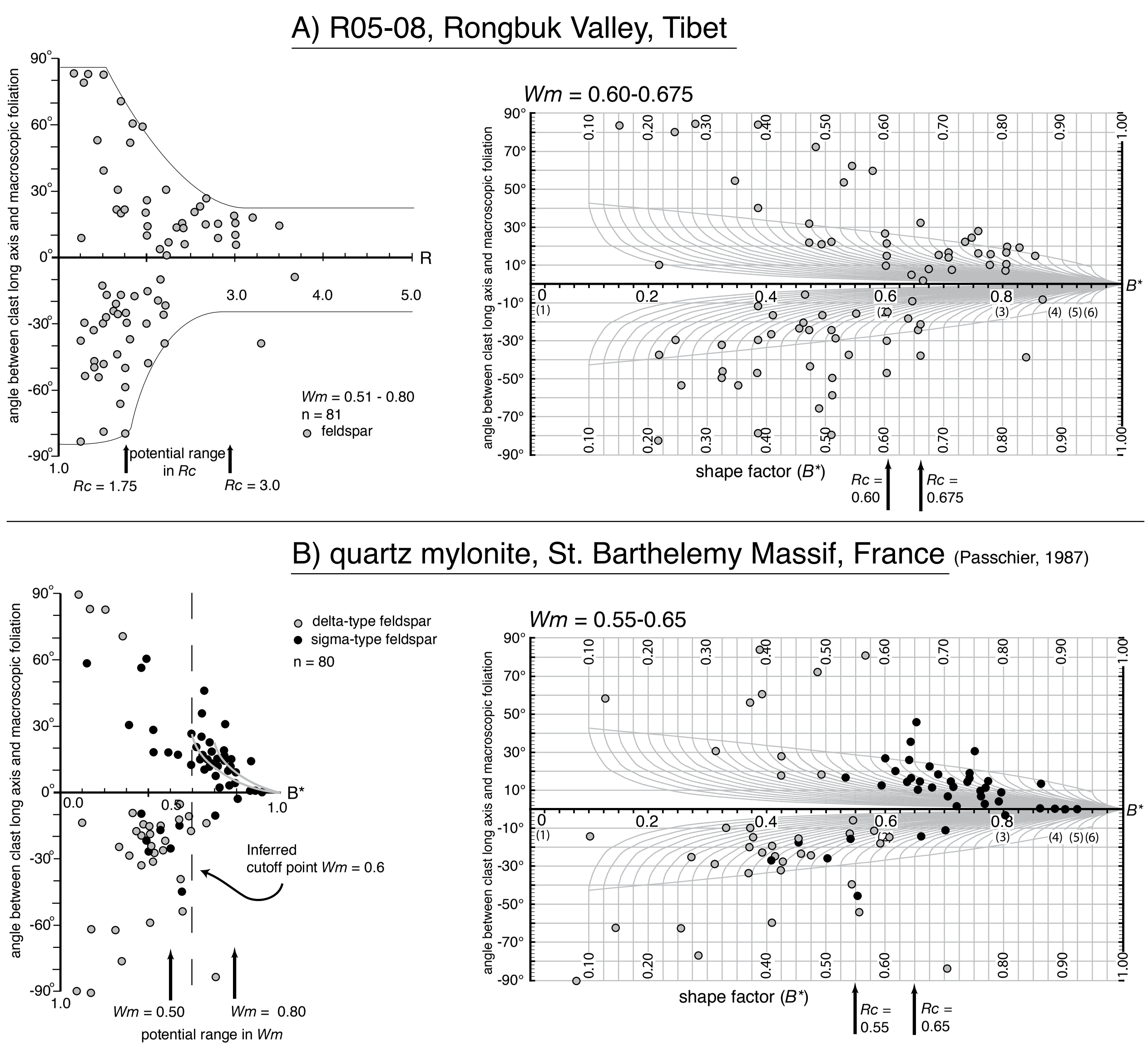

Figure 3.8. A) Porphyroclasts from sample R05-08 from Rongbuk Valley, Tibet (collected several 100 meters south of the Northern Transect of Jessup et al. (2006) at an altitude of 4840 m) plotted using both the RGN and the Wallis plot. B) Porphyroclasts from a quartz mylonite sample from the St. Barthelemy Massif, France from Passchier (1987; his Fig. 10) plotted on the RGN and the original Passchier plot. See text for details on how these comparisons demonstrate that the RGN helps limits ambiguity in estimating W_m.

unmetamorphosed Cambro-Ordovician limestone. Similar mylonitic leucogranites in the area are dated ~17 Ma by Murphy and Harrison (1999) who suggest that this provides a maximum age for ductile fabric development in Rongbuk Valley. Oriented samples were cut parallel to the stretching lineation and perpendicular to the foliation. When possible, rigid porphyroclasts from multiple thin sections were used. All samples are characterized by feldspar porphyroclasts (lacking evidence for internal plastic deformation) that are widely separated from each other within a foliated matrix of dynamically recrystallized quartz grains (Fig. 3.6). Elongate tails of recrystallized quartz surround many of the rigid feldspar porphyroclasts. Although many of these porphyroclasts have sigma-and delta-type tails, in order to clarify this comparison between different rigid grain methods for defining W_m, they are treated as tailless. Matrix quartz grains contain bulging grain boundaries and rims of strain-free subgrains that suggest a combination of grain boundary migration and subgrain rotation recystallization accommodated deformation at conditions intermediate between Regime 2 and 3 of Hirth and Tullis (1992) and temperatures of ~490-530°C (Stipp et al., 2002). Previous petrofabric investigations in Rongbuk Valley, demonstrated that deformation was characterized by plane strain deformation and supported monoclinic shear (Law et al., 2004; Jessup et al., 2006).

The choice of rigid porphyroclasts was highly selective, ignoring all but the most appropriate grains for estimating W_m (Simpson and De Paor, 1993; 1997). Two samples (G05-01, and G05-03) were selected to test the RGN and how it relates to the PHD and Wallis plots (Fig. 3.7; Table 2). PHD plots contain hyperbolas in the positive and negative fields as well as sections of the vertices curves. Because we are treating all these porphyroclasts as tailless, it is important to clarify that positive and negative θ values cannot uniquely determine whether porphyroclasts followed a forward-or back-rotated path in the sense of Passchier (1987) and Simpson and De Paor (1993; 1997).

Two thin sections of sample G05-01 contain 175 porphyroclasts, with a range in aspect ratios inclined at positive and negative θ values, which are appropriate for rigid grain analysis (Fig. 3.7A). On the Wallis plot, these grains define an upper and lower R_c of 2.0 and 1.75 (W_m = 0.60-0.51), respectively. We interpret the porphyroclast with anomalously high θ and R values as an outlier. Using the PHD method, tailless porphyroclasts were plotted on the HN. To distinguish the R_c value between porphyroclasts that rotated infinitely and those that reached a stable-sink position, excluding the obvious outlier, we choose two circles (R = 1.75-2.0) on the HN that envelopes porphyroclast that reach ± 90°. The distribution of porphyroclasts with negative θ values defines a slightly higher R_c (R = 2) than for positive (R_c = 1.75) values. Positive and negative hyperbolas were then chosen that envelope the majority of the data and touch the R_c value (circle R = 2.0) of the infinitely rotating grains. Plotting the vertices curve for this hyperbola ensures that the full range in stable-sink orientation is represented. Several outliers are present outside of the vertices curve in the positive and negative fields. Using the enveloping hyperbola with an opening angle of 53°yields a W_m = 0.60 that agrees with the limited rotating and infinitely rotating porphyroclasts. The average orientation (~28°) of shear bands is also shown on the PHD plot.

The RGN demonstrates how the distribution of tailless porphyroclasts in sample G05-01 compares with the predicted transitions to define R_c (Fig. 3.7A). B^*, as defined by positively inclined porphyroclasts, yields a W_m = 0.57 whereas the negatively inclined porphyroclasts define a W_m = 0.60. A cluster of positively oriented porphyroclasts plots slightly above the vertices curve on the RGN. We attribute this to either porphyroclasts rotating towards the stable-sink position or as an error of ± 3° in defining the foliation for these measurements. Other potential contributors to this error have previously been outlined by Passchier (1987). Porphyroclasts with $B^* > 0.6$ and θ < θ at R_c define a lateral cluster close to the vertices curve. Porphyroclasts continue to reach, but remain under, the vertices curve until $B^* < W_m$ at which point porphyroclasts are no longer in a stable-sink position and begin to rotate infinitely (Fig. 3.7A).

Sample G05-03 (n = 178) displays a well-defined R_c on the Wallis plot that yields a W_m estimate of 0.67 (Fig. 3.7B). Rather than relying on three outliers to define R_c and thereby W_m, as with G05-01, we prefer to rely on the majority of tailless porphyroclasts to define R_c. Tailless porphyroclasts are plotted on the HN using the same methods as described in detail for sample G05-01. Two circles define the upper-and lower-limits to the infinitely rotating grains (R_c = 1.8 to 2.25). Two hyperbolas and their vertices curves enclose the remaining porphyroclasts to define a W_m = 0.67. When plotted on the RGN, porphyroclasts from sample G05-03 define a range in W_m values between ~ 0.65 (defined by grains in the negative field) and ~ 0.70 (defined by grains in the positive field) that agrees with the Wallis plot and the PHD method (Fig. 3.7B). θ and R values of the majority of tailless porphyroclasts, instead of the three outlying points, are used to define R_c. The compatibility between W_m estimates generated for samples, using tailless porphyroclasts, demonstrate that the RGN unifies the Wallis and PHD methods (Fig. 3.7).

Two comparisons are made to demonstrate how the RGN limits ambiguity in estimating W_m. The first contrasts the porphyroclast distribution from sample R05-08 on a Wallis plot and the RGN (Fig. 3.8A). The second plots the porphyroclast distribution defined by Passchier's (1987) dataset from the St. Barthelemy Massif using both the Passchier plot and the RGN (Fig. 3.8B). The sample number in R05-08 is limited (n = 81) due to the large porphyroclast size. This gradation in values is more typical of previously published Wallis plots (e.g., Xypolias and Doutos, 2000; Xypolias and Koukouvelas, 2001; Law et al., 2004; Jessup et al., 2006) than the relatively well-defined R_c values in the Wallis plots for samples G05-01 & 03 (Fig. 3.7). Without an understanding of which porphyroclasts are predicted to define R_c, the values estimated by different interpretations of this Wallis plot could range from R =1.75 to 3.0, resulting in W_m estimates of 0.53 – 0.80 (Fig. 3.8A). When plotted using the RGN, the relative importance of porphyroclasts can be evaluated. For example, at higher $B*$ values the majority of porphyroclasts fall within the vertices curves in the positive and negative fields. One outlier in the negative field may be significant, but since it is a single analysis we caution against using it to define W_m. Instead, we use the transition defined by porphyroclasts in the positive and negative fields that correspond to a range of $W_m = 0.60$ - 0.675. This comparison demonstrates that the RGN reduces the potential range in R_c values, as defined by the Wallis plot ($R_c = 1.75$-3.0), to 0.60-0.675 and also helps clarify which porphyroclasts should be used to define R_c.

Using the distribution of porphyroclasts with delta-or sigma-type tails on the original Passchier plot, Passchier (1987) estimated a range of $W_m = 0.50$-0.80 and an inferred cutoff point of $W_m = 0.60$ for a quartz mylonite from the St. Barthelemy Massif, France (Fig. 3.8B). When plotted on the RGN, these same data define a transition above the vertices curve at $W_m = 0.65$ in the positive field and $W_m = 0.55$ in the negative field. Two outliers that plot above the vertices curves to define higher W_m estimates are excluded in order to maintain consistency with the earlier interpretations and emphasize the use the majority data to constrain R_c. The RGN also demonstrates that although a single porphyroclast defines a $W_m = 0.48$, it is lower than the majority of grains that define a $W_m = 0.55$-0.65. This comparison highlights how the modified version of the Passchier plot, that forms the basis of the RGN, can help limit ambiguity in estimating W_m.

As suggested by results from the four methods applied to the four samples discussed above, Wallis, PHD, Passchier and RGN plots yield consistent W_m estimates. Tailless porphyroclasts can define W_m on the HN, as demonstrated by using two hyperbolas in conjunction with a section of the vertices curves and a circle that envelope the infinitely rotating grains. The same results, however, are more easily plotted and less ambiguously interpreted using the RGN. The range in W_m estimated by the PHD, RGN and Wallis plots from the three natural test samples are within the range of those previously obtained using the Wallis and PHD plots in Rongbuk Valley, Tibet (Law et al., 2004; Jessup et al., 2006).

We limit this approach to the idealized models and a simple comparison between theoretical and natural data using four different plots (Figs. 3.7 and 3.8), to clearly present the RGN as an alternative method to estimate W_m. However, many exceptions to these idealized parameters do exist i.e., plane strain vs. non-plane strain and monoclinic vs. triclinic shear (Giorgis and Tikoff, 2004; Bailey et al., *in press*). Additionally, the sample must meet the five main requirements defined by Passchier (1987): 1) reasonably homogeneous deformation on the scale of the sample, 2) significant difference in grain size between the rigid porphyroclasts and the matrix, 3) high finite strain to rotate objects towards stable-sink positions, 4) porphyroclast shape that is close to orthorhombic, and 5) significant number of porphyroclasts with a range in aspect ratios and orientations. We also caution against over interpretation of W_m estimates. Future investigations may find the RGN provides additional information necessary to tackle more complex problems such as triclinic shear and the distribution of tailed vs. tailless porphyroclasts.

Conclusions

By building on the original work of Passchier (1987), we have created the RGN as an alternative method to estimate W_m and thereby unify rigid porphyroclast vorticity techniques that were previously proposed by Passchier (1987; Passchier plot), Simpson and De Paor (1993, 1997; PHD plot); Wallis (1995; Wallis plot). The RGN provides a series of modified semi-hyperbolas that define the predicted orientation of rotating porphyroclasts against which natural, more complex, data can be compared: a major advantage over existing methods. Because the same fundamental equations are used to construct the hyperbolas of the RGN and HN, they provide the same theoretical relationships against which natural data can be compared. To test this hypothesis, we used tailless porphyroclasts to constrain the transition between the stable-sink position and infinitely rotating porphyroclasts that define R_c and associated W_m. A comparison of W_m results from four test samples, using the Passchier, Wallis, PHD and RGN plots, demonstrates that the four methods yield internally consistent W_m estimates. By unifying these methods using tailless porphyroclasts, we confirm that tailless porphyroclasts yield W_m estimates that are at least as rigorous as those obtained using methods that rely on tailed porphyroclast i.e., the PHD method and Passchier plot. Through comparisons between how the distribution of less-than-ideal data from sample R05-03 defines W_m using the Wallis plot versus the RGN and between the Passchier plot and the RGN, we demonstrate that contrasting porphyroclast distributions with the orientations predicted by the RGN can help limit ambiguity in estimating W_m.

Another benefit of the RGN is that data from porphyroclasts can be entered into an Excel© worksheet and plotted directly on the RGN which can be imported as a background to an Excel© chart. This enables immediate feedback on the significance of each porphyroclast. The W_m curves on the RGN offer an easier means to define R_c within a sample and should help refine and standardize the results of future investigations. Because of its ease of use, ability to enhance and justify the choice of R_c, and potential to calibrate the presentation of various investigations, we offer the RGN as an alternative approach to estimating W_m in high strain zones.

Acknowledgements

We would like to thank Dennis Newell and John Cottle for their motivated efforts in the field and unnerving capacity to present the counter-hypothesis as well as Sonam Wangdu who brought us to his home, Gondasampa, where we collected the samples that formed the basis of this investigation. Also, we greatly appreciated insightful discussions with Jeff Lee, Benjamin Schwartz and Ryan Thigpen that helped clarify many sections of the manuscript. Many thanks to C. Bailey, D. De Paor, S. Wallis and P. Xypolias whose reviews greatly strengthened this manuscript. The expedition to Gondasampa and Rongbuk Valley (2005) was funded by a 2010 Fellowship from the College of Science, Virginia Tech and a Geological Society of America research grant to MJJ as well as a New Zealand TEC Bright Future Top Achiever Doctoral Scholarship to John Cottle.

References

Bailey, C.M., Polvi, L.E., Forte, A.M., *in press*. Pure shear-dominated high-strain zones in basement terranes. In: Hatcher, R.D.Jr., Carlson, M.P., McBride J.H., Catalán, J.R.M (Eds.) Four-Dimensional Framework of Continental Crust, Geological Society of America Memoir.

Bailey, C.M., Eyster, E.L., 2003. General shear deformation in the Pinaleno Mountains metamorphic core complex, Arizona. Journal of Structural Geology 25, 1883-1893.

Bretherton, F.P., 1962. The motion of rigid particles in shear flow at low Reynolds number. Journal of Fluid Mechanics 14, 284-301.

De Paor, D.G., 1983. $R_f/ø_f$ strain analysis using an orientation net. Journal of Structural Geology 10, 323-33.

Ghosh, S.K., Ramberg, H., 1976. Reorientation of inclusions by combination of pure and simple shear. Tectonophysics 34, 1-70.

Giorgis, S., Tikoff, B., 2004. Constraints on kinematics and strain from feldspar porphyroclast populations. In: Alsop, G.I., Holdsworth, R.E., McCaffrey, K.J.W., Hand, M. (Eds.) Flow Processes in Faults and Shear Zones. Geological Society of London Special Publications 224, 265-285.

Hirth, G., Tullis, J., 1992. Dislocation creep regimes in quartz aggregates. Journal of Structural Geology 14, 145-160.

Holcombe, R.J., Little, T.A., 2001. A sensitive vorticity gauge using rotated porphyroblasts and its application to rocks adjacent to the Alpine Fault, New Zealand. Journal of Structural Geology 23, 979-990.

Jeffrey, G.B., 1922. The motion of ellipsoidal particles immersed in a viscous fluid. Proceedings of the Royal Society of London A102, 161-179.

Jessup, M.J., Law, R.D., Searle, M.P., Hubbard, M.S., 2006. Structural evolution and vorticity of flow during extrusion and exhumation of the Greater Himalayan Slab, Mount Everest Massif, Tibet/Nepal: implications for orogen-scale flow partitioning. In: Law, R.D., Searle, M.P. & Godin, L. (Eds.) Channel Flow, Extrusion, and Exhumation in Continental Collision Zones. Geological Society, London, Special Publications 268, 379-414.

Klepeis, K.A., Daczko, N.R., Clarke, G.L., 1999. Kinematic vorticity and tectonic significance of superposed mylonites in a major lower crustal shear zone, northern Fiordland, New Zealand. Journal of Structural Geology 21, 1385-1406.

Law, R.D., Searle, M.P., Simpson, R.L., 2004. Strain, deformation temperatures and vorticity of flow at the top of the Greater Himalayan Slab, Everest massif, Tibet. Journal of the Geological Society, London 161, 305-20.

Murphy, M.A., Harrison, T.M., 1999. Relationship between leucogranites and the Qomolangma Detachment in the Rongbuk valley, south Tibet. Geology 27, 831-834.

Passchier, C.W., 1987. Stable positions of rigid objects in non-coaxial flow—a study in vorticity analysis. Journal of Structural Geology 9, 679-690.

Simpson, C., De Paor, D.G., 1993. Strain and kinematic analysis in general shear zones. Journal of Structural Geology 15, 1-20.

Simpson, C., De Paor, D.G., 1997. Practical analysis of general shear zones using porphyroclast hyperbolic distribution method: an example from the Scandinavian Caledonides. In: Sengupta, S. (Ed.) Evolution of Geological Structures in Micro- to Macro-scales. London, Chapman and Hall, 169-184.

Stipp, M., Stunitz, H., Heilbronner, R., Schmid, S., 2002. Dynamic recrystallization of quartz: correlation between natural and experimental conditions. In: De Meer, S., Drury, M.R., De Bresser, J.H.P. & Pennock, G.M. (Eds.) Deformation Mechanisms, Rheology and Tectonics: Current Status and Future Perspectives. Geological Society, London, Special Publications 200, 171-190.

Vissers, R.L.M., 1989. Asymmetric quartz c-axis fabrics and flow vorticity: a study using rotated garnets. Journal of Structural Geology 11, 231-24.

Wallis, S.R., 1992. Vorticity analysis in a metachert from the Sanbagawa Belt, SW Japan. Journal of Structural Geology 14, 271-280.

Wallis, S.R., 1995. Vorticity analysis and recognition of ductile extension in the Sanbagawa belt, SW Japan. Journal of Structural Geology 17, 1077-1093.

Wallis, S.R., Platt, J.P., Knott, S.D., 1993. Recognition of syn-convergence extension in accretionary wedges with examples from the Calabrian Arc and the Eastern Alps. American Journal of Science 293, 463-495.

Xypolias, P., Doutsos, T., 2000. Kinematics of rock flow in a crustal scale shear zone: implications for the orogenic evolution of the southwestern Hellenides. Geological Magazine 137, 81-96.

Xypolias, P., Koukouvelas, I.K., 2001. Kinematic vorticity and strain patterns associated with ductile extrusion in the Chelmos shear zone (External Hellenides, Greece). Tectonophysics 338, 59-77.

Xypolias, P., Kokkalas, S., 2006. Heterogeneous ductile deformation along a mid-crustal extruding shear zone: an example from the External Hellenides (Greece). In: Law, R.D., Searle, M.P., Godin, L., (Eds.) Channel flow, Extrusion, and Exhumation in Continental Collision Zones. Geological Society, London, Special Publications 268, 497-516.

Figure 3.A1

Rigid Grain Net (RGN)

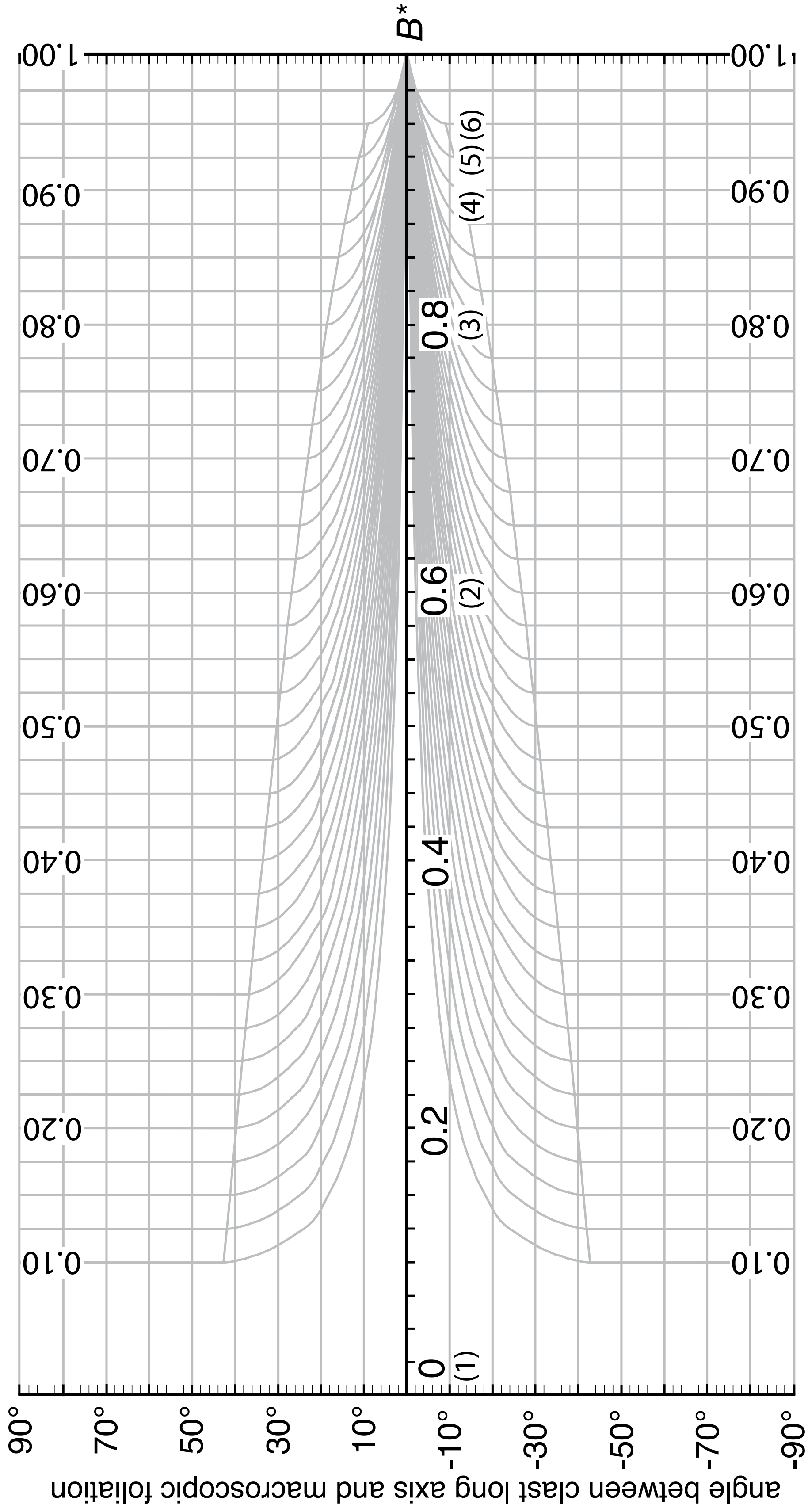

CHAPTER 4

P-T-t-D paths of Everest Series schist, Nepal

MICAH J. JESSUP[1], MICHAEL P. SEARLE[2], JOHN M. COTTLE[2], RICHARD D. LAW[1], DENNIS L. NEWELL[3], ROBERT J. TRACY[1] & DAVID J. WATERS[2]

[1.] *Department of Geosciences, Virginia Tech, Blacksburg, Virginia 24061, USA*
[2.] *Department of Earth Sciences, Oxford University, Oxford OX1 3PR, UK*
[3.] *Department of Earth and Planetary Science, University of New Mexico, Albuquerque, New Mexico 87131, USA*

Submitted to *Journal of Metamorphic Geology*, March 31, 2007.

Abstract

The metamorphic core of the Himalayas, the Greater Himalayan Sequence (GHS), is bounded by two north-dipping shear zones, the Main Central Thrust zone (MCTZ) below and South Tibetan Detachment system (STDS) above. In the Mt. Everest region, the STDS includes an upper brittle Qomolangma detachment (QD) and lower ductile Lhotse detachment (LD) that merge towards the north. Previous investigations proposed that following an abrupt upward increase in metamorphic grade through the MCTZ, metamorphic temperatures remained approximately isothermal structurally up-section towards the LD, and that the overlying Everest Series reached only greenschist facies. Detailed macro-and micro-structural analysis, U-Th-Pb geochronology and *P-T* estimates shed light on this critical transition. A gradation from garnets with diffusion profiles to those with growth zoning occurs across the LD. These samples record a decrease in temperature from 740 to 590°C and an increase in pressure from 4 - 6 kbar towards structurally higher positions. We interpret this as the result of complex juxtaposition of Everest Series with the underlying GHS during exhumation along the LD-QD system. A maximum age limit of 24.1 ± 1.2 Ma for movement on the LD is provided by the crystallization age of the Nuptse granite, a body that post-dates solid-state fabric development. Microstructural evidence suggests that deformation progressed from a distributed ductile shear zone into a discrete brittle detachment during the final stages of exhumation. When combined with existing thermobarometric data from the core of the GHS and MCTZ these results form the basis for a new model for the thermal evolution of the GHS exposed in the Mt Everest region, including an improved definition of the LD.

Introduction

The highest peaks and greatest relief in the Himalayas occur within the surface exposures of the 5-30 km thick metamorphic and anatectic core of the orogen known as the Greater Himalayan Sequence (GHS; Figs. 4.1-4.3). The GHS is bounded by a low-angle north-dipping normal fault above (South Tibetan detachment system; STDS) and a thrust system below (Main Central thrust zone; MCTZ). Assuming simultaneous movement on the MCTZ and STDS, channel flow and extrusion models propose that between ~ 33 and 16 Ma, gravity-driven southward extrusion of the GHS took place between the Tibetan plateau and the foreland of the Himalaya (Grujic et al., 1996, 2002; Hodges et al., 1998, 2001; Beaumont et al., 2001; 2006). The thermal structure of the GHS, including the inverted metamorphic sequence within the MCTZ, is often attributed to one of two processes; synmetamorphic ductile shearing (Jamieson et al., 1996, 2002) or as deformation and inversion of originally horizontal thermal gradients (Searle and Rex, 1989; Grujic et al., 1996; Grasemann et al., 1999). Both of these interpretations require as input the accurate documentation of the pressure-temperature-time-deformation (*P-T-t-D)* evolution during extrusion and exhumation of the GHS (Grujic et al., 1996; Grasemann et al., 1999; Vannay & Grasemann, 2001; Vannay et al., 2004).

Assumed by extrusion models is a general thermal profile for the GHS whereby metamorphic temperature increases up structural section to the high-grade core and then decrease towards structurally highest positions at the top of the GHS (Searle and Rex, 1989; Grujic et al., 1996; Hubbard, 1996; Carosi et al., 1999; Grasemann et al., 1999). Inverted metamorphic sequences at the base of the GHS are ubiquitous along the central Himalayas and have received considerable attention (Le Fort, 1975; Swapp and Hollister, 1991; Hubbard, 1988, 1996; Macfarlane, 1995; Harrison et al., 1997; Grasemann and Vannay, 1999; Walker et al., 1999; Goscombe and Hand, 2000; Catlos et al., 2001, 2002, 2004; Daniel et al., 2004; Kohn et al., 2005; Goscombe et al. 2006). Successful documentation of the decrease in metamorphic grade at the top of the slab, however, is limited to Zanskar, India where right way-up isograds have been mapped along the Zanskar Shear zone (e.g., STDS equivalent; Searle and Rex, 1989; Dezes, 1999; Searle et al., 1999b; Walker et al., 1999; Stephenson et al., 2000; Walker et al., 2001).

The thermal evolution of the Himalayas is often discussed in terms of an early Barrovian event (M1 or Eohimalayan) that was followed by a high temperature, low pressure event associated with decompression, migmatization and emplacement of leucogranite injection complexes and large sills and dikes (M2 or Neohimalayan; Hodges, 2000 and references therein). The pervasive nature of the high temperature M2 event often results in overprinting of the record for early fabric development and associated (M1) prograde compositional zoning in garnets. As a result, many models for the evolution of the GHS reflect the later, pervasive Neohimalayan event instead of a more complete *P-T-t-D* path. Another significant goal arising from a more complete thermal profile through the slab, where the progression in deformation and metamorphism can be characterized, is to determine if the current profile is the result of the folding of isograds from a single metamorphic event, or the juxtaposition of two different metamorphic histories, or some combination of both (i.e., Searle and Rex, 1989; Jamieson et al., 1996). The final motivation behind this investigation is to constrain deformation mechanisms responsible for exhumation of the GHS and how the interplay between deformation and metamorphism generated the apparently simple *P-T-t* profile through the GHS.

Characterizing the upper section of the GHS holds several implications for the tectonic evolution of the Mt Everest region and the remainder of the Himalayan orogen. This paper integrates field mapping, thermobarometry, THERMOCALC modeling, microstructural analyses and U-Th-Pb geochronology, to characterize the structurally highest sections of the GHS. Results from the top of the slab are compared with previous investigations that focused on the base and core of the GHS and a revised model for the thermal evolution of the GHS, exposed in the Everest region of Nepal-Tibet, is proposed.

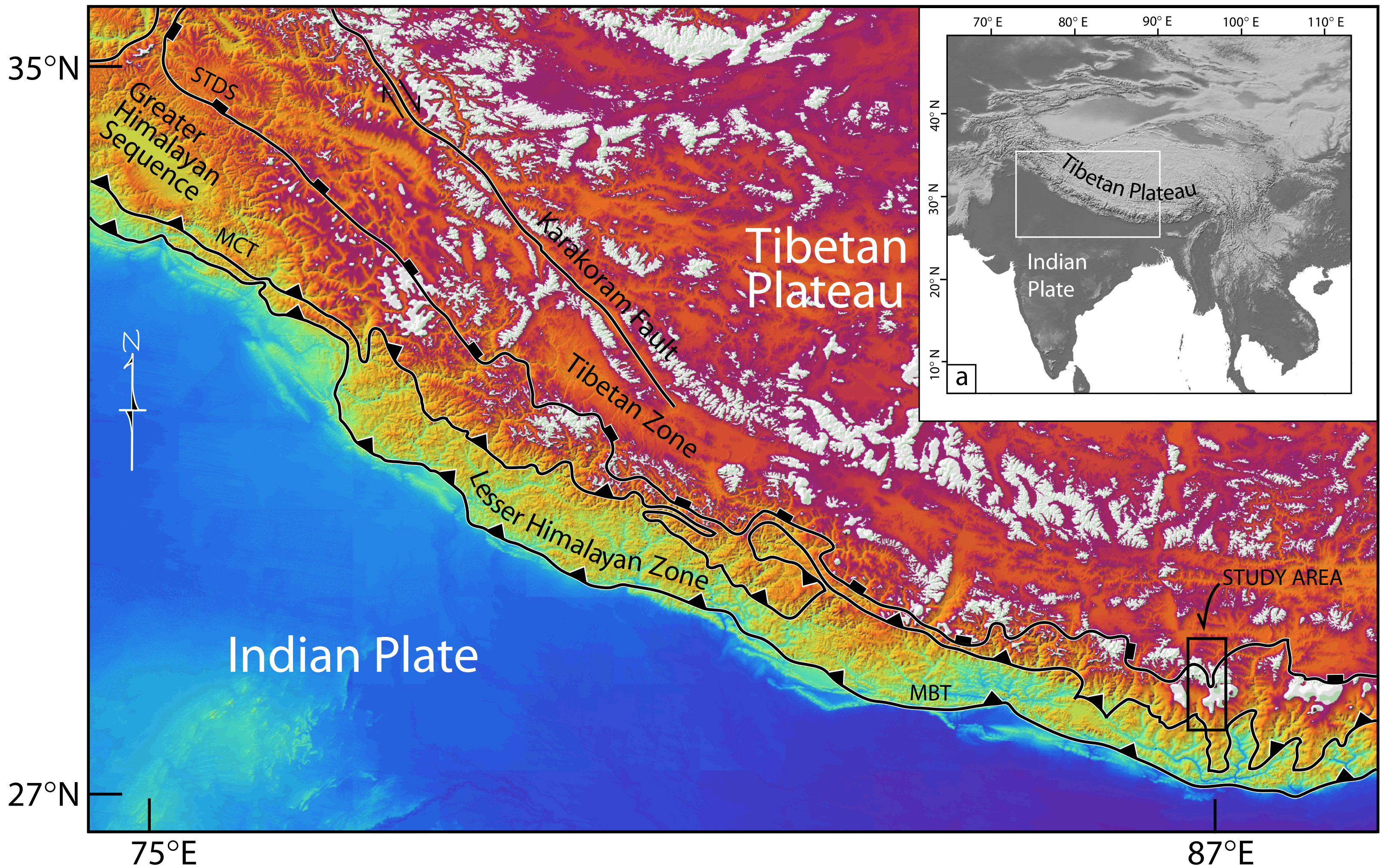

Figure 4.1. Digital elevation map (USGS GTOPO30) of the Himalayas depicting the main lithotectonic elements of the orogen. Location of thrusts and detachments are modified after Hodges (2000). Study area is enclosed by the black rectangle and represents area of detailed map in Figure 2. South Tibetan detachment system, STDS; Main Central thrust, MCT; Main Boundary thrust, MBT. Compiled by M.J. Jessup.

Geological Setting

The impressive topographic relief centered on the Mount Everest-Lhotse-Nuptse massif, provides a window into mid-crustal processes responsible for the present thermal structure of the GHS (Figs. 4.2 and 4.3). Rock types commonly found in the GHS include calc-silicates, quartzites, pelitic schists, and augen gneisses that are variably migmatized and injected by numerous leucogranite sills and dike complexes (Searle 1999b, Searle et al., 2003; Viskupic et al., 2005). To provide context for the results from this investigation, we synthesize the previously published geochronologic and geothermobarometric research conducted in the three main sections of the Everest region, the MCTZ, the GHS, and the STDS. Our review of the structural evolution of the Everest transect will be limited to the upper most section of the GHS; for a more complete treatment see Carosi et al. (1999), Searle et al. (2003) and Jessup et al. (2006).

Main Central Thrust Zone

The north-dipping MCTZ marks the base of the GHS and juxtaposes gneisses of the GHS with the Lesser Himalayan Sequence (LHS) below (Fig. 4.1). In the Dudh Kosi drainage, south of Everest, the MCTZ is a ~5 km wide zone of pelitic schists, marbles, and quartzites that is bounded by the Barun gneiss of the GHS above and the Okandunga gneiss of the LHS below (Figs. 4.2 and 4.3; Hubbard, 1989; Pognante and Benna, 1993). A variety of shear sense indicators including S-C fabrics and asymmetric sigma-type porphyroclasts tails consistently record top-to-the-south sense of shear. The sequential appearance of index minerals, from the base of the MCTZ to the core of the GHS, places qualitative constraints on an inverted sequence of metamorphic isograds (Hubbard, 1989). Subsequent geothermobarometric calculations (using the calibration of Ferry & Spear, 1978) by Hubbard (1989) quantified the increase in metamorphic grade towards higher structural positions and also demonstrated that these samples recorded a pressure gradient of 0.28 kbar/km, which Hubbard (1996) attributed to syn-metamorphic thrusting.

Based on a zone of distributed shear, index minerals (Grt, St, Ky, Sil) that pre-

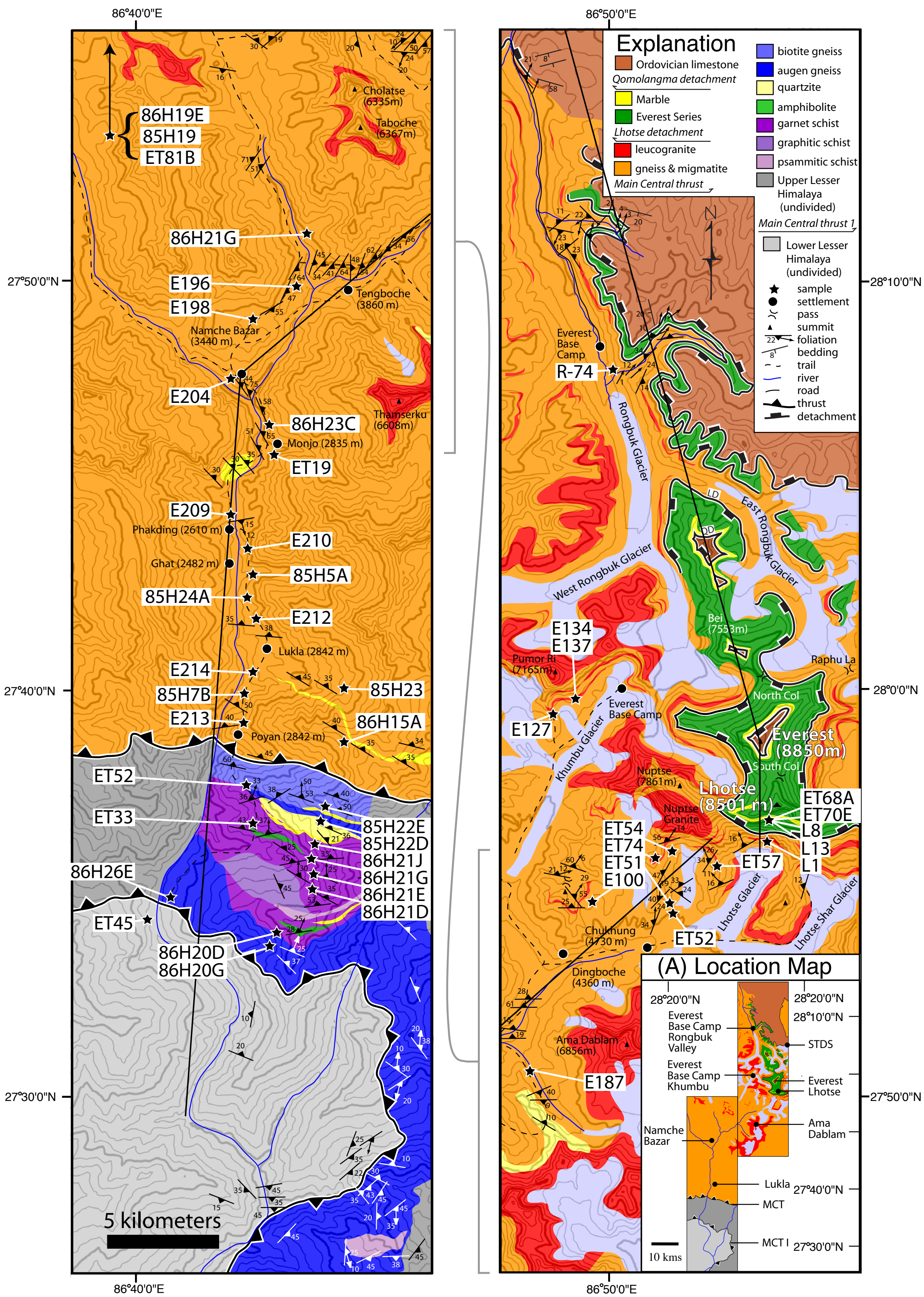
86°40'0"E
86H19E
85H19
ET81B
Cholatse (6335m)
Taboche (6367m)
86H21G
E196
E198
Tengboche (3860 m)
Namche Bazar (3440 m)
E204
Thamserku (6608m)
86H23C
Monjo (2835 m)
ET19
E209
Phakding (2610 m)
E210
Ghat (2482 m)
85H5A
85H24A
E212
Lukla (2842 m)
E214
85H23
85H7B
E213
86H15A
Poyan (2842 m)
ET52
ET33
85H22E
85H22D
86H21J
86H21G
86H21E
86H21D
86H26E
ET45
86H20D
86H20G
27°50'0"N
27°40'0"N
27°30'0"N
5 kilometers
86°50'0"E
Explanation
Ordovician limestone
Qomolangma detachment
Marble
Everest Series
Lhotse detachment
leucogranite
gneiss & migmatite
Main Central thrust
biotite gneiss
augen gneiss
quartzite
amphibolite
garnet schist
graphitic schist
psammitic schist
Upper Lesser Himalaya (undivided)
Main Central thrust 1
Lower Lesser Himalaya (undivided)
sample
settlement
pass
summit
foliation
bedding
trail
river
road
thrust
detachment
N
28°10'0"N
28°0'0"N
27°50'0"N
Everest Base Camp
R-74
Rongbuk Glacier
East Rongbuk Glacier
West Rongbuk Glacier
LD
QD
Bei (7553m)
Raphu La
North Col
E134
E137
Pumor Ri (7165m)
Everest Base Camp
E127
Khumbu Glacier
Everest (8850m)
South Col
Nuptse (7861m)
Lhotse (8501 m)
Nuptse Granite
ET68A
ET70E
L8
L13
L1
ET54
ET74
ET51
E100
ET57
Lhotse Glacier
Lhotse Shar Glacier
Chukhung (4730 m)
ET52
Dingboche (4360 m)
Ama Dablam (6856m)
E187
(A) Location Map
28°20'0"N
28°10'0"N
Everest Base Camp Rongbuk Valley
STDS
Everest Base Camp Khumbu
Everest
Lhotse
Ama Dablam
Namche Bazar
Lukla
27°40'0"N
MCT
MCT I
27°30'0"N
10 kms

Figure 4.2. Previous page. Simplified geologic map of the Mount Everest. Topographic base map (200 m contour intervals) and location map were created using the USGS GTOPO30 digital elevation model. Projected location of STDS in Tibet are based on Landsat 7 images. All structural data is original to this work except in the lower MCTZ, which are from Hubbard (1989), and the data in Rongbuk valley, which are from Burchfiel et al. (1992) and Murphy and Harrison (1999). Dashed line marks routes used during this investigation to access samples and map. Major contacts build on Lombardo et al. (1993) and Searle (2003). Samples collected by: Hubbard (1989), 85H7B-86H23C; Catlos (2002), ET19, ET33, ET45 and ET52; Searle et al. (2003), E100-E214; Hodges, et al. (1992), R-74; this study, ET51-ET74, L1-L13.

date mylonite formation (Fig. 4.3a and b) and metamorphic isograds that are sub-parallel to shear fabric (Fig. 4.3), Hubbard (1996) proposed that the inverted isograds were generated during ductile shearing that was accommodated by crystal-plastic processes (e.g., dislocation glide and creep, diffusion creep and recrystallization) during non-coaxial shear of originally right-way-up metamorphic isograds. These predictions agree with Jessup et al. (2006) who also demonstrated that mylonitic fabrics in the MCTZ post-date kyanite (Fig. 4.3a) and garnet (Fig. 4.3b) porphyroblast growth and that the vorticity of this flow ranged from W_m = 0.67-0.72 (where simple shear, W_m = 1; pure shear, W_m = 0; and equal contributions of both, W_m = 0.71). Assumed in this model (Hubbard, 1996 see her Fig. 3) is a section of right-way-up isograds at the top of the slab that was undocumented at the time.

Catlos et al. (2002) conducted additional thermobarometric calculations on three samples from the Khumbu MCTZ (Figs. 4.2 and 4.3; samples ET33, 45 and 52). Point transects across garnets provided chemical data that justified the garnet analysis used for thermobarometric calculations. Garnet zoning profiles that typify prograde garnet growth (decrease in X_{sps} from ~0.15 in the core to ~0.04 on the rim) were sampled from the lowest structural position that was reached by their investigation and yield temperature estimates of ~550°C, which agree with the Hubbard (1989) results (Figs. 4.3 and 4.4). Garnet profiles from other samples collected towards the upper limit to the 5 km wide MCTZ record an increase in X_{sps} from ~0.04 in the core to 0.08 at the rim and show

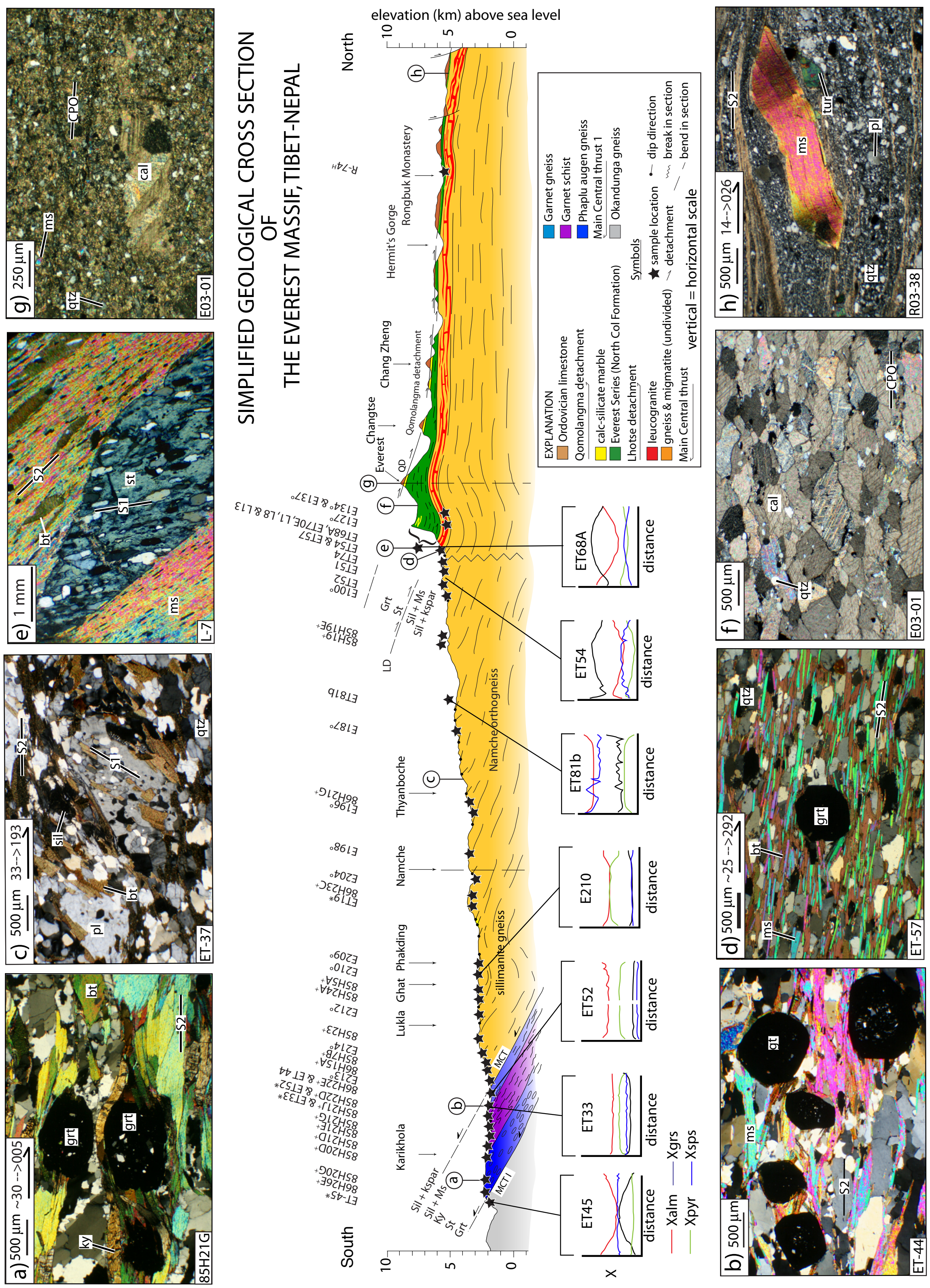
SIMPLIFIED GEOLOGICAL CROSS SECTION OF THE EVEREST MASSIF, TIBET-NEPAL
South
North
elevation (km) above sea level
vertical = horizontal scale
EXPLANATION
Ordovician limestone
Qomolangma detachment
calc-silicate marble
Everest Series (North Col Formation)
Lhotse detachment
leucogranite
gneiss & migmatite (undivided)
Main Central thrust
Garnet gneiss
Garnet schist
Phaplu augen gneiss
Main Central thrust 1
Okandunga gneiss
Symbols
sample location
detachment
dip direction
break in section
bend in section
Karikhola
Lukla
Ghat
Phakding
Namche
Thyanboche
Changtse
Everest
Chang Zheng
Hermit's Gorge
Rongbuk Monastery
Namche orthogneiss
sillimanite gneiss
Qomolangma detachment
MCT
MCT1
LD
QD
Sil + kspar
Sil + Ms
Ky
St
Grt
ET45
ET33
ET52
E210
ET81b
ET54
ET68A
distance
X
Xalm
Xpyr
Xgrs
Xsps
a) 500 μm ~30 --> 005
85H21G
b) 500 μm
ET-44
c) 500 μm 33--> 193
ET-37
d) 500 μm ~25 --> 292
ET-57
e) 1 mm
L-7
f) 500 μm
E03-01
g) 250 μm
E03-01
h) 500 μm 14--> 026
R03-38

Figure 4.3. Previous page. Simplified geologic cross section of the Mount Everest transect including the approximate sample locations are from Hubbard[+] (1989), Hodges[H] et al. (1992), Catlos[*] et al. (2002), Searle[°] et al. (2003) and this study are shown as stars. Insets a-h are photomicrographs taken with crossed polars of representative microstructures for various sections of the Mt. Everest transect (plunge and trend of lineation shown for in situ samples). Analytical transects across garnets from Catlos et al. (2002; ET45, ET33, ET52), Simpson (2002; E210), and this investigation (ET81b, ET54, ET68A) depict garnet zoning that is present in different structural positions within the Everest region. Images taken by M.J. Jessup.

evidence for alteration due to retrograde net transfer reactions (Fig. 4.3; Kohn and Spear, 2001; Catlos et al., 2002). Catlos et al. (2002) proposed that this transition between end-member garnet zoning profiles (samples ET45 and ET52) defines the MCTZ.

Simpson (2002) and Searle et al. (2003) reprocessed the mineral chemical data from the Hubbard (1989) samples using both modern calibrations for geothermobarometry (Holdaway, 2000) as well as using THERMOCALC to estimate pressure conditions (Fig. 4.4). Their results confirm the increase in metamorphic temperatures of 450-620°C, yet yield fairly constant pressure estimates of ~7.5 kbars across the MCTZ. Although the reprocessed mineral chemical data are an improvement on the original results, they rely on the original averaged rim composition data from Hubbard (1989) acquired without compositional maps of the garnets - a necessary step to ensure that the analyses were appropriate for making these calculations (i.e., evidence for retrograde net transfer reactions was not accounted for) and therefore should be used with caution (Kohn & Spear, 2001).

Timing constraints for movement along the MCTZ in the Everest region are based on $^{40}Ar/^{39}Ar$ thermochronology and *in situ* ion microprobe U-Th-Pb geochronology within the MCTZ (Hubbard and Harrison, 1989; Catlos et al., 2001, 2002, 2004). Assuming that deformation temperatures were lower than the closure temperature of hornblende, Hubbard and Harrison (1989) proposed that the ~21 Ma $^{40}Ar/^{39}Ar$ age from a sheared amphibolitic lens provided a maximum age for movement along that section of the MCTZ. Catlos et al. (2002) dated a series of monazite grains that were included in

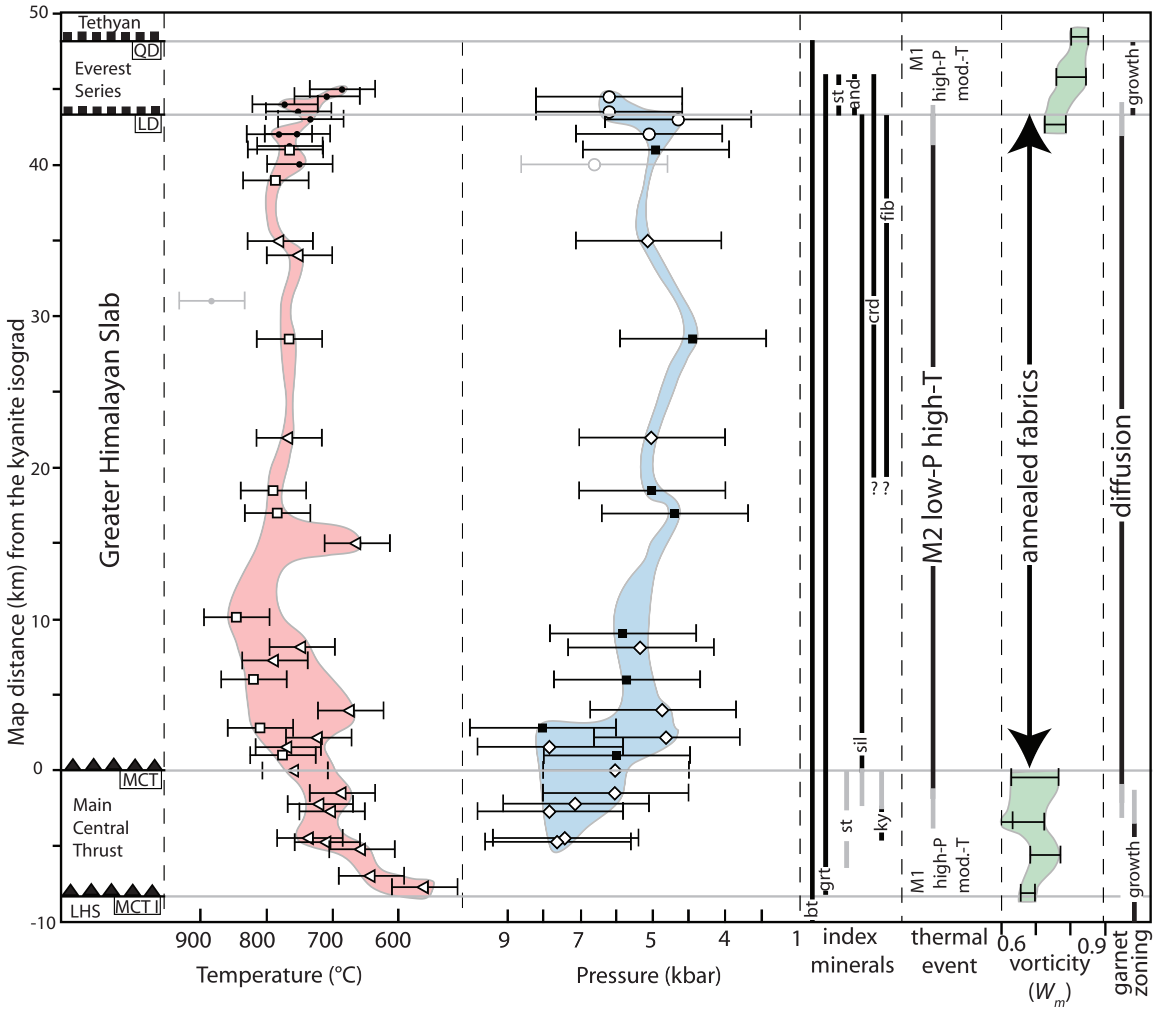

Figure 4.4. Synthesis of data located south of the summit of Everest. Pressure data are from this study (open circles; ET-52 shown as light gray, unreliable data), Searle et al. (2003; solid squares), and Hubbard (*reprocessed*; 1989; open diamonds). Temperature estimates are from this study (solid circle; ET-81b shown as light gray, sample projected ~20 km into cross section), Hubbard (*reprocessed*; 1989; open triangle), and Searle et al. (2003; open squares). Occurrence of index minerals is based on data from this investigation and Hubbard (1989). Vorticity results and microstructural summary are from Jessup et al. (2006). Concept of data presentation after Goscombe et al. (2006). See Table 4.1 for the sequence of samples.

garnet and matrix phases. Matrix monazite grains yielded ages that range between 24-29 Ma, which Catlos et al. (2002) interpreted as evidence for early movement on the MCTZ. Additional ages obtained by Catlos et al. (2002) within the MCTZ and lower section of the GHS range from 10.3 ± 0.8 to 14.5 ± 0.1, which these workers attributed to record subsequent movement on the MCTZ.

Table 4.1. P-T-estimates

Sample	distance (km)	Grt-Bt T (C°)	T (C°)	sd (T)	P (kbar)	sd(P)	corr	n	XH_2O
86H26E[*]	-7.75	458[+]	-	-	-	-	-	-	-
85H20D[*]	7	539	-	-	-	-	-	-	-
85H20G[*]	5.25	554	-	-	-	-	-	-	-
85H21D[*]	4.75	608	566	84	7.6	1.8	0.116	5	-
85H21E[*]	4.5	634	627	100	7.4	2	0.114	5	-
85H21G[*]	2.75	600	596	22	7.8	1.3	0.822	6	0.5
85H21J[*]	2.25	618	614	22	7.1	1.2	0.819	6	0.6
85H22D[*]	1.5	583	587	35	6	1.5	0.91	6	0.4
85H22E[*]	0	656	646	29	6	1.2	0.917	6	0.8
E213[#]	1	673	669	40	6	1.4	0.319	4	-
86H15A[*]	1.5	666	632	31	7.8	1.1	0.785	5	1
85H7B[*]	2.2	621	617	100	4.6	1.7	0.676	3	-
85H23[*]	4	571	508	85	4.7	1.6	0.729	3	-
E212[#]	6	719	718	46	5.7	1.4	0.349	4	-
86H24A[*]	7.25	687[+]	-	-	-	-	-	-	-
85H5A[*]	8.1	644	672	121	5.3	1.9	0.734	3	-
E210[#]	9	709	718	43	5.8	1.5	0.335	4	-
E209[#]	10.1	745	-						
86H23C[*]	15	561	-						
E204[#]	17	683	685	44	4.4	1.7	0.356	4	0.25
E198[#]	18.5	690	694	44	5	1.7	0.315	4	0.3
86H21G[*]	22	665	683	122	5	2	0.684	3	-
E187[#]	28.5	665	671	37	3.9	1.2	0.957	7	0.8
ET-81b	31	783 (4)	-	-	-	-	-	-	-
86H19C[*]	35	650	-						
86H19E[*]	36	679	717	129	5.1	1.9	0.715	3	-
E100[#]	39	685	-						
ET-52	40	649 (6)	648	37	6.6	1.1	0.726	6	0.45
E137[#]	41	664	651	41	4.9	0.4	0.315	4	0.4
ET-51	41.25	663 (6)	-	-	-	-	-	-	-
ET-54	42	653 (6)	-	-	-	-	-	-	-
ET-57	42	681 (5)	685	39	5.1	1.2	0.719	6	0.95
ET-68A	44	632 (4)	633	34	4.3	0.6	0.884	9	0.65
ET-70E	44	651 (6)	653	35	6.2	1.2	0.737	4	0.5
L-8	44	608 (6)	610	31	6.2	1	0.765	6	0.7
L-13	44	584 (4)	-	-	-	-	-	-	-

*average rim compositon of Hubbard (1989)
[#]Searle et al. (2003)
Searle et al. (2003) samples E214, E196, E127, 134, and E137 were are excluded from this compilation.
garnet-biotite thermomter used to calulate temperature using calibration 5AV of Holdaway (2000) at the pı
[+]Because of incomplete analysis temperatures were calculated using the thermometer of Bhattacharya (19

Greater Himalayan Sequence

Between the upper contact of the MCTZ and the base of the LD occurs a series of metasedimentary rocks and orthogneiss that are variably migmatized and constitute the GHS (Figs. 4.2 and 4.3). Restoration of the GHS shows that these gneisses are metamorphosed Proterozoic – Cambrian sedimentary rocks that were intruded by a series of Cambro-Ordovician granite – orthogneiss (Searle et al. 2006; fig. 5). To emphasize the metamorphic and microstructural evolution of the GHS and bounding shear zones, we treat the GHS as an undivided unit. Microstructures in the core of the GHS are characterized by quartz that reached Regime 3 recrystallization conditions as defined by Hirth and Tullis (1992), the onset of ductility within feldspar, and annealed fabrics (Fig. 4.3c). Several phases of folding and an early (S1) fabric included in feldspar grains suggest that a minimum of two fabric forming events created the dominant (S2) fabric preserved throughout the core of the GHS (Fig. 4.3c). Leucogranite sills and dike complexes increase in abundance towards progressively higher structural positions culminating in massive leucogranite bodies including the Everest, Makalu, and Nuptse leucogranites (Carosi et al., 1999; Searle, 1999b; Simpson et al., 2000; Searle et al., 2003; Viskupic et al., 2005). Emplacement mechanisms for these granites call upon increased magmatic pressure that drives forceful injection along pre-existing foliation (Weinberg and Searle, 1999; Searle, 1999b).

Pognante and Benna (1993) proposed a polyphase thermal evolution for the Khumbu region that involved three major events with M1 (550-680ºC, 8-10 kbars) related to subduction and early crustal thickening. Rocks from the lower and middle levels of the slab record an evolution from an M1 kyanite-bearing stage (only preserved in the lower most section of the MCTZ) to an M2 K-feldspar + sillimanite (muscovite absent) event associated with migmatization (650-750ºC, 4-7 kbar). Using cordierite growth during the break down of sillimanite and garnet they defined a third thermal pulse M3 (600-700ºC, 2-4 kbar), a high temperature low-medium pressure event associated with migmatization and leucogranite emplacement. As with the Hubbard (1989) results from the MCTZ, caution should be exercised when interpreting these *P-T* estimates as many of them are based on pairs of single point analyses that were selected without compositional maps or complete point transects (Kohn & Spear, 2001).

Simpson et al. (2000) used the U-Pb method to date monazite separated from two samples from the (core / upper section of) from the GHS, one collected near Pumo Ri base camp (E139) and the other on the ridge just west of Kala Pattar (E137; Figs. 4.2 and 4.3). One sample yielded a U-Pb metamorphic monazite age of 32.2 ± 0.4 Ma for a sample that contained garnet + biotite + sillimanite + cordierite + quartz + plagioclase + K-feldspar with a kyanite inclusion in a single garnet. This monazite age is interpreted as the age of peak Barrovian metamorphism, however the only index mineral unique to M1 is the kyanite inclusion, and therefore we prefer to treat this constraint as a minimum age for the M1 event. The second sample of granitic augen gneiss contained the assemblage K-feldspar + plagioclase + biotite + sillimanite + cordierite + muscovite and yielded an age of 22.7 ± 0.2 Ma and is interpreted as the age of the high temperature, low pressure M2 event (620°C, 4 kbar).

Searle et al. (2003) analyzed a series of garnet bearing samples, including those of Hubbard (1989) from Lukla (just above the upper contact of the MCTZ) to the summit of Kala Pattar (sample E127) on the flanks of Pumo Ri in the upper-core of the GHS (Figs. 4.2-4.4). Using compositional maps to characterize the compositional zoning in each garnet and a combination of geothermobarometry (Holdaway, 2000) for estimating temperatures and THERMOCALC to estimate pressures, they determined that following the increase in temperatures (450- 670°C) across the MCTZ (as previously discussed), temperatures only increase from 620-730°C to the top of the slab marked by the STDS. Pressure estimates, in contrast, range from 7-8 kbars along the MCTZ through 5 kbars in the core to 3 kbars along the upper section of the GHS at Kala Pattar (Figs. 4.2-4.4). Importantly, Kala Patar represents structurally lower conditions than the proposed location of the LD. Linear regression is used to estimate an average pressure gradient of 0.20 ± 0.09 kbar km^{-1} from the MCTZ through the GHS (Searle et al., 2003).

Based on U-Pb monazite and xenotime geochronology, Viskupic et al. (2005) proposed that Neohimalayan anatexis was a protracted event (~26-18 Ma), that crustal melting may have begun as early as ~ 25-26 Ma, and that melt migration occurred at ~ 21-22 Ma. $^{40}Ar/^{39}Ar$ thermochronology using amphibole and biotite yielded cooling ages of 22 Ma (below ~530°C) and 19 Ma (below ~380°C), respectively. Post-deformational dikes, however, record evidence for additional melt production between ~ 17.9 and

18.3 Ma. Viskupic et al. (2005) related 26-23 Ma crystallization ages to either: 1) decompression melting related to movement on the STDS, suggesting that the earliest melting occurred ~ 3 m.y. prior to the oldest leucogranites dated along the STDS; or 2) early anatexis that weakened the crust and focused deformation along the STDS.

South Tibetan Detachment System

As exposed on the Everest massif, the STDS contains two north-dipping detachments; the upper brittle QD and lower ductile LD (Searle 1999). Because the LD is proposed to dip less steeply than the QD, these two detachments merge into one composite structure in the northern limits of the Rongbuk valley, Tibet (Figs. 4.2 and 4.3). Between the two, lies a wedge of Everest Series schists (i.e., North Col formation), which Searle et al. (2003) described as biotite ± garnet grade, middle-to upper-greenschist facies pelites. Searle (1999a) proposed that an abrupt change from upper amphibolite sillimanite-gneiss, characteristic of the core of the GHS, to lower greenschist facies pelite of the Everest Series occurs across the LD. The type-locality for the LD is, unfortunately, exposed on inaccessible sections of the Everest-Lhotse-Nuptse massif. The location of the QD, immediately below the summit rocks, is confirmed by an abrupt transition in recrystallized grain size of calcite in slightly deformed Tethyan limestone (summit of Everest; 8850m; Fig. 4.3g) and the calc-silicate band (Yellow Band) below (Jessup et al. 2006). Additional calc-silicates located just below the South Col preserve a moderate LPO and Type I and Type II deformation twins suggesting deformation temperatures ≥ ~300ºC (Fig. 4.3f; Ferril et al, 2004). Previous attempts to estimate *P-T* conditions of the upper section of the GHS exposed in Rongbuk valley, where the LD and QD are well exposed and relatively accessible, have been thwarted by the lack of garnet bearing assemblages. A single *P-T* estimate from the mouth of Hermit's gorge in Rongbuk valley yields 630°C and 4.6 kbars (Figs. 4.2 and 4.3; Hodges et al., 1992; sample R-74). Deformation temperatures, as defined by the quartz c-axis thermometer (Law et al., 2004), increase from 450°C just below the QD (talus from above Rongbuk Monastery)

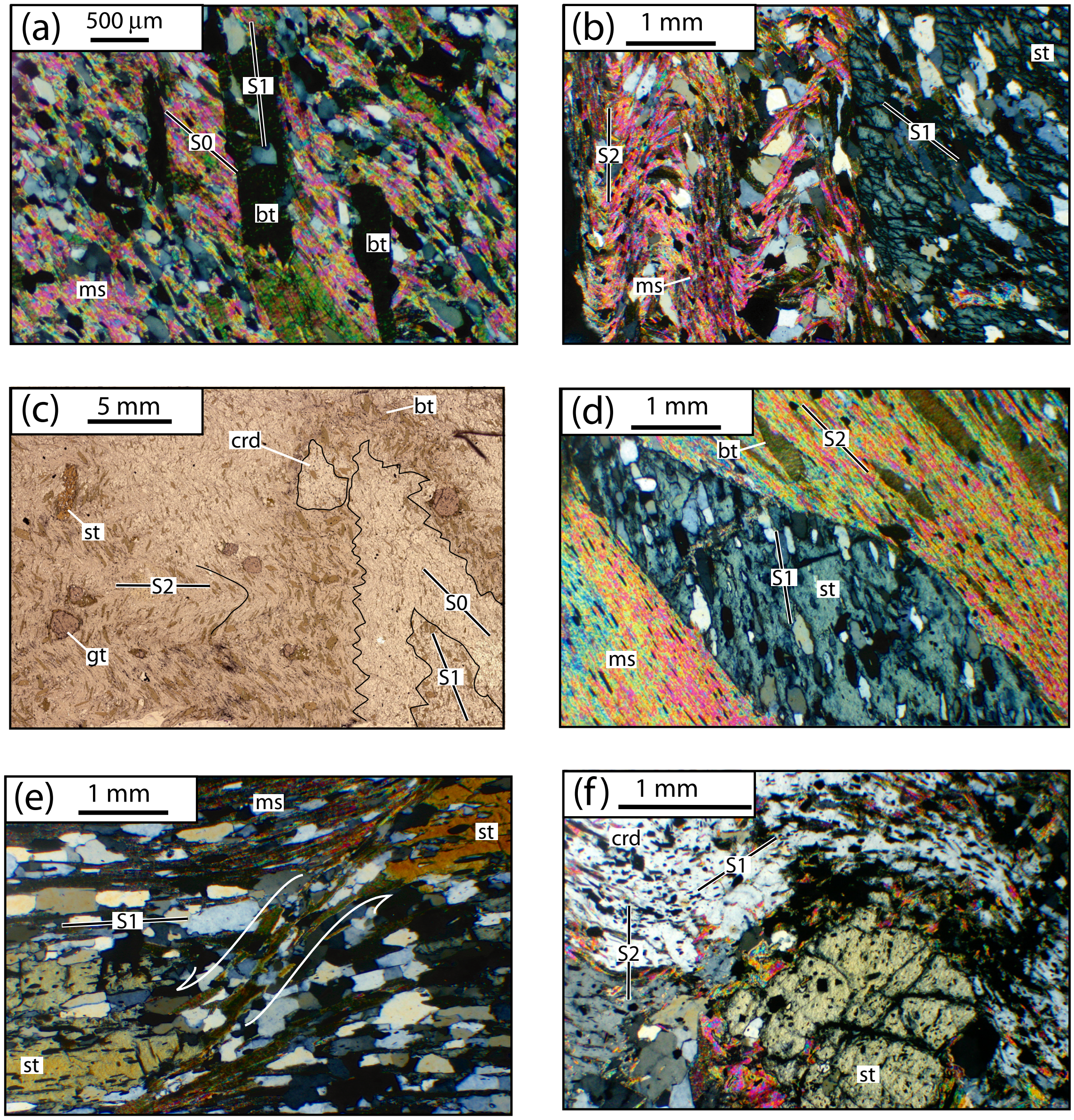

to 625°C at distances of ~ 600 m below the LD (Law et al., 2004). Timing constraints for granite emplacement and movement on the QD-LD system are provided by three geochronological investigations that focused on samples from Rongbuk valley. Hodges et al. (1992) originally proposed that mylonite formation along the detachment occurred between 22 and 19 Ma. Based on subsequent re-mapping and sampling of the same side valley to Rongbuk valley (Rongbuk Monastery) and a series of U-Th-Pb monazite ages on foliation parallel (16.2 ± 0.8 Ma) and crosscutting dikes (16.4 ± 0.6 Ma & 16.8 ± 0.8 Ma), Murphy and Harrison (1999) proposed that ductile deformation occurred ~17 Ma

Figure 4.5. Previous page. a) Photomicrograph with crossed polars of float sample L-10 that depicts the earliest fabric development. Muscovite defines an early fabric that we interpret as compositional layering (S0) while biotite defines a new axial planar foliation S2. b) Photomicrograph of float sample L-7 that shows a staurolite porphyroblast with S1 inclusion trails that are defined by quartz and opaques as well as a matrix of crenulated muscovite. c) Entire thin section scan of sample ET-68a that shows the relative timing of porphyroblasts growth and fabric development. Compositional layering (S0) is isoclinally folded by and F1 folds creating an axial planar S1 foliation. Staurolite porphyroclasts contain S1 inclusion trails. F2 crenulation folds deform the hinge zone of the F1 folds and the matrix muscovite and biotite. Crenulation folds rotate the staurolite and garnet porphyroblasts. Biotite also defines the axial plane to some of these folds (S2). Cordierite porphyroblasts overgrow the F2 crenulation folds. Thin section is cut perpendicular to the F2 fold hinges. d) Photomicrograph taken with crossed polars of a thin section cut perpendicular to the S2 foliation and parallel to the stretching lineation. Staurolite porphyroblasts with S1 inclusion trails are oriented at a high angle to the matrix foliation that is defined by muscovite and biotite. e) Photomicrograph with crossed polars. Thin section cut perpendicular to the S2 foliation and parallel to the lineation. Staurolite porphyroblast is broken by extensional shear bands. f) Photomicrograph with crossed polars of staurolite porphyroclasts with cordierite overgrowths. Images taken by M.J. Jessup.

and argued that the deformed leucogranites provide only a maximum age for movement on the detachment. Additional U-Pb ages of monazite separates from a mylonitic leucogranite sill in Rongbuk valley further constrain mylonitic deformation at 16.0 ± 0.2 Ma (Searle et al. 2003).

Petrography

Systematic mapping and sampling along the lower ramparts of the Nuptse-Lhotse wall over three field seasons (2003-2004) provide significant insights into the upper-section of the GHS and link previous investigations focused along the top (STDS), middle (GHS), and bottom (MCTZ) of the GHS. Petrographic and microstructural observations discussed in this section provide the foundation for the quantitative thermobarometric analyses that follow (Table 4.1). We divided this section into three parts; Nuptse-Lhotse wall float samples and the Lhotse detachment transition zone.

Nuptse-Lhotse wall float samples

The ~2.5 km tall Nuptse-Lhotse wall is inaccessible to all but the most elite Himalayan alpinists (Babanov, 2004), yet the information it holds is critical to understanding both the structural and thermal evolution recorded at the top of the GHS. This description is based on ~25 float samples collected along the upper-most reaches of the three prominent glaciers (Lhotse Shar, Lhotse, and Nuptse-Lhotse) that source at the base of this wall (Fig. 4.2). By mapping all the accessible ridges and valleys and tracing float towards progressively higher structural levels, we confirmed that, although as float it occurs in abundance, no outcrop of staurolite schist exists on these lower ramparts. Pelitic float samples contain staurolite + garnet + muscovite + biotite + quartz + plagioclase + chlorite + opaques ± cordierite ± andalusite.

Aligned biotite and muscovite laths define a foliation (S1) that forms the axial planar foliation to folded compositional layering defined by graded beds (Fig 4.5a). Muscovite and less abundant biotite were crenulated (F2) and larger biotite laths grew parallel to the axial plane (S2) of the crenulation cleavage. Fine grained muscovite and less common biotite grains define (S1) and are delicately draped around the (F2) crenulation folds (Fig. 4.5b), whereas large biotite porphyroblasts are more irregularly folded. Large biotite porphyroblasts occur at high angles to the hinge of the F2 crenulation to form an axial planar (S2) foliation during crenulation development (Fig. 4.5c). Quartz-rich layers are also folded, yet the amplitude of these folds is less than within the pelitic layers. Interlayered quartz-rich layers contain predominantly fine-grained muscovite and biotite.

Garnet porphyroblasts are euhedral to subhedral and contain quartz, tourmaline, and opaque inclusions. When viewed perpendicular to the crenulation fold axis/extension lineation some garnets preserve sigmoidal inclusion trails. Euhedral garnet and staurolite intergrowths are common and suggest they formed through a reaction such as:

$$\mathrm{Grt + Chl + Ms = St + Bt + H_2O} \qquad 1)$$

Poikiloblastic staurolite porphyroblasts contain either straight or slightly warped (S1) inclusion trails defined by quartz and oxides in a matrix of muscovite, chlorite, and quartz (Figs. 4.3e, 4.5b and d). In thin sections cut perpendicular to F2 crenulations, staurolite porphyroblasts are rotated and the S1 inclusions trails are deflected along their margins (Fig. 4.5d). We interpret this relationship as evidence for staurolite growth following the development of S1 and progressing into the initial stages of crenulation development (D2). Staurolite porphyroblasts with inclusion trails are also offset by conjugate sets of extensional shear bands (Fig. 4.5e). Chlorite is common along brittle fractures cutting both staurolite and garnet porphyroblasts suggesting some component of retrogression under brittle conditions.

Cordierite, in contrast, form amorphous poikiloblastic overgrowths that encase the crenulations (F2) suggesting that deformation associated with crenulation development (D2) formed prior to the cordierite porphyroblast overgrowths (Fig. 4.5f). Cordierite records a later, higher temperature-low pressure metamorphic event (M2). Andalusite is present in a single thin section from the Nuptse-Lhotse wall. We interpret the muscovite + biotite + staurolite + cordierite ± andalusite as a disequilibrium texture that involves at least two phases of metamorphism in which an early staurolite-bearing, higher pressure assemblage is overprinted by a lower pressure cordierite-bearing assemblage during isothermal decompression as proposed by Pattison et al. (1999) through the reactions:

$$St + Ms + Chl + Qtz = Crd + Bt + H_2O \qquad 2)$$

$$Ms + St + Qtz = And + Bt + H_2O \qquad 3)$$

$$And + Bt + Qtz + H_2O = Ms + Crd \qquad 4)$$

The lack of kyanite in these rocks suggests that either the maximum pressure did not exceed ~ 6.5 kbar or the bulk rock composition was inappropriate for the production of kyanite. However, the presence of andalusite indicates that the samples are aluminous enough to produce the low pressure Al_2SiO5_5 polymorph and therefore we prefer the former interpretation; i.e., that these rocks did not exceed the ~6.5 kbar pressure necessary to produce kyanite (Spear, 1995).

Quartz grains in the Lhotse wall float samples appear to be strain-free and triple junctions between grains are common. Vein quartz contains bulging grain boundaries and isolated strain-free subgrains suggesting deformation conditions in Regime 2-3 (Hirth and Tullis, 1992) and temperatures of 500-525ºC (Stipp et al., 2002): significantly lower temperatures than at deeper structural positions. Linearly distributed fluid inclusions mark abandoned grain boundaries and provide further evidence for a mix of grain boundary migration and the onset of grain boundary rotation (Hirth and Tullis, 1992).

We propose three deformational and two metamorphic events to describe the observed microstructural evolution of these float samples from the Nuptse-Lhotse wall, all of which are preserved in a single thin section (Fig. 4.5b): 1) early fabric development (S1) created by isoclinal folding (F1) of compositional layering (S0), 2) staurolite and garnet (M1) overgrow S1, 3) D2 crenulation (growth of biotite along S2), 4) shearing along the crenulation fold axes that rotated staurolite and garnet porphyroblasts, 5) cordierite porphyroblasts (M2) mark decompression that post-date fabric development.

Lhotse Detachment Transition Zone

Another set of oriented samples was collected at the highest accessible point (~5600 m) at the base of the Nuptse/Lhotse ridge (Figs. 4.2 and 4.3). Several garnet + biotite + plagioclase + muscovite (no Al_sSiO_5) bearing samples (ET-51 to 57) were collected at this structural level. Aligned biotite and muscovite interlayered with quartz-rich domains define a pervasive (S2) foliation (Fig. 4.3d). Garnets are sub- to anhedral with internal zoning defined by inclusion-rich cores and inclusion free rims. Inclusion trails (S1) in garnet are common and often at a high angle to the pervasive matrix fabric (S2) suggesting they, like the staurolite + garnet porphyroblasts in float samples from structurally higher positions, grew prior to the main fabric development (Fig. 4.A1). We interpret this as evidence for an early stage of deformation that created an initial foliation (S1) that was overprinted by the S2 foliation and therefore the *P-T* conditions recorded

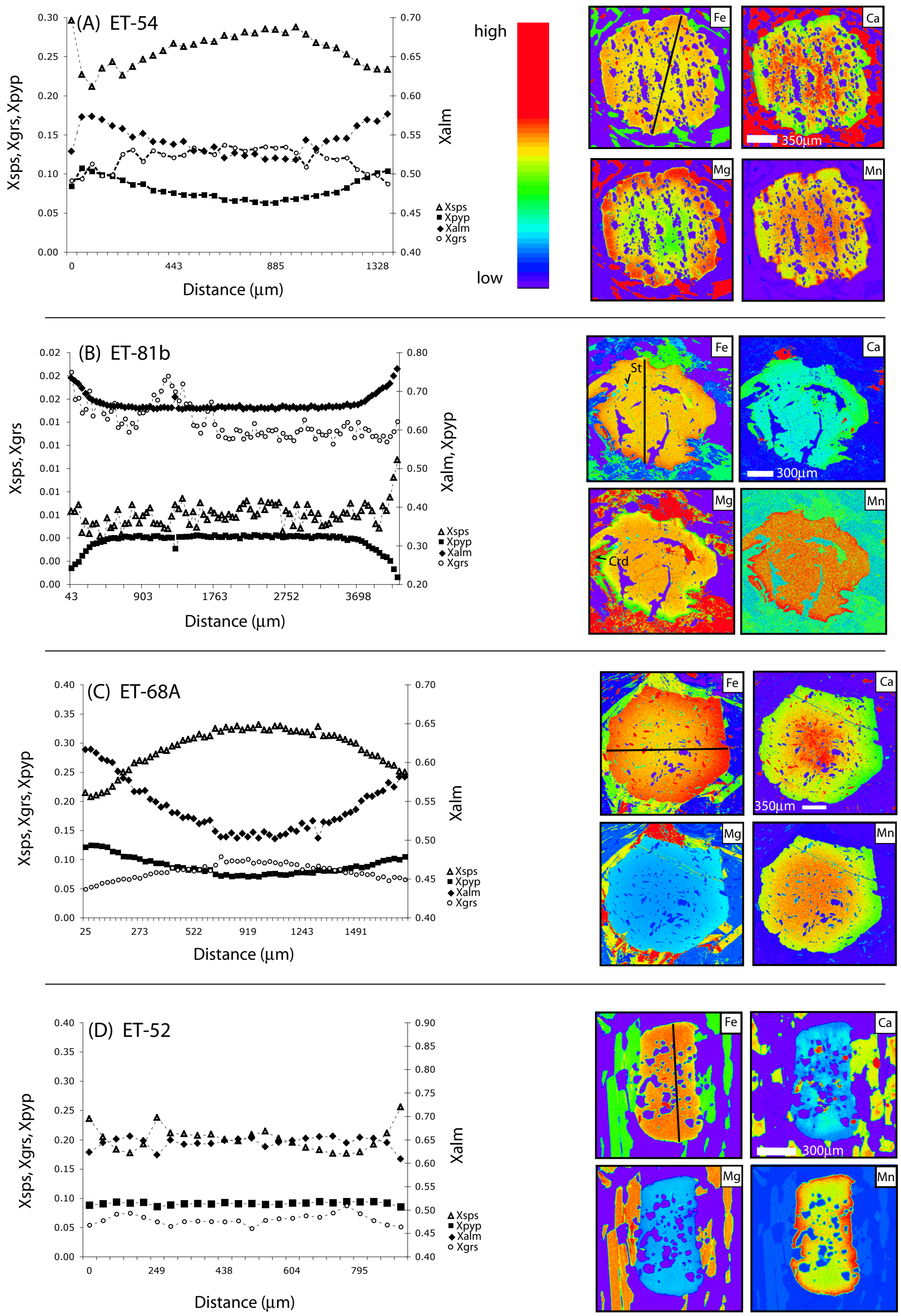

Figure 4.6. Representative garnet analyses for in situ samples from above (ET-68A; *float*), within (ET-52 & ET-54; *in situ*), and below (ET-81b) the Lhotse Detachment. Point analyses made along line transects across each porphyroclast are used in combination with compositional maps to determine which garnet analyses were used for calculating *P-T* estimates. See text for details.

by these samples pre-date S2 fabric development. All samples, except for ET-53, lack sillimanite, while ET-53 lacks garnet. Sillimanite is in the form of fibrolite tangles or intergrowths with biotite and muscovite, typical of the sillimanite-in reaction:

$$St + Chl = Bt + Sil + H_2O \qquad 5)$$

Quartz rich domains are fine-grained with near complete annealing recorded by the development of polygonal grain boundaries. Areas without polygonal grain boundaries contain many fine-grained strain free grains with slightly bulging grain boundaries. Common triple-junctions between nearly polygonal quartz grain boundaries, frequently inhibited by phylosillicates, suggests annealing has created a matrix of semi-polygonal strain-free grains by reducing the free-energy of the system through grain boundary area reduction (Passchier and Trouw, 2005). Elongate quartz and feldspar grains that are parallel to the S2 foliation are the result of muscovite and biotite pinning grain boundary migration (Fig. 4.3d).

A second variety of schist is present along the ridge between the Nuptse and Nuptse-Lhotse glaciers and contains the assemblage garnet + biotite + muscovite + quartz + plagioclase + tourmaline (Figs. 4.2 and 4.3). Aligned tourmaline and muscovite and biotite define a pervasive foliation. Microboudinage of tourmaline confirms that extension occurred parallel to the strong mineral lineation. Garnets from this location (ET-57) are inclusion-free subhedral porphyroblasts with muscovite and biotite tails (Fig. 4.A1c). Patches of amoeboidal grain boundaries in quartz-rich domains with strain-free subgrain formation suggest deformation temperatures characteristic of lower Regime 3 recrystallization conditions (Hirth and Tullis, 1992), whereas the majority of the thin section is dominated by annealed grain boundaries. Phyllosilicates, where present, pin the migration of quartz grains through the lattice resulting in elongate polygonal grain boundaries (Fig. 4.3d).

Table 4.2. THERMOCALC results

Sample	GB(P)	GB(T)	Grt-Bt (B)	GMPB (Fe)	GMPB (Mg)	assemblage	Activities (4 kbar, 600C)	fluid (XH_20)	T	sd(T) C	P (kbar)	sd(P) kbar	cor	fit	# of rxn	removed
ET-51	4	657	546			grt-bt										
	5	660	547													
	6	663	547													
	7	667	548													
	8	669	549													
ET-52	4	641	565	4.9		grt-bt-grt-	py 0.00148, alm 0.230, mu 0.710,	1	751	45	7.7	1.3	0.738	0.67	6	
	5	644	565			ms-plag	gr .00088, cel 0.00510, fcel	0.8	720	43	7.4	1.2	0.735	0.59	6	
	6	646	566				0.00360, pa 0.175, phl 0.0370, ann	0.6	682	40	7	1.2	0.731	0.48	6	
	7	649	567				0.0500, east 0.0390, ab 0.660, an	*0.5*	*660*	*38*	*6.7*	*1.1*	*0.728*	*0.42*	6	
	8	652	567				0.51	*0.45*	*648*	*37*	*6.6*	*1.1*	*0.726*	*0.38*	6	
								0.4	634	36	6.5	1.1	0.723	0.35	6	
								0.3	603	34	6.2	1	0.718	0.29	6	
ET-54	4	647	557			grt-bt										
	5	650	558													
	6	653	558													
	7	656	560													
	8	659	560													
ET-57	4	678	565	3.5	4.5	grt-bt-ms-	py 0.000740, grs .000088, alm	1	691	39	5.1	1.2	0.72	0.23	6	sps
	5	681	565			plag	0.210, sps .020, mu 0.770, cel	*0.95*	*685*	*39*	*5.1*	*1.2*	*0.719*	*0.21*	6	sps
	6	684	566				0.00750, fcel 0.00940, pa 0.240,	0.9	678	38	5	1.2	0.719	0.18	6	sps
	7	686	567				phl 0.0206, ann 0.0660, east	0.85	671	38	5	1.2	0.718	0.16	6	sps
	8	690	568				0.0300, ab 0.730, an .73	0.8	663	37	4.9	1.1	0.717	0.13	6	sps
ET-68A	4	632	559	3.8	4.9	grt-bt-plg-	py 0.002800, alm 0.220, grs	1	671	37	4.8	0.9	0.884	0.9	9	
	5	635	560			ms-st-crd	.00023, spss 0.00232, mu 0.720,	0.75	649	35	4.5	0.8	0.884	0.86	9	
	6	638	560				cel 0.00710, fcel 0.00490, pa	0.7	641	35	4.4	0.8	0.884	0.84	9	
	7	641	561				0.280, phl 0.0670, ann 0.0360, ab	*0.65*	*633*	*34*	*4.3*	*0.8*	*0.884*	*0.83*	9	
	8	644	562				0.670, crd 0.520, fcrd 0.0790	0.6	624	33	4.2	0.8	0.883	0.82	9	
ET-70E	4	645	597	4.3		grt-bt-st-crd-	py 0.00158, gr 0.00018, alm 0.43,	1	743	42	7	1.3	0.746	0.9	4	
	5	648	598			ms-plg	spss .00054, mu 0.74, pa 0.29, phl	0.8	712	40	6.7	1.3	0.744	0.79	4	
	6	651	599				0.0191, ann 0.040, east 0.041, an	0.6	675	37	6.4	1.2	0.74	0.65	4	
	7	654	600				0.46, ab 0.69	*0.5*	*653*	*35*	*6.2*	*1.2*	*0.737*	*0.56*	4	
	8	658	600					0.45	640	34	6.1	1.2	0.735	0.52	4	
								0.4	627	33	5.9	1.1	0.733	0.47	4	
ET-81b	4	783	741													
	5	786	742													
	6	790	742													
	7	794	743													
	8	798	744													
L-8	4	602	556				py 0.00142, gr 0.0019, alm 0.15,	1	650	34	6.6	1.1	0.77	0.59	6	
	5	605	557				spss 0.0087, mu 0.68, cel 0.0144,	0.9	638	33	6.5	1	0.768	0.55	6	
	6	608	558				fcel 0.0082, pa 0.30, phl 0.065, ann	0.8	625	32	6.4	1	0.767	0.5	6	
	7	610	558				0.040, east 0.057,	*0.7*	*610*	*31*	*6.2*	*1*	*0.765*	*0.46*	6	
	8	613	559					0.6	595	30	6.1	1	0.762	0.42	6	
								0.5	577	29	5.9	1	0.76	0.38	6	
L-13	4	584	552													
	5	587	552													
	6	590	553													
	7	593	554													
	8	595	554													

Core of the Greater Himalayan Sequence

Samples collected along the lower ridges leading up to the base of the Nuptse-Lhotse wall, and those structurally below, record a set of metamorphic reactions and microstructures that differ from those collected at the base of the wall (transition zone) and from float (Figs 4.2 and 4.3). Representative samples from this structural level have been described in detail by previous investigations (Pognante & Benna, 1996; Simpson, 2000; Searle et al. 2003) and are only reviewed briefly here. Polygonal quartz and feldspar intergrowths are common. Grain boundaries between quartz and feldspar are cuspate-lobate suggesting deformation at high-grade conditions (Passchier and Trouw, 2005). Aligned biotite defines the (S2) foliation. Fibrolitic sillimanite is common as either pods or fibrous zones interlayered with the biotite. When present, garnet is often sub-to-anhedral with quartz and cordierite embayments (Fig. 4.6b). Muscovite becomes progressively less abundant towards deeper structural positions within the slab. Sillimanite pods are common on the ridge just above Dingboche village. Here, they are folded by F2 crenulation folds and are elongate parallel to the fold axes. Sample ET-81b contains garnet + biotite + anthophyllite + graphite + cordierite + rutile + apatite + staurolite + quartz + plagioclase (Renjo La) and although it was collected ~20 km east of the Everest-Lhotse massif, it is representative of the GHS. We interpret the presence of cordierite + anthophyllite as evidence for premetamorphic alteration by hydrothermal fluids that removed Ca (Spear, 1995). Staurolite (M1) inclusions define an inclusion-rich concentric ring within the garnet (Fig. 4.6b). Matrix chlorite displays purple and gray birefringence and forms embayments into garnets. Graphite is interlayered with biotite. Sericitic alteration of feldspar is common. Quartz puddles in feldspar and lobate grain boundaries between quartz and feldspar suggests high deformation temperatures (Passchier and Trouw, 2005). Undulose extinction is present in quartz grains while irregular bulging grain boundaries suggest Regime 3 recrystallization conditions (Hirth and Tullis, 1992). The presence of only a few polygonal grain boundary junctions

Table 4.3. Representative garnet analyses.

Sample	ET-51		ET-52			ET-54			ET-57			ET-68A			
	rim	near rim	core	rim	near rim	core	rim	near rim	core	rim	near rim	core	rim	near rim	core
SiO2	36.11	37.12	37.53	37.64	38.27	37.93	38.12	38.41	38.14	38.02	37.97	37.68	38.27	38.39	37.28
TiO2	0.01	0.00	0.14	0.00	0.05	0.00	0.02	0.05	0.11	0.07	0.02	0.00	0.00	0.02	0.05
Al2O3	18.51	21.09	20.87	21.42	21.66	21.33	21.42	21.50	21.10	22.50	21.92	21.83	22.14	22.27	21.78
FeO	23.20	29.33	26.81	26.72	28.55	28.37	23.19	25.63	23.37	27.38	27.92	25.26	28.49	28.20	22.96
MnO	13.35	10.04	9.56	11.07	7.72	8.65	12.83	9.33	12.69	12.02	12.45	13.60	9.77	9.34	14.85
MgO	0.78	1.53	1.28	2.09	2.35	2.28	2.07	2.59	1.58	2.00	2.04	1.54	3.14	3.20	1.94
CaO	0.69	1.65	4.16	1.75	3.02	2.05	3.13	3.93	4.73	1.33	1.43	2.90	1.77	1.87	3.39
Total	92.65	100.75	100.34	100.70	101.63	100.61	100.78	101.44	101.73	103.32	103.76	102.82	103.58	103.28	102.26
Cations per 12 oxygens															
Si	3.15	3.00	3.02	3.02	3.02	3.03	3.03	3.03	3.02	2.97	2.97	2.97	2.97	2.98	2.95
Ti	0.00	0.00	0.01	0.00	0.00	0.00	0.00	0.00	0.01	0.00	0.00	0.00	0.00	0.00	0.00
Al	1.90	2.01	1.98	2.02	2.01	2.01	2.01	2.00	1.97	2.07	2.02	2.03	2.03	2.04	2.03
Fe	1.69	1.98	1.81	1.79	1.88	1.90	1.54	1.69	1.55	1.79	1.83	1.67	1.85	1.83	1.52
Mn	0.99	0.69	0.65	0.75	0.52	0.59	0.86	0.62	0.85	0.80	0.83	0.91	0.64	0.61	1.00
Mg	0.10	0.18	0.15	0.25	0.28	0.27	0.25	0.30	0.19	0.23	0.24	0.18	0.36	0.37	0.23
Ca	0.06	0.14	0.36	0.15	0.26	0.18	0.27	0.33	0.40	0.11	0.12	0.25	0.15	0.16	0.29
Total	7.90	8.00	7.98	7.98	7.97	7.97	7.96	7.97	7.99	7.98	8.01	8.01	8.01	8.00	8.03
X_{alm}	0.59	0.66	0.61	0.61	0.64	0.65	0.53	0.57	0.52	0.61	0.61	0.56	0.62	0.62	0.50
X_{pyr}	0.04	0.06	0.05	0.08	0.09	0.09	0.08	0.10	0.06	0.08	0.08	0.06	0.12	0.12	0.08
X_{sps}	0.35	0.23	0.22	0.26	0.18	0.20	0.30	0.21	0.28	0.27	0.27	0.30	0.21	0.21	0.33
X_{grs}	0.02	0.05	0.12	0.05	0.09	0.06	0.09	0.11	0.13	0.04	0.04	0.08	0.05	0.05	0.09
Fe/(Fe+Mg)	0.94	0.92	0.92	0.88	0.87	0.87	0.86	0.85	0.89	0.88	0.88	0.90	0.84	0.83	0.87

Table 4.3. Representative garnet analyses.

Sample	ET-70E		ET-81b			L-8			L-13	
	rim	core	rim	near rim	core	rim	near rim	core	rim	core
SiO2	38.11	37.70	38.62	39.47	39.39	38.12	37.81	38.03	37.60	38.00
TiO2	0.09	0.09	0.00	0.00	0.21	0.04	0.07	0.04	0.00	0.06
Al2O3	21.58	21.88	22.02	22.46	22.53	21.42	20.44	21.01	21.06	21.45
FeO	35.31	32.43	34.77	30.71	30.52	26.26	24.34	22.42	31.55	34.70
MnO	3.76	6.82	0.49	0.26	0.32	10.51	9.32	13.05	6.25	3.48
MgO	2.56	1.72	5.63	8.46	8.58	2.28	2.28	1.70	1.76	2.18
CaO	1.77	2.51	0.50	0.47	0.46	2.20	3.94	3.64	2.19	1.84
Total	103.17	103.16	102.03	101.82	102.00	100.83	98.20	99.88	100.40	101.71
Cations per 12 oxygens										
Si	2.99	2.97	3.00	3.00	2.99	3.03	3.07	3.05	3.03	3.02
Ti	0.01	0.01	0.00	0.00	0.01	0.00	0.00	0.00	0.00	0.00
Al	2.00	2.03	2.01	2.01	2.02	2.01	1.96	1.99	2.00	2.01
Fe	2.32	2.14	2.26	1.95	1.94	1.75	1.66	1.50	2.12	2.30
Mn	0.25	0.45	0.03	0.02	0.02	0.71	0.64	0.89	0.43	0.23
Mg	0.30	0.20	0.65	0.96	0.97	0.27	0.26	0.20	0.21	0.26
Ca	0.15	0.21	0.04	0.04	0.04	0.19	0.34	0.31	0.19	0.16
Total	8.01	8.01	7.99	7.99	7.99	7.96	7.94	7.95	7.97	7.98
X_{alm}	0.77	0.71	0.76	0.66	0.65	0.60	0.57	0.52	0.72	0.78
X_{pyr}	0.10	0.07	0.22	0.32	0.33	0.09	0.09	0.07	0.07	0.09
X_{sps}	0.08	0.15	0.01	0.01	0.01	0.24	0.22	0.31	0.14	0.08
X_{grs}	0.05	0.07	0.01	0.01	0.01	0.06	0.12	0.11	0.06	0.05
Fe/(Fe+Mg)	0.89	0.91	0.78	0.67	0.67	0.87	0.86	0.88	0.91	0.90

suggests little grain boundary area reduction occurred. We interpret staurolite inclusions in the garnets as a record of (M1) while the remaining phases in the thin section represent a later (M2) high temperature-low pressure event.

Methods

Ten samples were selected for detailed thermobarometric analyses to further constrain the thermal evolution of the upper section of the GHS exposed in the Everest-Lhotse-Nuptse massif. Electron microprobe analyses were conducted at the Department of Geosciences, Virginia Tech using a beam current of 20nA and an acceleration voltage of 15 kV. Our method involved three main stages; 1) backscatter electron (BSE) images were taken of phases selected for probe analyses, 2) compositional maps of Fe, Mg, Ca, and Mg were made for select garnet porphyroblasts, 3) point analyses and/or transects were conducted across garnet, biotite, muscovite, plagioclase, cordierite, and staurolite. Compositional maps of garnets from representative samples were created to characterize

Table 4.4. Representative cordierite analyses.

Sample	ET-81b	ET-68A
SiO_2	49.45	48.31
TiO_2	0.00	0.01
Al_2O_3	32.74	34.10
FeO	5.36	6.70
MnO	0.03	0.81
MgO	8.82	8.95
CaO	0.05	0.00
NaO	0.24	0.46
KO	0.00	0.00
Total	96.68	99.34

internal zoning and determine which areas are appropriate for thermobarometric calculations.

To quantify pressure and temperature estimates we combined geothermobarometry with the computer program THERMOCALC (version 3.25; employing the thermodynamic data set of Holland and Powell, 1998) and followed the methods previously employed in the Everest area by Searle et al. (2003). Activities of phases were calculated using the program AX. Since THERMOCALC is unable to calculate the Fe-Mg exchange reaction, to estimate temperature, we use the garnet-biotite exchange thermometer of Holdaway (2000) in combination with THERMOCALC for average *P-T* calculations. An initial temperature estimate was made using the garnet-biotite exchange reaction at a range in *P* (Table 4.2). THERMOCALC was then run in average *P-T* mode to calculate *P-T* estimates. The XCO_2 content was changed in increments until the range in *T* overlapped the temperature estimates from the garnet-biotite thermometer. Through this method we were able to choose the most appropriate THERMOCALC results as well as determine the XCO_2 content.

Many thermobarometric investigations in the Himalaya have used the rim composition of phases (e.g., Hodges et al. 1988a; Hubbard, 1989; Macfarlane, 1995; Vannay and Hodges, 1996) resulting in *P-T* profiles that apparently record isothermal

Table 4.5. Representative biotite & muscovite analyses.

Sample	ET-51 bt ave. matrix	ET-52 bt ave. matrix	ET-52 ms ave. matrix	ET-54 bt ave. matrix	ET-57 bt ave. matrix	ET-57 ms ave. matrix	ET-68A bt ave matrix	ET-68A ms ave matrix	ET-70E bt ave. matrix	ET-70E ms ave. matrix	ET-81b bt ave. matrix	L-8 ave. bt	L-8 ms ave. matrix	L-13 bt ave. matrix
SiO_2	34.74	35.78	45.59	36.49	34.14	45.34	36.77	45.33	33.79	45.20	37.30	36.34	46.15	35.83
TiO_2	2.87	2.08	0.81	2.32	2.94	0.87	1.56	0.44	1.79	0.39	3.21	1.50	0.40	1.45
Al_2O_3	19.39	19.78	34.80	18.34	20.35	36.40	19.82	35.49	19.70	35.72	16.53	19.47	35.03	19.95
FeO	23.50	19.52	2.90	18.55	21.52	1.48	17.76	2.67	23.00	2.64	17.05	17.97	2.92	21.62
MnO	0.49	0.43	0.01	0.40	0.65	0.02	0.27	0.03	0.16	0.01	0.02	0.31	0.01	0.11
MgO	5.91	9.02	0.69	10.85	7.29	0.66	11.66	0.64	8.34	0.58	12.94	11.30	0.86	8.71
CaO	0.00	0.04	0.04	0.01	0.02	0.03	0.00	0.00	0.00	0.00	0.02	0.01	0.00	0.00
Na_2O	0.18	0.29	0.66	0.19	0.13	0.62	0.34	1.00	0.24	1.05	0.33	0.26	1.01	0.34
K_2O	8.31	8.37	9.53	8.30	9.52	10.26	9.13	9.74	9.10	9.48	8.21	9.36	9.83	9.56
F	0.19	0.20	0.05	0.23	0.26	0.08	0.28	0.06	0.29	0.07	0.21	0.36	0.06	0.35
Total	95.58	95.52	95.08	95.68	96.83	95.77	97.61	95.41	96.41	95.14	95.81	96.87	96.28	97.94
Cations per 11 oxygens														
Si	2.69	2.71	3.06	2.75	2.61	3.01	2.72	3.03	2.61	3.03	2.79	2.72	3.06	2.70
Ti	0.17	0.12	0.04	0.13	0.17	0.04	0.09	0.02	0.10	0.02	0.18	0.08	0.02	0.08
Al	1.77	1.77	2.75	1.63	1.84	2.85	1.73	2.80	1.80	2.82	1.45	1.72	2.74	1.77
Fe	1.52	1.24	0.16	1.17	1.38	0.08	1.10	0.15	1.49	0.15	1.06	1.13	0.16	1.36
Mn	0.03	0.03	0.00	0.03	0.04	0.00	0.02	0.00	0.01	0.00	0.00	0.02	0.00	0.01
Mg	0.68	1.02	0.07	1.22	0.83	0.07	1.28	0.06	0.96	0.06	1.44	1.26	0.08	0.98
Ca	0.00	0.00	0.00	0.00	0.00	0.00	0.00	0.00	0.00	0.00	0.00	0.00	0.00	0.00
Na	0.03	0.04	0.09	0.03	0.02	0.08	0.05	0.13	0.04	0.14	0.05	0.04	0.13	0.05
K	0.82	0.81	0.82	0.80	0.93	0.87	0.86	0.83	0.90	0.81	0.78	0.89	0.83	0.92
Total	7.72	7.75	6.99	7.76	7.82	7.01	7.84	7.03	7.91	7.02	7.76	7.87	7.04	7.88
Fe/(Fe+Mg)	0.68	0.54			0.61		0.46		0.60		0.42	0.47		0.58

Table 4.6. Representative plagioclase analyses.

Sample	ET-52	ET-70E		ET-68A		ET-57	L-8
	rim	core	ave. rim	core	ave	rim	rim
SiO_2	60.17	59.72	60.68	60.29	60.00	61.64	58.92
Al_2O_3	26.22	26.19	25.57	25.81	26.46	25.11	27.05
CaO	7.01	7.14	5.83	6.51	7.03	5.54	7.70
FeO	0.10	0.05	0.08	0.00	0.02	0.26	0.03
Na_2O	7.63	7.54	7.84	7.83	7.72	8.46	7.11
K_2O	0.14	0.14	0.64	0.13	0.08	0.21	0.08
Total	101.27	100.78	100.65	100.58	101.32	101.23	100.88
Cations per 8 oxygens							
Si	2.65	2.64	2.68	2.67	2.64	2.71	2.61
Al	1.36	1.37	1.33	1.35	1.37	1.30	1.41
Fe	0.00	0.00	0.00	0.00	0.00	0.01	0.00
Ca	0.33	0.34	0.28	0.31	0.33	0.26	0.36
Na	0.65	0.65	0.67	0.67	0.66	0.72	0.61
K	0.01	0.01	0.04	0.01	0.00	0.01	0.00
Total	5.00	5.01	5.00	5.00	5.01	5.01	5.00
X_{An}	0.33	0.34	0.28	0.31	0.33	0.26	0.37

conditions due to re-equilibration during exhumation (Stephenson et al., 2000; Kohn et al., 2001). It has also been documented in a range of tectonic settings that cation exchange thermometers record the closure temperature of the reaction rather than the peak temperature reached by the sample (Vannay and Grasemann, 1998; Larson and Sharp, 2003, 2006). In this study, garnet compositions with the lowest Fe/Fe + Mg and Mn (i.e., near rim) were used as a close approximation of the garnet composition prior to resorption and diffusion effects during a high-grade metamorphic overprint. Alternatively, rim compositions were used in garnets that preserve growth zoning (e.g., L-13, ET-70E, ET-68A; Fig. 4.6; Table 4.3). Transects across cordierite (Table 4.4) and staurolite showed a minimal amount of chemical variability across porphyroblasts.

Matrix biotite compositions were analyzed as line transects across biotite clusters. To examine the relationship between Al and Ti, Ti cations were plotted vs. octahedral Al cations. Chemical zoning within biotite grains, from core to rim, is homogeneous in all samples. Outlying analyses that were identified using the previous plots were rejected from the final calculations. If the range in Ti cations is <0.05 we averaged the analyses

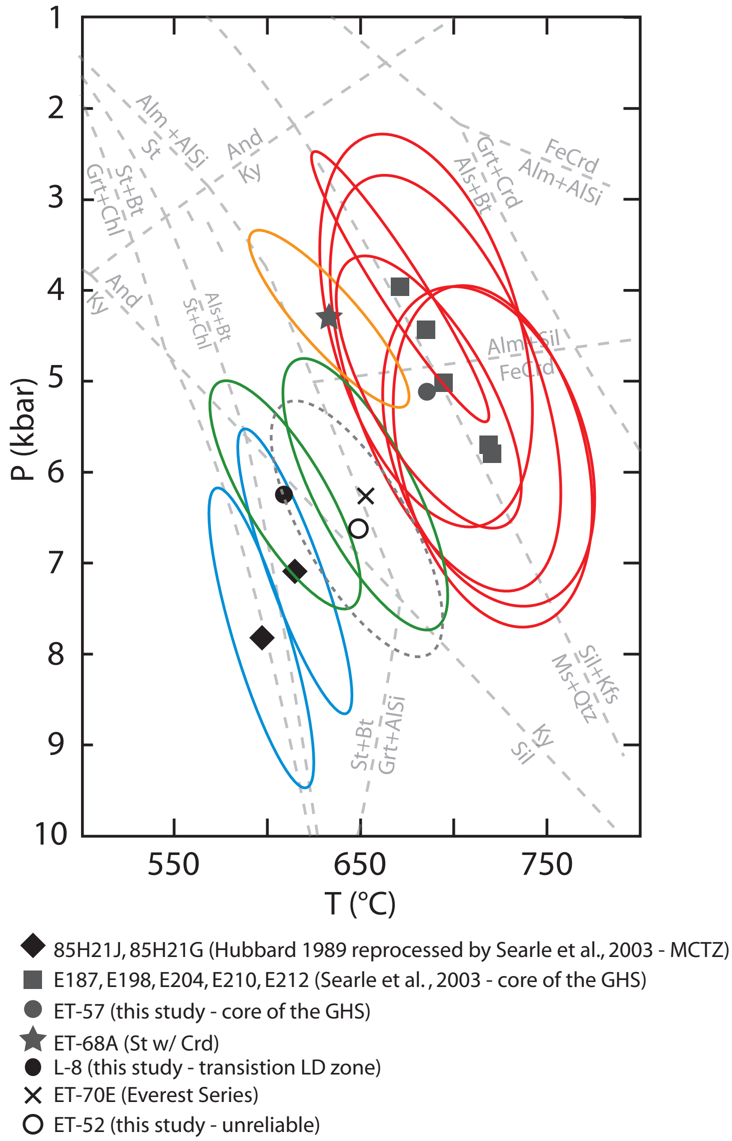

Figure 4.7. THERMOCALC results for samples from this investigation plotted with representative samples of previous investigations from the Everest transect (Searle et al., 2003). Samples 85H21J and 85H21G are from Hubbard (1989) and recalculated by Searle et al. (2003) and represent high-*P* moderate-*T* conditions recorded by garnets with growth zoning within the MCTZ (black diamonds; blue error ellipses). Samples E187, E189, E204, E210, and E212 are from Searle et al. (2003) and represent the high-T low-P conditions recorded by garnets with diffusion zoning that are common to the center of the GHS (dark gray squares; red error ellipses). Sample ET-70E contains garnet that preserves growth zoning and record moderate pressure conditions (black cross; green error ellipse). Sample L-8 represents the transition zone in the LD (black circle; green error ellipse). Sample ET-68A represents high temperature, low pressure conditions recorded by staurolite schist with cordierite overgrowths (gray star; orange error ellipse). Sample ET-52 represents an unreliable *P-T* estimate; see text for details (open circle; dashed error ellipse). 2-σ error ellipses calculated using the parameters from THERMOCALC (Table 4.2).

for thermobarometric calculations. Unless otherwise stated, an average of the matrix biotite analyses was used for geothermometric calculations (Table 4.5).

Muscovite analyses were conducted as line transects across several sheaths in the matrix of the sample. In samples where chlorite and muscovite were interlayered, the purest sections of muscovite were located using the optical microscope and subsequent probe analyses were evaluated for the presence of K; if chlorite is present, K should be low or absent. Plots of Si cations vs. Fe, Mg, Ti, and Na cations were used to explore the compositional variability within one transect or between transects. As with biotite, muscovite grains were analyzed at variable distances from garnet and showed minimal internal zoning or variability with different distances from the garnet and therefore an average of muscovite analyses was used (Table 4.5).

Plagioclase analyses were made as either point analyses or transects across individual grains. Plotting Ca/(Ca + Na + K) vs. Al-1/(Al + Si-3) highlighted trends in composition. Internal zoning is preserved within all plagioclase grains as predicted by the slow diffusion of Ca through the plagioclase grains. For most samples the Ca/(Ca + Na + K) vs. Al-1/(Al + Si -3) plots distinguish rim and core compositions. As a best estimate of pressure, at the peak temperatures, we chose the rim composition of plagioclase (Table 4.6).

Garnet Zoning

Characterizing and interpreting garnet zoning provides critical information about the thermal evolution of a sample and helps to determine which garnet compositions should be used for thermobarometric calculations (Tracy et al., 1977; Kohn and Spear, 2001). Garnets from the transition zone between the high-grade core of the GHS and Everest Series schists display a complete range from prograde growth zoning preserved at the upper-most structural positions (Fig. 4.6c) to diffusion zoning typical of the core of the GHS (Fig. 4.6b). Compositional maps of Fe, Ca, Mn, and Mg for four representative

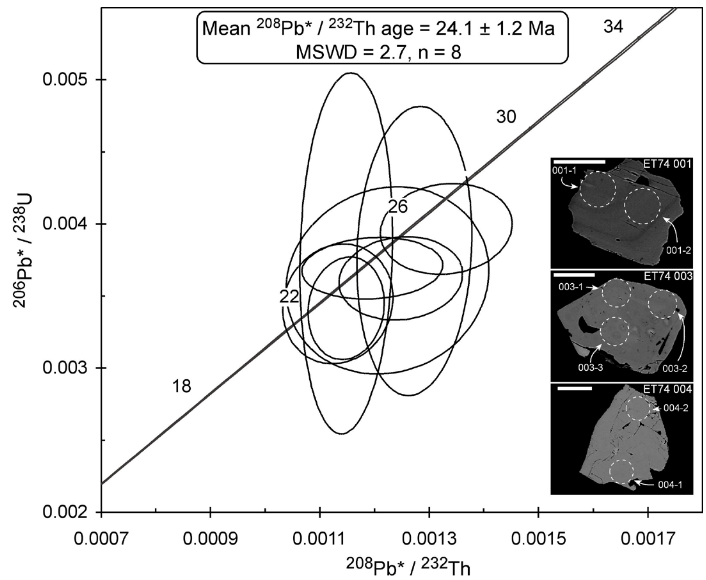

Figure 4.8. Common lead-corrected $^{208}Pb/^{232}Th$ - $^{206}Pb/^{238}U$ concordia plot (data plotted at the 2-σ confidence level) for monazites analysed from leucogranite sample ET-74. Inset shows backscatter electron (BSE), images of selected grains displaying relatively homogeneous chemical petrography. Full data set in Table 4.7.

Table 4.7. Isotopic results

			Uncorrected Isotopic Ratios				Uncorrected Ages			
Name	Th (ppm)[a]	Th/U[b]	$^{206}Pb/^{238}U$	2σ%	$^{208}Pb/^{232}Th$	2σ%	$^{206}Pb/^{238}U$	2σ (Ma)	$^{208}Pb/^{232}Th$	2σ (Ma)
Sample ET74 monazite										
001-1	38880	16.8	0.0035	5.624	0.0012	2.800	22.2	1.3	24.5	0.7
001-2	28801	1.9	0.0035	3.989	0.0012	3.176	22.8	0.9	23.5	0.7
005-1	49111	24.7	0.0036	5.699	0.0012	2.497	23.4	1.3	24.4	0.6
003-1	63711	7.3	0.0036	3.866	0.0012	2.266	23.0	0.9	25.0	0.6
003-2	39182	6.4	0.0033	4.699	0.0012	3.119	21.5	1.0	24.7	0.8
003-3	28351	6.5	0.0035	4.177	0.0012	3.361	22.5	0.9	24.4	0.8
004-1	43180	4.0	0.0035	3.695	0.0012	2.652	22.4	0.8	24.3	0.6
004-2	31778	3.2	0.0038	4.242	0.0013	2.686	24.5	1.0	26.0	0.7

Common-Pb Corrected Isotopic Ratios[d]					Common-Pb corrected Ages			
f206%[c]	$^{206}Pb/^{238}U$	2σ%	$^{208}Pb/^{232}Th$	2σ%	$^{206}Pb/^{238}U$	2σ (Ma)	$^{208}Pb/^{232}Th$	2σ (Ma)
5.809194	0.0038	21.475	0.0013	6.752	24.5	5.3	25.7	1.7
2.598509	0.0037	4.714	0.0012	8.808	23.8	1.1	24.2	2.1
3.281568	0.0038	26.940	0.0011	6.032	24.4	6.6	23.2	1.4
13.29063	0.0034	8.495	0.0011	4.963	22.0	1.9	23.2	1.2
5.876067	0.0034	9.839	0.0011	7.265	22.2	2.2	22.9	1.7
0.909395	0.0036	14.689	0.0012	12.381	23.2	3.4	24.7	3.1
-3.31681	0.0036	6.511	0.0012	7.398	23.3	1.5	25.2	1.9
-1.8036	0.0040	6.478	0.0013	7.394	25.5	1.7	26.9	2.0

garnets from the upper-section of the GHS (Fig. 4.6) are used to demonstrate this transition. Relative concentrations of pixel intensity acquired by the EMPA when making compositional maps were enhanced using NIH Image© and the *Rainbow Spectrum* (warm colors denote high concentrations and cool colors denote low concentration). A complete set of the remaining compositional maps is provided in Fig. 4.A1.

Compositional maps and point transects characterize internal zoning of a garnet porphyroblast from a representative sample (ET-68A) of Gt + St ± Crd schist (Fig. 4.6C). Fe concentration decreases from rim (X_{alm}= 0.62) to core (X_{alm} = 0.50), Ca defines an enriched core (X_{grs}=0.09) and relative to depleted rims (X_{grs}=0.05), Mg is relatively homogeneous, and Mn shows steady decrease from X_{sps}=0.33 in the core to X_{sps}=0.21 at the rim (Table 4.3). This “bell shaped” chemical zoning is characteristic of garnets from the staurolite-kyanite zone and has been interpreted as growth zoning that has remained unaltered by subsequent diffusion (Tracy, 1976; Yardley, 1977). Two edges of the garnet are euhedral and in contact with muscovite (blue) whereas the four remaining sides are subhedral and in contact with matrix biotite (yellow) and chlorite (green). The growth zoning is also truncated along these four subhedral sides suggesting that this section of the rim of the garnet has been removed by a retrograde reaction (Table 4.3).

Samples ET-54 and ET-52 (Fig. 4.6a and d) are representative of samples collected *in situ* at the base of the Nuptse-Lhotse wall (see Figure 4.A1 for compositional maps of ET-51, ET-57). Garnets contain straight quartz-rich inclusion trails (S1) that are at a high angle to the matrix fabric (S2) (Fig. 4.6a). Although these two samples are from similar structural positions, internal zoning of representative garnets differs. Garnet rim of ET-54 have X_{alm} = 0.53 and X_{pyr} = 0.08 while cores are enriched in X_{sps} = 0.28 and X_{grs} = 0.13 (Fig. 4.6a). We interpret that the core and near rim composition for this garnet preserve growth zoning (M1), whereas the Mn-rich rim is a resorption rind attributed to diffusion during a second metamorphic event (M2). Elongate poikilioblastic garnets are common in ET-52. The elongate porphyroblasts probably formed as more euhedral grains that were subsequently shaped by later events as is common within the MCTZ (Hubbard 1989; Jessup et al., 2006). A slight decrease in X_{sps} from core (0.20) to near rim (0.18) is observed, at which point it abruptly increases to the rim composition (0.26). X_{alm} decreases from core (0.65) to rim (0.61; Fig. 4.6d). The compositional map for Ca highlights patchy internal zoning suggesting a complex diffusion of Ca through the garnet.

Garnets from sample ET-81b typify those from the high-grade core of the GHS. Compositional maps of a representative garnet show that internal zoning is nearly homogeneous whereas the rims are marked by an abrupt increase in Mn and a slightly more gradational increase in X_{alm}, X_{grs} and decrease in X_{pry} (Fig. 4.6d). As with samples ET-52 and 54, we attribute the Mn-rich rind to diffusion during a second higher temperature thermal event when the prograde zoning was partially homogenized. Mg depletion is particularly pronounced where garnet is in contact with matrix chlorite and cordierite (red phases in Mg compositional map). Concentric inclusions of staurolite (light blue on Fe and Mg maps) are interpreted as a relict of the early (M1) event that has been overprinted by the M2 assemblages for this sample (garnet + biotite+ anthophyllite + graphite + cordierite + rutile + apatite + staurolite + quartz + plagioclase).

Details of geothermobarometric and THERMOCALC results from this investigation are presented in Tables 4.1 and 4.2. To update inconsistencies between the published results in Table 4.1 of Searle et al. (2003) and the original data from Simpson (2002) as well as to present all the available *P-T* data for the Everest region, corrected results of Searle et al. (2003) are also included in Tables 4.1 and 4.2. The only exceptions to our synthesis of data are samples from Searle et al (2003) where the overlap between the range in temperatures generated by THERMOCALC and those acquired through geothermometry are > 40°C in which case they were excluded (samples E127, E134, E196 and E214). Representative THERMOCALC results from this investigation (ET-52, ET-68A, ET-70E, L-8), the MCTZ (85H21J and 85H21G) and core of the GHS (E210, E212, E198, E204 and E187) are plotted in Figure 4.7.

Geochronology of the Nuptse Granite

In order to constrain the minimum timing of metamorphism and fabric development in the host metamorphic rocks, a sample of the Nuptse granite was collected from a klippen of the main body exposed on the summit of Chukhung (5857 m; Figs. 4.2 and 4.3). At ~2 km tall and 4 km wide, the Nuptse granite is one of the largest leucogranite bodies in the upper section of the Khumbu region (Lombardo et al., 1993;

Searle, 1999b; Searle et al., 2003). It is located along the contact between the anatectic core of the GHS and the overlying Everest Series schists and calc-silicates. The Nuptse granite is interpreted to represent the culmination of a network of sills and dikes that fed magma from the north (Weinberg and Searle, 1999; Searle, 1999b; Searle et al., 2003). Sample ET-74 is a medium-grained K-feldspar, quartz, plagioclase, biotite, muscovite, tourmaline leucogranite with accessory zircon and rare monazite. Microstructures preserve the original igneous texture and lack evidence for a solid-state fabric or high temperature recrystallization. Because at least the margin of the Nuptse granite lacks solid-state fabric development that is common in the host-rocks, we interpret it as syn-to post-kinematic with respect to the fabric development outlined above.

Monazites were extracted from sample ET-74 using standard heavy liquid and isodynamic separation techniques. The highest quality crack and inclusion free grains were hand picked under ethanol, mounted in a 1-inch diameter epoxy resin disc and doubly polished to reveal equatorial cross sections. Backscatter (BSE), U, Y and Th imaging revealed that most grains have a relatively simple chemical petrography (inset of Fig. 4.7). Some grains display oscillatory zoning while a minority contain lobate-cuspate zoning where portions of the grain have been recrystallized. Other grains examined also contain micro-inclusions (~1-5 μm) of zircon and Th-silicate.

A total of eight U-Th-Pb isotopic analyses on four monazite grains were obtained from sample ET-74 (Table 4.7, Fig. 4.8) using a Laser Ablation- Multi-Collector-Inductively Coupled Plasma Ionization Mass Spectrometery (LA-MC-ICPMS) pseudo-simultaneous acquisition method modified from Horstwood et al. (2003). All eight analyses cluster on a common lead-corrected ^{208}*Pb/^{232}Th - ^{206}*Pb/^{238}U concordia plot (Fig. 4.8). Some analyses are slightly reversely discordant which we interpret as the result of incorporation of excess ^{230}Th during crystallization leading to an excess of ^{206}Pb (Schärer, 1984; Parrish, 1990). With this in mind we take the ^{208}Pb*/^{232}Th dates as the most reliable estimates of the ages of these grains. All eight analyses give a weighted

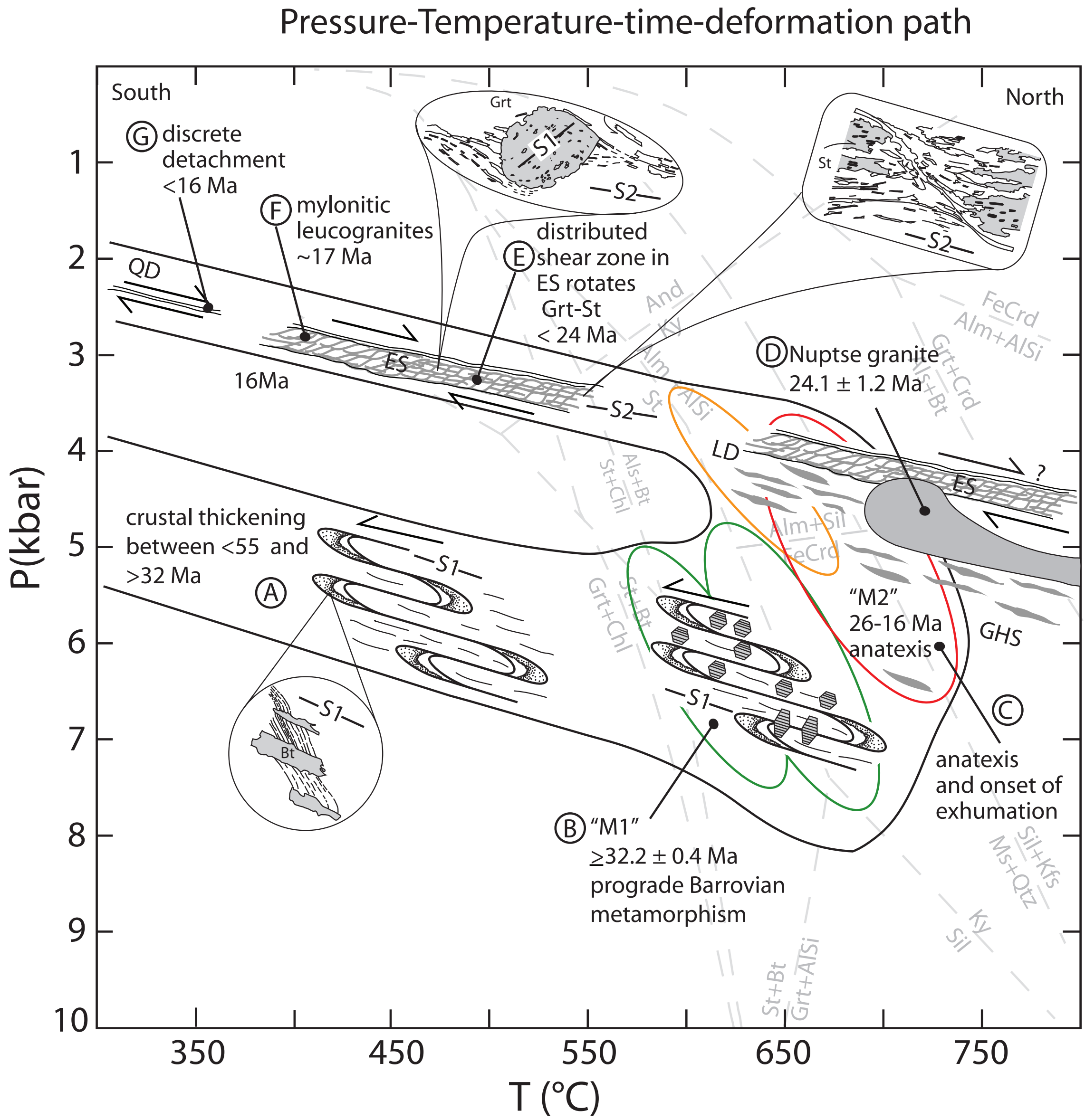

Figure 4.9. Pressure-Temperature-time-Deformation (*P-T-t-D*) path proposed for the Everest Series. Locations A-G represent stages in the evolution of these rocks that are discussed in detail in the text. 2-σ error ellipses for samples from this investigation are colored red for samples that represent the core of the slab with diffusion zoning preserved in garnet from within the GHS, green for samples that represent *P-T* conditions above the LD and contain garnets that preserves prograde compositional zoning, and orange for samples that contain evidence for early staurolite with cordierite overgrowths and record isothermal decompression between M1 and M2 events. Petrogenetic grid is modified after Holland and Powell (1998).

mean $^{208}Pb^{*}/^{232}Th$ age of 24.1 ± 1.2 Ma with an MSWD (Wendt & Carl, 1991) of 2.7, which we interpret as the crystallization age of the Nuptse granite.

Discussion

Garnet zoning, P-T estimates and microstructures

Float samples from the Nuptse-Lhotse wall record two main types of assemblages and garnet zoning: 1) garnet + staurolite with prograde compositional zoning, 2) garnet + staurolite + cordierite ± andalusite with slightly retrogressed garnet zoning. As an example of the first type, garnets in samples ET-70E, L-8, and L-13 record prograde compositional zoning and yield *P-T* estimates of 653 ± 35°C, 6.2 ± 1.2 kbar; 610 ± 31°C, 6.2 ± 1 kbar; and 590 ± 50°C (at 6 kbar), respectively (Fig. 4.6; Tables 4.1 and 4.2), that we interpret as a record of the M1 event. In contrast, sample ET-68A is representative of samples that contain cordierite overgrowths on staurolite and garnet as well as garnets that preserve prograde compositional zoning, yet the rims of the garnets are beginning to react with the matrix during retrograde reactions. Sample ET-68A yields a *P-T* estimate of 633 ± 34°C, 4.3 ± 0.8 kbar, a similar temperature yet ~ 2 kbar lower pressure than recorded by the pristine samples (Fig 4.7; Table 4.1). We interpret this *P-T* estimate as representative of the M1 event that was overprinted by cordierite during the M2 decompression event. In essence, ET-70E is a relict of the M1 event that is preserved at presumably higher structural positions on the Nuptse-Lhotse wall. This is similar to the Pognante and Benna (1993) model whereby samples from the MCTZ record the M1 event whereas the anatectic core is dominated by their M2 and M3 thermal events.

Macro-and microstructural evidence from these samples suggests that many of the porphyroblasts grew in the hinge zone of F1 folds and overgrew a pervasive S1 foliation that is now preserved as inclusions of quartz and opaque phases within garnet and staurolite porphyroblasts. A crenulation event (D2) folded (F2) S1 and rotated the (M1) porphyroblasts and therefore post-dates their growth. When viewed down the stretching lineation, amorphous porphyroblasts of cordierite over grow the F2 crenulations, suggesting that they formed during decompression that post-dated the S1 fabric forming events in the Everest Series. We interpret these *P-T* estimates as evidence for shearing within the Everest Series to accommodate exhumation after M1 (~610 ± 31°C, 6.2±1 kbar; ≥ 32 Ma) and syn-to post-M2 (633 ± 34°C, 4.3 ± 0.8 kbar) along the pervasive S2 fabric.

In situ samples from the base of the Nuptse-Lhotse wall record a transition zone marked by a range of *P-T* estimates. Garnet from sample ET-52 contains a well-developed resorption rind that is marked by an abrupt increase in X_{sps} near the rim. This sample yields *P-T* estimates of 648 ± 37°C, 6.6 ± 1.1 kbar (Fig 4.7; Table 4.1). However, because of the significant alteration by retrograde net transfer reactions and patchy internal zoning of Ca that reflects an intricate diffusion within the garnet, we consider this *P-T* estimate unreliable. Other, more reliable *P-T* data from this transition zone come from samples ET-51, ET-54, and ET-57. Sample ET-57 preserves prograde compositional zoning marked by a gradual decrease in X_{sps} from core to rim (Fig. 4.A1c). Ca is strongly zoned and is enriched in the core. Sample ET-57 yields a *P-T* estimate of 685 ± 39ºC, 5.1 ± 1.2 kbar (Fig 4.7; Table 4.1). Garnet zoning in ET-54 contains a core that is typical of growth zoning and a rim with variably developed elevated Mn levels. We interpret the garnet zoning in sample ET-54 to reflect partial retention of the prograde growth (M1) in the core that was partially resorbed during the M2 event. Garnet zoning in sample ET-51 (Fig. 4.A1d) contains rims with elevated X_{sps} and is more typical of those from the core of the GHS. Samples ET-51 and ET-54 yield temperature estimates (at 5 kbar) of 660 ± 50°C and 650 ± 50°C respectively (Fig 4.7; Table 4.1). Because these garnets contain inclusion trails (S1) that are at a high angle to the pervasive fabric (S2) they must have grown prior to the development of the S2 shear fabric. Based on the garnet zoning and fabric development, we interpret this area at the base of the Nuptse-Lhotse wall as a transition zone between pristine garnet + staurolite schist from structurally higher levels that are variably overprinted by the M2 event and the high grade garnets typical of the central part of the GHS (ET-81b).

P-T-t-D (Pressure-Temperature-time-Deformation) path

Through the integration of *P-T* estimates, micro-and macro-scale structural analysis of the Everest Series and U-Th-Pb dating of the Nuptse granite, we propose a generalized *P-T-t-D* path to describe the exhumation of the upper most section of the GHS as exposed in the Everest-Lhotse-Nuptse massif (Fig.4. 9). Isoclinal F1 folds that fold graded beds and are associated with an S1 axial planar fabric record the earliest deformation event (D1) in the massif (Fig. 4.9a; Jessup et al., 2006). Float samples with isoclinal F1 folds are also found with staurolite and garnet porphyroblasts containing inclusions trails that we interpret as S1. Our preferred model is that these early fabrics are related to crustal thickening *via* folding and thrusting that culminated in Barrovian metamorphism (M1) in the Everest region (Fig. 4.8b). The age of Barrovian metamorphism is bracketed between initial collision of India and Eurasia at ~55 Ma and the ~32 Ma age of Simpson et al. (2000). As previously mentioned, because the 32 Ma age is the oldest monazite within a sample that contains relicts of the M1 event (kyanite) as inclusions in garnet we prefer to interpret this as a minimum age for Barrovian metamorphism. Although our record of M1 is limited to samples preserved by pristine staurolite schist in the Everest Series float and as inclusions in garnets of the anatectic core of the GHS (ET-81b), we propose that *P-T* conditions reached by samples L-8 and ET-70E (~610 ± 31°C, 6.2±1 kbar) record the Eohimalayan event. As proposed by Pognante and Benna (1993) for the MCTZ, we interpret the presence of pristine staurolite as a record of the early Barrovian metamorphism preserved at the top of the GHS.

The pervasive Neohimalayan thermal event, associated with extensive leucogranite injection complexes and metamorphism that dominates most of the central portion of the Himalayas, overprinted this "snapshot" of the M1 event in the Everest region, such that it is preserved only in the upper (Everest Series) and lower

(MCTZ) margins of the GHS. Leucogranites and leucosomes with ages of 26-22 Ma, and metamorphic monazites yielding an age of 23 Ma, constrain the timing of the Neohimalayan event recorded in the Everest region and correlates well with the remainder of the orogen (Viskupic et al., 2005). Cordierite overgrowths on staurolite and garnet porphyroblasts in samples of Everest Series record a clockwise isothermal decompression path from ≤ 6 to 4 kbar for the upper section of the GHS (Fig. 4.9c). Pristine samples demonstrate that they reached ~6 kbar (ET-70E) pressures and then decompressed to 4 kbar (ET-68A).

We interpret this decompression path as evidence for the extrusion and exhumation of the anatectic core of the GHS at high temperatures and moderate to low pressure beneath the LD. The emplacement of the Nuptse granite at 24.1 ± 1.2 Ma marks the final stage of extrusion accommodated within the migmatitic core of the upper section of the GHS (Fig.4. 9d). As the upper section of the GHS continued to be exhumed through progressively lower temperatures, deformation was partitioned into a distributed shear zone (LD) within the Everest Series that rotated garnet and staurolite porphyroblasts at < 24 Ma (Fig. 4.9e). By ~17 Ma deformation was partitioned in the upper margin of the GHS as recorded by dated mylonitic leucogranites in Rongbuk valley (Fig. 9f; Murphy and Harrison, 1999). As the top of the slab exhumed through the brittle-ductile transition, deformation was partitioned into a discrete detachment system (QD) by < 16 Ma (Fig. 4.9g; Hodges et al., 1998).

Pressure-Temperature profile of the GHS

Many investigations have drawn *P-T* vs. distance from the MCTZ plots to summarize results from metamorphic investigations; however the relationship between *P-T* results compositional zoning, timing and deformation has been left relatively unexplored for the Everest region (Fig. 4.4; Hubbard 1989; Searle et al., 2003). We propose that the current distribution of pressure and temperature variations in the GHS exposed in the Everest region is an artifact of several thermal and deformational events.

Without more extensive geochronology, it is impossible to determine whether these events are spatially and temporally distinct, protracted or some combination of both. However, in order to present all of our results, we describe the evolution of these rocks in terms of individual episodes.

The upper section of the GHS records an early M1 event that (pristine staurolite bearing samples above the proposed location of the LD; Fig. 4.4) that yield *P-T* estimates of ~610 ± 31°C, 6.2±1 kbar and preserves prograde compositional zoning. In contrast, garnets with diffusion zoning record high-*T* low-*P* estimates (633 ± 34°C, 4.3 ± 0.8 kbar) associated with decompression dominate in the core of the GHS from the base of the Everest Series to the top of the MCTZ (Hubbard, 1989; Searle et al., 2003). The LD contains a complex transition zone between prograde garnets of the Everest Series above and retrogressed textures common to the core of the GHS below. The base of the GHS is marked by the occurrence of a series of metasedimetary rocks that preserve a downward transition in garnet zoning from the anatectic core to lower structural positions (Catlos et al., 2002). Incorporating this information into interpretations of the thermal profile of the GHS suggests that the high pressure-moderate temperature metamorphic conditions recorded in the margins of the GHS are relicts of the M1 event, whereas rocks in the core of the GHS record a the low pressure-high temperature M2 event.

Because fabric development in the MCTZ and LD post-dates most porphyroblast growth, except for cordierite in the Everest Series, we propose that exhumation of the GHS, during the Neohimalayan event, created a pervasive fabric (S2) that wraps around porphyroblasts that we interpret as Eohimalayan. Microstructural analysis of rocks across the Everest region and detailed kinematic analysis in the bounding shear zones demonstrate that rocks in the core of the GHS were unaffected by mylonite zones that are common to the margins of the GHS (i.e., MCTZ and STDS). Additionally, deformation temperatures recorded in the core of the GHS are much higher than those in the margins. Together this evidence suggests that following lateral mid-crustal flow at deformation temperatures well above the onset of feldspar rigidity in the core of the GHS, deformation was partitioned into the bounding shear zones to accommodate exhumation recorded during the Neohimalayan event. Kinematic analysis by Jessup et al (2006) quantified the relative contributions of pure and simple shear (mean kinematic vorticity; W_m) and suggest that the highest contribution of simple shear occurs along the top of the GHS while the highest contribution of pure shear is recorded in the MCTZ. Jessup et al. (2006) attribute the highest contribution of pure shear to the increased lithostatic pressure due to the overburden generated by the GHS.

Our preferred model implies that the current *P-T* profile of the GHS is the result of the complex juxtaposition of several thermal and deformation events that began with the development of paleoisotherms during early prograde metamorphism (Eohimalayan; M1) and culminated in Neohimalayan (M2) metamorphism that records decompression of the GHS. Therefore caution must be exercised when interpreting a complex juxtaposition of *P-T-t-D* paths in different sections of the GHS.

The Lhotse Detachment

The Lhotse detachment is a significant, but elusive, feature that corresponds to the complex transition zone between the anatectic core and overlying Everest Series schist (Searle, 1999b). In places (e.g., Gyachung Kang) the Lhotse Detachment appears as a clear-cut fault that places Everest Series above leucogranite, in other places, such as on the SW face of Everest, it is more a diffuse shear zone. Although the exact location of the LD is difficult to discern, *P-T-t-D* data from this investigation shed light on the nature of this transition zone. The LD marks a transition from garnet with growth zoning in the hangingwall to garnet zoning profiles dominated by diffusion zoning in the footwall of the anatectic core of the GHS below. Estimated metamorphic temperatures generally decrease upwards across this section, which we interpret as an artifact of the juxtaposition of two metamorphic events rather than a gradation in *P-T* conditions. We propose that metasedimentary rocks, and the *P-T* history recorded by them, are strongly telescoped within the Everest Series schists.

Because of the inaccessibly of the outcrop, it will be impossible to uniquely resolve the kinematic evolution of the LD in this region. For example, the apparent break in pressures across the LD could be interpreted as a thrust fault that brings a deeper structural position in the hanging wall (Everest Series) into contact with a shallower structural position in the footwall (GHS). Alternatively, the evidence outlined above might also be used to suggest that the transition zone goes from the core of the GHS recording M2 (± relict M1) through the ES recording M1 ± M2 up to the QD; an interpretation that essentially removes the need for the LD. Furthermore, the break in pressure across the LD could be due to the over printing (or not) of the M2 event in the core of the slab and not differential exhumation along a fault system.

Our results suggest that the proposed location of the LD coincides with a transition between: 1) garnet zoning, 2) disequilibrium textures between cordierite and staurolite, 3) relative timing between fabric development and porphyroblast growth and 4) the age of M1 staurolite bearing Everest Series schists (~32 Ma) and M2 cordierite event (~22 Ma). Our preferred interpret of zone as the upper boundary to the extruding GHS until the emplacement of the Nuptse granite at 24.1 ± 1.2 Ma when deformation was partitioned into the overlying Everest Series during exhumation.

Conclusions

Rocks at the top of the GHS, exposed in the Everest region, provide an important opportunity to constrain major unresolved components of the thermal structure of the GHS. We propose that the thermal profile across the GHS is an artifact of the superposition of at least two metamorphic events and several phases of deformation that may represent distinct or protracted events that are summarized as follows. Crustal thickening resulted in transposition of bedding into an S1 fabric, and culminated in the growth of porphyroblasts that preserve prograde compositional zoning and S1 inclusion trails, and staurolite inclusions. Pristine samples of staurolite bearing Everest Series with garnets that contain growth zoning yield *P-T* estimates of ~610 ± 31°C, 6.2 ±1 kbar. We interpret these conditions as a record of the early Eohimalayan Barrovian metamorphic event that is only preserved on the margins of the GHS within the MCTZ and Everest Series. Cordierite and rare andalusite overgrowths on staurolite record isothermal decompression during a second metamorphic event (633 ± 34°C, 4.3 ± 0.8 kbar) . Together these results suggest the LD marks a spatial and temporal break in pressure (6.2 - 4.3 kbar), garnet zoning (from growth zoning in the hanging wall to diffusion zoning in the footwall) and a general decrease in temperature between the Everest Series above and the core of the GHS below.

Emplacement of the syn to-post kinematic Nuptse granite at 24.1 ± 1.2 Ma marks the transfer in shearing from the core of the GHS to the overlying Everest Series. Our new results provide additional support for previously proposed models explaining relationships between emplacement of the Nuptse granite and movement on the Lhotse Detachment (Searle et al., 2003). Our preferred model for exhumation along the top of the slab also agrees with detailed vorticity and microstructural analysis from Jessup et al. (2006) who proposed that the deeper structural positions were juxtaposed beneath a shallower crustal position during exhumation along the STDS.

Acknowledgments

We thank Tashi Sherpa, Dawa Sherpa, and Ram Rai who worked as porters and helped with logistics during three field seasons to the Khumbu region, Nepal (2003-2004). For their impressive efforts in the field, we thank Laura Duncan, who collected sample ET-74 from the summit of Chukung and James Ashby. David Hamilton collected the summit and South Col samples in 2003. Many thanks to Victor Lygios and Clayton Leohn who helped with electron microprobe analyses at Virginia Tech. Thin sections from Mary Hubbard provided context for her geothermobarometric investigation in the MCTZ. M. Horstwood and V. Pashley (Natural Environment Research Council National Isotope Geoscience Laboratory, Keyworth) are thanked for their help in obtaining isotope analyses. Funding was provided by National Science Foundation grant EAR-207524 to R. D. Law and M. P. Searle and a Natural Environment Research Council NIGFSC grant (IP/846/0505) to M.P. Searle. Grants to M. J. Jessup from Geological Society of America, Sigma Xi, American Alpine Club, Department of Geological Sciences, Virginia Tech and a 2010 Fellowship from the Virginia Tech College of Science provided additional funding for this project.

REFERENCES

Babanov, V. 2004. Moonlight Sonata; *Alpinist*, **7**, 40-48.

Bhattacharya, A., Mohanty, L., Maji A., Sen, SK., & Raith, M., 1992. Non-ideal mixing in the phlogopite-annite binary: constraints from experimental data on Mg-Fe partitioning and a reformulation of the biotite-garnet thermometer. *Contributions to Mineralogy and Petrology*, **111**, 87-93.

Beaumont, C., Jamieson, R.A., Nguyen, M.H. & Lee, B., 2001. Himalayan tectonics explained by extrusion of a low-viscosity crustal channel coupled to focused surface denudation. *Nature*, **414**, 738-742.

Beaumont, C., Jamieson, R.A., Nguyen, M.H. & Medvedev, S. 2004. Crustal channel flows: 1. Numerical models with applications to the tectonics of the Himalayan – Tibetan orogen. *Journal of Geophysical Research*, **109**, B06406 29p.

Beaumont C., Nguyen, M., Jamieson, R. & Ellis, S., 2006. Crustal flow modes in large hot orogens. In: Law, R.D., Searle, M.P. & Godin, L. (eds) Channel Flow, Ductile Extrusion and Exhumation in Continental Collision Zones. *Geological Society, London, Special Publications*, **268**, 91-145.

Carosi, R., Lombardo, B., Molli, G., Musumeci, G. & Pertusati, P., 1998. The South Tibetan detachment system in the Rongbuk valley, Everest region. Deformation features and geological implications. *Journal of Asian Earth Sciences*, **16**, 299-311.

Carosi, R., Lombardo, B., Musumeci, G. & Pertusati, P., 1999a. Geology of the Higher Himalayan crystallines in Khumbu Himal (Eastern Nepal). *Journal of Asian Earth Sciences*, **17**, 785-803.

Carosi, R., Musumeci, G. & Pertusati, P.C., 1999b. Extensional tectonics in the higher Himalayan crystallines of Khumbu Himal, eastern Nepal. In: Macfarlane, A., Sorkhabi, R.B. & Quade, J. (eds) Himalaya and Tibet: Mountain Roots to Mountain Tops. *Geological Society of America Special Paper*, **328**, 211- 223.

Catlos, E.J., Harrison, T. M., Kohn, M.J., Grove, M. Ryerson, F.J.M., Manning, C.E.

& Upreti, B.N., 2001. Geochronological and thermobarometric constraints on the evolution of the Main Central Thrust, central Nepal Himalaya. *Journal of Geophysocal Research*, **106**, 177-16,204.

Catlos, E.J., Harrison, T.M., Manning, C.E., Grove, M., Rai, S.M., Hubbard, M. & Upreti, B.N., 2002. Records of the evolution of the Himalayan orogen from in situ Th-Pb ion microprobe dating of monazite: Eastern Nepal and western Garhwal. *Journal of Asian Earth Sciences*, **20**, 459-80.

Catlos, E.J., Dubey, C.S., Harrison, T.M. & Edwards, M.A., 2004. Late Miocene movement within the Himalayan Main Central Thrust shear zone, Sikkim, north-east India. *Journal of Metamorphic Geology*, **22**, 207-226.

Daniel, C.G, Hollister, L.S., Parrish, R.R., Grujic, D., 2003. Exhumation of the Main Central Thrust from lower crustal depths, Eastern Bhutan Himalaya. *Journal of Metamorphic Geology*, **21**, 317-334.

Dezes, P.J., Vannay, J.C., Steck, A., Bussy, F. & Cosca, M., 1999. Synorogenic extension; quantitative constraints on the age and displacement of the Zanskar shear zone (Northwest Himalaya). *Geological Society of America Bulletin*, **111**, 364-374.

Ferril, D.A., Morris, A.P., Evans, M.A., Burkhard, Groshong, R.H. & Onasch, C.M., 2004. Calcite twin morphology: a low temperature geothermometer. *Journal of Structural Geology*, **26**, 1521-1530.

Ferry, J.M., & Spear, F.S., 1978. Experimental calibration of the partitioning of FE and Mg between biotite and garnet. *Contributions to Mineralogy and Petrology*, **666**, 113-117.

Fraser, G., Worley, B. & Sandiford, M., 2000. High-precision geothermobarometry across the High Himalayan metamorphic sequence, Langtang Valley, Nepal. *Journal of Metamorphic Geology*, **18**, 665-681.

Goscombe, B., & Hand, M., 2000. Contrasting P-T paths in the Eastern Himalaya, Nepal; inverted isograds in a paired metamorphic belt. *Journal of Petrology*, **41**, 1673-

1719.

Goscombe, B., Gray, D. & Hand, M., 2006. Crustal architecture of the Himalayan metamorphic front in eastern Nepal. *Gondwana Research*, **10**, 232-255.

Grasemann, B., Fritz, H. & Vannay, J-C., 1999. Quantitative kinematic flow analysis from the Main Central Thrust zone, (NW Himalaya): implications for a decelerating strain path and the extrusion of orogenic wedges. *Journal of Structural Geology*, **21**, 837-53.

Grujic, D., Casey, M., Davidson, C., Hollister, L., Kundig, K., Pavlis, T. & Schmid, S., 1996. Ductile extrusion of the Higher Himalayan crystalline in Bhutan: evidence from quartz microfabrics. *Tectonophysics*, **260**, 21-43.

Grujic, D., Hollister, L. & Parrish, R.R., 2002. Himalayan metamorphic sequence as an orogenic channel: insight from Bhutan. *Earth and Planetary Science Letters*, **198**, 177-191.

Harrison, T. M., Ryerson, J., Le Fort, P., Yin, A., Lovera, O. & Catlos, E., 1997. A late Miocene-Pliocene origin for the Central Himalayan inverted metamorphism, *Earth and Planetary Science Letters*, **146**, 1-7.

Harrison, T. M., Grove, M., Lovera, O. M., Catlos, E. J. & Andrea, J.D., 1999. The origin of Himalayan anatexis and inverted metamorphism: Models and constraints. *Journal of Asian Earth Sciences*, **17**, 755-772.

Hirth, G. & Tullis, J., 1992. Dislocation creep regimes in quartz aggregates. *Journal of Structural Geology*, **14**, 145-160.

Hodges, K. V., 2000. Tectonics of the Himalaya and southern Tibet from two perspectives. *Geological Society of America Bulletin*, **112**, 324-350.

Hodges, K. V., Parrish, R. R., Housch, T. B., Lux, D. R., Burchfiel, B. C., Royden, L. H. & Chen, Z., 1992. Simultaneous Miocene extension and shortening in the Himalayan orogen. *Science*, **258**, 1466-1470.

Hodges, K. V., Bowring, S., Davidek, K., Hawkins, D. & Krol, M., 1998. Evidence for rapid displacement on Himalayan normal faults and the importance of tectonic denudation in the evolution of mountain ranges. *Geology*, **26**, 483-6.

Hodges, K.V., Hurtado, J.M. & Whipple, K.X., 2001. Southward extrusion of the Tibetan crust and its effect on Himalayan tectonics. *Tectonics*, **20**, 799-809.

Holdaway, M.J. 2000. Applications of new experimental and garnet Margules data to the garnet-biotite thermometer. *American Mineralogist*, **85**, 881-892.

Holland, T.J.B. & Powell, R., 1998. An internally consistent thermodynamic data set for phases of petrological interest. *Journal of Metamorphic Geology*, **16**, 309-344.

Horstwood, M.S.A., Foster, G.L., Parrish, R.R., Noble, S.R. & Nowell, G.M., 2003: Common-Pb corrected in situ U–Pb accessory mineral geochronology by LA-MC-ICP-MS. *Journal of Analytical Atomic Spectrometry,* **18**, 837 - 846.

Hubbard, M.S. 1988. Thermobarometry, 40Ar/39Ar geochronology, and structure of the Main Central Thrust zone and Tibetan Slab, eastern Nepal Himalaya. PhD thesis, Massachusetts Institute of Technology, Cambridge, 169 p.

Hubbard, M.S. 1989. Thermobarometric constraints on the thermal history of the Main Central Thrust Zone and Tibetan Slab, eastern Nepal Himalaya. *Journal of Metamorphic Geology*, **7**, 19-30.

Hubbard, M.S. 1996. Ductile shear as a cause of inverted metamorphism: Example from the Nepal Himalaya. *Journal of Geology*, **104**, 493-499.

Hubbard, M.S. & Harrison, T.M., 1989. $^{40}Ar/^{39}Ar$ age constraints on deformation and metamorphism in the Main Central Thrust zone and Tibetan Slab, eastern Nepal Himalaya. *Tectonics*, **8**, 865 - 880.

Jamieson, R.A., Beaumont, C., Hamilton, J., Fullsack, P., 1996. Tectonic assembly of inverted metamorphic sequences. *Geology*, **24**, 839–842.

Jamieson, R.A., Beaumont, C., Nguyen, M.H. & Lee, B., 2002. Interaction of metamorphism, deformation and exhumation in large convergent orogens. *Journal* *of Metamorphic Geology*, **20**, 9-24.

Jamieson, R. A., Beaumont, C., Medvedev & Nguyen, M.H., 2004. Crustal channel flows: 2. Numerical models with implications for metamorphism in the Himalayan-Tibetan orogen. *Journal Geophysical Research*, **109**, B06407, doi:10.1029/2003JB002811.

Jessup, M.J., Law, R.D., Searle, M.P. & Hubbard, M.S., 2006. Structural evolution and vorticity of flow during extrusion and exhumation of the Greater Himalayan Slab, Mount Everest Massif, Tibet/Nepal: implications for orogen-scale flow partitioning. In: Law, R.D., Searle, M.P. & Godin, L. (eds) *Channel Flow, Extrusion, and Exhumation in Continental Collision Zones*. Geological Society, London, Special Publications, **268**, 379-414.

Kohn, M.J. & Spear, F., 2001 Retrograde net transfer reaction insurance for pressure-temperature estimates, Geology, **28**, 1127-1130.

Kohn, M.J., Wieland, M.S., Parkinson, C.D. & Upreti B.N., 2005 Five generations of monazite in Langtang gneisses: implications for chronology of the Himalayan metamorphic core. *Journal of Metamorphic Geology*, **23**, 399–406

Kretz, R., 1983. Symbols for rock-forming minerals. American Mineralogist, **68**, 277-279.

Larson, T.E. & Sharp, Z.D., 2003. Stable isotope constraints on the Al_2SiO_5 "triple-point" from the Proterozoic Priest Pluton contact aureole, New Mexico, USA. *Journal of Metamorphic Geology*, **21**, 785-798.

Larson, T.E. & Sharp, Z.D., 2005. Interpreting prograde-growth histories of Al_2SiO_5 triple-point rocks using oxygen-isotope thermometry; an example from the Truchas Mountains, USA. *Journal of Metamorphic Geology*, **23**, 847-863.

Law, R.D., Searle, M.P. & Simpson, R.L. 2004. Strain, deformation temperatures and vorticity of flow at the top of the Greater Himalayan Slab, Everest massif, Tibet. *Journal of the Geological Society, London*, **161**, 305-20.

Le Fort, P., 1975. Himalayas: the collided range. Present knowledge of the continental arc. *American Journal of Science*, **275**, 1-44.

Lombardo, B., Pertusati, P. & Borgi, S. 1993. Geology and tectonomagmatic evolution of the eastern Himalaya along the Chomolungma - Makalu transect. In: Treloar, P.J. & Searle, M.P. (eds) *Himalayan Tectonics,* Geological Society, London, Special Publications, **74**, 341-355.

Macfarlane, A.M., 1995. An evaluation of the inverted metamorphic gradient at Langtang National Park, central Nepal Himalaya. *Journal of Metamorphic Geology*, **13**, 595-612.

Murphy, M.A. & Harrison, T.M., 1999. Relationship between leucogranites and the Qomolangma Detachment in the Rongbuk valley, south Tibet. *Geology*, **27**, 831-834.

Passchier, C.W. & Trouw, R.J., 2005. Microtectonics 2nd edition. Springer, Berlin, Federal Republic of Germany.

Pattison, D.R.M., Spear, F.S., Cheney, J.T., 1999. Polymetamorphic origin of muscovite + cordierite + staurolite + biotite assemblages; implications for the metapelitic petrogenetic grid for P-T paths. *Journal of Metamorphic Geology*, **17**, 685-703.

Parrish, R.R., 1990. U-Pb dating of monazite and its application to geological problems. *Geological Survey of Canada Contribution* **12090**.

Pognante, U. & Benna, P., 1993. Metamorphic zonation, migmatization and leucogranites along the Everest transect of eastern Nepal and Tibet: record of an exhumation history; In: Treloar, P.J. & Searle, M.P. (eds) Himalayan Tectonics, *Geological Society, London, Special Publications*, **74**, 323 - 340.

Schärer, U., 1984: The effect of initial ^{230}Th disequilibrium on young U-Pb ages: the Makalu case, Himalaya. *Earth and Planetary Science Letters,* **67**, *191-204*.

Searle, M.P., 1999a. Extensional and compressional faults in the Everest – Lhotse massif, Khumbu Himalaya, Nepal. *Journal of the Geological Society, London*, **156**. 227-40.

Searle, M.P., 1999b. Emplacement of Himalayan leucogranites by magma injection along giant sill complexes: examples from the Cho Oyu, Gyachung Kang and Everest leucogranites (Nepal Himalaya). *Journal of Asian Earth Sciences*, **17**, 773-83.

Searle, M.P., 2003. *Geological map of the Everest massif, Nepal and South Tibet*. Scale 1:100,000, Dept. Earth Sciences, Oxford University.

Searle, M.P. & Rex, A.J., 1989. Thermal model for the Zanskar Himalaya. *Journal of Metamorphic Geology*, **7**, 127-134.

Searle, M.P., & Szulc, A.G., 2005. Channel flow and ductile extrusion of the high Himalayan slab – Kangchenjunga-Darjeeling profile, Sikkim Himalaya. *Journal of Asian Earth Sciences*, **25**, 173-185.

Searle, M.P., Simpson, R.L., Law, R.D., Parrish, R.R. & Waters, D.J. 2003. The structural geometry, metamorphic and magmatic evolution of the Everest massif, High Himalaya of Nepal-south Tibet. *Journal of Geological Society, London*, **160**, 345-66.

Searle, M.P., Law, R.D. & Jessup, M.J., 2006. Crustal structure, restoration and evolution of the Greater Himalaya: implication for channel flow and ductile extrusion of the middle crust. In Law, R.D., Searle, M.P. & Godin, L. (eds) Channel Flow, Extrusion, and Exhumation in Continental Collision Zones. *Geological Society, London, Special Publications*, **268**, 355-378.

Simpson, R.L. 2002. Metamorphism, melting and extension at the top of the high Himalayan Slab, mount Everest Region, Nepal and Tibet. D.Phil. thesis, University of Oxford, 163 pp.

Simpson, R.L., Parrish, R.R., Searle, M.P. & Waters, D.J., 2000. Two episodes of monazite crystallization during metamorphism and crustal melting in the Everest region of the Nepalese Himalaya. *Geology*, **28**, 403-406.

Stephenson, B.J., Waters, D.J. & Searle, M.P., 2000. Inverted metamorphism and the Main Central thrust: field relations and thermobarometric constraints from the

Kishtwar Window, NW Indian Himalaya. *Journal of Metamorphic Geology*, **18**, 571-590.

Stephenson, B.J., Searle, M.P., Waters, D.J. & Rex, D.C., 2001. Structure of the Main Central thrust and extrusion of the High Himalayan deep crustal wedge, Kishtwar-Zanskar Himalaya. *Journal of the Geological Society, London*, **158**, 637-652.

Spear, F., 1995. Metamorphic phase equilibrium and pressure-temperature-time paths. *Mineralogical Society of America monograph*, 2nd edition, 799 pp.

Stipp, M., Stunitz, H., Heilbronner, R. & Schmid, S,, 2002. Dynamic recrystallization of quartz: correlation between natural and experimental conditions. In: De Meer, S., Drury, M.R., De Bresser, J.H.P. & Pennock, G.M. (eds) Deformation Mechanisms, Rheology and Tectonics: Current Status and Future Perspectives. *Geological Society, London, Special Publications,* **200**, 171-190.

Swapp, S.M. & Hollister, L.S., 1991. Inverted metamorphism within the Tibetan Slab of Bhutan: evidence for tectonically transported heat source. *Canadian Mineralogist*, **29**, 1019-1041.

Tracy, R.J., Robinson, P. & Thompson, A.B., 1976. Garnet composition and zoning in the determination of temperature and pressure of metamorphism, central Massachusetts. *American Mineralogist*, **16**, 762-775.

Vannay, J.-C. & Grasemann, B., 2001. Himalayan inverted metamorphism and syn-convergence extension as a consequence of a general shear extrusion. *Geological Magazine*, **138**, 253-276.

Vannay, J.-C., Grasemann, B., Rahn, M., Frank, W., Carter, A., Baudraz, V. & Cosca, M., 2004. Miocene to Holocene exhumation of metamorphic wedges in the NW Himalaya: evidence for tectonic extrusion coupled to fluvial erosion. *Tectonics*, **23**, TC1014.

Viskupic, K., Hodges, K.V. & Bowring, S.A., 2005. Timescales of melt generation and the thermal evolution of the Himalayan metamorphic core, Everest region, eastern

Nepal. *Contributions to Mineralogy and Petrology*, **149**, 1-21.

Walker, J.D., Martin, M. W., Bowring, S. A., Searle, M. P., Waters, D. J. & Hodges, K.V., 1999. Metamorphism, melting and extension: Age constraints from the High Himalayan slab of Southeastern Zanskar and Northwestern Lahoul. *Journal of Geology*, **107**, 473-95.

Walker, C.B., Searle, M. P. & Waters, D.J., 2001. An integrated tectonothermal model for the evolution of the High Himalaya in western Zanskar with constraints from thermobarometry and metamorphic modeling. *Tectonics*, **20**, 810-33.

Weinberg, R.F. and Searle, M.P., 1999. Volatile-assisted intrusion and autometasomatism of leucogranites in the Khumbu Himalaya, Nepal. *Journal of Geology*, **107**, 27-48.

Wendt, I. & Carl, C., 1991: The statistical distribution of the mean squared weighted deviation. *Chemical Geology,* **86**, 275-285.

Yardley, B.W.D. 1977. An empirical study of diffusion in garnet. *American Mineralogist*, **62**, 793-800.

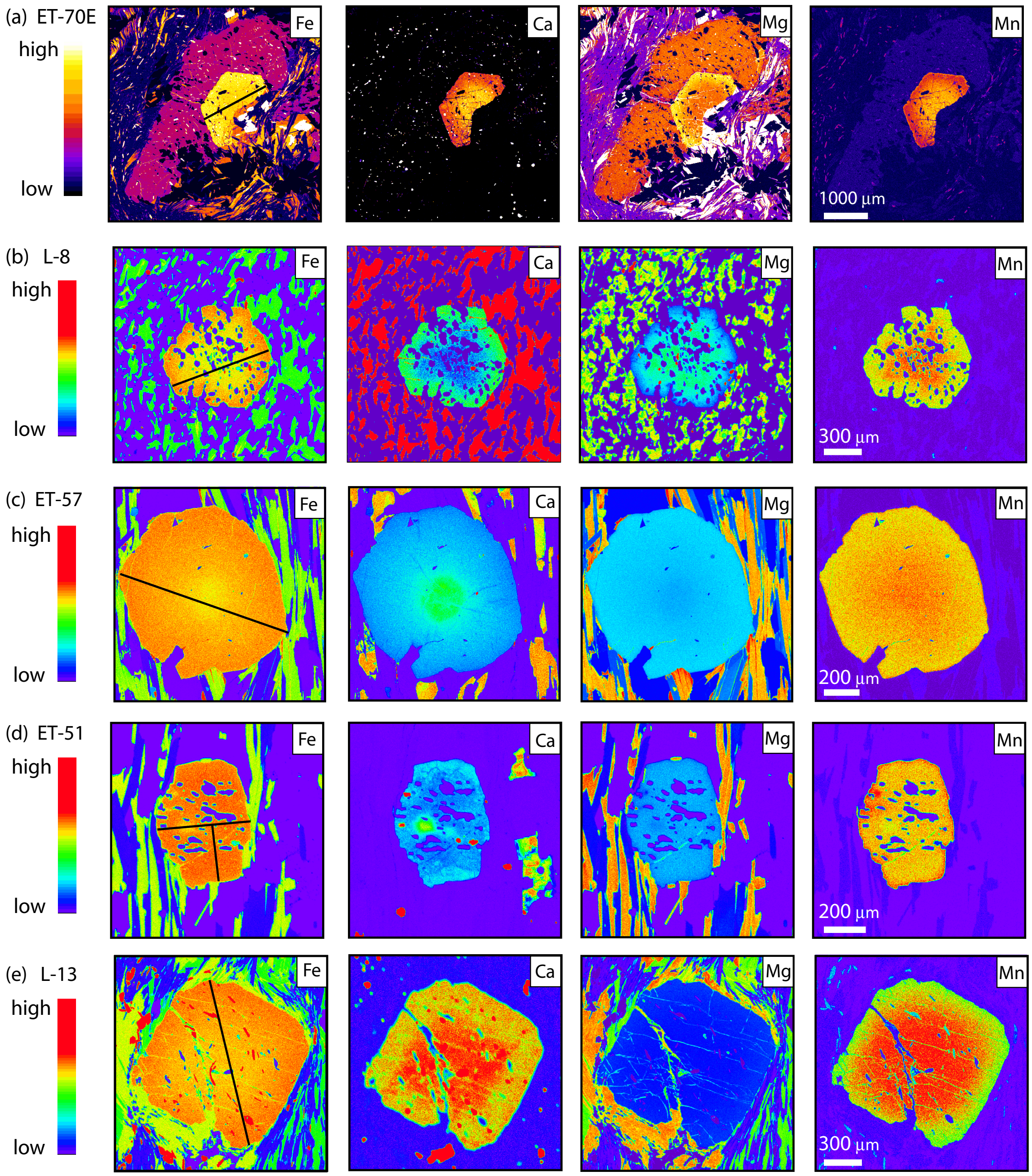

Figure 4.1A. Compositional maps for the remainder of samples uses for this investigation.

CHAPTER 5

Exhumation of the Ama Drime Massif during east-west extension coupled with focused denudation in a trans-Himalayan river gorge; testing the Himalayan paradigm

MICAH J. JESSUP

Department of Geosciences, Virginia Tech, Blacksburg, Virginia 24061, USA

Submitted proposal for a National Science Foundation International Research Fellowship in October 2006.

Project Summary

Intellectual merit of the proposed research

One of the most rapidly growing aspects of Earth Sciences is the growing body of evidence that focused precipitation, denudation and deformation are coupled in many active tectonic settings, including the Himalayan orogenic system. The complex interaction between fluvial incision, variable monsoonal precipitation gradients, variations in the stress field, and deformation are often described in terms of channel flow or tectonic aneurysm models. In these models, exhumation of mid-crustal rocks, enhanced by focused erosion and/or precipitation on the front of the Himalayas, is accommodated by thrust faults and low-angle detachment systems during crustal shortening. However, many locations along the range lack evidence for the active faulting that is implicit to these models, including the Mount Everest region. This is a request to fund an investigation to constrain the structural evolution and exhumation rates of the Ama Drime Massif (ADM), potentially the most tectonically active feature in the Everest region. New data, that form the basis for this proposal, indicate that the ADM, protruding 70-km-north from the crest of the Himalayas, is a core complex that is bounded by a detachment system that records east-west extension and offsets Quaternary deposits. Some of the highest precipitation levels in the Himalayas coincide with the trans-Himalayan Arun River gorge, which marks the southern end of the ADM. Furthermore, the only area of lithospheric thinning, as defined by earthquake focal mechanism solutions, that crosses the Himalayan front coincides with the ADM and the Arun River gorge. Together these and other observations point towards an important new hypothesis that needs to be tested:

> *Driven by the local extensional stress field, the Ama Drime range - potentially the most active feature in the Everest region - is being exhumed as a core complex with exhumation being enhanced by focused precipitation in the Arun River gorge.*

Two disciplines will be integrated to test this hypothesis and build on reconnaissance data and samples collected during 2005 and 2006: 1) field-and lab-based structural analysis, with an emphasis on the regional structure, spatial and temporal variability in deformation temperatures, and vorticity of flow (relative contributions of pure and simples shear) in the bounding shear zones, will constrain the mechanisms by which the range was uplifted; 2) thermochronology, including (U-Th)/He and apatite/zircon fission track conducted on samples from east-west transects across the range, will constrain exhumation rates. These results, when combined with existing geophysical, petrological, and geomorphological data, will enable the ADM to be tested against the Himalayan paradigm and provide new insight into the progression from south-directed mid-crustal flow as proposed in the rest of the Himalayas (Everest region) during the Miocene to east-west extension in one of the most active features today, the ADM.

Broader Impacts of the proposed research

This proposal would enable the applicant's current research to evolve into a more holistic approach to active tectonics that integrates low-temperature thermochronometry and tectonic geomorphology to test the potential coupling between erosion and exhumation of the ADM. Central to the proposal is the close mentoring of the applicant by Dr. Michael Searle and collaboration with and the Himalayan tectonics research group in the Department of Earth Sciences, Oxford University. This proposal will build on collaborative projects already initiated between the applicant and several graduate students at Oxford, including John Cottle (geochemist and geochronologist) and Mike Streule (metamorphic petrologist and geochronologist) who are working to the west and south of the ADM. Additionally, by working directly with the Himalayan tectonics group and the Department of Earth Sciences, Oxford University, the applicant will be exposed to new group of accomplished geoscientists whose specialties span an impressive range of disciplines. Following the research fellowship, the applicant

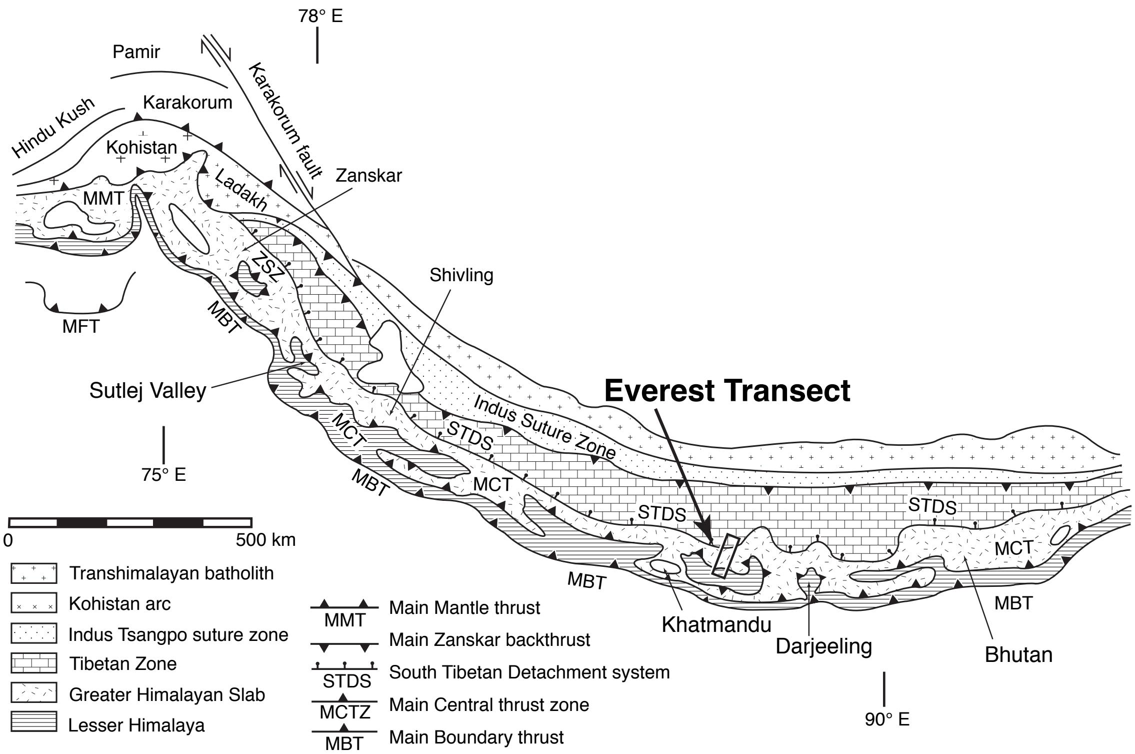

Figure 5.1. Overview map of the Himalayas.

will bring his range of research experience to an academic environment and apply it to teaching and mentoring graduate and undergraduate students. Furthermore, this experience will lay the foundation for continued collaboration between the applicant and the Himalayan tectonics group at Oxford University on future projects in the Himalayas and elsewhere that will incorporate graduate and undergraduate students from the UK and the US.

Introduction

Pioneering attempts to merge geological (structural geology, metamorphic petrology, geochronology and geomorphology) and geophysical data with the distribution of focused denudation from the Himalayan orogenic system culminated in channel flow (Beaumont et al., 2001, 2004) and tectonic aneurism models (Zeitler, 2001) that described the relationship between lateral flow of mid-crustal rocks and their exhumation to the surface as related to focused denudation along the orogenic front (Figs. 5.1 & 5.2A,

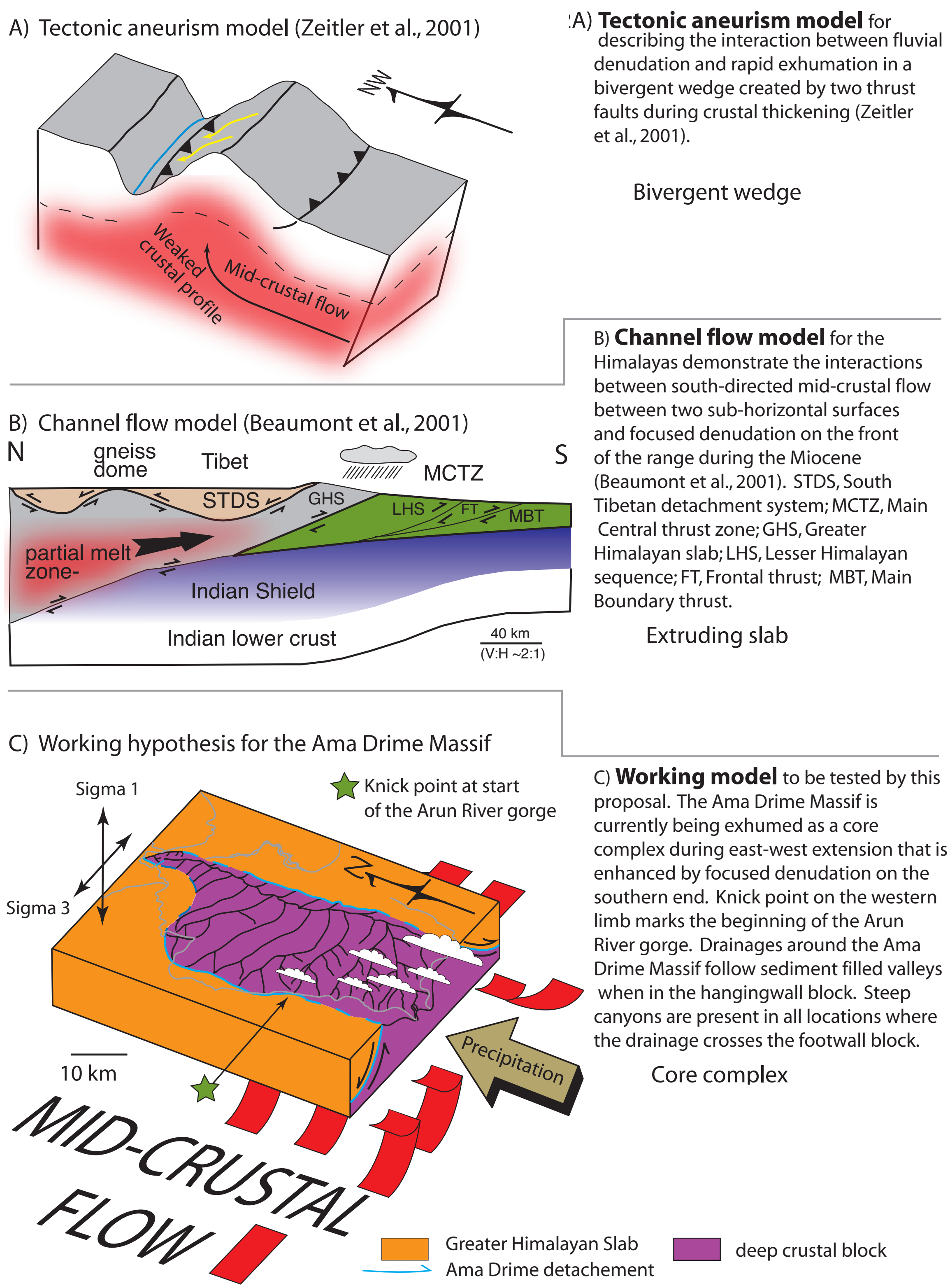

Figure 5.2. Exhumation models.

B). Tectonic aneurism models are applied to the eastern and western syntaxes where exhumation rates of mid-crustal rocks are extreme and metamorphic massifs coincide with major river systems (Fig. 5.2A). Tectonic aneurisms result from the incision of deep gorges across the uplifting mountain ranges by rivers which enable warm lower crust, driven by the local strain field, to extrude upwards as a wedge bounded by reverse faults (Zeitler et al., 1993, 2001; Schneider et al., 2001; Koons et al., 2002). More appropriate for the remainder of the orogen, are channel flow models which propose southward extrusion of a low viscosity mid-crustal channel beneath the Tibetan plateau that is driven by gradients in lithostatic pressure between the high elevation of Tibet and lowlands of the Indian plate (Fig. 5.2C; Grujic et al., 1996, 2002; Beaumont et al., 2001, 2004, 2006; Searle et al., 2003, 2006). The mid-crustal channel is exhumed to the surface as a slab of migmatitic rocks *via* focused denudation along the orogenic front of the Himalayas (Beaumont, 2001). Movement during the early tunneling stage as well as the exhumation of this mid-crustal slab are accommodated by coeval movement, during the Miocene, on two shear zones; the South Tibetan detachment system (STDS) above and the Main Central thrust zone below (MCTZ; Hodges et al., 2001).

Little evidence exists for active movement on either the STDS or MCTZ, including in the Everest region (Searle, 1999a, b; Searle et al., 2003, 2006). The majority of geochronological and structural data suggests that deformation along the base of the slab has propagated into the foreland, as predicted by orogenic wedge models (Thiede et al., 2004, 2005). $^{40}Ar/^{39}Ar$ thermochronometry from the Sutlej region of NW India demonstrates that exhumation of the region was accommodated by movement along the MCTZ and STDS until the early to middle Miocene and then migrated southward (as predicted in foreland propagating thrust systems) to the Lesser Himalaya which were exhumed during the Miocene to Pliocene (Thiede et al., 2005). Interestingly, the apatite-fission track analyses from the same suite of samples record synchronous exhumation through ~100°C across NE-SW striking, 80-40 km wide area that coincides with the

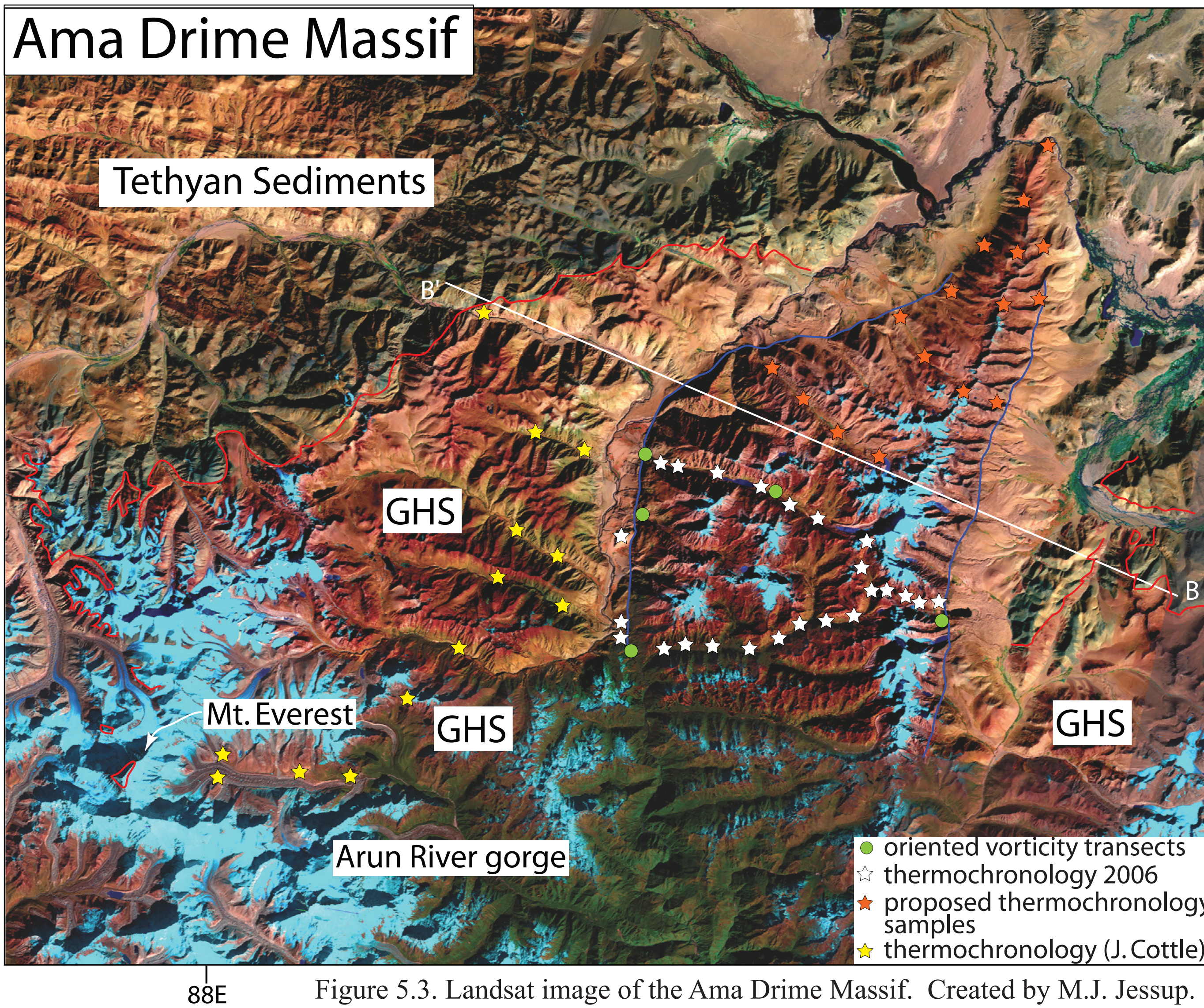

Figure 5.3. Landsat image of the Ama Drime Massif. Created by M.J. Jessup.

highest local precipitation rates (Thiede et a., 2004, 2005). This evidence demonstrates that, for many areas of the orogen, channel flow represents a "snapshot" of an extinct system that was active during the Miocene and thereby represents a much earlier part of the evolution of the Himalayas rather than the most recent tectonic setting (Thiede et al., 2004, 2005). A finer-scale interaction between mid-crustal flow, focused precipitation and exhumation has also been proposed for several other trans-Himalayan rivers (Finlayson et al., 2002; Montgomery & Stolar, 2007). A fundamental question arises from this conundrum:

If models predict that focused precipitation and denudation should result in active exhumation of a mid-crustal channel along known fault systems in response to the applied stress field, then why are these features inactive; more importantly where is this occurring today?

Since channel flow and tectonic aneurism models were first proposed, advances in low-temperature thermochronology as well as higher resolution digital elevation models and increasingly sophisticated geomorphology techniques have resulted in a new era of models (Willet et al., 2006) that convey a complex, but perhaps more accurate depiction of the Himalayas and other active tectonic settings. The Ama Drime Massif (ADM), located only ~55 km east of the summit of Everest, provides incredible exposure of mid-crustal rocks that have the potential to make an important new contribution to the existing models for the coupling of climate and erosion during the tectonic evolution of the Himalayas (Fig. 5.1). The bounding faults and shear zones strike north-south, parallel to the 70-km length of the range and record east-west extension that offset Quaternary deposits (Figs. 5.3-5.5 & 5.2C; Burchfiel et al., 1992). Focal mechanism solutions that divide the mid-to lower-crust of the Himalayas and Tibetan plateau into domains of lithospheric vertical thickening and thinning define an area of lithospheric thinning that crosses the orogenic front (Shapiro et al., 2004) beneath the ADM (Fig. 5.6). Annual precipitation in the Himalayas is highest in the Arun River gorge and the eastern syntaxis

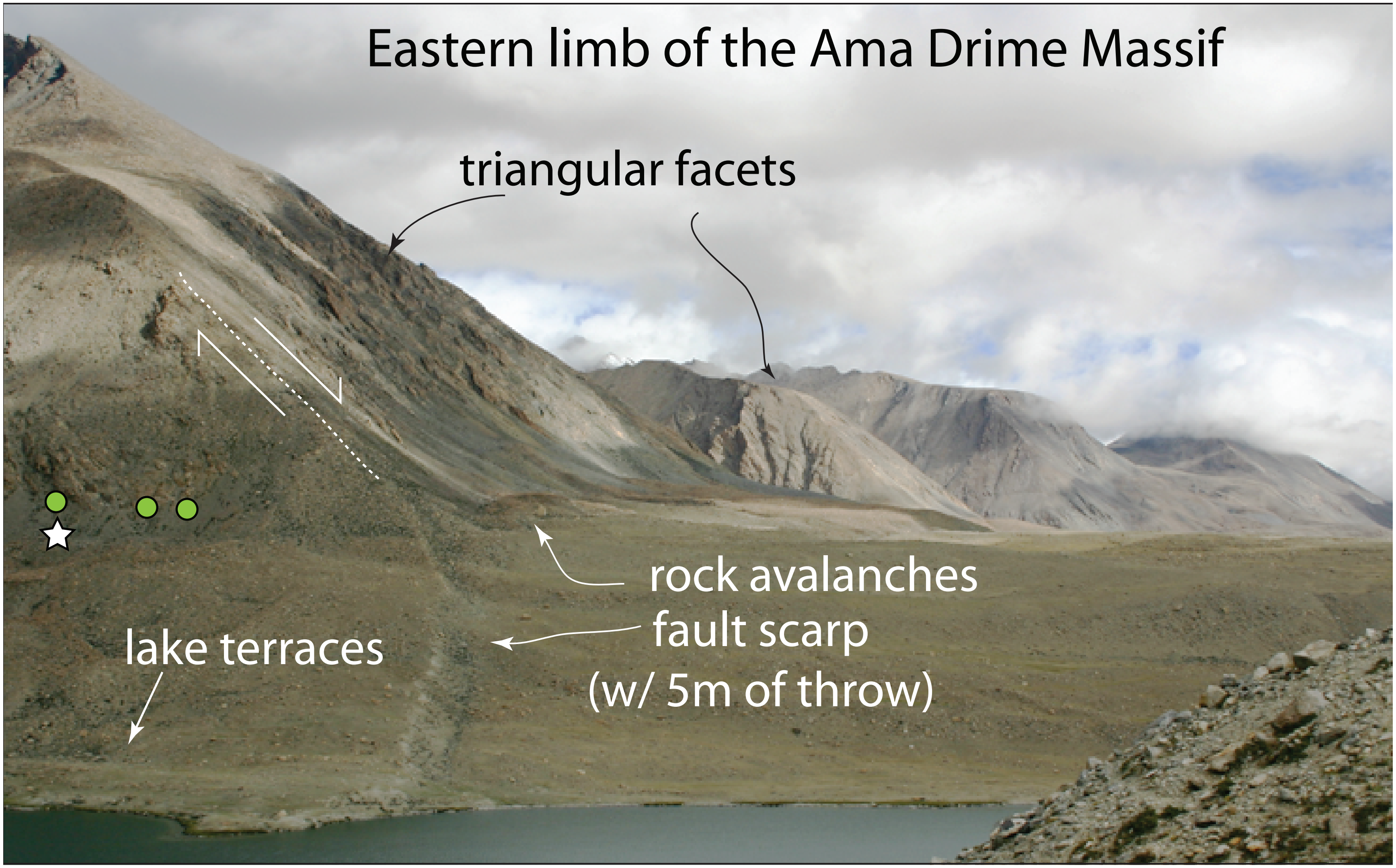

Figure 5.4. Photograph of the Ama Drime detachment on the eastern limb of the Ama Drime Massif. Taken by M.J. Jessup.

(Fig. 5.6; Finlayson et al., 2002). The erosion index for the Arun River is much higher than the surrounding area so that localized denudation in the Arun River gorge might result in focused exhumation of mid-crustal rocks (Finlayson et al., 2002; Montgomery & Stolar, 2007). Despite recent remote geomorphological investigations, the John Cottle (Oxford University) and I were the first scientists to cross the range while mapping the major structures and collecting samples in August 2006 that provide the basis of this proposal (Fig. 1). This is a funding request for a two-year international research fellowship at Oxford University to test the following novel hypothesis that builds on these expeditions, the existing literature and the applicant's experience in the Everest region:

Driven by the local extensional stress field, the Ama Drime range - potentially the most active feature in the Everest region - is being exhumed as a core complex with exhumation being enhanced by focused precipitation in the Arun River gorge.

Scientific Rationale

The Himalayan orogenic system records the collision of the Indian and Eurasian plates that began ~55 Ma and continues today (Fig. 5.1; Searle et al, 1987; Bilham et al., 1996). The resulting uplift has created the ~2500 km long Himalayas, containing the highest peaks in the world, and the Tibetan plateau with an average elevation of ~5000 m (Fielding et al., 1994). The highest peaks and greatest topography in the Himalaya occur within the surface exposures of the 5-30 km thick metamorphic and anatectic core of the orogen known as the Greater Himalayan slab (Figs. 5.1A & 5.2B; GHS). The GHS is bounded above by a north-dipping normal fault (STDS) and below by a reverse fault (Fig. 5.2B; MCTZ). The range is wrapped ~180° around the syntaxes which occur at the eastern and western extremities of the orogen resulting in complex bivergent wedge structures (Figs. 5.1, 5.2A & 5.7A; Whittington, 2004).

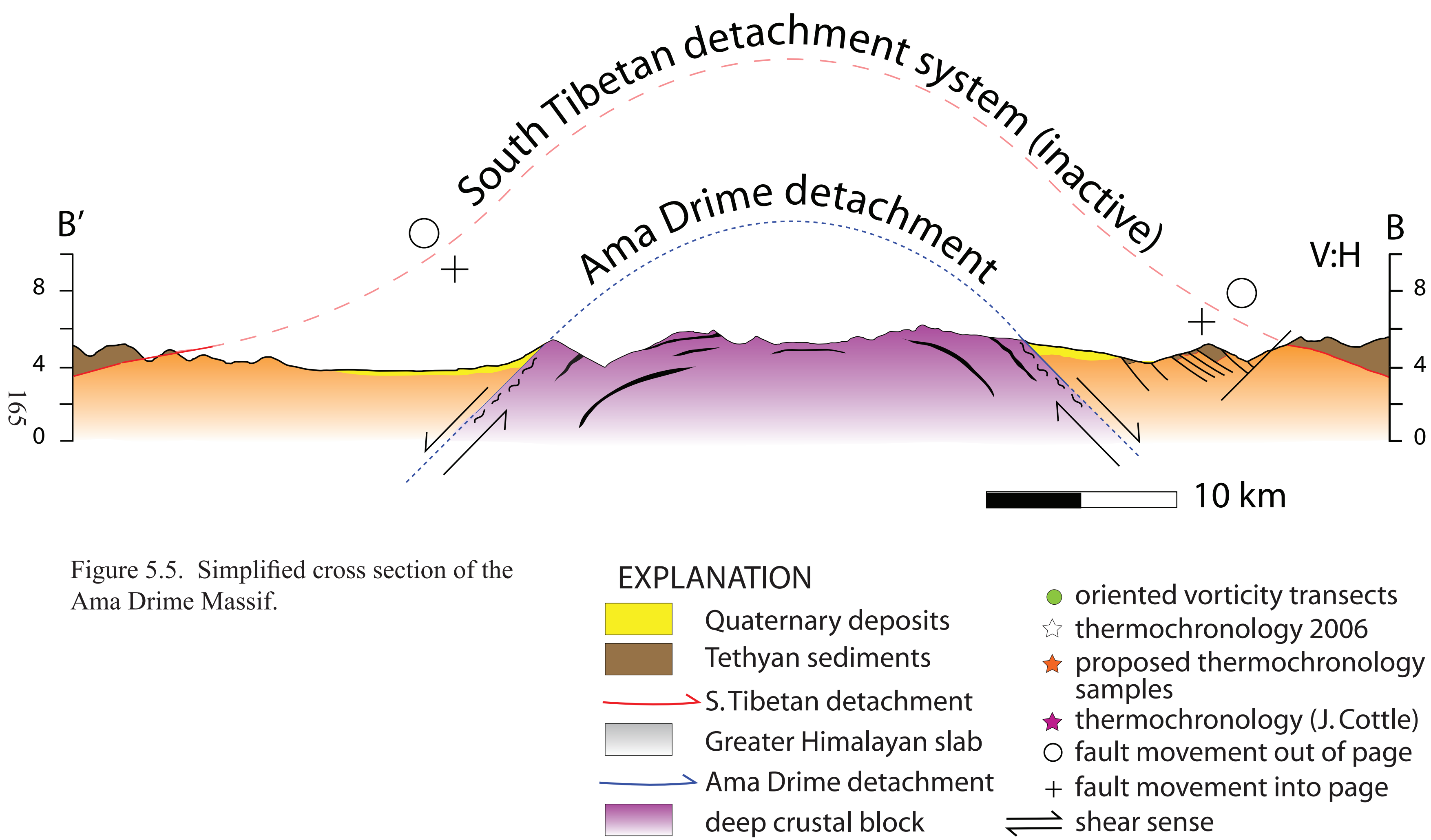

Figure 5.5. Simplified cross section of the Ama Drime Massif.

The occurrence young metamorphic massifs that coincide with either major trans-Himalayan rivers or the crest of the range are some of the most intriguing aspects of Himalayan tectonics (Brookfield, 1998; Hodges, 2000; Zeitler, 2001; Finlayson et al., 2002; Thiede et al., 2004, 2005). For this proposal, the abundant models that describe the coupling between denudation and exhumation in the Himalayas (Grujic et al., 1996; Grasemann et al., 1999) will be simplified into two main types: channel flow (Beaumont et al., 2001) and tectonic aneurism models (Zeitler et al., 2001).

Tectonic aneurisms: Geological and geophysical evidence from the eastern and western syntaxes suggests that tectonic aneurisms are responsible for very rapid exhumation of Indian plate material to the surface *via* a positive feed back between fluvial denudation and shortening accommodated by bivergent wedges (Figs. 5.1A & 5.2A; Zeitler et al., 2001; Koons et al., 2002). In the western syntaxis, the Nanga Parbat Massif, bounded by oppositely-dipping young reverse faults creates a crustal-scale pop-up structure (Figs. 5.2A & 5.7; Butler & Prior, 1988; Butler et al., 1997, 2002; Schneider et al., 1999, 2001). Steep gorges of the Indus River coincide with the Nanga Parbat Massif resulting in high fluvial erosion rates (Fig. 8; Brookfield, 1998; Zeitler et al., 2001). The main structure of the eastern syntaxis is a northeast-striking antiform that is bounded by two northeast striking strike-slip faults that results in exhumation due to rapid denudation of an active growing crustal-scale fold (Burg, 1998). Focused denudation that is enhanced by the highest precipitation rates in the Himalayas are proposed to be intimately involved with the exhumation of the Namche Barwa Massif (Zeitler et al., 2001). The main geological and geophysical evidence from the Nanga Parbat Massif that lead to the tectonic aneurism model include: 1) the bivergent wedge that bounds the massif with steep thrust faults and shear zones to create the pop-up structure, 2) the spatial coincidence of a young metamorphic massif with the Indus River gorge, 3) young anatectic dikes (1-3 Ma) in the center of the massif (Zeitler & Chamberlain, 1991), 4) cordierite-K-feldspar gneiss which reached high temperature, low pressure conditions

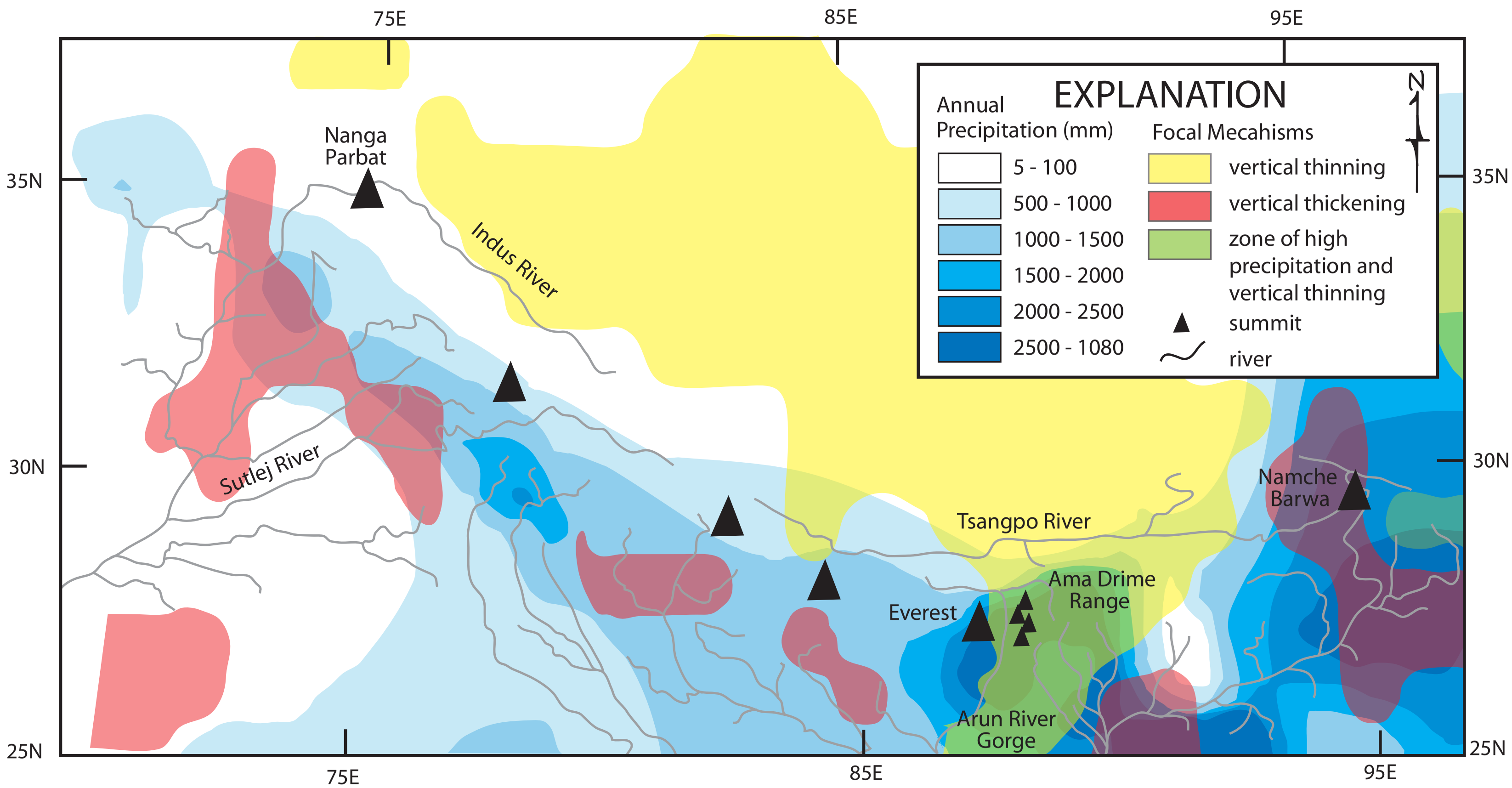

Figure 5.6. Compilation of precipitation (Finlayson et al., 2002) and geophysical data (Shapiro et al., 2004) for the Tibetan plateau and Himalayas. Blue spectrum shows precipitation variations along the orogen with the darkest shade representing highest annual precipitation (Finlayson et al., 2002). Yellow represents area where earthquakes that record crustal thinning are detected within a 200-km radius and earthquakes that record crustal thickening are absent (after Shapiro et al., 2004). Red domains contain earthquakes associated with crustal thickening within a 200-km radius and no earthquakes associated with crustal thinning (after Shapiro et al., 2004). Areas where crustal thinning and highest precipitation overlap appear as green and are spatially coincident with the Ama Drime range (small black peaks) and the Arun River gorge.

at ~3 Ma (Zeitler et al., 1993), 5) a shallow brittle ductile transition, 6) the lack of extension structure that were active < 15-20 Ma (Schneider et al., 1999). The tectonic aneurism model hypothesizes that local feedback between tectonic and surfical processes results in the formation of large metamorphic massifs. The concept central to this model is that river incision conveys eroded crustal material out of the orogenic system and aggressively cuts down to warm lower-crustal material. In response, warm lower-crustal material flows laterally, controlled by the local stress field (contractional) into the upwelling material thereby generating a young, active metamorphic massif that coincides with a major river (Fig. 5.2A; Zeitler et al., 2001).

Channel flow models: For the remainder of the orogen, south-directed extrusion models, enhanced by focused denudation along the crest of the Himalayas, are used to describe the evolution of the Himalayas during the Miocene (Fig. 5.2B; Beaumont, et al., 2001, 2004, 2006; Searle & Rex, 1989; Searle et al., 2002, 2003, 2006). Assuming simultaneous movement on the MCTZ and STDS, channel flow models propose that between ~ 22 and 16 Ma, gravity-driven southward extrusion of the GHS took place between the Tibetan plateau and the foreland of the Himalaya (Fig. 5.2B; Hodges, 2000, Hodges et al., 1992; Beaumont et al., 2001; 2004). Implicit to channel flow models are geological and geophysical evidence from decades of research in the Himalayas and Tibetan plateau including: 1) the presence of bright spots internal to the Tibetan plateau that are interpreted to represent zones of partial melt or pore-filling brine solution (Wei et al., 2001; Unsworth et al., 2005), 2) simultaneous movement on the MCTZ and STDS that provide semi-rigid boundaries to the mid-crustal channel (Burchfiel and Royden, 1985; Hodges, 2000), 3) significant partial melt (~2%) within the channel to lower the effective viscosity (Mecklenburgh & Rutter, 2003; Rosenberg & Handy, 2005), 4) gradients in lithospheric pressure between the Tibetan plateau and the Indian plate (Burchfiel and Royden, 1985; Hodges et al., 2001), 5) focused denudation on the front of the Himalayas which acts as the impetus for the tunneling mid-crustal channel

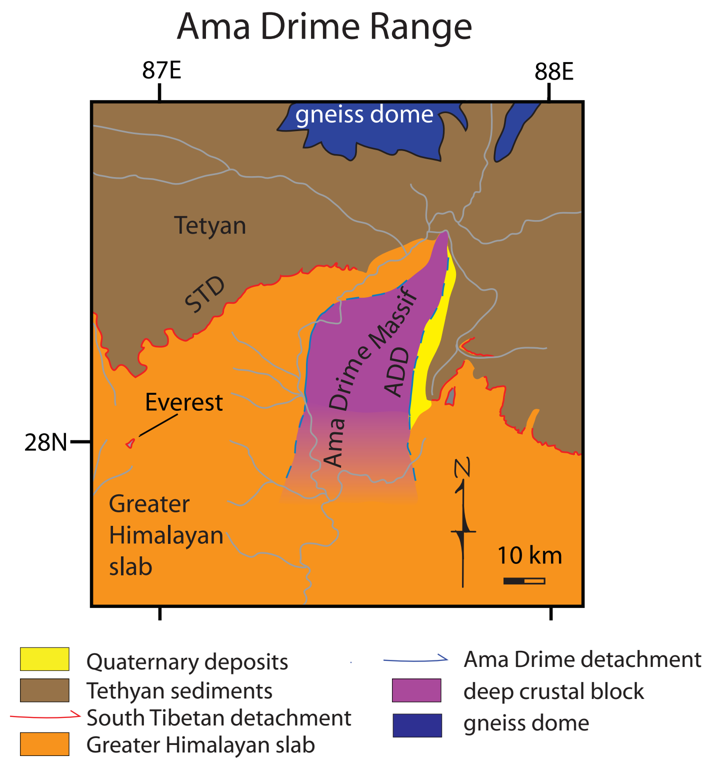

Figure 5.7. General geology of the the Ama Drime range core complex.

to reach the surface (Beaumont et al., 2001), 6) the coupling of focused denudation and exhumation of the mid-crustal channel creates a positive feed back between the two processes (Beaumont et al., 2001). Although the channel flow model focuses on the evolution of the Himalayas during the Miocene, some recent data suggest that some minor area along the MCTZ still contain out of sequence active structures (Wobus et al., 2003).

The rate-of-erosion index (EI) for Himalayan rivers suggests that the coupling between mid-crustal flow and focused denudation, a relatively well-documented phenomenon for the syntaxes, could occur on a finer scale in drainages throughout the orogen, particularly those associated with high levels of precipitation and metamorphic massifs (Finlayson et al., 2002). $^{40}Ar/^{39}Ar$ white mica ages from the Sutlej region demonstrates that exhumation of the GHS occurred during early to middle Miocene, at

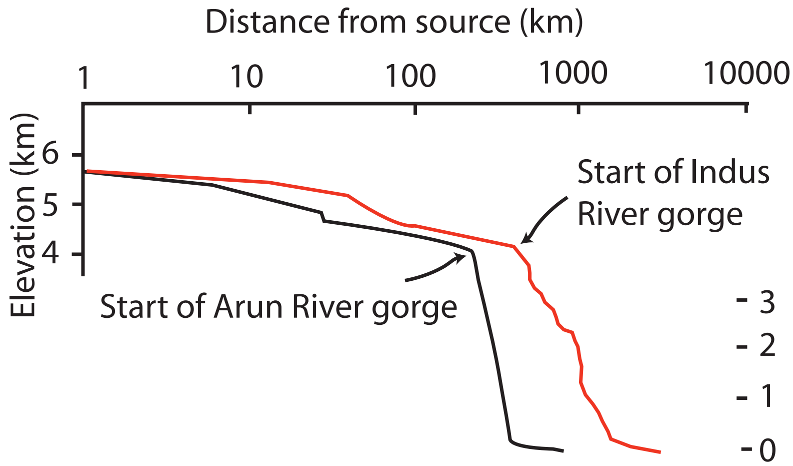

Figure 5.8. Comparison of river profiles for the Arun (black line) and Indus (red line) after Brookfield (1998).

which point the locust of exhumation migrated southward to the Lesser Himalaya which were exhumed during the Miocene to Pliocene (Thiede et al., 2005). Apatite fission track analyses from the same suite of samples record synchronous exhumation across NE-SW striking, 80-40 km wide area that coincides with the highest local precipitation rates (Thiede et a., 2004, 2005). Of the trans-Himalayan rivers that have higher EI potential (Arun, Indus, Sutlej & Tsangpo) than the remainder of the Himalayas, the Arun is particularly promising for exploring the interaction between denudation and exhumation (Finlayson, et al., 2002). The Arun River profile is as steep and, in places, steeper than the Indus River (Fig. 5.8; Brookfield, 1998; Zeitler et al., 2001) and coincides with the highest precipitation in the Himalayas, comparable only to the eastern syntaxis (Finlayson et al., 2002). The Arun River also follows the Arun antiform. These observations lead Montgomery & Stolar (2006) to posit that the occurrence of the Arun River and the Arun antiform was not a coincidence associated purely with antecedence, but rather a reflection of a potentially very important interaction between denudation and exhumation related to localized mid-crustal flow. Despite having strong geomorphological evidence for a potential interaction between the mid-crust, exhumation and denudation in the Arun River and the Arun anticline, without accurate structural data Montgomery & Stolar (2006) were unable to identify the processes responsible for their observations.

Furthermore, focal mechanism solutions for this part of the Himalayas show that the mid-to lower-crust are actively thinning where thickening is generally predicted to be dominant (Shapiro et al., 2004).

Geology of the Ama Drime Massif

Aside from reconnaissance work on the eastern limb by Burchfiel et al., (1992) and general descriptions, prior to this investigation the detailed structural setting of the ADM, whose southern end is deeply rooted in the Arun River gorge was essentially unknown or improperly mapped (Carosi, 1999; Visona & Lombardo, 2002). The following section provides an overview of the main geologic features that we mapped and sampled during two-field season in the summer 2005 & 2006 that form the basis for this proposal. The ADM trends north-south and extends northwards ~ 70 km from the crest of the Himalayas. Over this length, the width of the ADM progressively thins from 30 km to a narrow point where the high grade gneisses of the range plunges beneath the overlying low-grade metasedimentary rocks (Fig. 5.3). The margins of the ADM are clearly defined by a physiographic transition from the rugged topography created by the gneiss common to the internal sections of the range and the surrounding expansive alluvial fans and rock avalanche deposits (Fig. 5.3). 200 – 300 m thick high-strain zones within marble, calc-silicate, augen gneiss and quartzite bound the widest part of the ADM and are here termed the Ama Drime detachment (ADD). These strike north-south, dip 45° away from the core and record a complete transition from distributed shear zones, through mylonites and into ultramylonites (Fig. 5.4). When viewed parallel to the well-developed down-dip stretching lineation, asymmetric forward-and back-rotated sigma and delta clasts and S-C extensional shear bands consistently record extensional shear sense. Brittle detachments also record top-down extensional shear sense and are filled with fault gouge. Our results from the ADD agree with Burchfiel et al., (1992) for the eastern limb, but disagree with Carosi (1999) and Visona & Lombardo (2002) whose maps suggest that the western limb of the ADD is the MCTZ. The shear zones split the migmatitic gneiss common to the Greater Himalayan slab in the hanging wall above and the deep crustal block with granulite facies mafic lenses below. Triangular facets, between the gorges with the best exposure of the mylonite zones, are interpreted to be the fault surfaces that dip beneath the alluvial fans (Fig. 5.4). Rock avalanche deposits that accumulate at the base of these triangular facets are sourced high on the fault surface. A fault scarp with a vertical offset of ~5 m offsets young lacustrine, fluvial and alluvial deposits on the eastern limb of the range, suggesting recent seismic activity (Fig. 5.4). The internal structure of the ADM includes a pervasive fabric, with foliation parallel mafic lenses; higher strain zones occasionally occur. Based on the progression of deformation mechanisms and consistent shear sense the ADM is interpreted to be a core complex that is exhuming a deep crustal block during east-west extension (Fig. 5.5). The northern extent of the ADD is impossible to determine without additional field constraints, however several possibilities exist: 1) the shear zones continue to the nose of the range, 2) the shear zone displacement decreases northward towards the north until the nose where there is essentially no displacement, 3) a transition occurs from shear zones to folded limbs of an antiform (Fig. 5.3).

Interpreting the ADM as a core complex implies that lithospheric thinning attenuates the crust (pure shear) and an upwelling dome of mid-crustal material is exhumed to the surface along a detachment system (Lister and Davis, 1989). Interestingly, of the three main types of geometries for rapidly exhuming mid-crustal rocks - bivergent wedge (Fig 5.2A), channel flow (Fig 5.2B), and core complex (Fig 5.2C) - the most rapid exhumation is predicted to occur for core complexes due to the combined force of extension and buoyancy driven doming (Whittington, 2004).

Core complexes are typically found in tectonic settings dominated by lithospheric thinning such as the Basin and Range, USA or the Cordillera of western Canada. A few core complexes have been observed in the Himalayas, particularly the

South Tibetan gneiss domes (Chen et al., 1990) but subsequent investigation proposed that these were features whose doming was related to the evolution of the Himalayas during the Miocene and do not represent modern extension (Lee & Whitehouse, 2006; Lee et al., 2004). Other domes along the front of the Himalayas (i.e., Gurla Mandhata) have been attributed to complex transpressional accommodation zones were major strike-slip faults (e.g., the Karakoram fault; Searle et al, 1996) intersect the Himalayas (Murphy et al., 2001).

Pressure-temperature estimates for footwall rocks in the core complex are limited to data from the western limb and preliminary data from my collaborator, John Cottle (PhD candidate at Oxford University). The footwall is composed of migmatitic gneiss and leucogranite sills that are parallel to the main fabric in addition to cross cutting leucogranite dikes that post-date the main fabric-forming event. Preliminary petrography on foliation parallel mafic lenses and pods suggests that these reached granulite facies metamorphic conditions. Upon further petrographic inspection, the core of these mafic lenses preserves pristine eclogites. Based on this preliminary information, the footwall rocks are interpreted to include the deepest structural position exposed in the central Himalayas. Dating the eclogite lenses, migmatitic gneiss and late-stage crosscutting leucogranite dikes constitutes a major component of John Cottle's Ph.D. project and complements this research proposal.

The ADM displaces the STDS (Fig. 5.5) which has several implications for constraining the tectonic evolution of the ADM and the Himalayas: 1) exhumation of the ADM as a core complex during east-west extension must post-date the last top-to-the-north extensional motion on the STDS (generally thought to be <17 Ma in the Everest region (Murphy & Harrison, 1999). Since the STDS and MCTZ are thought have acted simultaneously, this also suggests that exhumation of the ADM post-dated southward extrusion of the GHS during the Miocene (i.e., channel flow models). This evidence suggests that following south-directed extrusion of the GHS to accommodate crustal shortening, as recoded in the Everest region the stress field changed to lithospheric thinning (Shapiro et al., 2004). The agreement between field observations and geophysical data suggest that this area of the Himalayas is experiencing lithospheric thinning - not thickening.

A working hypothesis for the Ama Drime Massif

The critical observations about the ADM, from the new data presented in this proposal as well as existing research in the remainder of the Himalayas, that lead to the working hypothesis for the ADM are as follows: 1) the mid-to lower-crust beneath the ADM is dominated by lithospheric thinning – not thickening (Shapiro et al., 2004), 2) the deepest structural position in this part of the Himalayas is exposed by the ADM, 3) the highest modern precipitation levels outside of the eastern syntaxis occur in the Arun River gorge on the southern end of the ADM (Finlayson et al., 2002), 4) the Arun River gorge is as steep or steeper than the Indus River gorge (Brookfield, 1998; Zeitler et al., 2001) and 5) the ADM is a core complex that record active east-west extension. These data are the basis for the proposed hypothesis (Fig. 5.2C):

> *Driven by the local extensional stress field, the Ama Drime range - potentially the most active feature in the Everest region - is being exhumed as a core complex with exhumation being enhanced by focused precipitation in the Arun River gorge.*

Proposed Research

Introduction

There are several tests to determine if ADM is a core complex that exhumes a deep crustal block during east-west extension that is coupled to focused precipitation/ erosion: 1) the regional structure of the range, including the northern extent of the bounding faults; 2) the spatial and temporal variability in flow of the mid-and-lower crust, particularly in high-strain zones; 3) spatial and temporal variability in the exhumation history of the range. To constrain these parameters this project will integrate field mapping and vorticity investigations with (U-Th)/He and zircon-and apatite-fission track low-temperature thermochonometry. Much of this work will rely heavily on samples and field mapping produced during two field seasons conducted by M. Jessup and J. Cottle (PhD candidate, Oxford) in 2005 and 2006. An additional field season is proposed for the summer 2008 to map and sample the northern section of the ADM. Vorticity analysis will focus on samples collected from the eastern and western limbs of the ADD. Collected during 2005 and 2006, 30 oriented samples from three drainages on the western limb and 10 (see green circles Fig. 5.4) from a single valley on the eastern limb are very promising for vorticity analysis (Fig. 5.9). Zircon-and apatite-fission track as well as (U-Th)/He thermochonometry will be conducted on a suite of 40 samples through the range. The suite collected during 2006 included three hangingwall and 21 footwall samples. The footwall samples are from the two major drainages on the eastern limb, a pass (5300m) a minor summit (5500m) and the eastern limb of the ADM (white stars Fig. 5.4). During the 2008 expedition, 16 additional samples will be collected on several smaller transects across the northern section of the range including the hinge zone at the "nose" of the range (orange stars, Fig. 5.4).

Once constrained, the spatial and temporal distribution in vorticity of flow and exhumation of mid-crustal rocks in the ADM will be combined with existing thermobarometric, geophysical and geomorphological data to test the working hypothesis presented in this proposal. Equally important, is that these results will compliment current research projects within the Himalayan tectonics group at Oxford aimed at dating eclogites, migmatization and crosscutting dikes and thermobarometry in the hangingwall and footwall of the ADD (J. Cottle), as well as the exhumation history of the hangingwall on the western (see red stars on Fig. 4) and southern sides of the ADM as constrained by low-temperature thermochonometry (M. Streule).

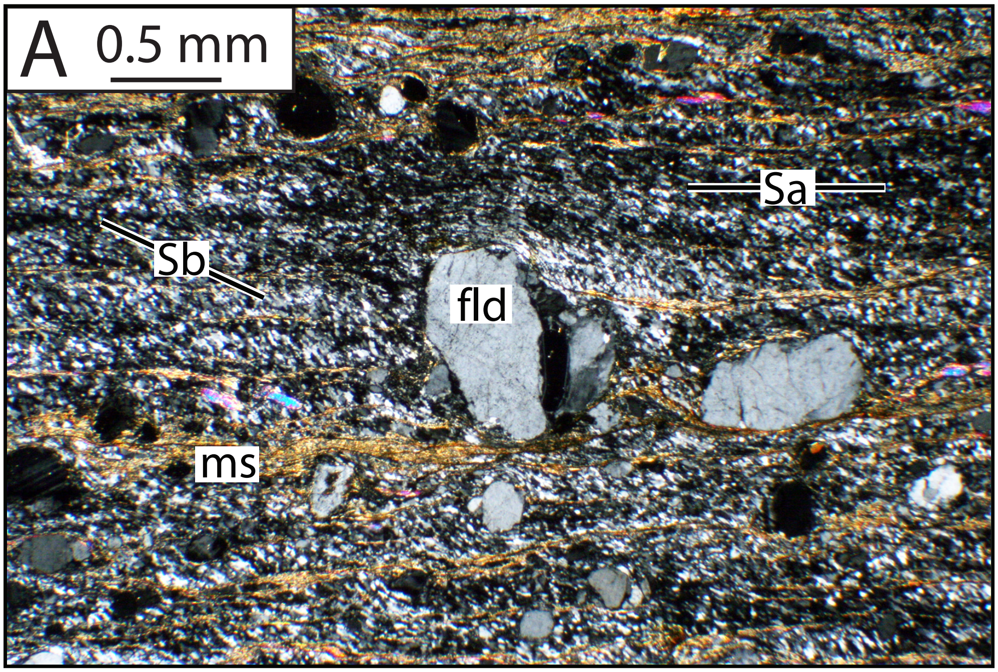

Figure 5.9. Photomicrograph with crossed polars of a mylonite sample KA-05-01 collected in 2005. Rigid porphyroclasts of feldspar are rotating in a ductile quartz matrix. The main fabric (Sa) is well-developed and associated with an oblique fabric defined by aligned quartz (Sb) form and angle of ~23° from each other. B. Preliminary vorticity results on sample KA-05-01 using the Rigid Grain Net (RGN) after Jessup et al., (2007) of 96 feldspar porphyroclasts. The red zone highlights the range in W_m = 0.60 - 0.70 estimates as defined by the transition between grains that rotate infinity (B* < 0.60) and those that reach a stable sink position (B* > 0.70). Image taken by M.J. Jessup.

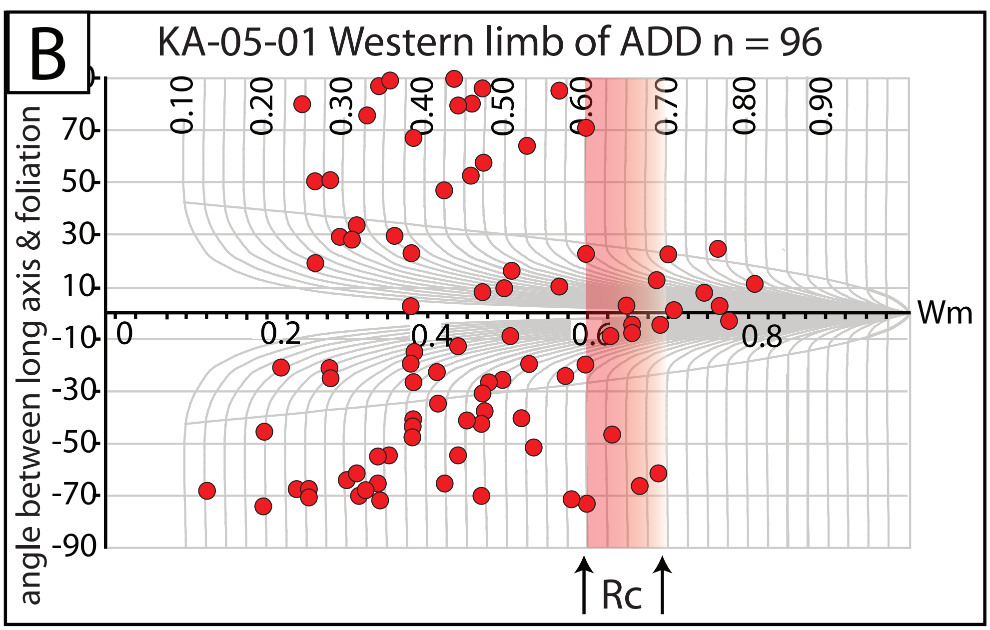

Spatial and temporal variations in vorticity of flow

To characterize the type of mid-crustal flow that was involved in the exhumation of the ADM, including deformation temperatures, shear sense and the relative contribution of pure and simple shear, this project will involve detailed kinematic and vorticity analyses of the ADD. Standard petrographic analyses will constrain the dominant deformation mechanisms in phases such as quartz and feldspar, which in turn provide general estimates of deformation temperatures (Hirth and Tullis, 1992). Defining shear sense is another priority for early stages of petrography. Appropriate samples will be used for vorticity analysis to quantify the relative contributions of pure and simple shear. Mean kinematic vorticity number (W_m) is a direct estimate of the relative contributions of pure ($W_m = 0$) and simple ($W_m = 1$) shear during steady-state flow in high strain zones (Means et al., 1980). Vorticity analysis is now commonly employed to characterize flow within shear zones in a variety of tectonic settings (e.g., Klepeis et al., 1999; Xypolias and Doutos, 2000; Holcombe and Little, 2001; Xypolias and Koukouvelas, 2001; Bailey and Ester, 2003; Law et al., 2004; Jessup et al., 2006). Recent, and on-going, vorticity analysis on samples from within the STDS and MCTZ exposed by the Everest Massif attest to its applicability to shear zones in the Himalayas (Law et al., 2004; Jessup et al., 2006). These results demonstrated that exhumation of the GHS was partitioned in the bounding shear zones (Jessup et al., 2006), rather than being distributed throughout the slab, as predicted by some variations of extrusion models (Grujic et al., 1996, 2002). More specifically, Jessup et al., (2006) indicate that the highest contributions of simple shear are recorded by calc-mylonites in the STDS, while the base of the slab records higher contributions of pure shear which they attribute to increased lithostatic pressure created by the overlaying GHS. Because of this early effort, identifying high strain zones in the Himalayas that are appropriate for estimating W_m is now much more robust.

An additional outcome of vorticity work in the Everest region, is a new vorticity method (the Rigid Grain Net) that has also proven to be the most appropriate for vorticity analysis of Himalayan shear zones (Jessup et al., 2007). Attempts to use the aspect ratio and orientation of rigid objects rotating in a non-Newtonian fluid (flowing matrix) to define W_m began with the pioneering work of Jeffery (1922) and Ghosh and Ramberg (1976). Subsequent investigations contributed further to these founding principles by applying the early theory to geologic samples (Passchier, 1987; Simpson and De Paor, 1993, 1997; Wallis, 1992, 1995; Wallis et al., 1993). Models for the rotation of elliptical objects in a non-Newtonian fluid demonstrate that during simple shear (W_m = 1), rigid objects will rotate infinitely, regardless of their aspect ratio. With increasing contributions of pure shear ($0 < W_m < 1$), porphyroclasts will either rotate with the simple shear component (forward) or against it (backward) until they reach a stable-sink (R_c) that is unique to W_m (Fig. 5.5B; Ghosh and Ramberg, 1976; Passchier, 1987; Simpson and De Paor, 1993, 1997). The Rigid Grain Net (RGN) standardizes vorticity analysis using rigid porphyroclast in a flowing matrix, eases plotting of data, and limits ambiguity in estimating W_m. All samples analyzed for vorticity will employ the RGN and the methods as descried by Jessup et al., (2007).

Field observations and preliminary petrographic analysis demonstrates that the bounding shear zones contain the mylonites that are optimal for vorticity analysis. Because the shear zones form within a variety of protolith material, including calc-silicates, quartzite and granites, the mylonites zones contain a matrix of quartz with rigid porphyroclasts that display a range in orientations and aspect ratios that are ideal for vorticity analysis using the RGN (Fig. 5.9A, B). Preliminary vorticity analysis from a mylonitic quartzite on the zone on the eastern limb of the ADD yields a well-define critical threshold between grains that rotate infinitely ($W_m \leq 0.60$) and those that reach a stable-sink position ($W_m \geq 0.70$; Fig. 5.9B) indicating a W_m = 0.60-0.70.

Low-temperature thermochronology

To constrain the exhumation of the ADM, as well as any spatial and temporal variability in exhumation rates, low-temperature thermochronology will be conducted on samples collected on the margins as well as the core of the ADM. Thermochronology dates the time at which particular minerals in a rock are exhumed through a specific temperature interval (Dodson, 1973). If more than one thermochronological system is used, then exhumation rates can be interfered by calculating the time lapse between when the rock was exhumed through both known closure systems (Kirby et al., 2001; Reiners et al., 2003; Thiede et al., 2005). The typical range of temperatures recorded by low-temperature thermochronometers is ~70°C for (U-Th)/He on apatite (Wolf et al., 1996, 1998; Shuster & Farley, 2003), ~100° for apatite-fission track and ~175°C for zircon-fission track (Gunnell, 2000). (U-Th)/He dating of apatite relies on radioactive decay of U and Th isotopes that contribute to the accumulation of He (Wolf et al., 1996). Samples are analyzed on a mass spectrometer to measure the concentration of each isotope, which is then used to solve the age equation iteratively to calculate the final age. The apatite and zircon fission track method involves counting tracks (damage zones) created by spontaneous fission of ^{238}U isotopes during irradiation of the sample. If complete annealing of apatite (i.e., temperatures exceed the partial annealing zone (PAZ; ~60-100°C)) occurred then the age apatite fission tracks (AFT) can be used to constrain the exhumation history through ~100°± 20°C (Naeser & Faul 1969). Since the number of tracks is directly related to age, by counting the number of tracks in a sample an age can be calculated. The track length distribution with the AFT age has the potential to constrain the temperature-time history of the rock (Gleadow et al. 1986). Apatite fission tracks are longer for rocks that cooled quickly and shorter for those that cooled slowly through the closure temperature (Gleadow et al. 1986). Exhumation rates of the samples are then inferred from these thermochronometers. Estimating exhumation rates in extensional setting must be made with caution because range bounding faults bring relatively hot footwall into juxtaposition with a relatively cool hanging wall block and thereby disturb the geotherm (Mancktelow & Grasemann, 1997; Ehlers et al., 2001).

Thermochonometry will be conducted with the London Thermochronology Research Group, University College London under the supervision of Dr. Andrew Carter. Dr. Carter is currently working with M. Streule and J. Cottle on other samples from the Everest region. I will be involved with all aspects of data acquisition from sample preparation, fission track counting and (U-Th)/He isotopic analysis on the Quadrupole mass spectrometer. The Oxford Himalayan tectonics research group is currently working on several projects with the Thermochronology Research Group and the relatively close proximity to Oxford makes it the best option for processing these samples.

Expedition to the Ama Drime Massif

A two-month-long expedition to the northern half of ADM in the summer 2008 will have two main priorities: 1) sample for thermochronology in the core and margins of the ADM (see orange stars Fig. 5.4), 2) map the extent of the ADD while sampling appropriate material for vorticity analysis. My experience from four scientific expeditions to this area of Tibet will be used to ensure that all the standard logistics of a successful expedition are accounted for. Mandatory for exploring remote reaches of the ADM is a field assistant, to help with sampling and for safety reasons. J. Cottle or M. Streule are the most appropriate candidates for a field assistant during this expedition. Samples will be sent to Oxford from Kathmandu. Oriented samples for kinematic analysis will be cut and processed into thin sections using the thin section lab in the Dept. of Earth Sciences, Oxford University.

Timeline of Project

Although the scope of this project is large, successful execution of the objectives outlined in this proposal should be possible in the two-year period as a research fellow at Oxford University because the majority of fieldwork and sample collection was conducted during the summer 2005 and 2006. This project will involve the close collaboration between the applicant and the Himalayan tectonics research group at Oxford University and their on-going projects in the Everest region. During this time Dr. Michael Searle will mentor the applicant throughout the two-year project in the field, laboratory and writing manuscripts.

Year One

The first year will initially center on processing the samples collected during previous expeditions to the Ama Drime Massif. Petrographic work will focus standard microstructural analysis as well as more involved vorticity analysis on appropriate samples. Samples for thermochronology will be processed at London Thermochronology Research Group, University College London under the supervision of Dr. Andrew Carter. The applicant will present results at the annual Himalayan-Tibet workshop meeting in the spring. A two-month expedition to the Ama Drime Massif in the summer of 2008, with a field assistant (potentially John Cottle or Mike Streule), will access the northern section of the range. Goals of this trip include mapping the northern limits of the bounding shear zones, taking additional oriented samples for structural analysis as well as larger samples for the thermochronology.

Year Two

During the second year, the applicant will be based in Oxford University and continue to analyze thermochronology and vorticity samples. At this time, ages from other on-going projects in the Oxford Himalayan tectonics group will be near completion and a regional tectonic history of the Everest region will begin to be pieced together. Again, the applicant will present results at Himalayan-Tibet workshop in the spring and publish several manuscripts.

Long-term research goals

The success of a modern structural geologist's contribution to tectonic-scale research hinges on many things, but perhaps most important is the ability to tie research specialties into the broader tectonic context, to envision creative opportunities that integrate them with other disciplines, and to work within a collaborative research team. This approach cultivates a movement away from small, focused research projects and towards a more holistic approach to geoscience in the larger context of Earth Systems Science. The prospect of integrating my specialties, structural geology and metamorphic petrology, with interdisciplinary and collaborative research aimed at constraining cutting-edge tectonic questions, as well as bringing a diverse group of graduate and undergraduate students into this research, motivate me to pursue a career in academic geoscience. To elevate and expand my research to a competitive level that will help me bring my research program to the professional level necessary for being a competitive applicant for the next step towards an academic career in geosciences, I am applying for a two-year NSF international research fellowship to work with Dr. Michael Searle and the Himalayan tectonics group at the Department of Earth Sciences, Oxford University.

Budget Breakdown and justification

This budget proposal includes two years of support for Micah J. Jessup as a research fellow at Oxford University, analytical costs for thermochronology, and a two-month-long field season during the summer 2008.

ROUNDTRIP AIRFARE

Roanoke VA, US to London, UK			**$1,500**

RELOCATION ALLOWANCE **$2,500**

LIVING ALLOWANCE

Maximum per diem for Oxford	$332/day		
Full-rate first month		$9,960/month	
Half-rate thereafter		$4,980/month	
Monthly stipend	$5,395/month		
Maximum stipend		$5,000/month	
Total stipend 24 months			
		$120,000	

HEALTH INSURANCE	$150/month	**$3,600**
ATTENDING CONFERENCES		**$3,000**
INSTITUTIONAL ALLOWANCE	$500/month	**$12,000**

LABORATORY WORK AND SUPPLIES

Thermochonometry will be conducted with the London Thermochronology Research Group, University College London. Prices included in this proposal are minimum costs based on the applicant's involvement in all levels of data acquisition from sample preparation to analysis. The Oxford Himalayan tectonics research group is currently working on several projects with the Thermochronology Research Group and the relatively close proximity to Oxford makes it the best option for processing these samples. Oriented samples for vorticity analysis will be processed into thin sections using the thin section lab at the Department of Earth Sciences, Oxford University. Cost estimates are based on in-house fees for 100 thin sections.

Thermochronology Analyses for 40 samples

Apatite fission track	$190/ea	$7,600
Zircon fission track	$190/ea	$7,600
(U-Th)/He	$190/ea	$7,600

100 Thin sections

Thin sections	$5/ea	$500	
Total			**$23,300**

IN-COUNTRY TRAVEL

When processing samples at the University College London travel to and from Oxford will be by train. Cost estimates included this is for 25 trips during the two years in Oxford.

Round-trip train tickets from Oxford to London $26/ea * 25 **$650**

EXPEDITION COSTS

A two-month-long expedition to the Ama Drime range in the summer 2008 will enable the applicant to map and sample for thermochronology and vorticity along the margins and the northern part of the Ama Drime range. Cost estimates for this trip are based on expenses during a field season to the same area in 2006 and are kept to an absolute minimum. Because ground travel between Kathmandu, Nepal and Tibet are often delayed due to inclement weather, a requisite four-day pre-and post-expedition "buffer" in Kathmandu is included in this budget proposal. Cost estimates for eight days in Kathmandu are using maximum per diem rates. A field assistant is mandatory for exploring remote reaches of the Ama Drime range and cost for this are included in the budget proposal.

Airfare London to Kathmandu			
Applicant		$1,400	
Field Assistant			$1,400
8 days of Kathmandu per diem for applicant	$157/day		$1256
8 days of Kathmandu per diem for assistant	$157/day		$1256

Kathmandu to Tibet border		$400	
Jeep hire for two months	$7600		
Applicant Tibet visas for US nationalities		$63	
Assistant Tibet visas for British nationalities		$63	
Applicant Entry permit and service fees	$50		
Assistant Entry permit and service fees		$50	
Provisions for two months		$1000	
TOTAL			**$14,538**

TOTAL BUDGET	**$181,088**

References Cited

Bailey, C.M. & Eyster, E.L. 2003. General shear deformation in the Pinaleno Mountains metamorphic core complex, Arizona. *Journal of Structural Geology*, **25**, 1883-1892.

Beaumont, C., Jamieson, R.A., Nguyen, M.H. & Lee, B., 2001. Himalayan tectonics explained by extrusion of a low-viscosity crustal channel coupled to focused surface denudation. *Nature*, **414**, 738-742.

Beaumont, C., Jamieson, R.A., Nguyen, M.H. & Medvedev, S. 2004. Crustal channel flows: 1. Numerical models with applications to the tectonics of the Himalayan – Tibetan orogen. *Journal of Geophysical Research*, **109**, B06406 29p.

Beaumont C., Nguyen, M., Jamieson, R. & Ellis, S. 2006. Crustal flow modes in large hot orogens. *In*: Law, R. D., Searle, M. P. & Godin, L. (eds) *Channel Flow, Extrusion, and Exhumation in Continental Collision Zones.* Geological Society, London, Special Publications, **268**, 91-145.

Bilham, R., Larson, K.M., Freymueller, J.T., Jouanne, F., Le Fort, P., Leturmy, P., Mugnier, J.L, Gamond, J.F., Glot, J.P., Martinod, J., Chaudury, N.L., Chitrakar, G.R., Gautam, U.P., Koirala, B.P., Pandey, M.R., Ranabhat, R., Sapkota, S.N., Shrestha, P.L., Thakuri, M.C., Timilsina, U.R., Tiwari, D.R., Vidal, G., Vigny, C., Galy, A., de Voogd, B. 1997. GPS measurements of present-day convergence across the Nepal Himalaya. *Nature*, **386**, 61-64.

Brookfield, M.E. 1998. The evolution of the great river systems of southern Asia during the Cenozoic India-Asia collision; river draining southwards. *Geomorphology*, **22**, 285-312.

Burchfiel, B.C., Zhiliang, C., Hodges, K.V., Yuping, L., Royden, L., Changrong, D. & Jiene, X. 1992. The South Tibetan Detachment System, Himalayan Orogen: extension contemporaneous with and parallel to shortening in a collisional mountain belt. *Geological Society of America Special Paper*, **269**, 41 p.

Burchfiel, B.C. & Royden, L.H. 1985. North-south extension within the convergent Himalayan region. *Geology*, **13**, 10; 679-682.

Burg, J-P, Nievergelt, P., Oberli, F., Seward, D., Davy., P., Maurin, J-C., Dia, Z., Martin, M. 1998. The Namche Barwa syntaxis; evidence for exhumation related to compressional crustal folding. *Journal of Asian Earth Sciences*, **16**, 239-252.

Butler, R. & W.H., Prior, D. 1988. Tectonic controls on the uplift of the Nanga Parbat Massif, Pakistan Himalayas. *Nature*, **333**, 247-250.

Butler, R.W.H., Harris, N.B.W., & Whittington, A.G. 1997. Interactions between deformation, magmatism and hydrothermal activity during active crustal thickening. *Mineralogical Magazine*, **61**, 37-51.

Butler, R.W.H., Casey, M., Lloyd, G.E., Bond, C.E., McDade, P., Shipton, Z. & Jones, R. 2002. Vertical stretching and crust thickening at Nanga Parbat, Pakistan Himalaya; a model for distributed continental deformation during mountain building. *Tectonics*, **21**, 17.

Carosi, R., Lombardo, B., Musumeci, G. & Pertusati, P. 1999. Geology of the Higher Himalayan crystallines in Khumbu Himal (Eastern Nepal). *Journal of Asian Earth Sciences*, **17**, 785-803.

Chen, Z., Liu, Y., Hodges, K.V., Burchfiel, B.C., Royden, L.H. & Deng, C. 1990. The Kangmar Dome: A metamorphic Core Complex in Southern Xizang (Tibet): *Science*, **250**, 1552-1556.

Dodson, M.H. 1973. Closure Temperature in Cooling Geochronological and Petrological Systems. *Contributions to Mineralogy and Petrology*, **40**, 259-274.

Ehlers, T.A., Armstrong, P.A. & Chapman, D.S. 2001. Normal fault thermal regimes and the interpretation of low-temperature thermochronometers. *Physics of the Earth and Planetary Interiors*, **126**, 179-194.

Fielding, E., Isacks,B., Barazangi, M. & Duncan, C. 1994. How flat is Tibet? *Geology*, **22**, 163-7.

Finlayson, D.P., Montgomery, D.R. & Hallet, B. 2002. Spatial coincidence of rapid inferred erosion with young metamorphic massifs in the Himalayas. *Geology*, **30**, 219-222.

Ghosh, S. K. & Ramberg, H. 1976. Reorientation of inclusions by combination of pure and simple shear. *Tectonophysics*, **34**, 1-70.

Gleadow, A.J.W., Duddy, I.R., Green, P.F. & Hegarty, K.A. 1986. Fission track lengths in the apatite annealing zone and the interpretation of mixed ages. *Earth and Planetary Science Letters*, **78**, 245-254.

Grasemann, B., Fritz, H. & Vannay, J-C. 1999. Quantitative kinematic flow analysis from the Main Central Thrust zone, (NW Himalaya): implications for a decelerating strain path and the extrusion of orogenic wedges. *Journal of Structural Geology*, **21**, 837-53.

Grujic, D., Casey, M., Davidson, C., Hollister, L., Kundig, K., Pavlis, T. & Schmid, S. 1996. Ductile extrusion of the Higher Himalayan crystalline in Bhutan: evidence from quartz microfabrics. *Tectonophysics*, **260**, 21-43.

Grujic, D., Hollister, L. & Parrish, R.R. 2002. Himalayan metamorphic sequence as an orogenic channel: insight from Bhutan. *Earth and Planetary Science Letters*, **198**, 177-191.

Grujic, D. 2006. Channel flow and continental collision tectonics: an overview. *In*: Law, R. D., Searle, M. P. & Godin, L. (eds) *Channel Flow, Extrusion, and Exhumation in Continental Collision Zones.* Geological Society, London, Special Publications, **268**, 25-37.

Gunnell, Y. 2000. Apatite fission track thermochronology: an overview of its potential and limitations in geomorphology. *Basin Research*, **12**, 115-132.

Hirth, G. & Tullis, J. 1992. Dislocation creep regimes in quartz aggregates. *Journal of Structural Geology*, **14**, 145-160.

Hodges, K. V., Parrish, R. R., Housch, T. B., Lux, D. R., Burchfiel, B. C., Royden, L. H. & Chen, Z. 1992. Simultaneous Miocene extension and shortening in the Himalayan orogen. *Science*, **258**, 1466-1470.

Hodges, K. V. 2000. Tectonics of the Himalaya and southern Tibet from two perspectives. *Geological Society of America Bulletin*, **112**, 324-350.

Hodges, K.V., Hurtado, J.M. & Whipple, K.X. 2001. Southward extrusion of Tibetan crust and its effect on Himalayan tectonics. *Tectonics*, **20**, 799-809.

Holcombe, R.J. & Little, T.A. 2001. A sensitive vorticity gauge using rotated porphyroblasts and its application to rocks adjacent to the Alpine Fault, New Zealand. *Journal of Structural Geology,* **23**, 979-990.

Jeffrey, G. B. 1922. The motion of ellipsoidal particles immersed in a viscous fluid. *Proceedings of the Royal Society of London.* **A102**, 161-179.

Jessup, M.J., Law, R.D., Searle, M.P. & Hubbard, M.S. 2006. Structural evolution and vorticity of flow during extrusion and exhumation of the Greater Himalayan Slab, Mount Everest Massif, Tibet/Nepal: implications for orogen-scale flow partitioning. In: Law, R.D., Searle, M.P. & Godin, L. (eds) *Channel Flow, Extrusion, and Exhumation in Continental Collision Zones*. Geological Society, London, Special Publications, **268**, 379-414.

Jessup, M.J., Law, R.D. & Frassi, C. 2007. The Rigid Grain Net (RGN): An alternative method for estimating mean kinematic vorticity (W_m). *Journal of Structural Geology*.

Kirby, E., Reiners, P.W., Krol, M.A., Whipple, K.X., Hodges, K.V., Farley, K.A., Tang, W. & Chen, Z. 2002. Late Cenozoic evolution of the eastern margin of the Tibetan Plateau: Inferences from $^{40}Ar/^{39}Ar$ and (U-Th)/He thermochronology. *Tectonics*, **21**, 1029.

Klepeis, K.A., Daczko, N.R. & Clarke, G.L. 1999. Kinematic vorticity and tectonic significance of superposed mylonites in a major lower crustal shear zone, northern Fiordland, New Zealand. *Journal of Structural Geology*, **21**, 1385-1406.

Koons, P.O., Zeitler, P.K., Chamberlain, C.P., Craw, D. & Meltzer, A.S. 2002. Mechanical links between erosion and metamorphism in Nanga Parbat, Pakistan Himalaya. *Journal of Science*, **302**, 749-773.

Law, R.D., Searle, M.P. & Simpson, R.L. 2004. Strain, deformation temperatures and vorticity of flow at the top of the Greater Himalayan Slab, Everest massif, Tibet. *Journal of the Geological Society, London*, **161**, 305-20.

Lee, J., Hacker, B.R. & Wang, Y. 2004. Evolution of North Himalayan Gneiss Domes: Structural and metamorphic studies in Mabja Dome, southern Tibet. *Journal of Structural Geology*, **26**, 2297-2316.

Lee, J. & Whitehouse, M. 2006. Onset of middle crustal flow, southern Tibet, *Journal of Asian Earth Sciences*, **26**, 148.

Lee, J. & Whitehouse, M. 2007. Onset of middle crustal extensional flow in southern Tibet: Evidence form U/Pb zircon zircon ages. *Geology*, **35**, 45-48.

Lister, G.S. & Davis, G.A. 1989. The origin of metamorphic core complexes and detachment faults formed during Tertiary continental extension in the northern Colorado River region, USA: *Journal of Structural Geology*, **11**, 65-94.

Mancktelow, N.S. & Grasemann, B. 1997. Time-dependent effects of heat advection and topography on cooling histories during erosion. *Tectonophysics*, **270**, 167-195.

Means, W.D. 1989. Stretching faults. *Geology*, **17**, 893-896.

Means, W.D., Hobbs, B.E., Lister, G.S. & Williams, P.F. 1980. Vorticity and non-coaxiality in progressive deformations. *Journal of Structural Geology*, **2**, 371-378.

Mecklenburgh, J. & Rutter, E.H. 2003. On rheology of partially molten synthetic granite. *Journal of Structural Geology*, **25**, 1575-1585.

Montgomery, D.R. & Stolar, D.B. 2006. Reconsidering Himalayan anticlines. *Geomorphology*, **82**, 4-15.

Murphy, M.A. & Harrison, T.M. 1999. Relationship between leucogranites and the Qomolangma Detachment in the Rongbuk valley, south Tibet. *Geology*, **27**, 831-834.

Murphy, M.A., Yin, An., Kapp, P., Harrison, T.M., Manning, C.E., Ryerson, F.J., Ding, L. & Jinghui, G. 2002. Structural evolution of the Gurla Mandhata detachment system, Southwest Tibet; implications for the eastward extent of the Karakoram fault system. *Geological Society of America Bulletin*, **114**, 428-447.

Naeser, C.W. & Faul, H. 1969, Fission track annealing in apatite and sphene. *Journal of Geophysical Research*, **74**, 705-710.

Passchier, C. W. 1987. Stable positions of rigid objects in non-coaxial flow—a study in vorticity analysis. *Journal of Structural Geology*, **9**, 679-690.

Reiners, P.W., Zhou, Z., Elhers, T.A., Xu, C., Brandon, M.T., Donelick, R.A. & Nicolescu, S. 2003. Post-orogenic evolution of the Dabie Shan, Eastern China, from (U-Th)/He and fission-track thermochronology. *American Journal of Science*, **303**, 489-518.

Rosenberg, C.L. & Handy, M.R. 2005. Experimental deformation of partially melted granite revisited; implications for the continental crust. *Journal of Metamorphic Geology*, **23**, 19-28.

Schneider, D.A., Edwards, M.A., Kidd, W.S.F., Asif Khan, M., Seeber, L. & Zeitler, P.K. 1999. Tectonics of Nanga Parbat, western Himalaya; synkinematic plutonism within the doubly vergent shear zones of a crustal-scale pop-up structure. *Geology*, **27**, 999-1002.

Schneider, D.A., Zeitler, P.K., Kidd, W.S.F. & Edwards, M.A. 2001. Geochronological constraints on the tectonic evolution and exhumation of Nanga Parbat, western Himalayan syn taxis, revisited. *Journal of Geology*, **109**, 563-583.

Searle, M.P. & Rex, A.J. 1989. Thermal model for the Zanskar Himalaya. *Journal of Metamorphic Geology*, **7**, 127-134.

SEARLE, M.P. 1996. Cooling history, erosion, exhumation, and kinematics of the Himalaya-Karakorum-Tibet orogenic belt. *In*: Yin, A. & Harrison, T.M. (eds) *The Tectonic Evolution of Asia*. Cambridge University Press, Cambridge, 110-137.

SEARLE, M.P. 1999a. Extensional and compressional faults in the Everest – Lhotse massif, Khumbu Himalaya, Nepal. *Journal of the Geological Society, London*, **156**. 227-40.

SEARLE, M.P. 1999b. Emplacement of Himalayan leucogranites by magma injection along giant sill complexes: examples from the Cho Oyu, Gyachung Kang and Everest leucogranites (Nepal Himalaya). *Journal of Asian Earth Sciences*, **17**, 773-83.

SEARLE, M.P., WINDLEY, B.F., COWARD, M.P., COOPER, D.J.W., REX, A.J., REX, D., TINGDONG, L., XUCHANG, X., JAN, M.Q., THAKUR, V.C. & KUMAR, S. 1987. The closing of Tethys and the tectonics of the Himalaya. *Geological Society of America Bulletin*, **98**, 678-701.

SEARLE, M.P., SIMPSON, R.L., LAW, R.D., WATERS, D.J. & PARRISH, R.R. 2002. Quantifying displacement on the South Tibetan detachment normal fault, Everest massif, and the timing of crustal thickening and uplift in the Himalaya and South Tibet. *Journal of Nepal Geological Society*, **26**, 1-6.

SEARLE, M.P., SIMPSON, R.L., LAW, R.D., PARRISH, R.R. & WATERS, D.J. 2003. The structural geometry, metamorphic and magmatic evolution of the Everest massif, High Himalaya of Nepal-south Tibet. *Journal of Geological Society, London*, **160**, 345-66.

SEARLE, M.P., LAW, R.D. & JESSUP, M.J. 2006. Crustal structure, restoration and evolution of the Greater Himalaya: implication for channel flow and ductile extrusion of the middle crust. In LAW, R.D., SEARLE, M.P. & GODIN, L. (eds) *Channel Flow, Extrusion, and Exhumation in Continental Collision Zones*. Geological Society, London, Special Publications, **268**, 355-378.

SHAPIRO, N.M., RITZWOLLER, M.H., MOLNAR, P. & LEVIN, V. 2004. Thinning and flow of Tibetan crust constrained by seismic anisotropy. *Science*, **305**, 233-236.

SHUSTER, D.L. & FARLEY, K.A. 2003. $^4He/^3He$ thermochronometry. *Earth and Planetary Science Letters*, **217**, 1-17.

SIMPSON, C. & & DE PAOR, D. G. 1993. Strain and kinematic analysis in general shear zones. *Journal of Structural Geology,* **15**, 1-20.

Simpson, C. & & De Paor, D. G. 1997. Practical analysis of general shear zones using porphyroclast hyperbolic distribution method: an example from the Scandinavian Caledonides. In: Sengupta, S. (ed) Evolution of Geological Structures in Micro- to Macro-scales. London, Chapman and Hall, pp. 169-184.

Thiede, R.C., Bookhagen, B., Arrowsmith, J.R., Sobel, E.R. & Strecker, M.R. 2004. Climate control on rapid exhumation along the Southern Himalayan front. *Earth and Planetary Letters*, **22**, 791-806.

Thiede, R.C., Arrowsmith, J.R., Bookhagen, B., McWilliams, M.O., Sobel, E.R. & Strecker, M.R. 2005. From tectonically to erosionally controlled development of the Himalayan orogen. *Geology*, **33**, 689-692.

Unsworth, M.J., Jones, A.G., Wei, W., Marquis, G., & Spratt, J.E. 2005. Crustal rheology of the Himalaya and southern Tibet inferred from magnetotelluric data. *Nature*, **438**, 78-81.

Visona, D. & Lombardo, B. 2002. Two-mica and tourmaline leucogranites from the Everest-Makalu region (Nepal-Tibet); Himalayan leucogranite genesis by isobaric heating? *Lithos*, **62**, 125-150.

Wallis, S. R. 1992. Vorticity analysis in a metachert from the Sanbagawa Belt, SW Japan. *Journal of Structural Geology,* **14**, 271-280.

Wallis, S. R. 1995. Vorticity analysis and recognition of ductile extension in the Sanbagawa belt, SW Japan. *Journal of Structural Geology*, **17**, 1077-1093.

Wallis, S. R., Platt, J.P. & Knott, S.D. 1993. Recognition of syn-convergence extension in accretionary wedges with examples from the Calabrian Arc and the Eastern Alps. *American Journal of Science*, **293**, 463-495.

Wei, W., Unsworth, M., Jones, A., Booker, J., Tan, H., Nelson, D.L., Li, S., Solon, K., Bedrosain, P., Jin, S., Deng, M., Ledo, J., Kay, D. & Roberts, B. 2001. Detection of widespread fluids in the Tibetan crust by magnetotelluric studies. *Science*, **292**, 716-718.

Whittington, A.G. 2004. The exhumation of gneiss domes in bivergent wedges: Geometrical concepts and examples from the Himalayan syntaxes. *In*: Whitney, D.L., Teyssier, C, & Siddoway, C.S. (eds) *Gneiss domes in orogeny.* Geological Society of America, Special Paper, **380**, 35-46.

Willet, S.D., Hovius, N., Brandon, M.T. & Fisher, D.M. 2006. Introduction. *In* Willet, S.D., Hovius, N., Brandon, M.T. & Fisher, D.M. (eds) *Tectonics, Climate, and Landscape Evolution*. Geological Society of America Special Paper, **398**, Penrose Conference Series, vii-xi.

Wobus, C., Heimsath, A., Whipple, K. & Hodges, Kip. 2005. Active out-of-sequence thrust faulting in the central Nepalese Himalaya. *Nature*, **434**, 1008-1011.

Wolf, R.A., Farley, K.A. & Shuster, L.T. 1996. Helium diffusion and low-temperature thermochronometry of apatite. *Geochimica et Cosomochimica Acta*, **60**, 4231-4240.

Wolf, R.A., Farley, K.A. & Kass, D.M. 1998. Modeling of the temperature sensitivity of the apatite (U-Th)/He thermochronometer. *Chemical Geology*, **148**, 105-114.

Xypolias, P. & Doutsos, T. 2000. Kinematics of rock flow in a crustal-scale shear zone: implications for the orogenic evolution of the southwestern Hellenides. *Geological Magazine*, **137**, 81-96.

Xypolias, P. &, Koukouvelas, I. K. 2001. Kinematic vorticity and strain patterns associated with ductile extrusion in the Chelmos shear zone (External Hellenides, Greece). *Tectonophysics*, **338**, 59-77.

Xypolias, P. & Kokkalas, S. 2006. Heterogeneous ductile deformation along a mid-crustal extruding shear zone: an example from the External Hellenides (Greece). *In*: Law, R. D., Searle, M. P. & Godin, L. (eds) *Channel Flow, Extrusion, and Exhumation in Continental Collision Zones.* Geological Society, London, Special Publications, **268**, 497-516.

Zeitler, P.K., Meltzer, A.S., Koons, P.O., Craw, D., Hallet, B., Chamberlain, C.P., Kidd, W.S.F., Park., S.K., Seeber, L., Bishop, M. & Shroder, J. 2001. Erosion, Himalayan geodynamics, and the geomorphology of metamorphism. *GSA Today*, **11**, 4-9.

Zeitler, P.K., Chamberlain, C.P., & Smith, H.A. 1993, Synchronous anatexis, metamorphism, and rapid denudation at Nanga Parbat (Pakistan Himalaya): *Geology*, **21**, 347-350.

CHAPTER 6

Coupled crustal extension, exhumation and denudation in the trans-Himalayan Arun River Gorge, Ama Drime Massif, Tibet-Nepal

MICAH J. JESSUP[1], DENNIS L. NEWELL[2], & JOHN M. COTTLE[2]
1) Department of Geosciences, Virginia Tech., Blacksburg, Virginia 24061, USA
2) Dept. of Earth & Planetary Sciences, University of New Mexico, Albuquerque, 87131
3) Dept. of Earth Sciences, University of Oxford, Oxford OX1 3PR, UK

Submitted March, 20 2007 to *Geology*

Cover image: Eastern limb of the Ama Drime Massif viewed towards the north-northwest with Demon's lake in the foreground (4950m). 1 km tall triangular facets mark the trace of the fault towards the north. Footwall rocks contain a north-south striking mylonitic foliation with abundant evidence for top-down-to-the-east sense of shear. Fault scarps offset recent lacustrine, fluvial and colluvial deposits. M. Jessup 2006.

Abstract

Focused denudation and mid-crustal flow are coupled in many active tectonic settings, including the Himalaya, where they are often described in terms of channel flow or tectonic aneurysm models. In these models, exhumation of mid-crustal rocks is accommodated by thrust faults and low-angle detachment systems during crustal shortening. Our results suggest that the most tectonically active feature in the Everest region is the Ama Drime Massif (ADM), a trans-Himalayan antiform that protrudes north from the crest of the Himalayas. Previous investigations interpreted the shear zones that bound the ADM as the Main Central thrust; however, our new structural analysis demonstrate that these are 100-300 m thick normal-sense shear zones that are kinematically linked to young brittle faults that offset Quaternary deposits and record active east-west crustal extension. By combining our new structural interpretation for the ADM with existing remote sensing data we propose that, driven by the local extensional stress field, the ADM is being exhumed as a core complex that is coupled with denudation in the trans-Himalayan Arun River gorge. Furthermore, our data provide important insights into the dynamic links between regional-scale climate and crustal-scale tectonics.

Introduction

Pioneering attempts to merge geological and geophysical data from the Himalayas culminated in channel flow (Beaumont et al., 2001, 2004) and tectonic aneurism models (Zeitler, 2001) that described the coupling between the flow of mid-crustal rocks, exhumation and denudation along the orogenic front. Tectonic aneurism models are applied to the eastern and western syntaxes where exhumation rates of mid-crustal rocks are extreme and metamorphic massifs coincide with major river systems. Tectonic aneurisms result from the fluvial incision of deep gorges across the uplifting mountain ranges that enable warm lower crust, driven by the local stress field, to extrude upwards as a bivergent wedge (Zeitler et al., 1993, 2001; Schneider et al., 2001; Koons et al., 2002). Channel flow models propose southward extrusion of a low viscosity mid-crustal channel beneath the Tibetan plateau (Nelson et al., 1996) that is driven by the gradient in lithostatic pressure between the Tibet Plateau and lowlands of the Indian plate (Grujic et al., 1996, 2002; Beaumont et al., 2001, 2004; Searle et al., 2003, 2006). The spatial coincidence between elevated rapid inferred erosion index and young metamorphic massifs along the Himalayas is used as evidence for a fine-scale coupling between mid-crustal flow and denudation along the range, including the trans-Himalayan Arun River gorge (Finlayson et al., 2002; Montgomery and Stolar, 2006). The trans-Himalayan Arun River flows along the western limb of the Ama Drime Massif (ADM), or Arun antiform, before it enters the Arun River gorge where is passes into the eroded core of the ADM and continues into the foothills of the Nepal (Brookfield, 1998; Fig. 6.1). Accurate characterization of the trans-Himalayan zone is important to testing the coupling between tectonics, denudation and mid-crustal flow, however structural interpretation of the ADM remains ambiguous. When existing data are reviewed and integrated into our detailed structural analysis across the ADM a new context in which to view the evolution of this part of the Himalayas emerges. We believe that this is the first documentation of the coupling between crustal extension and denudation in a trans-Himalayan gorge.

Previous interpretations of the Ama Drime Massif

The ADM is an anomalous region of elevated topography that protrudes 70 km northward from the Himalayan crest (Odell, 1925). Prior to this investigation few westerners had crossed the entire ADM to constrain the major physiographic features and structures responsible for the architecture of the range (Shipton, 1938). Instead, their efforts focused on the eastern (Burchfiel et al., 1992) and western margins (Lombardo et al., 1998; Lombardo and Rolfo, 2000; Visona and Lombardo, 2002) of the ADM and resulted in two different interpretations. Burchfiel et al. (1992) documented that the

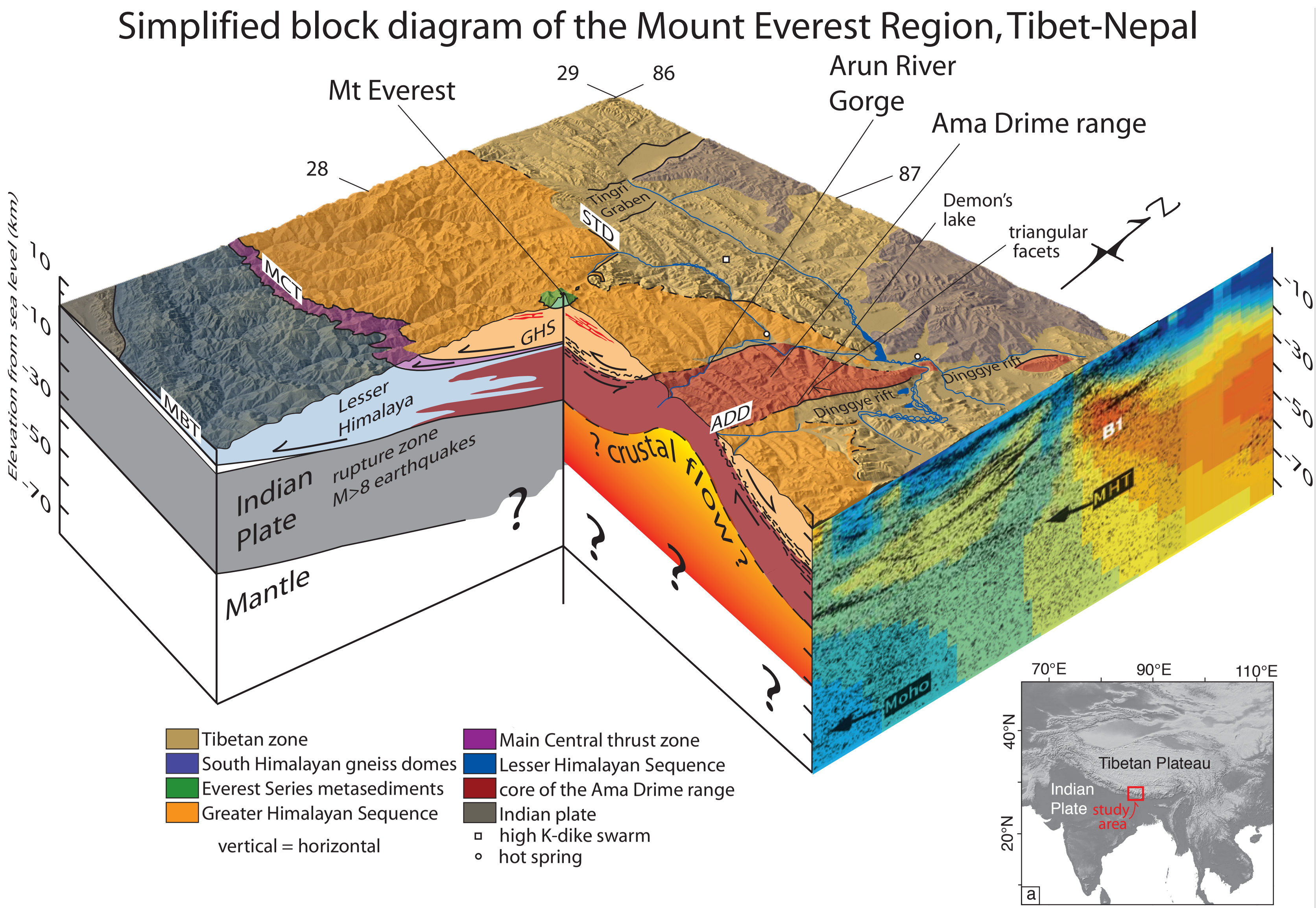
Simplified block diagram of the Mount Everest Region, Tibet-Nepal
Mt Everest
29
86
28
87
Arun River
Gorge
Ama Drime range
Demon's
lake
triangular
facets
N
Tingri
Graben
STD
MCT
GHS
MBT
Lesser
Himalaya
ADD
Dinggye rift
Dinggye rift
B1
MHT
Moho
Indian
Plate
rupture zone
M>8 earthquakes
? crustal flow ?
Mantle
Elevation from sea level (km)
10
-10
-30
-50
-70
Tibetan zone
South Himalayan gneiss domes
Everest Series metasediments
Greater Himalayan Sequence
vertical = horizontal
Main Central thrust zone
Lesser Himalayan Sequence
core of the Ama Drime range
Indian plate
high K-dike swarm
hot spring
70°E
90°E
110°E
40°N
20°N
Tibetan Plateau
Indian
Plate
study
area
a

Figure 6.1. Previous page. Simplified interpretive block diagram of the Everest region, Tibet-Nepal. Inset A. Location of the study area. Magnetotelluric data from Unsworth et al. (2005) with INDEPTH results (Nelson et al., 1996) for the INDEPTH line ~200 km east of the Everest region to emphasize the proposed partial melt zone (warm colors) beneath the Tibetan plateau. See text for details.

eastern limb is defined by a north-south striking fault that dips 45ºE (down-dip lineation) and contains a mylonite zone in the footwall rocks with a well-developed S-C fabric that records hanging wall-down (top-down-to-the-east) sense of shear. 1 km high triangular facets define the fault trace, fault scarps offset Quaternary deposits and the fault offsets the South Tibetan detachment (STD) by 20 km of right-lateral separation (Fig. 6.1). The Xainza-Dinggye rift is present in the Dinggye valley to the east of the ADM and extends north into the Tibetan Plateau (Fig. 6.1; Zhang & Lei, 2007). By offsetting the STD, these younger features provide compelling evidence that the STD is inactive in this region.

On the western margin of the ADM, rocks types within the bounding shear zone include quartzite, marble, calc-silicate, gneiss and leucogranite. Rocks exposed above the shear zone are composed of migmatitic, sillimanite and cordierite bearing orthogneiss of the Greater Himalayan sequence (GHS) i.e., Kharta Gneiss Complex. Rocks beneath the shear zone include granulite facies, migmatitic Ama Drime orthogneiss with mafic lenses cored by eclogite (Lombardo et al., 1998; Lombardo and Rolfo, 2000; Groppo et al., 2007; Cottle et al., *in prep*). This shear zone was originally interpreted as thrust sheets of the Main Central thrust (MCT; Lombardo et al., 1998). U-Th-Pb ages suggest that ductile fabric within the shear zone development at ~12-13 Ma (Liu et al. 2007). Sm/Nd model ages of leucogranites jump from 2.0 Ga in the hanging wall to 2.9 Ga in the footwall of the western limb of the ADM (Visona et al., 2002). Visona and Lombard (2002) suggest that the model ages are similar to paragneiss from the base of the GHS (2.0 Ga) and orthogneiss of the Lesser Himalayan sequence (LHS) (2.5 Ga) in Nepal (Robinson, et al., 2001). Granite in the hanging wall located near the intersection of the Dzakaa Chu and the STD (Cottle et al., *in review*) have ENd(0) of -17.8 that Liu et al. (2007) compare to average ENd(0) of -16 for the GHS (Robinson, et al., 2001). Footwall rocks from the western margin of the ADM yield ENd(0) of -23.4 (Liu et al., 2007), which is similar to average ENd(0) of -21.5 for the LHS (Robinson, et al., 2001). Therefore based on isotopic evidence, the core of the ADM is interpreted as LHS and the bounding shear zone as the MCT. Subsequent investigations have either projected the MCT along the western side (Borghi et al., 2003) of the ADM, or around the entire ADM (Lombardo and Rolfo, 2000; Groppo et al., 2007; Liu et al., 2007; Zhang and Lei, 2007).

Structure of the Ama Drime Massif

Four prominent drainages along the western margin of the ADM expose 100 m thick shear zone in leucogranites, calc-silicates, quartzites and marbles that are bounded above by the Kharta Valley Gneiss complex and below by the Ama Drime orthogneiss. Within the shear zone the foliation (S1) strikes north-south and dips 45º W with a down-dip stretching lineation (Fig. 6.1). A transition from high-grade gneisses where feldspar deformed plastically to mylonite zones where feldspar behaves as rigid porphyroclasts exists within the shear zone. Asymmetric tails on porphyroclasts and S-C fabrics in all rocks types within the zone consistently records hanging wall-down (top-down-to-the-west) sense of shear. Brittle faults filled with fault gouge oriented parallel to the shear fabric also record hanging wall-down sense of shear.

Mapping during two east-west transects across the ADM documents a foliation that dips west on the western limb, becomes subhorizontal in the core and dips east on the eastern limb creating an elongate structural dome (Fig. 6.1). Mafic lenses, common in the core of the ADM, are parallel to the main foliation and frequently boudinaged. Extensional shear bands are common in the variably migmatitic augen gneiss. U-Th-Pb geochronology of a leucogranite dike that cross cuts the dominant foliation indicate a crystallization age of ~12 Ma and constrain a maximum age for the development of this fabric (Cottle et al., *in prep*).

On the eastern limb of the range, near Demon's Lake (Fig. 6.1), we mapped a 300 m wide, north-south striking shear zone within leucogranite and orthogneiss that is very similar to features described by Burchfiel et al. (1992). S-C fabrics in the augen gneiss record top-down-to-the-east sense of shear. The fault zones preserve early high-temperature shear fabrics with a pervasive north-south striking foliation and down-dip stretching lineation. Narrow mylonite zones with rigid feldspar porphyroclasts and a

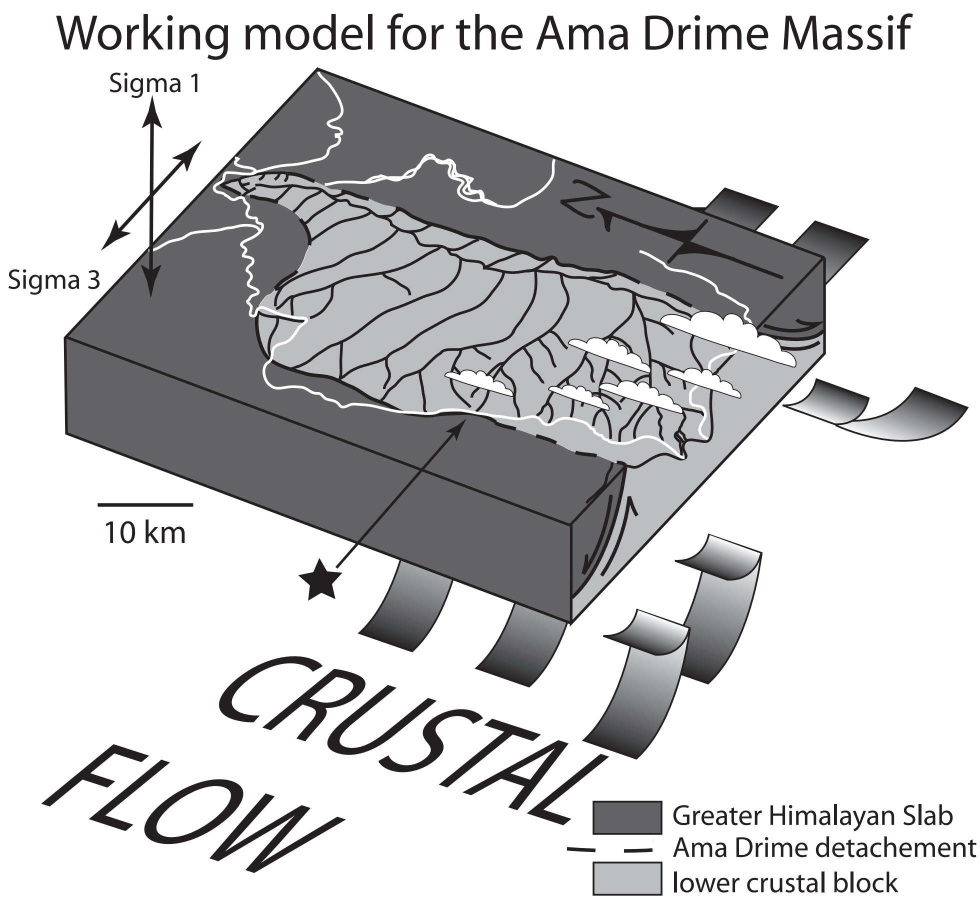

Figure 6.2. Model proposed for the Ama Drime Massif. Exhumation of the ADM as a core complex during east-west extension and crustal thinning coupled with denudation in the Arun River gorge. Knick point on the western limb marks the beginning of the trans-Himalayan Arun river gorge. Drainages around the ADM are in sediment-filled valley when in the hanging wall block. Steep gorges are present in all locations where the drainages cross the footwall block. High precipitation defined by Finlayson et al. (2002) represented by cartoon clouds.

ductile quartz matrix form parallel to the early high temperature fabrics. S-C fabrics as well as delta and sigma-type asymmetric tails on porphyroclasts consistently record east-west extension. Fault scarps, subparallel to 1 km tall triangular facets, offset recent lacustrine, fluvial and colluvial deposits.

Discussions and Conclusions

Structural data from the ADM indicate that the major range bounding faults and shear zones mapped in the central section of the ADM record crustal extensional and are here termed the Ama Drime detachment (ADD; Figs. 6.1 and 6.2). We use the consistency in fabric orientation between the high-to low-grade deformation and the progression into brittle detachments (Sibson, 1977) within the ADD to suggest that these formed during crustal extension and exhumation as a core complex. We emphasize that the extensional fabrics dominate the macro-and micro-scale structure and overprint any evidence for early thrusting along the shear zone on the western limb. Our new constraints on the structural evolution of the western limb essentially mirror those of Burchfiel et al. (1992), which are further supported by our mapping along Demon's Lake on the eastern limb. Since the Sm/Nd model ages and ENd(0) data suggest that the core of the ADM is part of the LHS, we propose that the ADD may be an unconformity with an early history as a thrust fault. However, we caution against calling this contact the MCT, because the MCT, by definition, occurs in the foreland of the Himalayas (Gansser, 1964).

This implies that reactivation of preexisting structural weaknesses or unconformities may have played a significant role in accommodating the transition from crustal thickening to thinning during the evolution of this section of the Himalayas. We prefer to interpret the ADD as a fundamental transition between the GHS and LHS originally located at a much greater depth than currently exposed in the foreland. We propose that the core of the ADM represents the deepest structural position, essentially the lower crust, exposed in this part of the Himalayas as an erosional window. Offset Quaternary deposits on the eastern limb of the ADM suggest that east-west crustal extension remains active today. This is further supported by geophysical data that suggests the only area of crustal thinning, defined by the distribution of the normalized component of the seismic moment tensor that crosses the Himalayan front, coincides with the ADM (Shapiro et al., 2004). Geochemical and isotopic data from CO_2-rich hot springs along the western limb and nose of the ADD are the hottest observed in the Everest region and carry volatiles with carbon and nitrogen isotope values suggestive of high temperature devolatilization of lower crustal rocks or mantle materials (Newell et al., *submitted*). Together these provide compelling evidence that the ADM is a core complex that exhumes a lower crustal block during active east-west crustal extension.

The highest precipitation levels in the Himalayas, outside of the eastern syntaxis (Finlayson et al., 2002) as well as high rapid inferred erosion (Finlayson et al., 2002) coincides with the trans-Himalayan Arun River gorge on the southern end of the ADM. Previous investigators suggested that the Arun River gorge and antiform are prime candidates for exploring the coupling between erosion, climate and tectonics (Montgomery and Stolar, 2006). We contribute our new field observations and data to this hypothesis and propose that exhumation of the ADM as a core complex during east-west crustal extension is coupled with denudation in the Arun River gorge. We also propose that the active faults of the ADD might link mid-crustal flow interpreted from imaged low-velocity and resistivity zones beneath the Tibetan Plateau today (Nelson et al., 1996; Unsworth et al., 2005) with focused denudation in a major trans-Himalayan gorge during crustal thinning (Figs. 6.1 and 6.2).

Acknowledgments

For discussions regarding the evolution of the ADM we thank J. Fletcher, R. Law, R. Parrish, J. Lee and K. Karlstrom. We are deeply indebted to our guide Sonam Wangdu for helping us cross the ADM and for finding and feeding us after an unplanned bivouac at 5000m. Our expeditions were funded by American Alpine Club, Sigma Xi, Virginia Tech Geosciences research grants and 2010 Fellowship from the College of Science, Virginia Tech to M. Jessup, a National Science Foundation Integrative Graduate Education and Research Traineeship (DGE-9972810), Geological Society of America Research Grant, and University of New Mexico research grants to D. Newell and a New Zealand TEC Bright Future Top Achiever Doctoral Scholarship to J. Cottle.

References

Beaumont, C., Jamieson, R.A., Nguyen, M.H., and Lee, B., 2001, Himalayan tectonics explained by extrusion of a low-viscosity crustal channel coupled to focused surface denudation: Nature, v. 414, p. 738-742.

Beaumont, C., Jamieson, R.A., Nguyen, M.H. & Medvedev, S., 2004, Crustal channel flows: 1. Numerical models with applications to the tectonics of the Himalayan – Tibetan orogen: Journal of Geophysical Research, v. 109, B06406 29p.

Borghi, A., Castelli, D., Lombardo, B., and Visona, D., 2003, Thermal and baric evolution of garnet granulites from the Kharta region of S Tibet, E Himalaya: European Journal of Mineralology, v. 15, p. 401-418.

Brookfield, M.E., 1998, The evolution of the great river systems of southern Asia during the Cenozoic India-Asia collision; river draining southwards: Geomorphology, v. 22, p. 285-312.

Burchfiel, B.C., Zhiliang, C., Hodges, K.V., Yuping, L., Royden, L., Changrong, D., and Jiene, X., 1992, The South Tibetan Detachment System, Himalayan Orogen: extension contemporaneous with and parallel to shortening in a collisional mountain belt: Geological Society of America Special Paper, 269, 41 p.

Cottle, J.M., Jessup, M.J., Newell, D.L, Searle, M.P., Law, R.D., and Noble, S.R, *in review*, Structural Evolution of the South Tibetan Detachment System, Dzakaa Chu section, Kharta region, Eastern Himalaya*: Submitted to* Journal of Structural Geology.

Cottle, J.M., Noble, S.R, Jessup, M.J., Newell, D.L, Parrish, R.R., and Waters, D.J., *in prep*, Structure, petrology and high precision U-Th-Pb geochronology of Eclogites from the Ama Drime Massif, Southern Tibet: *In preparation for* Earth and Planetary Science Letters.

Finlayson, D.P., Montgomery, D.R., and Hallet, B., 2002, Spatial coincidence of rapid inferred erosion with young metamorphic massifs in the Himalayas: Geology, v. 30, p. 219-222.

Koons, P.O., Zeitler, P.K., Chamberlain, C.P., Craw, D. and Meltzer, A.S., 2002, Mechanical links between erosion and metamorphism in Nanga Parbat, Pakistan Himalaya: Journal of Science, v. 302, p. 749-773.

Gansser, A., 1964, The Geology of the Himalayas: Wiley Interscience, New York.

Groppo, C., Lombardo, B., Rolfo, F., and Pertuati, P., 2007, Clockwise exhumation path of granulitized eclogites from the Ama Drime range (Eastern Himalayas): Journal of Metamorphic Geology, v. 25, p. 51-75.

Grujic, D., Casey, M., Davidson, C., Hollister, L., Kundig, K., Pavlis, T., and Schmid, S., 1996, Ductile extrusion of the Higher Himalayan crystalline in Bhutan: evidence from quartz microfabrics: Tectonophysics, v. 260, p. 21-43.

Grujic, D., Hollister, L., and Parrish, R.R., 2002, Himalayan metamorphic sequence as an orogenic channel: insight from Bhutan: Earth and Planetary Science Letters, v. 198, p. 177-191.

Liu, Y., Siebel, W., Massonne, H-J., and Xiao, X., 2007, Geochronological and petrological constraints for tectonic evolution of the central Greater Himalayan sequence in the Kharta area, southern Tibet: The Journal of Geology, v. 115, p. 215-230.

Lombardo, B., Pertusati, P., Rolfo, F., and Visona, D., 1998, First report of eclogites from the E Himalaya: implications for the Himalayan orogeny: Memorie di Scienze Geologiche, v. 50, p. 67-68.

Lombardo, B., and Rolfo, F., 2000, Two contrasting eclogite types in the Himalayas: implications for the Himalayan orogeny: Journal of Geodymanics, v. 30, p. 37-60.

Montgomery, D.R. and Stolar, D.B., 2006, Reconsidering Himalayan anticlines: Geomorphology, v. 82, p. 4-15.

Nelson, K.D., and the INDEPTH group, 1996, Partially Molten Middle Crust Beneath Southern Tibet: Synthesis of Project INDEPTH Results: Science, v. 274, p. 1684-1688.

Newell, D.L., Jessup, M.J., Cottle, J.M., Hilton, D.R., Fischer, T. and Sharp, Z., *submitted*, Mineral springs of southern Tibet: a geochemical window into three structural levels of the lithosphere beneath the Tibetan plateau: *Submitted to* Earth and Planetary Science Letters.

Odell, N.E., 1925, Observations on the rocks and glaciers of Mount Everest: The Geographical Journal, v. 4, p. 389-215.

Robinson, D.M., DeCelles, P.G., Patchett, J. and Garzione, C.N., 2001, The kinematic evolution of the Nepalese Himalaya interpreted from Nd isotopes: Earth and Planetary Science Letters, v. 192, p. 507-521.

Schneider, D.A., Zeitler, P.K., Kidd, W.S.F. & Edwards, M.A., 2001, Geochronological constraints on the tectonic evolution and exhumation of Nanga Parbat, western Himalayan syntaxis, revisited: Journal of Geology, v. 109, p. 563-583.

Searle, M.P., Simpson, R.L., Law, R.D., Parrish, R.R. and Waters, D.J., 2000, The structural geometry, metamorphic and magmatic evolution of the Everest massif, High Himalaya of Nepal-south Tibet: Journal of Geological Society, London, v.160, p. 345-66.

Searle, M.P., Law, R.D. and Jessup, M.J., 2006, Crustal structure, restoration and evolution of the Greater Himalaya: implication for channel flow and ductile extrusion of the middle crust, *in* Law, R.D., Searle, M.P. and Godin, L., eds., Channel Flow, Extrusion, and Exhumation in Continental Collision Zones. Geological Society, London, Special Publications, v. 268, p. 355-378.

Shapiro, N.M., Ritzwoller, M.H., Molnar, P., and Levin, V., 2004, Thinning and flow of Tibetan crust constrained by seismic anisotropy. Science, v. 305, p. 233-236.

Shipton, E.E., 1938, The Gyangkar (Nyonno Ri) Range, *in* Tilman, H.W., Shipton, E. E. and Fischer, E. C., The Mount Everest Expedition of 1938: The Geographical Journal, v. 92, p. 481-490.

Sibson, R.H., 1977, Fault rocks and fault mechanics: Journal of Geological Society of London, v. 133, p. 191-213.

Unsworth, M.J., Jones, A.G., Wei, W., Marquis, G., & Spratt, J.E., 2005, Crustal rheology of the Himalaya and southern Tibet inferred from magnetotelluric data: Nature, v. 438, p. 78-81.

Visona, D. and Lombardo, B., 2002, Two mica- and tourmaline leucogranites from the Everest-Makalu region (Nepal-Tibet): Himalayan leucogranite gneiss by isobaric heating? Lithos, v. 62, p. 125-150.

Zeitler, P.K., Chamberlain, C.P., and Smith, H.A., 1993, Synchronous anatexis, metamorphism, and rapid denudation at Nanga Parbat (Pakistan Himalaya): Geology, v. 21, p. 347-350.

Zeitler, P.K., Meltzer, A.S., Koons, P.O., Craw, D., Hallet, B., Chamberlain, C.P., Kidd, W.S.F., Park., S.K., Seeber, L., Bishop, M. & Shroder, J., 2001., Erosion, Himalayan geodynamics, and the geomorphology of metamorphism: GSA Today, v. 11, p. 4-9.

Micah J. Jessup
Born 09.17.1975 Boston, Massachusetts
Curriculum Vitae
Department of Geosciences
Virginia Tech, Blacksburg, VA, 24061

Education

- Ph.D., Candidate, Geosciences — Virginia Tech — 2003-2007
  "Kinematic Evolution, Metamorphism and Exhumation of the Greater Himalayan Sequence, Mount Everest Massif, Tibet/Nepal"
- M.S., Geology (with distinction) — University of New Mexico — 2000-2003
  "Tectonic history of Proterozoic rocks in the Black Canyon of the Gunnison, Colorado"
- Advanced Field Camp — University of New Mexico — Summer 2000
- B.A., Geology — Hampshire College — 1994-1998
  "Examination of REE signatures in shoreline tufa, Panamint Valley, California; Reconstructing Pleistocene climate change"

Research Interests

- Field-and lab-based structural analysis.
- Constraining the spatial and temporal variability of flow in shear zones.
- Testing extrusion/channel flow models for the Himalayas.
- Constructing Pressure/Temperature/time/Deformation paths.
- Developing new vorticity techniques for quantifying flow in shear zones.
- Integrating U/Pb zircon-titanite geochronology, *in situ* monazite geochronology, and $^{40}Ar/^{39}Ar$ thermochronology to reconstruct the tectonic evolution of the continental crust.
- Fluid flux, penetration depth, and displacement along detachment systems.
- Coupling of erosion and tectonics in active orogens.

Awards

- 2010 Graduate Fellowship Award, College of Science, VT — 2006-2007

Analytical Skills

- Vorticity and strain analysis using a petrographic microscope
- Quartz petrofabric analysis using the universal stage
- CamScan Series 2 Scanning Electron Microscope
- Cameca SX-50 Electron Probe Microanalyzer
- *In situ* monazite geochronology

Memberships Of Professional Organizations

- Geological Society of America
- American Geophysical Union
- American Alpine Club

Teaching Assistantships

Course title	Supervisor	Institute	Term/Year
• Advanced Structure	(R. Law)	Virginia Tech	Fall 2005
• Structural Geology	(R. Law)	Virginia Tech	Spring 2005
• Structural Geology	(R. Law)	Virginia Tech	Spring 2004
• Advanced Field Camp	(K. Karlstrom)	UNM	Summer 2003
• Advanced Field Camp	(K. Karlstrom)	UNM	Summer 2002
• Petrology	(J. Selverstone)	UNM	Spring 2002
• Advanced Field Camp	(K. Karlstrom)	UNM	Summer 2001
• Structural Geology	(K. Karlstrom)	UNM	Spring 2001
• N.M. Field Geology	(J. Geissman)	UNM	Fall 2000
• Evolution of the Earth	(J. Reid)	Hampshire College	Fall 1997

Student Mentoring

- Paul M. Betka, B.S. 2006 *Structural evolution of the Sauratown quartzites; implications for transport direction during the Grenville Orogeny*.

Research Grants

• NSF supplementary grant submitted through R.D. Law	$15000	Spring 2006
• American Alpine Club Research Grant	$1000	Spring 2006
• W. D. Lowry Geosciences Graduate Research Award, VT	$1000	Spring 2006
• Graduate Research and Development Program Grant, VT	$375	Spring 2006
• Sigma Xi Research Grant	$800	Spring 2006
• Southeast Geological Society of America Research Grant	$800	Spring 2005
• Geological Society of America IGC Grant	$1000	Summer 2004
• Geological Society of America Research Grant	$1300	Spring 2004
• Sherman A. Wengerd Traveling Scholarship, UNM	$1200	Summer 2003
• Geology Alumni Scholarship, UNM	$950	Summer 2002
• Sherman A. Wengerd Traveling Scholarship, UNM	$600	Summer 2001
• Howard Hughes Medical Institute (HHMI) Grant	$2000	Fall 1997
• Lemelson Foundation Young Inventors Grant	$800	Fall 1997

Fieldwork

• Ama Drime range, Tibet (1 month)	Summer 2006
• Kharta valley, Tibet (1.5 months)	Summer 2005
• Khumbu, Nepal (1 month)	Fall 2004
• Kangshung valley, Tibet (1 month)	Fall 2004
• Khumbu, Nepal (1 month)	Fall 2003
• Rongbuk valley, Tibet (1 month)	Fall 2003
• Khumbu, Nepal (1 month)	Spring 2003
• Black Canyon of the Gunnison, CO (5 months)	2000-2003
• Greiner shear zone, Alps (2 weeks)	Summer 2002
• Grand Canyon, AZ (5 river trips)	2000-2003
• Panamint valley, CA (5 weeks)	1995-1998

Independent Himalayan Expeditions

- Annapurnas, Nepal — Fall 1998
- China (Xinjiang, Tarim Basin, Tibet) — Fall 1998
- Lobsang Spire International Expedition, Karakoram, Pakistan — Spring 1996

Refereed Publications

Jessup, M.J., Law, R.D. & Frassi, C. (2007) The Rigid Grain Net (RGN); an alternative method for estimating mean kinematic vorticity (W_m). *Journal of Structural Geology* 29, 411-421.

Jessup, M.J., Law, R.D., Searle, M.P. & Hubbard, M.S. (2006) Structural evolution and vorticity of flow during extrusion and exhumation of the Greater Himalayan Slab, Mount Everest Massif, Tibet/Nepal: implications for orogen-scale flow partitioning. In: Law, R.D., Searle, M.P. & Godin, L. (eds) *Channel Flow, Extrusion, and Exhumation in Continental Collision Zones*. Geological Society, London, Special Publications, 268, 379-414.

Jessup, M.J., Jones, J.V., Karlstrom, K.E., Connelly, J.N., Williams, M.L., & Heizler, M.T. (2006) Three Proterozoic orogenic episodes and an intervening exhumation event in the Black Canyon of the Gunnison region, Colorado. *Journal of Geology*, 114, 555-576.

Jessup, M.J., Karlstrom, K.E., Connelly, J., Williams, M.L., Livaccari, R., Tyson, A. & Rogers, S.A. (2005) Complex Proterozoic crustal assembly of southwestern North America in an arcuate subduction system: The Black Canyon of the Gunnison, southwestern Colorado. In: Karlstrom, K.E. & Keller, R.G. (eds) *The Rocky Mountain Region: An Evolving Lithosphere*. American Geophysical Union monograph, 154, 21-38.

Searle, M.P., Law, R.D. & **Jessup, M.J.** (2006) Crustal structure, restoration and evolution of the Greater Himalaya: implication for channel flow and ductile extrusion of the middle crust. In Law, R.D., Searle, M.P. & Godin, L. (eds) *Channel Flow, Extrusion, and Exhumation in Continental Collision Zones*. Geological Society, London, Special Publications, 268, 355-378.

Publications (*submitted*)

Jessup, M.J., Newell, D.N., & Cottle, J.M. (*submitted)* Coupled crustal extension, exhumation and denudation in the trans-Himalayan Arun River Gorge, Ama Drime Massif, Tibet-Nepal. Submitted to *Geology.*

Jessup, M.J., Searle, M.P., Cottle, J.M., Law, R.D., Tracy, R.J., Newell, D.L. & Waters, D.J. (*submitted*) P-T-t-D paths of the Everest Series schist, Nepal. Submitted to *Journal of Metamorphic Geology*.

Cottle, J.M., **Jessup, M.J.**, Newell, D.L., Searle, M.P., Parrish, R.R., Nobel, S.R. & Waters, D.J. (*in review*) Structural evolution of the South Tibetan detachment system, Dzakaa Chu section, Kharta region, Eastern Himalaya. Submitted to *Journal of Structural Geology*.

Cottle, J.M., Noble, S.R, **Jessup, M.J.**, Newell, D.L, Parrish, R.R. & Waters, D.J. (*submitted*) Structure, petrology and high precision U-Th-Pb geochronology of Eclogites from the Ama Drime Massif, Southern Tibet. Submitted to *Earth and Planetary Science Letters*.

Newell, D.L., **Jessup, M.J.**, Cottle, J.M., Hilton, D.R., Fischer, T. & Sharp, Z. (*in review*) Geochemistry of mineral springs of the southern Tibetan Plateau, Mount Everest region; a geochemical window into three structural levels. Submitted to *Earth and Planetary Science Letters*.

Searle, M.P., Law, R.D., **Jessup, M.J.**, Streule, M.J., Cottle, J.M., Godin, L. & Larson, K. (*in prep*) Defining the Himalayan Main Central Thrust in Nepal. In preparation for *Geological Society of London*.

Karlstrom, K.E., Whitmeyer, S.J., Williams, M.L., Bowring, S.A., & **Jessup, M.J.** (*submitted*) Does the arc-accretion model adequately explain the Paleoproterozoic evolution of southern Laurentia: An expanded interpretation—Comment. Submitted to *Geology*.

Abstracts (*mentored undergraduate author)

Cottle, J.M., **Jessup, M.J.,** Newell, D.L., Searle, M.P., & Law, R.D. (2007) Structural Evolution of the South Tibetan Detachment System and its implications for Exhumation of the High Himalaya. Tectonic Studies Group Meeting, Glasgow Jan, 2007.

Jessup, M.J., Cottle, J.M., Newell, D.L., Searle, M.P., Law, R.D. & Tracy, R.J. (2006) Spatial and temporal variability in deformation, metamorphism, and displacement along the South Tibetan detachment system; insights into the exhumation of the Greater Himalayan Slab, Tibet. Geological Society of America Abstract with Programs, Vol. 38, No. 7, p. 239.

Jessup, M.J., Newell, D.L. & Cottle, J.M. (2006) Exhumation of a Himalayan core complex during east-west extension enhanced by focused precipitation along the Arun River gorge; the Ama Drime Massif. Eos Trans. AGU, 87(52), Fall Meet. Suppl., Abstract T34C-03.

Newell, D.L., **Jessup, M.J.**, Cottle, J.M., Hilton, D.R., Fischer, T. & Sharp, Z. (2006) Mineral Springs of Southern Tibet, Everest Region: geochemical window to three structural levels. Eos Trans. AGU, 87(52), Fall Meet. Suppl., Abstract T34C-08.

Cottle, J.M., **Jessup, M.J.**, Newell, D.L., Parrish, R., Searle, M.P., Noble, S. & Waters, D.J. (2006) Structure, Petrology and High Precision U-Th-Pb Geochronology of Eclogites From the Ama Drime Massif, Southern Tibet. Eos Trans. AGU, 87(52), Fall Meet. Suppl., Abstract T34C-05.

Jessup, M.J., Karlstrom, K.E., Connelly, J.N., Williams, M.L., Jones, J.V & Heizler, M.T. (2006) Multiple Proterozoic orogenic episodes and an intervening exhumation event in the Black Canyon of the Gunnison region, Colorado. Geological Society of America, Rocky Mountain Section, Abstracts

with Programs. Vol. 38, No. 6, p. 3. **Session Chair**

*Betka, P. M., **Jessup, M.J.** & Law, R. D. (2006) Structural evolution of the Sauratown Mountain quartzites; Evidence for polyphase deformation and shearing. Southeastern Section-Geological Society of America Abstracts with Programs. Vol. 38, No. 3, p. 34.

Jessup, M.J., Cottle, J.M., Newell, D.L., Searle, M.P., Law, R.D. & Tracy, R.J. (2006) Vorticity of flow and displacement along the South Tibetan Detachment System, Gondasampa region, Tibet. 21st Himalaya-Karakoram-Tibet Workshop. Fitzwilliam College, Cambridge, U.K. 29-31. Journal of Asian Earth Sciences 26 (2) p. 143.

Newell, D.L., **Jessup, M.J.,** Cottle, J.M., Hilton, D.R. & Fisher, T.P. (2006) Geochemistry of travertine-depositing springs along the South Tibetan Detachment System, Mount Everest region, Tibet: implications for fluid origins and lithospheric structure. 21st Himalaya-Karakoram-Tibet Workshop. Fitzwilliam College, Cambridge, U.K. 29-31 March 2006. Journal of Asian Earth Sciences 26 (2) p. 154.

Cottle, J.M, **Jessup, M.J.,** Newell, D.L., Searle, M.P. & Law, R.D. (2006) Structure of the South Tibetan Detachment System, Kharta region south Tibetan Himalaya. 21st Himalaya-Karakoram-Tibet Workshop. Fitzwilliam College, Cambridge, U.K. 29-31 March 2006. Journal of Asian Earth Sciences 26 (2) p. 132.

Law, R.D., **Jessup, M.J.,** Searle, M.P., Cottle, J.M., Waters, D.J. & Hubbard, M.S. (2006) Vorticity of flow within the Greater Himalayan Slab, Everest transect. 21st Himalaya-Karakoram-Tibet Workshop. Fitzwilliam College, Cambridge, U.K. 29-31 March 2006. Journal of Asian Earth Sciences 26 (2) p. 148.

Cottle, J.M, **Jessup, M.J.,** Newell, D.L., Searle, M.P. & Law, R.D. (2006) Structure and kinematics of the South Tibetan Detachment System, Kharta region south Tibetan Himalaya (2006). Tectonic Studies Group AGM. University of Manchester, U.K. 4-6 January 2006.

Law, R.D., **Jessup, M.J.,** Searle, M.P., Cottle, J.M., Waters, D.J., & Hubbard, M.S. (2006) Vorticity of flow and extrusion of the Greater Himalayan Slab. Tectonic Studies Group AGM. University of Manchester, U.K. 4-6 January 2006.

Jessup, M.J., Searle, M.P., Tracy, R., Law, R.D., Cottle, J.M. & Waters, D.J. (2005) Thermal-mechanical evolution of the upper-section of the Greater Himalayan Slab, Everest-Lhotse massif, Nepal. Geological Society of America, Annual meeting, Abstracts with Programs, Vol. 37, No. 7, p. 388. **Session Chair**

Newell, D.L., **Jessup, M.J.,** Cottle, J.M. & Crossy, L.J. (2005) Geochemistry of travertine-depositing springs near and along the South Tibetan Detachment system, Mount Everest region, Tibet. Geological Society of America, Annual meeting, Abstracts with Programs, Vol. 37, No. 7, p. 378.

Karlstrom, K.E., Whitmeyer, S.J. & **Jessup, M.J.** (2005) Proterozoic rocks of the Southwest: Episodic crustal growth, long-lived (1.8 to 1.0 Ga) plate margin along southern Laurentia, and preservation of Proterozoic subduction scars in the modern-day lithosphere. Rocky Mountain Section, Geological Society of America, Abstracts with Programs, Vol. 37, No. 6, p. 41.

Jessup, M.J., Searle, M.P., Tracy, R. & Law, R.D. (2004) Staurolite schist marks right-way up metamorphic isograds at the top of the High Himalayan Slab, Mount Everest, Tibet/Nepal. (abstract) In: Searle, M.P. Law, R.D. & Godin, L. (convenors) Programme and abstracts for conference on: Channel Flow, Ductile Extrusion and Exhumation of Lower-mid Crust in Continental Collision zones, 6th-7th December 2004, Geological Society, London.

Searle, M.P., Law, R.D., **Jessup, M.J.** & Simpson, R.L. (2004) Crustal structure, restoration and evolution of the Greater Himalaya: implications for channel flow and ductile extrusion of the middle crust. (abstract) In: Searle, M.P. Law, R.D. & Godin, L. (convenors) Programme and abstracts for conference on: Channel Flow, Ductile Extrusion and Exhumation of Lower-mid Crust in Continental Collision zones, 6th-7th December 2004, Geological Society, London.

Law, R.D., **Jessup, M.J.** & Searle M.P. (2004) Strain, deformation and vorticity of flow at the top of the Greater Himalayan slab, Everest massif, Tibet and Nepal. (abstract) In: Searle, M.P. Law, R.D. & Godin, L. (convenors) Programme and abstracts for conference on: Channel Flow, Ductile Extrusion and Exhumation of Lower-mid Crust in Continental Collision zones, 6th-7th December 2004, Geological Society, London.

Law, R.D, **Jessup, M.J.** & Searle, M.P. (2004) Strain, deformation temperatures and vorticity of flow within the Greater Himalayan Slab, Everest Massif, Tibet and Nepal. 32nd International Geological Congress, Florence, Italy. 20-28 August 2004.

Law, R. D., Cook, B. S., **Jessup, M.J.** & Searle, M. P. (2004) Strain symmetry and vorticity of flow in mylonites from the Caledonide (Norway, Scotland) and greater Himalayan Slab (Everest Massif): Implications for space problems, extrusion and exhumation: Geological Society of London, Joint meeting of the Tectonic Studies Group and the Petroleum Group - Continental Tectonics: Discussion Meeting in Memory of the Life and Work of Mike Coward. Geological Society, London, U.K. 27-28 May 2004.

Williams, M.L., Karlstrom, K.E., **Jessup, M.J.,** Jones, J.V. & Connelly, J.N. (2003) Proterozoic Rhyolite-Quartzite Sequences of the Southwest: Syntectonic "Cover" and Stratigraphic Breaks (~1695 and ~1660 Ma) Between Orogenic Pulses. Geological Society of America, Abstracts with Programs, v. 35, no. 5, p. 42.

Jessup, M.J., Karlstrom, K.E., Connelly, J.N., Jones, J.V. & Williams, M.L. (2002a) Tectonic evolution if the Black Canyon of the Gunnison, Colorado: New U/Pb geochronology and evidence for both Paleoproterozoic and Mesoproterozoic deformation and metamorphism. Geological Society of America, Abstracts with Programs, v. 34, no. 6, p. 181.

Jessup, M.J., Karlstrom, K. E., Connelly, J.N. & Livaccari, R.F. (2002b) Complex crustal assembly of southwestern north America involving northwest and northeast-striking fabrics: The Black Canyon of the Gunnison, southern Colorado. Geological Society of America Abstracts with Programs, v. 34, no. 4, p. 48.

Jessup, M.J., Karlstrom, K.E. & Shaw, C.A. (2001) Cross section of Proterozoic rocks of the Black Canyon, Colorado and use of dated plutons as "snap shots" of evolving deformational conditions: Geological Society of America Abstracts with Programs, v. 33, no. 5, p. 43.

Jessup, M.J., Roof, S. & Reid, J.B. (1998) Examination of REE signatures in shoreline tufa, Panamint Valley, California; reconstructing Pleistocene climate change: Geological Society of America Abstracts with Programs v. 30, no. 1, p. 28.

Reid, J.B., Jr., Connolly, N.T. & **Jessup, M.J.** (1996) Conditions in Long Valley Caldera prior to the 600 yr BP Inyo Crater eruptions; is history repeating itself? Eos, Transactions, American Geophysical Union, v. 77, n. 46, p. 803.

Reid, J.B., Jr., Connolly, N.T., **Jessup, M.J.,** Pack, S.M., Polissar, P.J., Reynolds, J.L., Winship, L.J. & Hainsworth, L.J (1996) A pumice filled oxbow in the floodplain of the Owens River, Long Valley Caldera, California; clues to the events around the 600 yr BP Inyo Crater eruptions. Eos, Transactions, American Geophysical Union v. 77, no. 46, p. 80.